University of California, Irvine

The diverse roles of CDCP1 in cancer and metabolism

DISSERTATION

Submitted in partial satisfaction of the requirements for the degree of

DOCTOR OF PHILOSOPHY

In Molecular Biology and Biochemistry

by

Heather Wright

Dissertation Committee:
Professor Olga Razorenova, Chair
Professor David Fruman
Professor Craig Walsh

2017

DEDICATION

This dissertation is dedicated to

My family,
Mark Wright, Richard Wright, and Katherine Peters

In recognition of their constant love, support, and encouragement.

“Maybe you are searching in the branches

for what only appears in the roots.”

-Jalal al-Din Rumi

TABLE OF CONTENTS

DEDICATION ii

LIST OF FIGURES AND TABLES iv

LIST OF SUPPLEMENTAL FIGURES vi

LIST OF SUPPLEMENTAL TABLES viii

ACKNOWLEDGEMENTS ix

CURRICULUM VITAE xii

ABSTRACT OF DISSERTATION xvi

CHAPTER 1: INTRODUCTION 1

CHAPTER 2: CDCP1 CLEAVAGE IS NECESSARY FOR HOMO-DIMERIZATION-INDUCED MIGRATION OF TRIPLE-NEGATIVE BREAST CANCER 19

CHAPTER 3: CDCP1 DRIVES TRIPLE-NEGATIVE BREAST CANCER METASTASIS THROUGH REDUCTION OF LIPID DROPLET ABUNDANCE AND STIMULATION OF FATTY ACID OXIDATION. 48

CHAPTER 4: STRUCTURAL INSIGHTS INTO THE CDCP1 HOMO-DIMERIZATION INTERFACE 86

CHAPTER 5: SURROGATE BIOMARKERS FOR CDCP1 ACTIVITY IN BREAST CANCER 98

CHAPTER 6: CDCP1 IN LIVER DISORDERS AND WOUND HEALING 111

CHAPTER 7: DISCUSSION AND FUTURE DIRECTIONS 125

REFERENCES 134

LIST OF FIGURES AND TABLES

Figure 1.1 | CDCP1 amino acid sequence and orientation in the cell membrane……2

Figure 1.2 | CDCP1 regulation and signaling pathways……4

Figure 1,3 | Overview of lipid metabolism and microscopic measurement of oxidative phosphorylation……..……...12

Figure 1.4 | Overview of putative differential requirements of CDCP1 in a physiological setting and pathological setting……18

Figure 2.1 | CDCP1 is overexpressed and cleaved in TNBC……..…..22

Figure 2.2 | Western blot analysis demonstrating that cCDCP1 activates PKCδ, ERK 1/2, and p38 MAPK……25

Figure 2.3 | CDCP1 cleavage stimulates cell migration……27

Figure 2.4 | CDCP1 cleavage is necessary for dimer formation, which is independent of cCDCP1's phosphorylation status……..29-30

Figure 2.5 | Co-expression of Extracellular Cleaved portion of CDCP1 (ECC) inhibits cCDCP1 dimerization and downstream signaling……32-33

Figure 2.6 | ECC inhibits TNBC cell invasiveness, decreases proliferation and induces apoptosis in 3D culture……...35

Figure 2.7 | Proposed model of CDCP1 activation and signal transduction……37

Figure 3.1 | CDCP1 lowers intracellular Lipid Droplet (LD) abundance of breast cancer cells……...53

Figure 3.2 | Expression of cleaved CDCP1 isoform correlates with breast cancer cell invasiveness and causes appearance of low-lipid broken acini in 3D culture……54

Figure 3.3 | CDCP1 interacts with ACSL family of proteins involved in lipid metabolism..56

Figure 3.4 | CDCP1 regulates ACSL activity……...58

Figure 3.5 | Low lipid content favors pro-migratory phenotype of TNBC……..60-61

Figure 3.6 | CDCP1 knockdown reduces FAO in TNBC cells……63

Figure 3.7 | Expression of a CDCP1-blocking fragment, ECC, increases LD abundance and reduces metastasis……65

Figure 3.8 | CDCP1 interacts with CPT2 involved in FAO……..……..68

Figure 4.1 | CDCP1 amino acid sequence and notable features for modeling dimerization……88

Figure 4.2 | Effect of CUB domains on cCDCP1 dimerization and MDA-MB-231 invasiveness……89

Figure 4.3 | Robetta modeling and molecular dynamic simulation of CUB2 3D model…..91

Figure 4.4 | ROSIE docking of CUB2-CUB2 homo-dimers……93

Figure 4.5 | Validation of putative residues involved in dimerization by split luciferase assay…… 94

Figure 5.1 | CDCP1 cleavage in primary tissue can be analyzed by Western blot……...101

Figure 5.2 | Phospho-PKCδ Y311 can be detected by IHC……102

Figure 5.3 | Correlation of CDCP1 cleavage and PKCδ phosphorylation……104

Figure 6.1 | CDCP1 knockout mice have more lipid accumulation in the liver than CDCP1 heterozygous mice……114

Figure 6.2 | CDCP1 mRNA expression in mouse skin during wound healing……...116

Figure 6.3 | CDCP1 KO mouse keratinocytes have deficient migratory potential……117

Table 1.1 | Definitions of MetS (adapted from *Huang. 2009, Dis Model Mech.*)……16

LIST OF SUPPLEMENTAL FIGURES

Supplemental Figure 2.1 | CDCP1 is expressed and cleaved in primary human TNBC samples……..148

Supplemental Figure 2.2 | Phosphorylation of cCDCP1 is induced by hypoxia……149

Supplemental Figure 2.3 | Schematics of CDCP1 constructs……150

Supplemental Figure 2.4 | Membrane localization of CDCP1 overexpressed in HEK 293T cells……151

Supplemental Figure 2.5 | CDCP1 cleavage stimulates cell migration……..152

Supplemental Figure 2.6 | Y734F mutation in cCDCP1 disrupts its phosphorylation and downstream signaling to PKCδ……...153

Supplemental Figure 2.7 | CDCP1 cleavage is necessary for dimer formation……154

Supplemental Figure 2.8 | flCDCP1 does not form a homo-dimer with flCDCP1 or heterodimer with cCDCP1 as judged by split-luciferase assay……..155

Supplemental Figure 2.9 | ECC does not interfere with CDCP1 expression or firefly luciferase function……156

Supplemental Figure 2.10 | ECC staining in 3D……157

Supplemental Figure 3.1 | CDCP1 interacts with proteins involved in metabolism……..158

Supplemental Figure 3.2 | Lipid types affected by CDCP1 expression……159

Supplemental Figure 3.3 | All antibodies used for PLA in Figure 3 work for immunofluorescence……160

Supplemental Figure 3.4 | ACSL3 knockdown increases invasiveness and metastasis of TNBC cells……161

Supplemental Figure 3.5 | Representative images of migration assays at 0 hours (T0) and 6 hours (T6) after Triacsin C addition (5 μM) used for quantitation in Figure 5…....162

Supplemental Figure 3.6 | ACSL3 increases TNBC cell proliferation and CDCP1 does not……...163

Supplemental Figure 3.7 | CDCP1 knockdown increases LD abundance and decreases ORR, which can be rescued by ACSL3 co-knockdown……...164

Supplemental Figure 3.8 | CDCP1 knockdown reduces ORR, indicating that they become less oxidative, and FAO in TNBC……165

Supplemental Figure 3.9 | Etomoxir increases LD abundance and reduces migration of TNBC cells……166

Supplemental Figure 3.10 | CDCP1 knockdown does not affect mitochondrial mass of cells……167

Supplemental Figure 3.11 | Expression of a CDCP1-blocking fragment, ECC, increases LD abundance and reduces metastasis of UCI-082014 and MDA-MB-231 tumors……168

Supplemental Figure 3.12 | Myc expression analyzed by Western blot in the cell lines used in Figures 1 and 2……169

LIST OF SUPPLEMENTAL TABLES

Supplemental Table 2.1: Characterization of cell lines……170

Supplemental Table 3.1: CDCP1 interacts with lipid metabolism proteins……...171

Supplemental Table 1: Antibodies……..172-175

Supplemental Table 2: Primers……..176-180

ACKNOWLEDGEMENTS

I would like to acknowledge all of the people in my life who contributed to making this thesis possible. My parents, Mark Wright and Katherine Peters, and my brother, Richard Wright. My dad has been the biggest influence in my life; a beacon of stability, encouragement, and adventure. He is the strongest person I know and I am eternally grateful for his existence and how he raised me and my brother. I think it was his constant reminder that his home was always open and that I could and should take a break from everything whenever I wanted was an odd sort of driver to find and do the things that I did not feel the need to take a break from, like science.

My best friends Maggie Jordan, Cristina Parker, and Madison Broderick as well as other friends from high school, college, and graduate school kept me grounded and sane throughout the whole process. Not many people have a group of friends that they consider siblings and have known for half of their life. I am extremely thankful that I have Maggie, Cristina, and Madison. I would be a basket case-weirdo if I did not have them to pull me out of my bubble grad school life to laugh, get silly, and explore the beautiful planet.

My boyfriend, Jeremy, has been my true partner during the last portion of my doctoral studies. His mid-west attitude is a lovely respite when I am feeling very stressed. I appreciate our scientific debates and the wisdom that he has shared from his trip through graduate school. I have a wealth of adventurous memories with him tucked away that have made me a more interesting and passionate person in general. In the same line as this I would like to acknowledge that I would be a hollow person if I had never discovered and explored my passion for running, yoga, backpacking, and live music. When I think about why I enjoy doing research I think about the quote on the Dedication Page by

Jalaluddin Rumi. My interpretation is that we must look deeper than a phenotype to understand and correct it.

Olga Razorenova took a chance on me my first year and maintained trust in my creative and experimental decisions. I would not have become nearly as independent and confident a scientist if it were not for her mentorship. I would also like to acknowledge my committee members David Fruman and Craig Walsh for their interesting conversations, academic advice, and constructive criticism which helped guide my projects towards publication.

I would like to acknowledge Peter Donovan, who acted as a second mentor and was instrumental in guiding my professional development. He let me bend his ear to the point of nearly breaking it off on more occasions than I'd like to mention and was an invaluable source of wisdom through some of the oddest times in my graduate career. However, he still owes me a beer.

I am lucky to have worked with Jordan Thompson and Luke Nelson. I appreciated Luke's truly awful jokes and exquisite cocktail making skills. Both of them were also extremely helpful and informative during lab meetings. I hope that I enjoy my post-doc lab mates as much as them.

My undergraduate student, Binzhi Xi, is relentlessly curious and excited about science. He made teaching fun for me and I hope that his future is full of great scientific achievements.

I'd also like to acknowledge my collaborators Jue Hou, Bruce Tromberg, Alice Police, and Erin Lin. Jue was amazing to work with and Bruce is a wealth of knowledge. Alice was an amazing mentor and I am thankful for her allowing me to attend weekly

Tumor Board meetings. I am also very thankful for her support and advice during troubled times during my PhD. Furthermore, I am grateful to Alice and Erin for providing fresh breast cancer tissue to me for my first publication.

The department of Molecular Biology and Biochemistry administration needs to be acknowledged for helping me apply for the F31 (Joyce Penh) and all of the other paperwork required for traversing my PhD (Morgan Oldhamm, Bessy Varela, and Cecilia Arceo).

Finally, I would like to thank the funding sources that supported this thesis work. The NCI F31CA196226 fellowship awarded to me for up to three years of support. The Concern Foundation Award CF-204722 grant awarded to my advisor, Olga Razorenova, for supporting the cost of the experiments I performed. The NCI R01CA142989, NIBIB P41EB015890, and Arnold and Mabel Beckman Foundation Award grants awarded to our collaborator, Dr. Bruce Tromberg, for funding a substantial amount of work presented in Chapter 3.

The text of Chapter 2 and Chapter 3 of this dissertation is a reprint of the material as it appears in “CDCP1 cleavage is necessary for homodimerization-induced migration of triple-negative breast cancer,” which was co-authored by Janahan Arulmoli, Maryam Motazedi, Luke Nelson, Scott Heinemann, Lisa Flanagan, and Olga Razorenova; and “CDCP1 drives triple-negative breast cancer metastasis through reduction of lipid droplet abundance and stimulation of fatty acid oxidation,” currently in press, which was co-authored by Jue Hou, Binzhi Xu, Marvin Cortez, Eric Potma, Bruce Tromberg, and Olga Razorenova.

CURRICULUM VITAE

Heather Wright

EDUCATION

B.S. in Chemistry, concentration in Biochemistry, 2012
Minor in Physics
San Jose State University, San Jose, CA
GPA: 3.7

Ph. D. in Molecular Biology and Biochemistry, 2017
UC Irvine, Department of Molecular Biology & Biochemistry
Advisor: Olga Razorenova, PhD
GPA: 3.95

Dissertation Research: Investigated the mechanisms of activation and signaling through the transmembrane glycoprotein, CDCP1, and its role in cancer progression of metastasis. Used triple-negative breast cancer (TNBC) as a model system to analyze the benefit of inhibiting CDCP1 function on migration and metastasis using molecular biology techniques and an orthotopic mouse model of TNBC metastasis. Developed a small biologic to inhibit CDCP1 function.

RESEARCH TRAINING

GRADUATE

01/2013-04/2013 **Research Rotation**
UC Irvine, Department of Molecular Biology & Biochemistry
Christopher Hughes, PhD

Developed a fibrin gel bead assay for three- dimensional *in vitro* drug screening platform. Conducted screening using the UCI drug library and a library of drugs from NCI in the bead assay to identify candidates that exhibit anti-angiogenic phenotypes. Investigated the effects of these drugs in 2D (monolayer) and 3D (bead assay).

09/2012-12/2012 **Research Rotation**
UC Irvine, Department of Pharmacology
Young Jik Kwon, PhD

Investigated methods to simultaneously express and silence antagonistic genes for synergistic gene therapy. Synthesized chimeric nanoparticles (ChNPs) containing an AAV core surrounded by siRNA against encased in a positively charged polymeric shell. Investigated the efficiency of these ChNPs to simultaneously express a tumor suppressor (TNF) and silence an oncogene (FLIP) and effect on viability in multiple prostate cancer cell lines.

05/2011-08/2011 **NSF Biological Research Experience for Undergraduates**
Johns Hopkins University, Biology Department
Xin Chen, PhD

Studied the epigenetic regulation of *D. melanogaster* germ cell differentiation from a stem cell lineage. Discovered that *bam* is post-transcriptionally regulated in stem cell niche via miR-275 induced translation inhibition. Found an application to mammalian *bam* ortholog.

09/2008-05/2012 **Laboratory Research**
San Jose State University, Chemistry Department
Elaine Collins, PhD

Investigated Tat peptide- TAR RNA interaction in HIV virus. Synthesized Tat peptide variants to apply as biotherapeutics to inhibit this interaction. Tested their ability to competitively inhibit WT Tat peptide interaction with TAR RNA using isothermal titration calorimetry.

TEACHING ASSISTANCESHIPS (University of California, Irvine)

2015, winter quarter	M98B: Biochemistry (lecture)
	M125: Molecular Biology of Cancer (lecture)
2014, spring quarter	M118L: Microbiology Laboratory
	M125: Molecular Biology of Cancer (lecture)
2014, winter quarter	M118L: Microbiology Laboratory
	B25: Biology of Cancer (lecture)

PUBLICATIONS

Wright HJ, Hou J, Xi B, Cortez M, Potma EO, Tromberg BJ, Razorenova OV. (**2017**)**.** CDCP1 drives triple-negative breast cancer metastasis by reducing lipid droplet abundance and stimulating fatty acid oxidation. *PNAS*, In Press.

Wright HJ, Police AM, Razorenova OV. (**2016**). Targeting CDCP1 dimerization in triple-negative breast cancer. *Cell Cycle*, 15(18):2385-6.

Arulmoli J, **Wright HJ**, Phan DT, Sheth U, Botten GA, Pathak, MM, Zarembinski TI, Yanni, DS, Razorenova OV, Hughes CC, Flanagan LA. (**2016**). Combination scaffolds of salmon fibrin, hyaluronic acid, and laminin for human neural stem cell tissue engineering. *Acta Biomateriala*, 43: 122-38.

Hou J, **Wright HJ**, Chan N, Tran R, Razorenova O, Potma E, Tromberg B. (**2016**). Correlation between Two Photon Excited Fluorescence and Seahorse Flux Analysis for Determining Breast Cancer Cellular Metabolic State. *JBO*, 0001;21(6): 060503.

Wright HJ, Arulmoli J, Motazedi M, Nelson LJ, Heinemann, FS, Flanagan L, Razorenova OV. (**2016**). CDCP1 cleavage is necessary for homodimerization-induced migration of triple-negative breast cancer. *Oncogene*, 35: 4762-72.

Eun S, Stoiber PM, **Wright HJ**, McMurdie KE, Choi CH, Gan Q, Lim C, Chen X. (**2013**) MicroRNAs downregulate Bag of marbles to ensure proper terminal differentiation in Drosophila male germline lineage. *Development*, 140:23-30.

PRESENTATIONS

Wright HJ, Arulmoli J, Motazedi M, Nelson LJ, Heinemann FS, Razorenova OV. (**2016**). CDCP1: A new therapeutic target for triple-negative breast cancer?

- Presented at the University of Copenhagen, Department of Cellular and Molecular Medicine, Max Planck Institute for Molecular Biomedicine, Dana Farber Cancer Institute, Fred Hutchinson Cancer Research Center.

Wright HJ, Arulmoli J, Motazedi M, Nelson LJ, Heinemann FS, Razorenova OV. (**2015-2016**). CDCP1 cleavage is necessary for homodimerization-induced migration of triple-negative breast cancer.

- Presented at San Antonio Breast Cancer Symposium, AACR Annual Meeting, and Gordon Research Conference: Mammary Gland Biology, **poster presentation**.

Wright HJ, Arulmoli J, Motazedi M, Nelson LJ, Heinemann FS, Razorenova, OV. (**2015-2016**). CDCP1 cleavage is necessary for homodimerization-induced migration of triple-negative breast cancer.

- Presented at Chao Family Comprehensive Cancer Center Research in Progress Series, **oral presentation**.

Wright HJ, Arulmoli J, Motazedi M, Quintero Salazar M, Nelson LJ, Heinemann FS, Razorenova, OV. CDCP1 cleavage is necessary for homodimerization-induced migration of triple-negative breast cancer.

- Presented at Department of Molecular Biology and Biochemistry Research in Progress Seminar, **oral presentation**.

Wright HJ, Motazedi M, Quintero Salazar M, Razorenova OV. (**2015**). Investigating the mechanism of CDCP1 activation to inhibit CDCP1-mediated metastasis of triple-negative breast cancer.

- Presented at Campus Wide Symposium on Basic Cancer Research, **poster presentation**.

Wright HJ, Motazedi M, Razorenova OV. (**2015**). Investigating the mechanism of CDCP1 activation to inhibit CDCP1-mediated metastasis.

- Presented at Department of Molecular Biology and Biochemistry Research in Progress Seminar, **oral presentation**.

Wright HJ, Motazedi M, Razorenova OV. (**2015**). Investigating the mecahnism of CDCP1 activation to inhibit CDCP1-mediated metastasis.

- ❖ Presented at Molecular Biology & Biochemistry Departmental Retreat, **oral presentation**.

Wright, HJ, Tran BG, Razorenova OR. (**2014**). Investigating the mechanism of CDCP1 activation and its role in breast cancer metastasis.

- ❖ Presented at Department of Molecular Biology & Biochemistry Retreat, **poster presentation**.

Wright HJ, Tran BG, Razorenova OV. (**2014**). Investigating the mechanism of CDCP1 activation in cancer.

- ❖ Presented at Department of Molecular Biology and Biochemistry Research in Progress Seminar, **oral presentation**.

Wright H, Eun SH, Gan Q, Chen X. (**2011**). *bag-of-marbles* is post-transcriptionally regulated in *Drosophila* male germline.

- ❖ Presented at Society for Advancement of Chicanos and Native Americans in Science, **poster presentation**.

AWARDS

2015-2018 NIH Ruth L Kirschstein Predoctoral National Research Service Award
2012 Anfinsen-Morgan Fellowship, Johns Hopkins University
2010 John A. Neptune Scholarship for Academic Excellence, SJSU

HONORS

2014 Honorable Mention, NSF Graduate Research Fellowship Program
2012 Cum Laude, SJSU
2010-2012 Golden Key Honor Society, SJSU
2008-2012 Dean's Honor List, SJSU

COMMUNITY PROJECTS

2015 **Equal Pay Day (April 14th, 2015)**
University of California, Irvine
2010 **Development of High School Curriculum on Biofuels**
San Jose State University and San Jose School District

ABSTRACT OF DISSERTATION

The diverse roles of CDCP1 in cancer and metabolism

By

Heather Wright

Doctor of Philosophy in Molecular Biology and Biochemistry

University of California, Irvine, 2017

Professor Olga Razorenova, Chair

CUB Domain Containing Protein 1 (CDCP1) is a transmembrane glycoprotein that has mainly been implicated in driving migration and metastasis of carcinoma cells. We focus on its role in triple-negative breast cancer (TNBC) metastasis, liver metabolic disorders (metabolic syndrome, non-alcoholic fatty liver disease, and type-2 diabetes mellitus), and wound healing.

In TNBC cells, we uncovered a novel mechanism of CDCP1 activation via cleavage and homo-dimerization to promote trans-phosphorylation of its downstream target, PKCδ, by Src kinase. Furthermore, we uncovered a novel role of CDCP1 as a regulator of lipid metabolism in TNBC. We found that CDCP1 reduces cytoplasmic lipid droplet (LD) abundance and promotes fatty acid β-oxidation (FAO) in TNBC cells. We found that CDCP1 regulates lipid metabolism partially by reducing Acyl-CoA Synthetase Ligases (ACSLs). All of this leads to CDCP1-induced TNBC metastasis, which can be inhibited by blocking CDCP1 homo-dimerization via overexpression of the extracellular portion of cleaved CDCP1 (ECC). ECC reduces phosphorylation of PKCδ and increases

ACSL activity and LD abundance in TNBC cells to reduce metastasis of TNBC tumors to the lungs.

Physiologically, we found that CDCP1 regulates LD abundance in the livers of mice; CDCP1 knockout (KO) mice had higher LD abundance than CDCP1 heterozygous (Het) mice. We also found that CDCP1 KO mice had reduced wound healing capacity of dermal punch biopsy wounds compared to CDCP1 Het mice.

Further, we present preliminary findings in the quest to identify important residues in CDCP1 dimerization and the development of a surrogate biomarker of CDCP1 activity in breast cancer.

Combined, these studies give a comprehensive look at the broad range of pathological and physiological effects CDCP1 has and contributes groundwork for future investigation into these diverse and potentially organ-type specific roles of CDCP1.

CHAPTER 1: INTRODUCTION

Opening Statement. The work presented here focuses on the protein complement C1r/C1s, Uegf, Bmp1 (CUB)-domain containing protein 1 (CDCP1) primarily in the context of triple-negative breast cancer (TNBC). This work presents a novel mechanism of CDCP1 regulation through homo-dimerization and a novel pathway regulated by CDCP1, lipid metabolism. This work demonstrates that both CDCP1 homo-dimerization and regulation of lipid metabolism are interconnected and drive metastasis. The physiological role of CDCP1 is also demonstrated in the context of liver disease and wound healing. Finally, the potential of a surrogate biomarker to detect CDCP1 activity in breast cancer is demonstrated and discussed.

But first to introduce our protein of interest…

The discovery of CDCP1. CDCP1, also known as SIMA135 , Trask, and CD318, is a type-1 transmembrane glycoprotein initially identified using representational difference analysis and cDNA chip technology in a comparison between normal colon and colorectal cancer tissue[1]. It was then identified by subtractive immunization two years later in multiple carcinoma cell lines[2]. CDCP1 contains an N-terminal signal peptide used for its translocation from the endoplasmic reticulum (ER) to the cell membrane where it is expressed[2]. CDCP1 contains 12 extracellular asparagine residues that are putative sites of glycosylation. This is evident by the difference in the predicted molecular weight (92 kDa) and the actual molecular weight of the full-length form of CDCP1 (flCDCP1, ~140 kDa). The role of glycosylation in CDCP1 activity has yet to be determined.

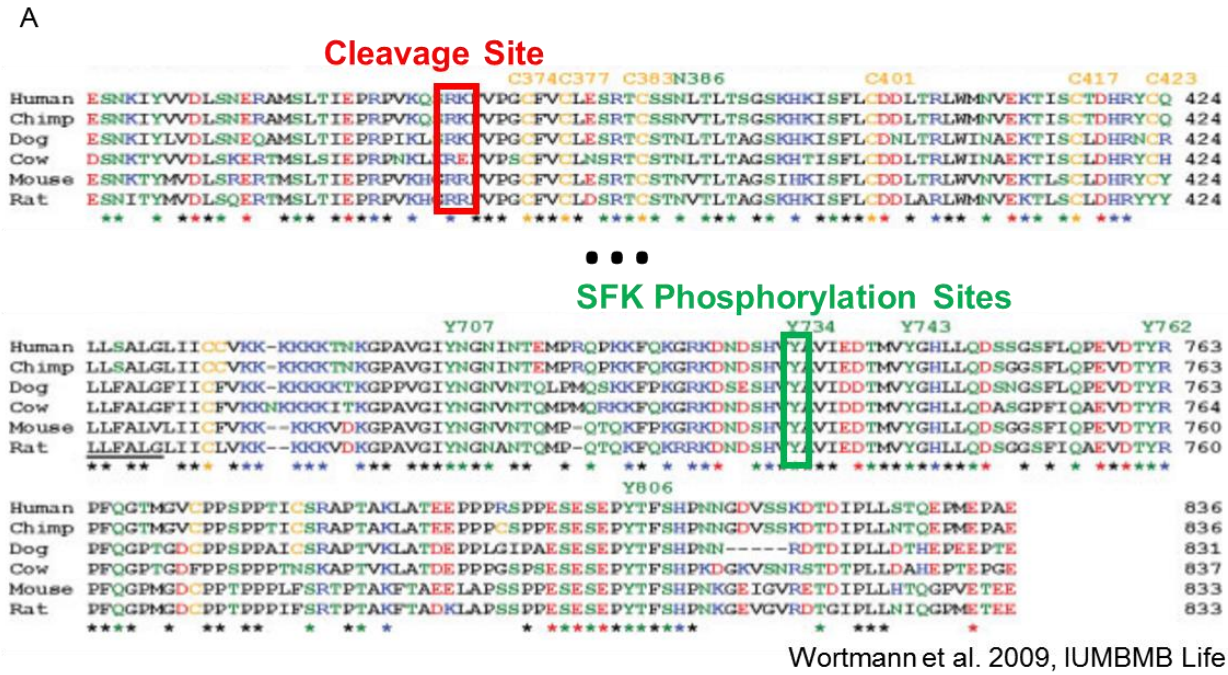

Wortmann et al. 2009, IUMBMB Life

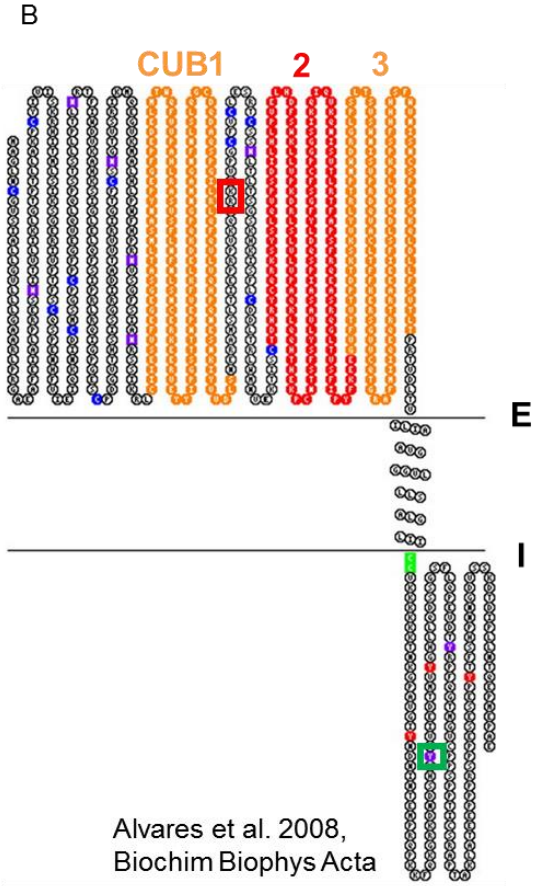

Figure 1.1 | CDCP1 amino acid sequence and orientation in the cell membrane. A) The CDCP1 amino acid sequence is highly conserved among vertebrate species. Important features of CDCP1 in these studies are its extracellular cleavage site (red box) and intracellular tyrosine (Y) phosphorylation sites, specifically Y734 (green box). The gap in sequence from amino acids 424-678 is represented by the (…) between amino acids 424 and 713. This figure was adapted from *Wortmann et al. 2009, IUMBMB Life*. **B**) CDCP1 is a type I-transmembrane protein. It's N'terminus is expressed extracellularly (E) where CUB1-3 reside with the cleavage site between CUBs 1 and 2 (red box). There is a single-pass transmembrane domain and a small intracellular domain where there are 5 sites of putative Y-phosphorylation, Y734 is represented in the green box. This figure was adapted from *Alvares et al. 2008, Biochim Biophys Acta*.

CDCP1 regulation and signaling. CDCP1's protein sequence is highly conserved among vertebrate species including the sites of extracellular cleavage and intracellular phosphorylation[3] (Figure 1.1A). The full-length form of CDCP1 (flCDCP1) contains three CUB domains, CUB1, 2, and 3, in its extracellular domain (Figure 1.1B). CUB domains are known to be involved in protein-protein interactions[4-6] and are the site of regulation of proteins containing them during development[7]. CDCP1 can be cleaved by serine proteases trypsin, plasmin, and matriptase,[8-12] between CUB1 and CUB2 resulting in a 70 kDa membrane bound fragment (cCDCP1) and a 65 kDa fragment that is released into the extracellular space. CDCP1 interacts with multiple proteins at the cell surface. Among these are membrane proteins β1-integrin[13], HER2[14], cytoplasmic proteins Src family kinases (SFKs)[15, 16] and PKCδ[5, 17], contributing to cell migration. CDCP1 can be phosphorylated at five tyrosine (Y) residues on its intracellular domain by SFKs[11]. There is indication that phosphorylation of CDCP1 at multiple residues is required for Yes, SFK member, binding[18], Y734 phosphorylation is required for its interaction with Src and phosphorylation of Y762 is required for its interaction with PKCδ[19] (Figure 1.2). However, in our hands this is more of a trend than a rule.

CDCP1 can be upregulated by hypoxia[17, 20], rat sarcoma (Ras)/extracellular signal regulated kinase (ERK) 1/2 signaling[21], ADAM9 metallopeptidase[22], Calveolin-1[23], and stabilized at the cell membrane by Epidermal Growth Factor (EGF) stimulation[24]. It is possible that the effect of EGF on CDCP1 protein stability is through direct interaction of EGF-bound EGF receptor (EGFR) and CDCP1 as EGFR is also known as HER1 and CDCP1 is known to directly bind another HER family member, HER2[14]. CDCP1 is downregulated by CD82/KAI1[25] and has been demonstrated as a target of miR-218 and

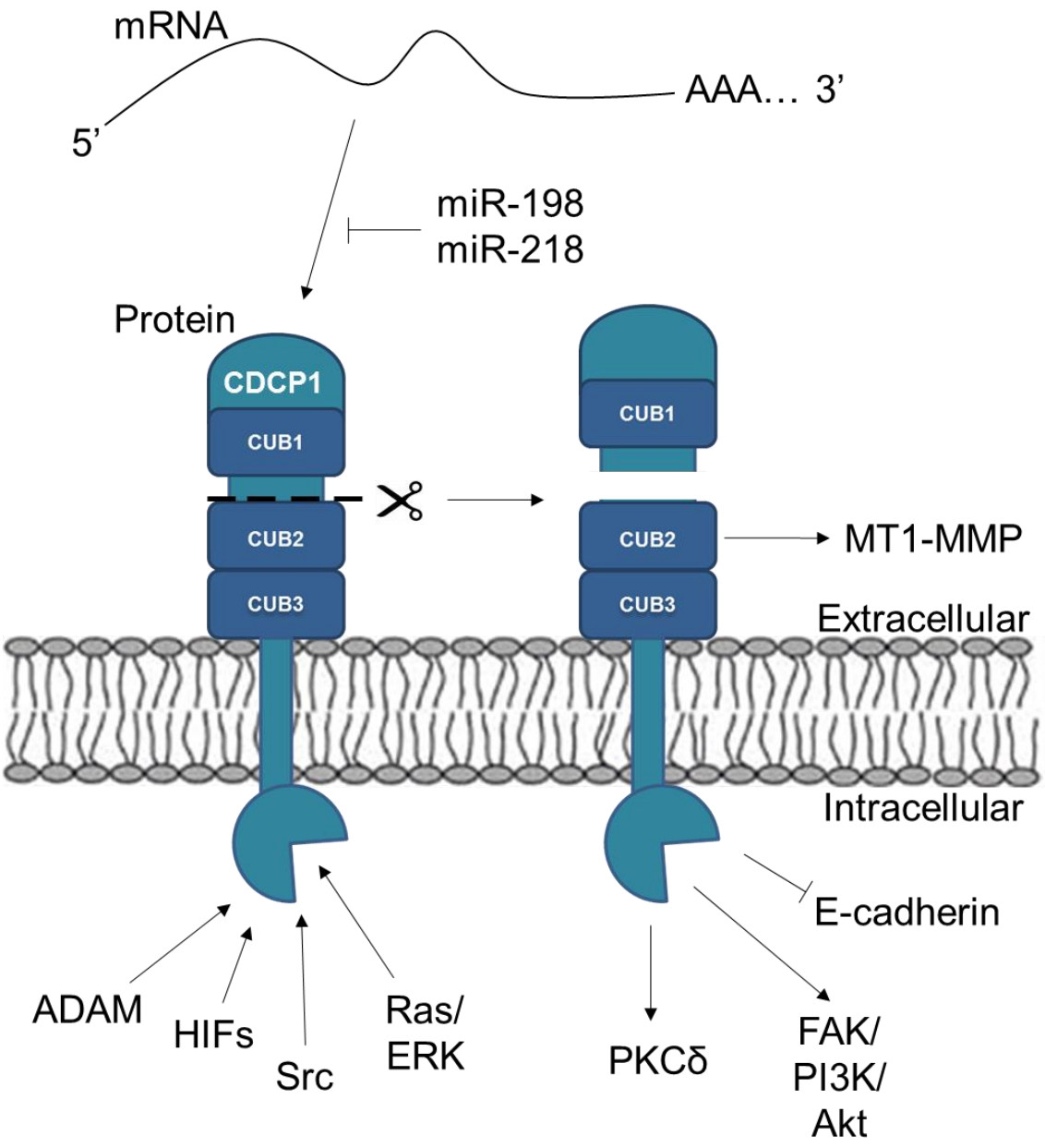

Figure 1.2 | CDCP1 regulation and signaling pathways. CDCP1 translation is inhibited by miRs 198 and 218. CDCP1 expression is activated by numerous other oncogenic pathways. CDCP1 can be cleaved on the extracellular side and stimulates multiple signaling pathways in cancer, in some cases, without having to be cleaved, like in clear-cell renal cell carcinoma.

miR-198, which act to decrease CDCP1 translation[22, 26]. CDCP1 acts as an anchor to stimulate trans-phosphorylation of PKCδ by Src[5, 17, 27]. CDCP1 has been implicated in regulating several other pathways to induce proliferation, anoikis resistance, and migration. These include stimulating FAK/PI3K/Akt pathway[13, 28], MT1-matrix metallopeptidase (MT1-MMP) activity[29], reducing E-cadherin localization at the cell membrane[30], and suppressing autophagy by an undefined mechanism[31] (Figure 1.2).

Physiological roles of CDCP1. The physiological role of CDCP1 remains to be fully established. However, CDCP1's expression has been demonstrated in human skin tissue, primarily in the epidermis and is important for keratinocyte migration, as a function-blocking antibody targeting CDCP1 reduces *in vitro* migration of keratinocytes[32]. CDCP1 expression in blood plasma has been positively correlated with age[33]. CDCP1 expression has also been demonstrated in a CD146 negative subpopulation of bone marrow fibroblasts[27]. Furthermore, CDCP1 was demonstrated as a novel marker of immature hematopoietic progenitor cell subsets[34]. This data was validated by another group who showed that the promoter of CDCP1 was not methylated in the K562 hematopoietic cell line but highly methylated in the differentiated Jurkat lymphocyte cell line[35] indicating that CDCP1 protein expression is higher in undifferentiated hematopoietic cells. Finally, copy number loss of the chromosome containing CDCP1, 3p21.31, has been associated with increased risk of hyperlipidemia of smooth muscle cells and myocardial infarction (heart attack)[36].

"CDCP1-gate": the debate of CDCP1's role in cancer. CDCP1 was initially discovered in colorectal cancer. A debate remains about CDCP1's role as a tumor-suppressor gene or an oncogene. Spassov et al. demonstrated that overexpressing CDCP1 in NIH 3T3v-src fibroblasts reduced tumor burden of these cells in mice. Furthermore, overexpressing CDCP1 in MCF7 breast cancer cells reduced metastasis in an orthotopic model of breast cancer and knocking down CDCP1 expression in L3.6pl pancreatic cancer cells increased metastasis in an orthotopic model of pancreatic cancer[37]. The Moasser group showed that germ-line knockout of CDCP1 increased tumor burden in the MMTV-PyMT spontaneous mouse model of breast cancer[38]. All of these studies allude to CDCP1's role as a tumor suppressor gene in cancer. Yet, these findings have not been reproducible in the same mouse models on different genetic backgrounds. This may indicate that their results were an artifact of the model being used and this discrepancy deserves further investigation.

However, mounting evidence supports the role of CDCP1 as an oncogene. CDCP1 is upregulated in multiple forms of carcinoma including colorectal[39], lung[40], prostate[41], ovarian[42], pancreatic[43, 44], endometrioid[45], gastric scirrhoous[46], melanoma[47], renal, triple-negative[5, 30], and non-triple negative breast cancers[14, 48]. CDCP1 has mainly been studied as a driver of anoikis resistance[31, 49] correlating with survival of metastatic cells in the blood stream, migration/invasion[5, 17, 44, 50] and multiple steps in metastasis[13, 21, 22, 28, 47, 51-53], including intravasation[13] into and extravasation[52] out of blood vessels. CDCP1 has also been implicated in stimulating proliferation of breast cancer cells[48] and tumor growth of NIH 3T3 fibroblasts[54], ovarian cancer[42], renal cancer[20], and HER2+ breast cancer[14] cell lines has also been described.

Triple-negative breast cancer. TNBCs do not express estrogen (ER) and progesterone (PR) hormone receptors or HER2 receptor. This makes them insensitive to hormone and HER2 targeted therapies that are widely used to treat non-TNBC. To date, there are no targeted therapies to treat TNBC. One third of TNBC patients that receive neoadjuvant anthracycline and taxane based chemotherapy have a pathological complete response (pCR), which is higher than the response of ER+ breast cancer. However, TNBC patients that have any residual invasive disease after neoadjuvant treatment have a significantly higher risk of recurrence and mortality than non-TNBC patients[55].

Many clinical trials have shown a statistically significant benefit for targeted therapies in combination with chemotherapies. These include everolimus, which inhibits the mammalian target of rapamycin (mTOR). TNBC patients have a 36% overall progression free survival (PFS) of 3 months in combination with carboplatin[56]. However, there was no significant benefit when combined with paclitaxel[57]. The efficacy of targeting the androgen receptor (AR) in luminal AR+ TNBCs has shown that treatment with bicalutamide resulted in a median PFS of 12 weeks[58]. Furthermore, a phase II trial using Enzalutamide demonstrated a PFS of 14.7 weeks in 10% of patients[55, 59].

On the other hand, there have been some disappointing trials. A Phase III trial using the vascular epidermal growth factor (VEGF) inhibitor, bevacizumab, failed to increase progression free survival[60]. EGFR inhibitors (gefitinib, erlotinib, afatinib, and osimertinib, erlotinib, necitumumab) currently approved for use in non-small cell lung, pancreatic, colorectal, and head and neck squamous cell carcinoma[61] have failed in multiple clinical trials in combination with chemotherapy in adjuvant and neoadjuvant

settings to treat TNBC[61]. Pre-clinical models using the bromodomain and extra-terminal (BET) protein inhibitor, JQ-1, demonstrated its efficacy in treating TNBC[62]. However, as Shu et al. describe, the heterogeneity of TNBCs makes them prone to develop resistance to JQ-1[62] and it will be interesting the see how JQ-1 performs in the clinic.

The reason for the disappointing clinical trial results may be in the fact that TNBC encompasses an extremely heterogeneous disease. It can be categorized into five clinically actionable groups: 1) basal-like TNBC with DNA-repair deficiency or growth factor pathways; 2) mesenchymal-like TNBC with epithelial-to-mesenchymal transition and cancer stem cell features; 3) immune-associated TNBC; 4) luminal/apocrine TNBC with androgen-receptor overexpression; and 5) HER2-enriched TNBC[63]. Because of this, it may be necessary to stratify clinical trials based on molecular subtyping in the future to obtain more meaningful results and personalize treatment.

TNBC overexpresses CDCP1[5, 30], reported to drive metastasis in multiple *in vivo* models[64]. While CDCP1 expression in cancer has been correlated with invasiveness, we[5] and others[13, 28, 30] have demonstrated that cleavage of CDCP1 is important for its activity in TNBC and prostate cancers. The studies presented in Chapter 2 focus on TNBC as CDCP1 is not only overexpressed but exists mostly in the cleaved form in multiple TNBC cell lines and primary human samples compared to normal breast cell lines[5, 30, 37].

Targeting CDCP1 in TNBC: To date, the CDCP1 activation cascade includes three levels: phosphorylation, cleavage, and dimerization. Currently there are antibody therapeutics developed that inhibit CDCP1 cleavage[13, 28]. There are also therapeutics capable of indirect inhibition of CDCP1 cleavage, such as dexamethasone[30], a steroid

therapeutic, and aprotinin (Trasylol) (NCT00354900, trial in advanced breast cancer terminated). However, the last two therapeutics have substantial off-target effects. Steroids in particular not only decrease patient quality of life, but may also cause disease conditions like hypertension and hyperglycemia, which increase the risk of co-morbidities. As we will demonstrate in Chapter 2, our discovery of the involvement of cCDCP1's extracellular domain (including CUB2 and CUB3) in dimerization opens up a new avenue for therapeutic development. This approach is justified by multiple successful FDA-approved therapies that inhibit homo- and hetero-dimerization of cell surface receptors driving tumor progression. These include trastuzumab targeting extracellular domain IV of HER2, inhibiting ligand-independent homo-dimerization (HER2-HER2), as well as ligand-independent hetero-dimerization (HER2-HER3 and also HER2-HER1 and HER2-HER4); pertuzumab targeting extracellular domain II of HER2, inhibiting ligand-dependent hetero-dimerization with the other HER family members, especially HER3; cetuximab targeting domain III of EGFR/HER1 inhibiting its interaction with the ligands, which is needed for a conformational change stimulating HER1 homo-dimerization or hetero-dimerization with the other HER family members. Thus, dimerization of cell surface receptors represents a rational therapeutic target and further research is needed to test the existing antibodies recognizing cCDCP1 for their ability to block its dimerization, as well as development of new antibodies specifically inhibiting dimerization. In addition the soluble extracellular fragment of cCDCP1, identified in our study as an inhibitor of cCDCP1 dimerization and its downstream signaling, represents a lead compound for development of another potent protein-based agent. Since CDCP1 cleavage stimulates

its dimerization, therapeutics blocking CDCP1 cleavage should indirectly block its dimerization.

Importantly, CDCP1 knock-out mice are viable, have no developmental and postnatal pathology, and no apparent decrease in life span as shown by Spassov et al.[64] and Wright et al. (unpublished observations), indicating that CDCP1 blocking agents should be well tolerated. In support of this, administration of antibodies that inhibit CDCP1 cleavage to mice bearing prostate tumors did not cause any notable side effects, but reduced metastatic burden[13]. Thus, CDCP1 might represent an example of a protein exploited by cancer cells to promote their metastatic ability, the function of which may be dispensable or redundant in normal cells.

CDCP1 represents a rational therapeutic target for the treatment of TNBC, where current targeted therapies are failing. Since CDCP1 is expressed and cleaved in multiple carcinomas in addition to TNBC, including prostate, colorectal, lung and pancreatic carcinomas, further research is needed to evaluate its dimerization status in those cancers, and therapeutic potential of dimerization-blocking agents.

Difficulties in targeting CDCP1 and utilizing CDCP1 as a biomarker of disease progression: Historically, bioactive compounds were isolated and used to treat disease without a complete understanding of their molecular targets[65]. With the development of X-ray diffraction in 1932 and the rapid evolution of chemical structure identification techniques since then, drug design and optimization is increasingly becoming structure-based[66]. Structure-based drug design is defined as the means of developing drugs against a target based off of the crystal structure of that target.

One big roadblock to optimizing therapeutics to inhibit CDCP1 cleavage or dimerization is that there is no structure of CDCP1 available. In Chapter 4 we describe our efforts to elucidate a chemical structure based on 3D modeling of extracellular portion of cCDCP1 (ECC), in which we believe the dimer interface lies.

As mentioned above, CDCP1 is highly cleaved in TNBC. There is evidence supporting the correlation between CDCP1 expression and decreased distant disease-free survival[67]. However, this is only when combined with node status. A less invasive measure of distant-disease free survival lies in the ability to derive the information from a biopsy or tumor resection without having to sample lymph nodes. We believe that the ability to distinguish cCDCP1 activity from flCDCP1 could solve this problem. However, there is no antibody that distinguishes cCDCP1 from flCDCP1. In Chapter 5 we describe our efforts to develop a surrogate biomarker for cCDCP1 activity, phospho-PKCδ Y311 staining.

Lipid metabolism and cancer progression. In Chapter 3, we demonstrate our discovery that CDCP1 regulates lipid metabolism. The initial phenotype identified in these studies was a significant increase in LD abundance upon knockdown of CDCP1. LDs are dynamic structures within the cytoplasm of cells. They can be visualized by multiple means (Figure 1.3A). In Chapter 3 and 6 we rely heavily on coherent anti-Stokes Raman scattering (CARS) microscopy to visualize endogenous lipids, as it is a label-free system. CARS measures the vibrational frequency in the carbon-hydrogen (C-H) bond, which is highly abundant in saturated lipids (Figure 1.3B). Lipids from LDs can be incorporated in the cell membrane, used for protein modification or enter fatty acid β–oxidation (FAO).

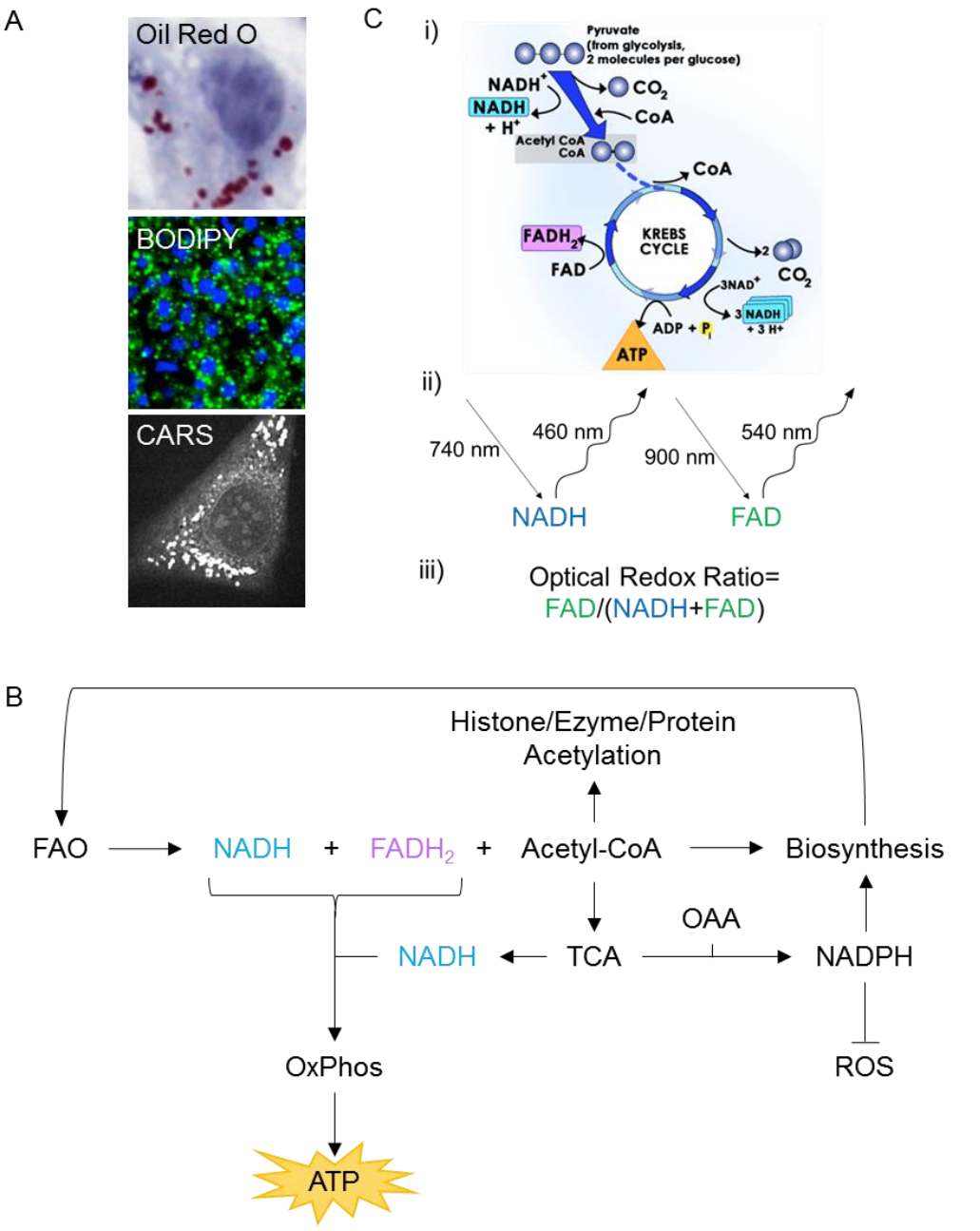

Figure 1.3 | Overview of lipid metabolism and microscopic measurement of oxidative phosphorylation. A) LDs can be visualized by various means. Shown here is colorimetric staining (Oil Red O), Fluorescent staining (BODIPY), and label free visualization by coherent anti-Stokes Raman scattering (CARS) microscopy. **B**) Diagram of the links between FAO, TCA, and OxPhos. **C**) Scheme for analyzing oxidative state of a cell. i) diagram of NADH and FAD produced/ consumed during TCA. ii) excitation and emission wavelengths used to image NADH and FAD. iii) Calculation of ORR used to determine oxidative state of cells (higher ORR= more oxidative).

The products of FAO can feed into tricarboxylic acid (TCA) cycle, oxidative phosphorylation (OxPhos), biosynthetic pathways, and protein modification pathways (Figure 1.3B). In Chapter 3 we use two-photon excited fluorescence (TPEF) microscopy to measure the rate of FAO and OxPhos in the cells. We use a surrogate calculation as a measure of OxPhos, which we call the optical redox ratio (ORR) (Figure 1.3C). ORR directly correlates with OxPhos measured by the commercially available Seahorse metabolic flux analyzer[68].

Dysregulated lipid metabolism has recently been linked to breast cancer progression. Photoacoustic imaging of the MMTV-PyMT-driven breast cancer model demonstrated that transformation of normal breast tissue to invasive carcinoma resulted in a progressive decrease of cytoplasmic LD abundance[69]. In line with this, pharmacological activation of peroxisome proliferator-activated receptor γ (PPARγ) caused accumulation of LDs in breast cancer cells and decreased their proliferation[70]. Furthermore, Src[71] and Myc[72] oncogenes were recently reported to contribute to lipid metabolism dysregulation in TNBC.

Lipid metabolism dysregulation has also been reported in other types of cancer. Pharmacological inhibition of Myc in neuroblastoma increases LD abundance, accompanied by growth arrest and apoptosis *in vitro* and increased animal survival *in vivo*[73]. High-passage prostate cancer cells (comparable to metastatic cells) have lower LD abundance than their low-passage (comparable to primary tumor) counterparts[74]. In a spontaneous mouse model of pancreatic cancer the synthesis of acyl-CoA-modified lipids was found to be the most downregulated metabolic pathway compared to normal

pancreatic tissue[75]. These data indicate that dysregulated lipid metabolism is characteristic of progression of multiple forms of cancer.

Tumor cell metastasis: Approximately 90% of cancer-related mortality is due to dispersion and expansion of cancer cells from the primary tumor to distant organs, resulting in reduced organ function and systemic organ failure. The process of cancer cells leaving primary tumors to seed other organs and form distant tumors is termed metastasis. The mechanisms underlying metastasis have been studied for over a century, when Steven Paget first coined the “seed and soil” hypothesis to explain the propensity of cancer cells to colonize certain organs over others[76]. A wealth of clinical data has since substantiated this hypothesis that organ-preference is the product of favorable interactions between metastatic tumor cells (the “seed”) and their organ microenvironment (the “soil”)[77].

Metastasis is characterized by six major steps: 1) detachment of a cancer cell from its primary tumor, 2) intravasation of the cancer cell into a vessel, 3) survival of the cancer cell in the circulatory system, 4) extravasation of the cancer cells from the vessel into the distant organ, 5) survival of the cancer cell within the distant organ, and 6) eventual colonization of the distant organ to form a metastasis[78]. The extensive findings of the molecular signaling pathways involved have been reviewed multiple times[78-85]. These include cell autonomous pathways like signaling through FAK[86], ERK[87], integrins[88], and CDCP1[64] pathways, the mutational landscape of a tumor[89], and, importantly, metabolic reprogramming[85]. Cell non-autonomous microenvironmental regulators such as hypoxia[79], extracellular matrix composition[90], and stromal cell paracrine contributions[91]

have also been strongly implicated in driving cancer progression and metastasis. All of these cell-autonomous and non-autonomous regulators are tightly intertwined with each other and the metabolic state of cancer cells[83, 92, 93]. As will be discussed further in Chapter 3, lipid metabolism has recently been highlighted as being important for metastatic potential of cancer cells[71-73].

Metabolic syndrome and wound healing. Dysregulated systemic metabolism has not only been demonstrated to drive late stages of tumor progression but has also been correlated with increased risk of developing colorectal, endometrial, renal, esophageal, pancreatic, liver, and postmenopausal breast cancers[94] as well as non-malignant diseases, such as cardiovascular problems, stroke, and type 2 diabetes mellitus. The broad set of factors that define one's risk for developing cardiovascular problems, diabetes, and cancer are referred to collectively as metabolic syndrome (Table 1.1).

Among the many side effects of type 2 diabetes mellitus morbidity, the most common cause of lower limb amputation is the establishment of chronic wounds. These wounds are unable to heal properly for many reasons including the dysregulated proliferation, migration, and differentiation of keratinocytes at the wound site[95]. As mentioned above, CDCP1 is known to be expressed in and important for the migration of keratinocytes. However, we have also seen that CDCP1 is expressed in the livers of mice, which will be discussed in more detail in Chapter 6.

Our CDCP1 knockout mouse model has yet to be fully characterized. However, we have preliminary evidence that CDCP1 expression is important in both the liver and the skin and may play dual roles in regulating liver metabolic function and proper wound

Table 1.1 | Definitions of MetS (adapted from *Huang. 2009, Dis Model Mech.*).

	NCEP ATP III (2005 revision)	WHO (1998)	EGIR (1999)	IDF (2005)
Absolutely required	None	Insulin resistance* (IGT, IFG, T2D or other evidence of IR)	Hyperinsulinemia‡ (plasma insulin >75th percentile)	Central obesity (waist circumference§): ≥94 cm (M), ≥80 cm (F)
Criteria	Any three of the five criteria below	Insulin resistance or diabetes, plus two of the five criteria below	Hyperinsulinemia, plus two of the four criteria below	Obesity, plus two of the four criteria below
Obesity	Waist circumference: >40 inches (M), >35 inches (F)	Waist/hip ratio: >0.90 (M), >0.85 (F); or BMI >30 kg/m^2	Waist circumference: ≥94 cm (M), ≥80cm (F)	Central obesity already required
Hyperglycemia	Fasting glucose ≥100 mg/dl or Rx	Insulin resistance already required	Insulin resistance already required	Fasting glucose ≥100 mg/dl
Dyslipidemia	TG ≥150 mg/dl or Rx	TG ≥150 mg/dl or HDL-C: <35 mg/dl (M), <39 mg/dl (F)	TG ≥177 mg/dl or HDL-C <39 mg/dl	TG ≥150 mg/dl or Rx
Dyslipidemia (second, separate criteria)	HDL cholesterol: <40 mg/dl (M), <50 mg/dl (F); or Rx			HDL cholesterol: <40 mg/dl (M), <50 mg/dl (F); or Rx
Hypertension	>130 mmHg systolic or >85 mmHg diastolic or Rx	≥140/90 mmHg	≥140/90 mmHg or Rx	>130 mmHg systolic or >85 mmHg diastolic or Rx
Other criteria		Microalbuminuria†		

*IGT, impaired glucose tolerance; IFG, impaired fasting glucose; T2D, type 2 diabetes; IR, insulin resistance; other evidence includes euglycemic clamp studies.
†Urinary albumin excretion of ≥20 μg/min or albumin-to-creatinine ratio of ≥30 mg/g.
‡Reliable only in patients without T2D.
§Criteria for central obesity (waist circumference) are specific for each population; values given are for European men and women.
Rx, pharmacologic treatment.

repair which can both be studied in the context of type 2 diabetes mellitus and metabolic syndrome.

As discussed above, CDCP1 plays a role in normal physiology and we will present evidence that it acts to suppress the development of metabolic syndrome, allowing us to hypothesize that CDCP1 may physiologically act to prevent tumorigenesis.

Closing statement: These studies give novel insight into the mechanism of activation and signaling of CDCP1 in pathological and physiological systems. They also demonstrate that CDCP1 may function bimodally in the body: 1) physiologically regulating lipid homeostasis to suppress diseased states and 2) upon transformation of a cell into a cancer cell, pathologically driving cancer metastasis (Figure 1.4).

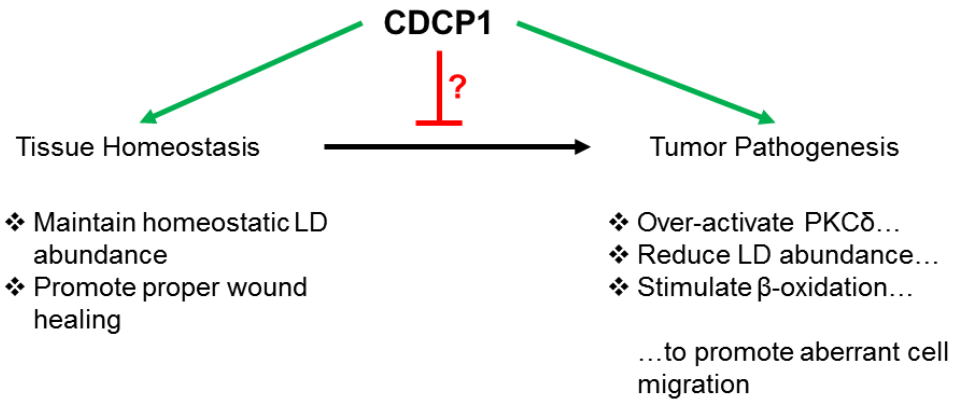

Figure 1.4 | Overview of putative differential requirements of CDCP1 in a physiological setting and pathological setting. Physiologically, CDCP1 seems to maintain liver LD abundance at a homeostatic level, which may prevent disease development. However, once cells are transformed, overactivated CDCP1 reduces LD abundance to promote aberrant cell migration.

CHAPTER 2: CDCP1 CLEAVAGE IS NECESSARY FOR HOMO-DIMERIZATION-INDUCED MIGRATION OF TRIPLE-NEGATIVE BREAST CANCER

Introduction

Breast cancer is the second leading cause of death of women in the United States; most of these fatalities are caused by metastatic disease. Many therapies have been developed to target aggressive breast cancer, including receptor-targeted therapies (Herceptin) and anti-hormone therapies (aromatase inhibitors). However, triple-negative breast cancer (TNBC) patients are not candidates for many of these therapies as they do not express the respective drug targets, HER2, estrogen, and progesterone receptor. Moreover, TNBC is a highly aggressive form of breast cancer that is associated with advanced stage at diagnosis, early peak of recurrence and poorer outcome in comparison to non-TNBCs; in the advanced setting responses to chemotherapy and radiation therapy lack durability [96]. Finally, women who are diagnosed with TNBC tend to be younger than non-TNBC patients. Thus, there is an urgent need to develop a targeted therapy to inhibit the progression and metastasis of TNBC.

The transmembrane protein, CUB-domain containing protein 1 (CDCP1), is upregulated in TNBC and is correlated with the cancer's aggressiveness [30]. Importantly, CDCP1 is involved in metastasis in multiple animal models of cancer, including lung adenocarcinoma, gastric scirrhous carcinoma, melanoma, and prostate and ovarian carcinomas [13, 28, 41, 42, 46, 47, 49]. The many signaling pathways induced by CDCP1 have been described in Chapter 1. Importantly, CDCP1 activity seems to be dependent on cleavage. In addition to cleavage, CDCP1 activity depends on phosphorylation and both

flCDCP1 and cCDCP1 are phosphorylated by Src Family Kinases (SFKs), Src, Fyn, and Yes first at Y734 and then at Y743, Y762, Y707, and Y806 [2, 11, 15, 16, 19, 48, 49, 97, 98]. CDCP1 can stimulate migration/invasion through a variety of signaling pathways, including PKCδ [17, 44], Protein Kinase B (Akt) [13, 28, 42], β_1 integrin [13], matrix metalloproteinase secretion [29], and others. Besides its well established role in cancer cell migration, CDCP1 was reported to degrade adherens junctions [15, 30], protect against anoikis [49], and inhibit autophagy [31] contributing to tumor progression.

CDCP1 contains three CUB-domains located in its ectodomain, the specific role of which remains unclear. CUB domains are expressed in many developmentally regulated proteins and participate in interactions with CUB domains of other proteins [7]. The first CUB domain is removed upon CDCP1 cleavage, potentially stimulating important protein-protein interactions through CUB2 and CUB3, leading to the enhancement of CDCP1 signaling. Casar et al. recently reported the decrease in metastasis upon inhibition of CDCP1 cleavage, hinting at the necessity of cleavage for CDCP1 activity [13, 28]. In support of this, Law et al. showed that inhibition of CDCP1 cleavage refined the borders of *ex vivo* tumors, proposing the inhibition of CDCP1 cleavage as a rational neoadjuvant therapeutic for TNBC [30]. Although these data indicate that CDCP1 cleavage stimulates its activity, the mechanism of cCDCP1 activation has not been elucidated.

Here, we demonstrate that CDCP1 expression is upregulated in TNBC and it is cleaved and phosphorylated in TNBC cell lines and primary TNBC specimens. We find that CDCP1 cleavage leads to cCDCP1 homo-dimerization, uncovering the mechanism of cCDCP1 activation. The homo-dimer acts as a docking station for Src to induce phosphorylation of a key CDCP1 downstream target, PKCδ, stimulating pro-migratory

signaling. We provide evidence that dimerization is a key step in CDCP1 activation by breaking dimerization with the extracellular portion of cCDCP1 (ECC), which blocks CDCP1's downstream signaling, leading to inhibition of migration, invasion, proliferation, and induction of apoptosis. Therefore, CDCP1 dimerization is a rationale target for therapeutic intervention to inhibit metastasis of TNBC.

Results

CDCP1 is overexpressed and cleaved in TNBC. The data acquired from The Cancer Genome Atlas (TCGA, http://cancergenome.nih.gov/) indicated that *CDCP1* mRNA is upregulated in TNBC compared to normal breast tissue (Figure 2.1A), suggesting CDCP1's role in breast cancer progression. Consistent with the data extracted from TCGA, we found that the average CDCP1 expression in MDA-MB-231, MDA-MB-453, MDA-MB-468, and UCI-082014 (Supplemental Table 2.1) TNBC cells was 1.8 fold higher than the average expression in Primary Mammary Epithelium (PME) and immortalized non-tumorigenic MCF10A breast cells (Figure 2.1B).

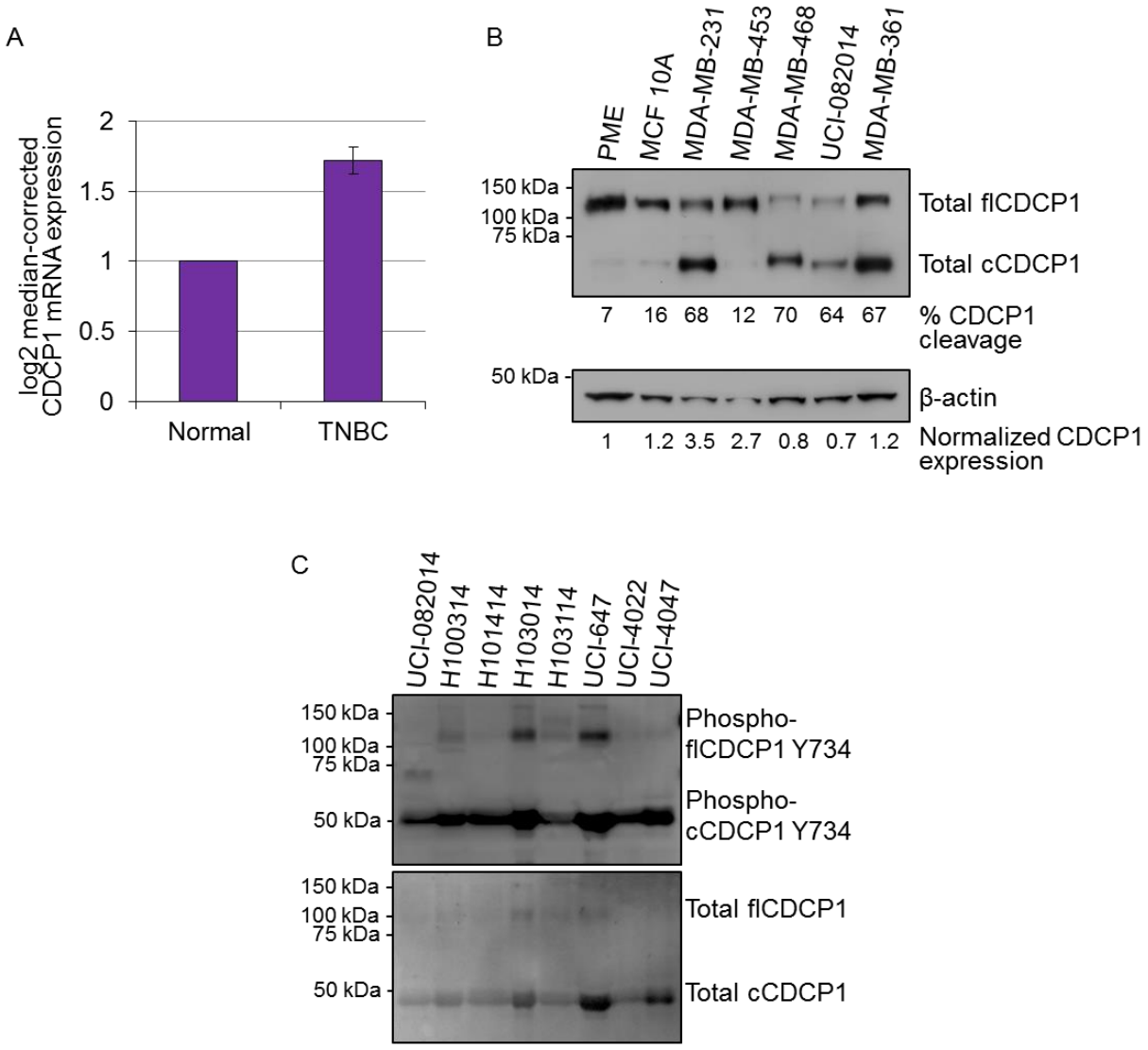

Figure 2.1 | CDCP1 is overexpressed and cleaved in TNBC. (**a**) TCGA data showing normalized mRNA expression of CDCP1 in 57 TNBC and matched normal tissue samples, P=0.002 calculated by one-way ANOVA with multiple comparison post hoc T-test and error bars represent SEMs. (**b**) Western blot analysis of CDCP1 expression in breast cancer cell lines. CDCP1 is mostly full length in PME cells and the immortalized, non-tumorigenic breast cell line, MCF10A, and is mostly cleaved in TNBC cell lines and metastatic non-TNBC cells, MDA-MB-361. Quantitated percent of CDCP1 cleavage was obtained by band densities in ImageJ (top row)=(2)*100. Quantitated relative CDCP1 expression was obtained by band densities in ImageJ (bottom row)=(flCDCP1+cCDCP1)/β-actin, CDCP1 expression in PME was normalized to 1 and all other lanes were normalized to that for comparison. (**c**) Primary human TNBC samples express cleaved and phosphorylated CDCP1. Equal protein amounts were loaded in each lane.

Recent reports indicated that cleavage stimulates CDCP1 protein activity [9, 13, 28, 30]. Figure 2.1B shows that CDCP1 is highly cleaved in all of the TNBC cell lines listed above (54% cleaved) compared to PME and MCF10A cells, where CDCP1 exists primarily in the full-length form (12% cleaved). We also found that CDCP1 is cleaved in the non-TNBC cell line derived from a brain metastasis, MDA-MB-361 (Figure 2.1B). Furthermore, we found that eight out of eight TNBC patient samples analyzed by Western blot express CDCP1, which is mostly cleaved and phosphorylated (Figure 2.1C and Supplemental Figure 2.1).

Previously, we and others have shown CDCP1 expression is regulated by Hypoxia Inducible Factors (HIFs) in ccRCC [17, 20]. Since breast tumors contain areas of low oxygen tension [79], we investigated if *CDCP1* is regulated by hypoxia in the TNBC cell line MDA-MB-231. We found that, though the mRNA and protein levels of CDCP1 were not upregulated in hypoxia, the phosphorylation of cCDCP1 and its downstream target, PKCδ, were increased in hypoxia, indicating that CDCP1 activity increases (Supplemental Figure 2.2).

Both flCDCP1 and cCDCP1 interact with PKCδ and Src but only cCDCP1 stimulates downstream signaling. To test the functional difference between flCDCP1 and cCDCP1 we created Flag-tagged constructs to express each CDCP1 isoform (Supplemental Figure 2.3). The signal peptide (SP) located at the N-terminus of flCDCP1 was added at the N-terminus of cCDCP1 to ensure proper localization. We overexpressed a vector control (VC), cCDCP1-Flag or flCDCP1-Flag in HEK 293T cells, which do not express

endogenous CDCP1, and do not cleave exogenous flCDCP1. As expected, immunostaining confirmed that both CDCP1 isoforms localized on the cell membrane (Supplemental Figure 2.4). We found that, while both isoforms of CDCP1 could be phosphorylated at Y734, only cCDCP1 could induce robust phosphorylation of its downstream target, PKCδ, as well as ERK1/2 and p38 MAPK, other kinases known to be involved in migration [99] (Figure 2.2A). Interestingly, previous findings indicate that CDCP1 expression is regulated by ERK1/2 signaling downstream of Ras in non-small cell lung carcinoma [21], suggesting a potential positive feedback loop between CDCP1 and ERK1/2. Based on previous reports that CDCP1 binds Src and PKCδ, stimulating PKCδ phosphorylation by Src at Y311 [9, 17, 19, 28, 44, 49], we compared the ability of both CDCP1 isoforms to associate with Src and PKCδ. We immunoprecipitated (IP) each CDCP1 isoform by Flag-tag and probed the membrane with anti-Src and anti-PKCδ antibodies. We found that both flCDCP1 and cCDCP1 could associate with Src and PKCδ. However, only cCDCP1 co-precipitated phosphorylated PKCδ (Figure 2.2B). Since Law et al. demonstrated the ability of dexamethasone to inhibit CDCP1 cleavage in TNBC cells [30]; we treated MDA-MB-231 cells with a PBS vehicle control or 100 nM dexamethasone for 48 hours. We found that inhibiting CDCP1 cleavage in TNBC cells inhibited PKCδ phosphorylation (Figure 2.2C). These data indicate the necessity of CDCP1 cleavage for signaling through PKCδ.

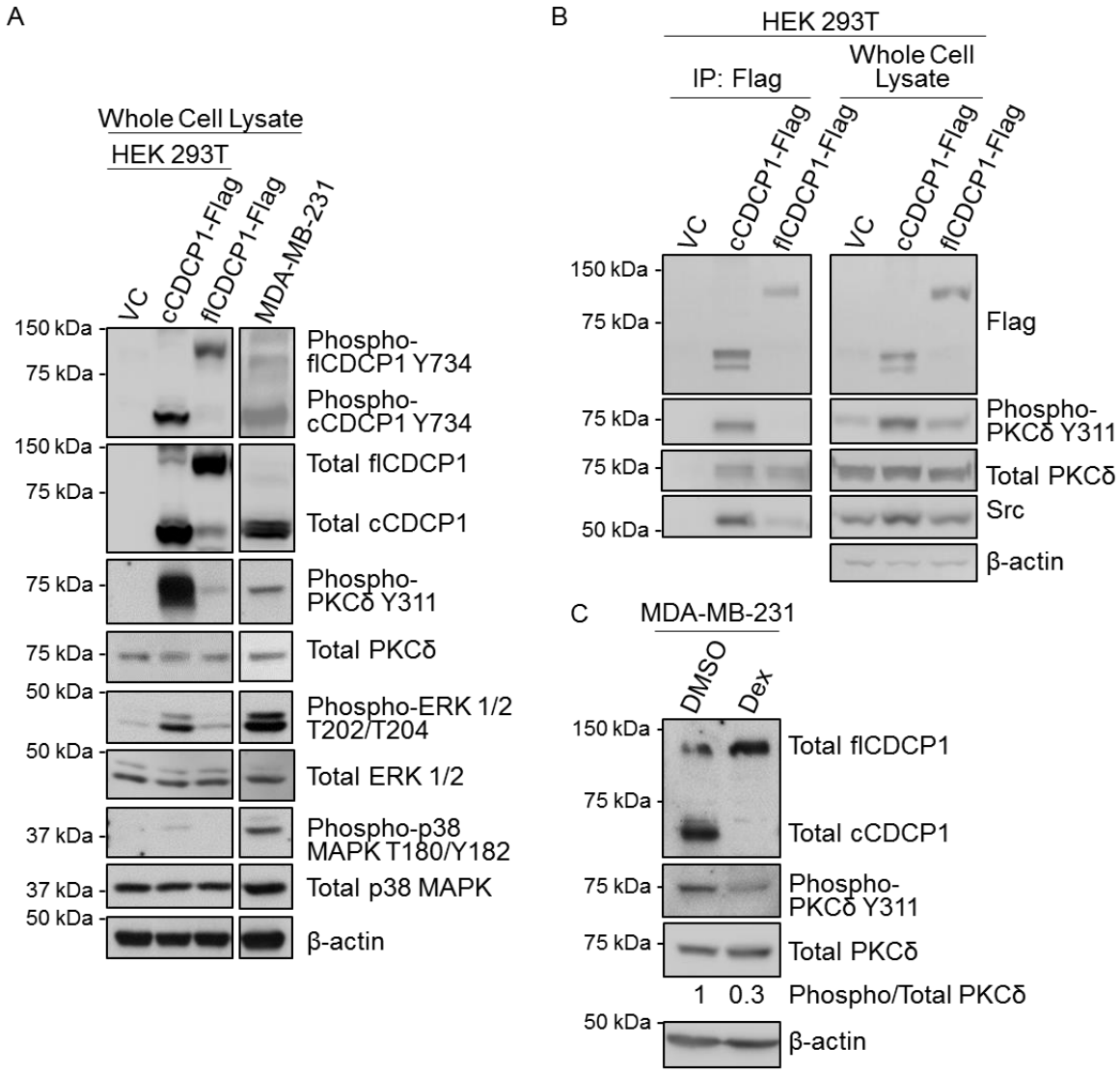

Figure 2.2 | Western blot analysis demonstrating that cCDCP1 activates PKCδ, ERK 1/2, and p38 MAPK. (**a**) Cell lysates of HEK 293T transfected with vector control (VC), cCDCP1, or flCDCP1, and MDA-MB-231 cells were analyzed by Western blot. cCDCP1 stimulates phosphorylation of PKCδ, ERK 1/2, and p38 MAPK in HEK 293T cells, while flCDCP1 does not. TNBC cells, MDA-MB-231, express and phosphorylate high levels of cCDCP1 and its downstream targets, PKCδ, ERK1/2, and p38 MAPK. Cell lysates of HEK 293T and MDA-MB-231 were run on the same gel and equal amounts of protein were loaded. (**b**) HEK 293T cells were co-transfected with PKCδ and Src, along with cCDCP1-Flag or flCDCP1-Flag. Cell lysates were immunoprecipitated with anti-Flag antibody. Both cCDCP1 and flCDCP1 are able to bind to PKCδ and Src. However, only PKCδ bound to cCDCP1 is phosphorylated at Y311. (**c**) MDA-MB-231 cells overexpressing PKCδ were treated with a vehicle control (DMSO) or 100 nM dexamethasone (Dex) for 48 hours. This treatment inhibited CDCP1 cleavage and caused a reduction of PKCδ phosphorylation at Y311 as analyzed by Western blot. Quantitated phospho/total PKCδ ratio was obtained by band densities in ImageJ, the value for DMSO-treated cells was normalized to 1. Quantitation shown is the average of three independent experiments.

cCDCP1 stimulates cell migration. Due to the ability of cCDCP1 to induce robust phosphorylation of PKCδ, which we have previously linked to pro-migratory signaling [17], we aimed to analyze the effect of each CDCP1 isoform on cellular migration. To do this, we overexpressed VC, cCDCP1-Flag, or flCDCP1-Flag in HEK 293T cells and analyzed migration through fibronectin-coated transwell inserts after 24 hours. We found that cCDCP1 significantly induced migration of HEK 293T cells, while flCDCP1 did not (Figure 2.3A).

Based on these data and the high level of CDCP1 cleavage in MDA-MB-231 cells (Figure 2.1B and 2.2A), we assessed the contribution of cCDCP1 in MDA-MB-231 cell migration in a scratch assay. We knocked down endogenous CDCP1 with two shRNAs targeting two different sites on *CDCP1*'s mRNA. Migration of MDA-MB-231-shCDCP1-1 and MDA-MB-231-shCDCP1-7 cells were severely inhibited compared to MDA-MB-231-shScramble cells. Importantly, this migratory defect was rescued by overexpression of cCDCP1 and not shCDCP1-insensitive non-cleavable CDCP1 (sh-ins-ncCDCP1) (Figure 2.3B and Supplemental Figures 2.3 and 2.5). We validated these data in another TNBC cell line, MDA-MB-468, where CDCP1 knock down inhibited migration through fibronectin-coated transwell inserts, which was rescued by cCDCP1 and not sh-ins-ncCDCP1 overexpression (Figure 2.3C).

cCDCP1 forms a dimer independently of its phosphorylation status. CUB domains have known roles in protein-protein interaction [4, 100, 101], including the potential CUB domain-CUB domain interaction of CDCP1 with matriptase [11]. flCDCP1 has three CUB

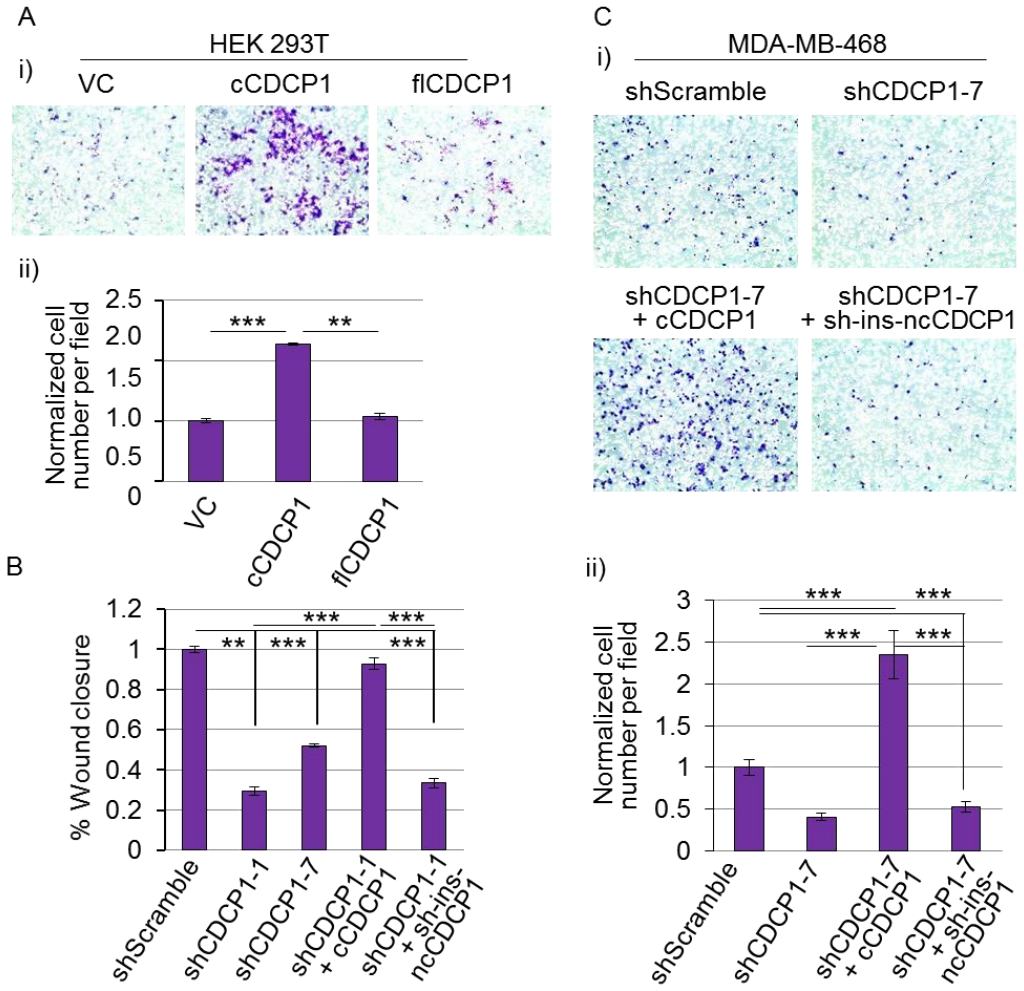

Figure 2.3 | CDCP1 cleavage stimulates cell migration. (**a**) Representative images of stained transwells (i) used for quantitation of cell migration (ii). HEK 293T cells were transfected with VC, cCDCP1, or flCDCP1 as indicated. CDCP1 expression was verified by Western blot in Figure 2b. cCDCP1 induces migration of HEK 293T cells, while flCDCP1 does not. The cell number per field of HEK 293T cells transfected with vector control (VC) was normalized to 1, and all other samples were normalized to that for comparison. (**b**) CDCP1 depletion by shRNA blocks migration of MDA-MB-231 cells, which can be restored by cCDCP1 overexpression, and not sh-ins-ncCDCP1 overexpression. The data represents average percent wound closure. (**c**) Representative images of stained transwells (i) used for quantitation of cell migration (ii). CDCP1 depletion by shRNA blocks migration of MDA-MB-468 cells, which can be restored by cCDCP1 overexpression, and not sh-ins-ncCDCP1 overexpression. All of the experiments in this figure were done in duplicate and repeated three times. **P≤0.005, ***P≤0.0005. P values were analyzed by one way ANOVA with multiple comparison post hoc T-test and error bars represent SEMs.

domains (1, 2, and 3) and cCDCP1 has two CUB domains (2 and 3). Thus, we decided to test if either isoform of CDCP1 could form a dimer. To do this, we created C-terminal His-tagged cCDCP1 and flCDCP1 constructs. We overexpressed Flag- and His-tagged CDCP1 constructs alone or in combination in HEK 293T cells (Figure 2.4A). The Flag-tag was immunoprecipitated and dimerization was analyzed by immunoblotting for the His-tag. Our results indicate that only cCDCP1 could form a dimer (Figure 2.4A).

Since interactions of CDCP1 with other proteins at the membrane are dependent on its phosphorylation [8, 13, 19, 49, 102], we analyzed the dependency of the dimer on CDCP1's phosphorylation status. To do this, we created cCDCP1-Y734F-Flag and cCDCP1-Y734F-His constructs, which are phosphorylation incompetent (Supplemental Figure 2.6). We then repeated co-immunoprecipitation experiments in HEK 293T cells by expressing Flag- and His-tagged constructs of cCDCP1 and cCDCP1-Y734F alone or in combination and found that cCDCP1 was capable of forming a dimer independently of its phosphorylation status. However, overexpression of cCDCP1 Y734F-Flag did not stimulate phosphorylation of PKCδ at Y311 (Figure 2.4B).

To determine if CDCP1 forms a dimer endogenously in TNBC cells, we used the Duolink proximity ligation assay (PLA). We found that CDCP1 formed a dimer in MDA-MB-231 cells visualized by the red punctate signal (Figure 2.4C). This signal was lost in MDA-MB-231-shCDCP1-1 cells and regained upon rescue with cCDCP1 overexpression, but not with shRNA-insensitive non-cleavable version of flCDCP1 (sh-ins-ncCDCP1) (Figure 2.4C, Supplemental Figure 2.7).

An extracellular fragment of cCDCP1 can block the cCDCP1 dimer formation. Based on the above data, we propose that cCDCP1 forms a dimer through its extracellular

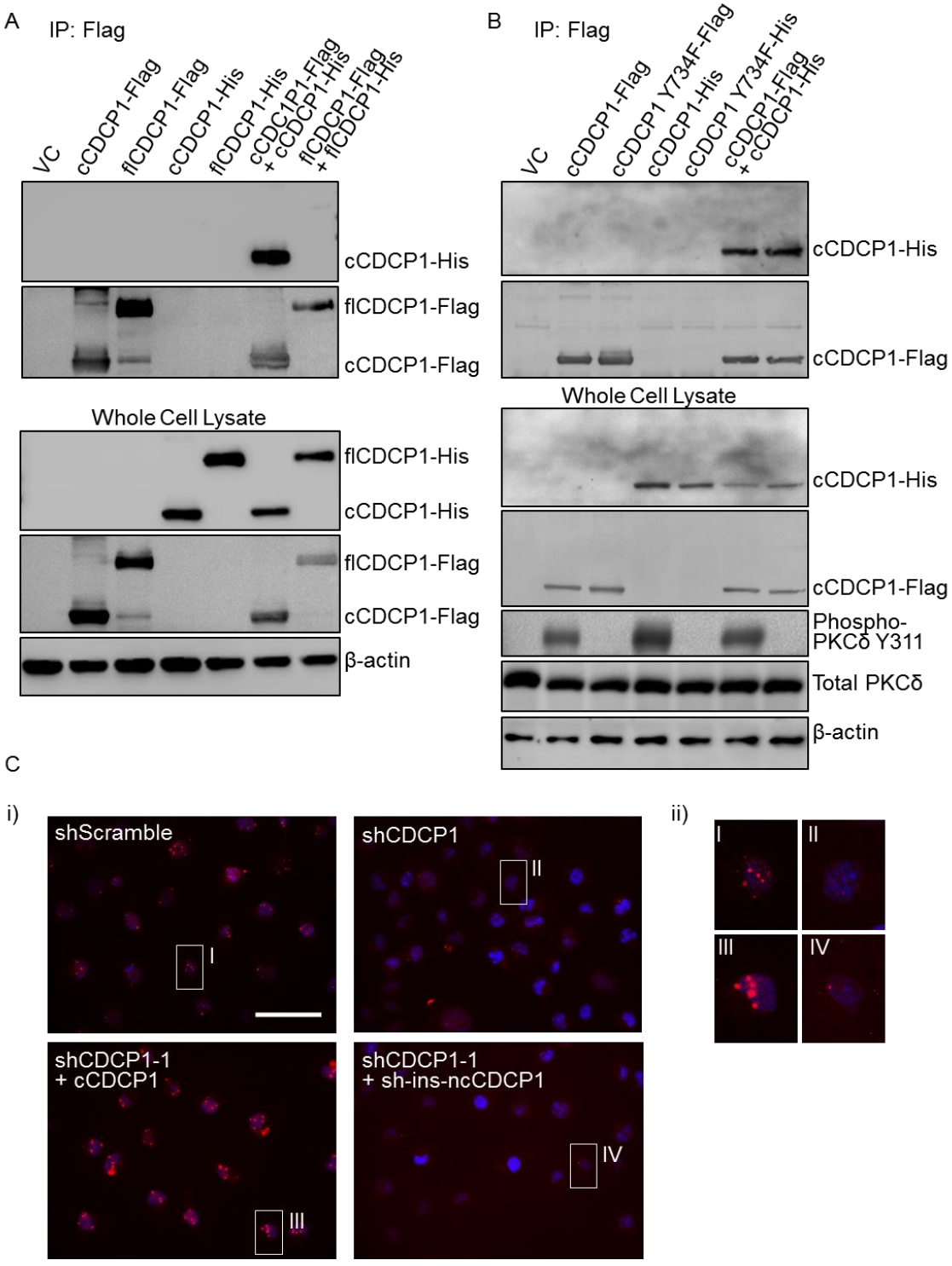
A
IP: Flag
VC
cCDCP1-Flag
flCDCP1-Flag
cCDCP1-His
flCDCP1-His
cCDC1P1-Flag + cCDCP1-His
flCDCP1-Flag + flCDCP1-His
cCDCP1-His
flCDCP1-Flag
cCDCP1-Flag
Whole Cell Lysate
flCDCP1-His
cCDCP1-His
flCDCP1-Flag
cCDCP1-Flag
β-actin
B
IP: Flag
VC
cCDCP1-Flag
cCDCP1 Y734F-Flag
cCDCP1-His
cCDCP1 Y734F-His
cCDCP1-Flag + cCDCP1-His
cCDCP1-His
cCDCP1-Flag
Whole Cell Lysate
cCDCP1-His
cCDCP1-Flag
Phospho-PKCδ Y311
Total PKCδ
β-actin
C
i)
shScramble
I
shCDCP1
II
shCDCP1-1 + cCDCP1
III
shCDCP1-1 + sh-ins-ncCDCP1
IV
ii)
I
II
III
IV

Figure 2.4 | CDCP1 cleavage is necessary for dimer formation, which is independent of cCDCP1's phosphorylation status. (**a**) HEK 293T cells were transfected with Flag- and His-tagged CDCP1 constructs alone or in combination (as indicated). After 48 hours, CDCP1 was immunoprecipitated (IP) by the Flag-tag. Co-immunoprecipitation (co-IP) samples were then analyzed by Western blot for the presence of flCDCP1-His tag or cCDCP1-His tag, indicating the formation of a dimer. Only cCDCP1-His tag was detected in the co-IP, indicating that cCDCP1 forms a dimer. (**b**) HEK 293T cells were transfected with either WT or Y734F mutant cCDCP1-Flag tag and cCDCP1-His tag constructs (as indicated). Samples were analyzed as in (a). cCDCP1 Y734F-Flag is able to co-IP cCDCP1 Y734F-His but is unable to co-IP phospho-PKCδ. Thus, cCDCP1 dimerization is phosphorylation independent. (**c**) cCDCP1 forms a dimer endogenously in TNBC cells. (i) CDCP1 dimerization was monitored by the PLA assay using oligonucleotide-conjugated anti-CDCP1 antibody. MDA-MB-231-shCDCP1-1 and MDA-MB-231-shCDCP1-1+cCDCP1 were used as negative and positive controls respectively. MDA-MB-231-shCDCP1-1+sh-ins-ncCDCP1 do not show signal, indicating the dimer is forming only through cCDCP1. Scale bar represents 50 μm. (ii) larger pictures of the cells shown in (i).

domain, specifically through one or both of its CUB domains. To test this hypothesis, we made a construct expressing the extracellular portion of cCDCP1 (ECC) with an N-terminal SP and a C-terminal His-tag (Figure 2.5A i). To monitor CDCP1 dimerization, we utilized a firefly split-luciferase system [103] in which the N-terminal domain or C-terminal domain of firefly luciferase was attached to the intracellular C-terminus of cCDCP1, resulting in cCDCP1-N'luc and cCDCP1-C'luc constructs, respectively (Figure 2.5A ii-iii). We also created flCDCP1-N'luc and flCDCP1-C'luc constructs. Using the split-luciferase system in HEK 293T cells we confirmed that only cCDCP1, not flCDCP1, forms a dimer and no heterodimer is formed between cCDCP1 and flCDCP1 (Figure 2.5B and Supplemental Figure 2.8). Next, we expressed the cCDCP1-N'luc and cCDCP1-C'luc constructs in combination with VC or ECC. Importantly, ECC was able to decrease the D-luciferin luminescence, indicating blockage of the cCDCP1 dimer formation (Figure 2.5B). The observed effect of ECC on cCDCP1 dimer blockage is specific since ECC had no effect on cCDCP1 expression as well as luciferase enzyme activity (Supplemental Figure 2.9). Since ECC has a SP at its N-terminus, which is necessary for secretion [11], as expected we found secreted ECC in the media of transfected HEK 293T cells (Figure 2.5C).

To validate the importance of the cCDCP1 dimerization in pro-migratory signaling, we analyzed the effect of ECC on PKCδ phosphorylation and migration of MDA-MB-231 cells. We found that overexpressing ECC in MDA-MB-231 cells inhibited PKCδ phosphorylation (Figure 2.5D). We further found that transfer of ECC-conditioned media from ECC-transfected HEK 293T cells to MDA-MB-231 cells inhibited their migration (Figure 2.5E). We also validated the inhibitory effect of ECC on migration through

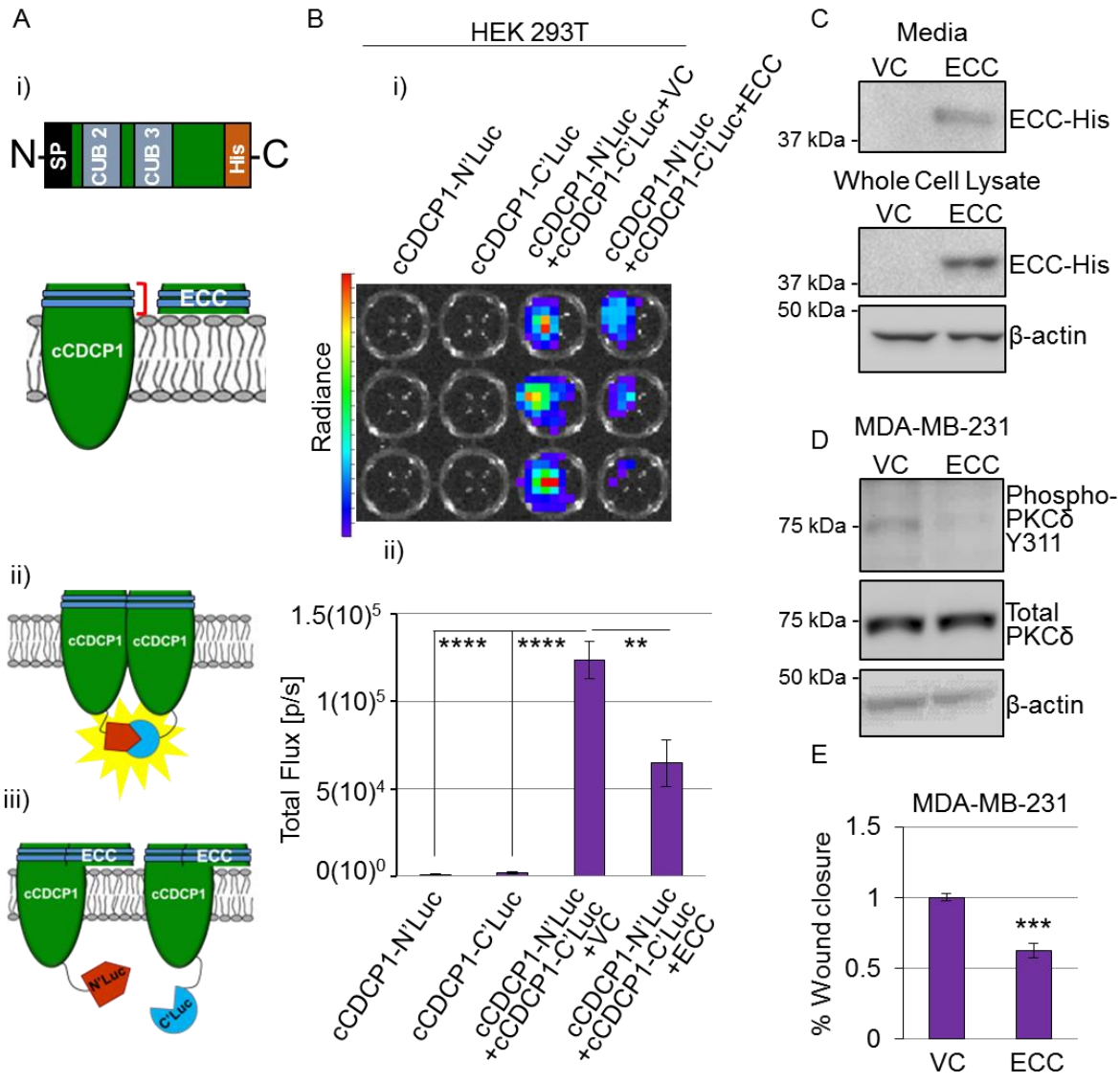
A
i)
N-
SP
CUB 2
CUB 3
His
-C
ECC
cCDCP1
ii)
cCDCP1
cCDCP1
iii)
ECC
ECC
cCDCP1
cCDCP1
N'Luc
C'Luc
B
HEK 293T
i)
cCDCP1-N'Luc
cCDCP1-C'Luc
cCDCP1-N'Luc +cCDCP1-C'Luc+VC
cCDCP1-N'Luc +cCDCP1-C'Luc+ECC
Radiance
ii)
Total Flux [p/s]
1.5(10)5
1(10)5
5(10)4
0(10)0
****
****
**
cCDCP1-N'Luc
cCDCP1-C'Luc
cCDCP1-N'Luc +cCDCP1-C'Luc +VC
cCDCP1-N'Luc +cCDCP1-C'Luc +ECC
C
Media
VC
ECC
37 kDa
ECC-His
Whole Cell Lysate
VC
ECC
37 kDa
ECC-His
50 kDa
β-actin
D
MDA-MB-231
VC
ECC
75 kDa
Phospho-PKCδ Y311
75 kDa
Total PKCδ
50 kDa
β-actin
E
MDA-MB-231
% Wound closure
1.5
1
0.5
0
***
VC
ECC
F
i)
MDA-MB-468
VC
ECC
ii)
Normalized cell number per field
1.5
1
0.5
0
***
VC
ECC
G
i)
UCI-082014
VC
ECC
ii)
Normalized cell number per field
1.5
1
0.5
0
***
VC
ECC

Figure 2.5 | Co-expression of Extracellular Cleaved portion of CDCP1 (ECC) inhibits cCDCP1 dimerization and downstream signaling. (**a**) Schematics of the ECC construct (i), the cCDCP1-based split luciferase system for monitoring cCDCP1 dimerization (ii), and the tentative mechanism of how ECC breaks the dimer (iii). SP, signal peptide for proper translocation to the cell membrane/secretion; blue, CUB domains. (**b**) Split luciferase constructs were transfected into HEK 293T cells individually or together with vector control (VC) or ECC, as indicated. After the addition of D-luciferin, the luminescence was imaged with an IVIS Lumina system. The representative image is shown in (i). The quantitation shown in (ii) is the average of four independent experiments each done in triplicate. **P=0.01, ****P<$1(10)^{-5}$. P values were analyzed by one way ANOVA with multiple comparison post hoc T-test. Error bars represent SEMs. (**c**) HEK 293T secrete ECC-His into the media 48 hours post-transfection. (**d-e**) MDA-MB-231 cells overexpressing PKCδ were treated with VC or ECC conditioned media for 24 hours. (**d**) ECC inhibits phosphorylation of PKCδ. (**e**) ECC inhibits cell migration in a scratch assay. (**f-g**) ECC inhibits migration of MDA-MB-468 (**f**) (after 16 hours) and UCI-082014 (**g**) (after 6 hours) TNBC cell lines through fibronectin-coated transwells when compared to VC. Representative images of stained transwells are shown in (i) and used for quantitation of cell migration in (ii). Quantitation is the average of three independent experiments each done in triplicate. ***P<0.001. P value was analyzed by paired T-test and error bars represent SEMs.

transwell inserts using two additional TNBC cell lines, MDA-MB-468 and UCI-082014, expressing either VC or ECC (Figure 2.5 F-G). Together, these data validate that cCDCP1 dimerization facilitates PKCδ phosphorylation and stimulates cell migration.

ECC inhibits TNBC cell invasiveness, decreases proliferation and induces apoptosis in 3D culture. To analyze the effect of ECC on TNBC cells in 3D [104], we cultured MDA-MB-231, MDA-MB-468, and UCI-082014 TNBC cells expressing VC or ECC in 1:1 collagen:matrigel gels for 6 days. We found that TNBC cells expressing ECC had less and smaller stellate structures and invaded less into the matrix (Figure 2.6A), had decreased proliferation as analyzed by a mitotic marker, phospho-histone H3 staining (Figure 2.6B), and increased apoptosis as analyzed by cleaved caspase 3 staining (Figure 2.6C) when compared to TNBC cells expressing VC. The lack of any cleaved caspase 3 staining in the MDA-MB-231 VC cells (Figure 2.6C) is supported by reports showing increased resistance of MDA-MB-231 cells to apoptosis compared to MDA-MB-468 [105-107]. Staining of ECC using an anti-His-tag antibody revealed that after secretion ECC concentration builds around the cells (Supplemental Figure 2.10), likely leading to saturation of cCDCP1 dimer inhibition at the membrane. Thus, the cCDCP1 inhibition by ECC leads to a more dramatic phenotype in 3D as opposed to 2D culture, where ECC is secreted into the culture media.

Discussion

Our studies have elucidated a new step in the CDCP1 activation cascade: cCDCP1 homo-dimerization, which is critical for phosphorylation of PKCδ and migration of TNBC

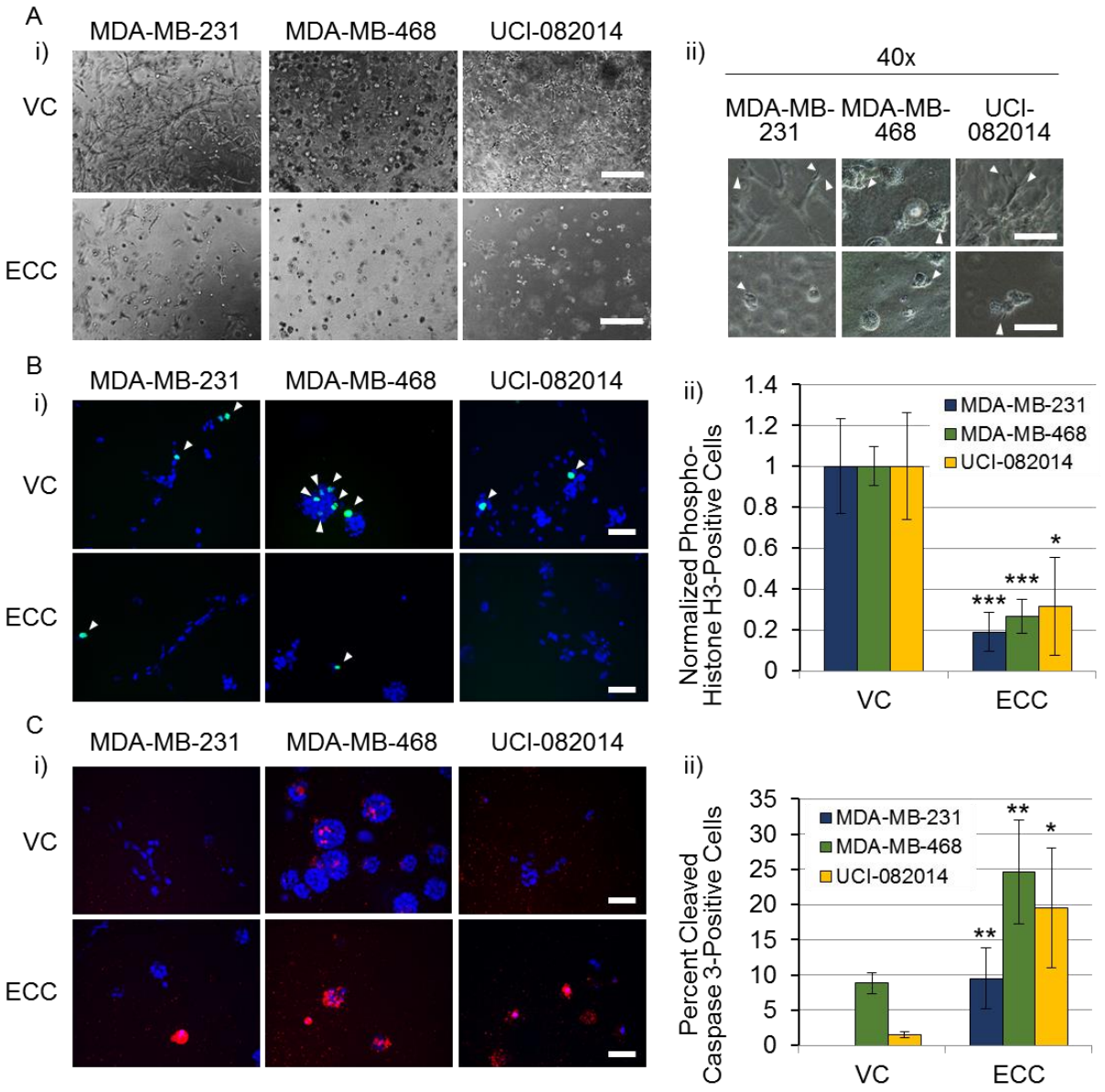

Figure 2.6 | ECC inhibits TNBC cell invasiveness, decreases proliferation and induces apoptosis in 3D culture. (**a**) (i) 10x phase contrast images of the cell lines indicated grown in 3D. (ii)Scale bar, 400 μm. 40x phase contrast images, arrows point to stellate structures invading the matrix. Scale bar, 200 μm. ECC inhibits TNBC cell invasiveness by blocking the stellate structure formation. (**b**) (i) 20x phospho-histone H3 images of the cell lines indicated grown in 3D. Blue, DAPI; green, phospho-histone H3. Scale bar, 50 μm. White arrows point to DAPI and phospho-histone H3 co-stained nuclei. The results are quantitated in (ii). The number of phospho-histone H3-positive nuclei in VC-transduced cells was normalized to 1. ECC inhibits TNBC cell proliferation in 3D as shown by the reduction of phospho-histone H3-positive nuclei in comparison to VC-expressing cells. (**c**) (i) 20x cleaved caspase 3 images of the cell lines indicated grown in 3D. Blue, DAPI; red, cleaved caspase 3. Scale bar, 50 μm. The results are quantitated in (ii). ECC stimulates TNBC cell apoptosis in 3D as shown by the increase of cleaved caspase 3 in comparison to VC-expressing cells. Quantitation in **b** and **c** is the average of three independent experiments performed in triplicate. *P<0.05, **P<0.01, ***P<0.001. P value was analyzed by one way ANOVA with multiple comparison post hoc T-test and error bars represent SEMs.

cells. Figure 2.7 illustrates an updated model for CDCP1 activation, including its phosphorylation, cleavage, and dimerization. We suggest that the cCDCP1 dimer acts as a docking station to facilitate PKCδ phosphorylation by Src: cCDCP1 dimer is important for binding of Src to one subunit and PKCδ to the other subunit, bringing Src and PKCδ into close proximity, allowing the phosphorylation of PKCδ by Src. This signaling cascade further leads to phospho-PKCδ-stimulated migration. Our model also explains the ability of flCDCP1 to bind to Src and PKCδ without stimulating PKCδ phosphorylation: Src and PKCδ are not bound to flCDCP1 at the same time. These data are in line with *ex vivo* data in TNBC [30] and *in vivo* data in prostate cancer [13, 28] showing that CDCP1 cleavage is required to induce cellular dissemination and multiple-organ metastasis. Although the positive and negative regulators of CDCP1 dimerization remain to be elucidated, we have shown that ECC represents a way to inhibit dimerization of cCDCP1, disrupting cCDCP1 pro-migratory signaling.

Our data in 3D showing an increase in ECC-expressing TNBC cell apoptosis are in line with previous studies demonstrating that CDCP1 knockdown by si/shRNA induces apoptosis in lung and breast cancer cells cultured in anchorage-free conditions [12, 49, 108], a study showing that inhibition of CDCP1 cleavage *in vivo* induced apoptosis of prostate cancer cells [28], and studies demonstrating that a function blocking antibody against CDCP1 inhibited cell invasiveness in a 3D culture system and tumor growth in a xenograft model of breast cancer [54, 109]. The induction of apoptosis in the presence of extracellular matrix (ECM) components, collagen I and matrigel (collagen IV, laminin, enactin/nidogen-1, and proteoglycans), may indicate that ECC inhibits stellate structure formation, which is indicative of cell binding and anchoring to these substrates during

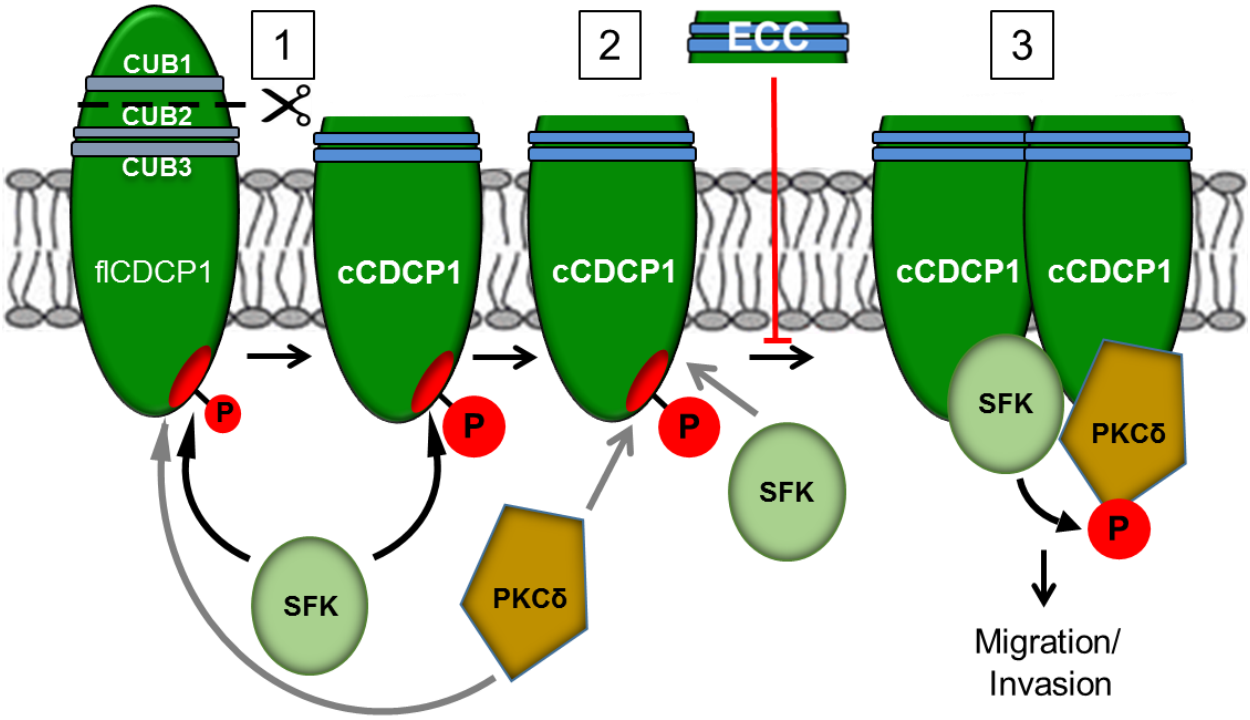

Figure 2.7 | Proposed model of CDCP1 activation and signal transduction. 1) CDCP1 is cleaved on the extracellular side of the membrane between CUB1 and CUB2. SFKs (Src/Fyn/Yes) can phosphorylate both flCDCP1 and cCDCP1. **2**) SFKs and PKCδ bind to flCDCP1 or cCDCP1 protein monomers, presumably to overlapping/close binding sites, but signal transduction from SFKs to PKCδ does not occur. **3**) cCDCP1 is capable of forming a dimer, which allows SFKs and PKCδ to bind to each individual subunit of a dimer, leading to PKCδ phosphorylation by SFKs. Activated PKCδ induces pro-migratory signaling, ultimately leading to migration. ECC is capable of inhibiting cCDCP1 dimerization, PKCδ phosphorylation, and migration of TNBC cells. We propose that targeting CDCP1 dimerization will lead to blockade of SFK/PKCδ signaling and inhibit CDCP1-mediated migration and invasion in TNBC. Black arrows, phosphorylation by SFKs; grey arrows, binding; blue, CUB domains; red, binding site; P in red circle, phosphorylation.

invasion. This explanation is supported by the study showing preferential and direct binding of β_1 integrin to cCDCP1 over flCDCP1 [13]. Our data suggest that cCDCP1 may promote β_1 integrin activity, which is inhibited in the presence of ECC. It also remains to be investigated whether ECC is specific to the cCDCP1 homo-dimer or also inhibits cCDCP1 interactions with other proteins. The increased efficacy of ECC in 3D culture remains to be validated in an orthotopic mouse model of TNBC, where we expect the same accumulation of ECC extracellularly to inhibit cell-ECM adhesion, proliferation, and induce apoptosis.

The ability of CDCP1 to form a dimer is supported by previous findings that treatment of NIH3T3 and MCF7 cells overexpressing exogenous CDCP1 with a bivalent anti-CDCP1 antibody stimulates CDCP1 activity, presumably by stimulating its clustering in lipid rafts [54]. Kollmorgen et al. proposed that CDCP1 forms a dimer through the transmembrane or intracellular dimer interface [16] but they did not investigate the dependence of dimer formation on CDCP1 cleavage. Although we do not exclude the possibility that CDCP1 forms a dimer through transmembrane or intracellular domains as well, our data support dimer formation through the extracellular CUB domains, with the secreted ECC portion capable of inhibiting dimerization of cCDCP1. Our data show that cCDCP1 forms a dimer, although we do not exclude the possibility that it is capable of forming a tetramer or higher molecular complex. Further research is needed to test this possibility.

It remains to be investigated how flCDCP1 stimulates signaling through PKCδ in ccRCC. For instance, 786-0 cells express almost exclusively flCDCP1 and we have shown previously that flCDCP1 stimulates migration of ccRCC cells through PKCδ [17].

One striking difference between ccRCC and TNBC lies in abundance of lipid droplets, which are extremely high in ccRCC [110], and rather low in TNBC [111, 112]. Since CDCP1 is present in Triton X-100 insoluble lipid rafts [29, 54], we propose that the high lipid content of ccRCC cells facilitates clustering of flCDCP1 at the membrane in lipid rafts, which leads to stimulation of PKCδ phosphorylation by Src. On the other hand, TNBC relies on CDCP1 cleavage to induce cCDPC1 dimerization to stimulate PKCδ phosphorylation by Src. In line with this, Casar et al. showed that PC3 and HEK 293T cells, which have low lipid content [113, 114], are dependent on CDCP1 cleavage for cellular dissemination *in vitro*, in chick embryo and mouse models of metastasis [13, 28].

Although we found that CDCP1 is not hypoxia-inducible at the mRNA and protein level in TNBC, the phosphorylation of cCDCP1 and PKCδ are hypoxia-inducible. Importantly, we [17] and others [20] have shown that CDCP1 is hypoxia-inducible through the HIF pathway at the mRNA and protein levels in ccRCC. Cell type specific hypoxic induction of HIF target genes has been described previously [115], which could explain the discrepancy between ccRCC and TNBC. Emerling et al. demonstrated that Src Y416 and CDCP1 Y734 phosphorylation are hypoxia inducible in ccRCC [20], which we replicated in TNBC. The mechanism of stimulation of these types of phosphorylation under hypoxia deserves further investigation.

The CDCP1 signaling cascade has not been investigated in depth in TNBC and other types of breast cancer. It was previously reported that cCDCP1 promotes TNBC migration by sequestering E-cadherin intracellularly [30] and TNBC invasion by stimulating membrane type 1 matrix metalloproteinase (MT1-MMP) activity [29]. Our studies suggest that cCDCP1 promotes TNBC migration through dimerization, which is important for

PKCδ phosphorylation and potentially ERK1/2, and p38 MAPK phosphorylation (requires further investigation). In addition, it was recently shown that CDCP1 directly interacts with HER2 and stimulates progression of HER2-positive tumors [14]. On the other hand, a correlation between estrogen and progesterone receptor status and CDCP1 expression has not been found [45]. Thus, the dependence of CDCP1 activity on cleavage and dimerization in hormone receptor positive breast cancers remains to be investigated.

Our data validate the previously demonstrated therapeutic potential of targeting cleaved isoform of CDCP1 to inhibit cancer metastasis [13]. However, we provide novel insight into the CDCP1 activation mechanism and propose targeting a step downstream of CDCP1 cleavage: dimerization.

Materials and Methods

Cell lines and media: HEK 293T, MDA-MB-231, MDA-MB-453, MDA-MB-468, MDA-MB-361 cells lines were grown in DMEM (Genesee, San Diego, CA #25-500) with 10% Fetal Bovine Serum (Omega Scientific, Tarzana, CA #FB-12), 2 mM L-glutamine, 100 u/mL penicillin and 100 µg/mL streptomycin. Cells were grown in mixed gas CO_2 water-jacketed incubators (21% O_2, 5% CO_2). MCF10A cells were grown in the same media as above supplemented with 20 ng/mL EGF (PeproTech, Rock Hill, NJ #AF-100-15) and 10 µg/mL insulin (Roche, San Francisco, CA #11376497001). MDA-MB-231 and MDA-MB-468 cell lines, extensively used for *in vitro* experiments in this study, were validated using short tandem repeat (STR) profiling by the American Type Culture Collection (Manassas, VA). All cells were regularly tested for mycoplasma contamination and confirmed to be negative.

Primary specimen acquisition and lysis: Fresh TNBC specimens were acquired from Hoag pathology and frozen upon arrival. Frozen TNBC specimens were obtained from the UC Irvine Medical Center. For lysis, specimens were thawed on ice and then homogenized in cell lysis buffer (20 mM Tris-HCl [pH 7.5], 150 mM NaCl, 1 mM EDTA, 1 mM EGTA, 1% Triton X100, 2.5 mM $Na_4P_2O_7$, 1 mM β-glycerophosphate, 1 mM Na_3VO_4) with protease inhibitors (Fisher Scientific, Pittsburgh, PA #P1-88266) and phosphatase inhibitors (Roche #04906845001).

Western blotting (WB): Protocol was adapted from Razorenova et al. [116]. Briefly, cells were lysed using cold cell lysis buffer (see recipe above) with protease inhibitors (Fisher Scientific). Protein was measured using BCA Protein Assay kit (Pierce, Rockford, IL #PI-23225). 40 µg protein was loaded/lane of 10% bis-acrylamide gels and transferred onto 0.2 µm nitrocellulose membranes (BioRad, Hercules, CA). Membranes were incubated with primary antibodies overnight at 4 °C with gentle agitation then incubated with secondary antibodies for 1 hour at room temperature (RT) with gentle agitation and the signal was developed using Amersham ECL Prime WB substrate (GE Healthcare, Scottsdale, AZ #RPN2236) or SigmaFast BCIP/NBT substrate (Sigma Aldrich #B5655) for HRP or AP conjugates, respectively. WB analysis of phospho-signaling downstream of CDCP1 was conducted 48 hours post-transfection: cells were serum starved for 6 hours and then stimulated for 20 minutes with 10% FBS (Gibco, Carlsbad, CA #16000-044-1399) before lysing. All antibodies used for WB are listed in Supplemental Table 1.

Construction of shRNA and cDNA overexpression constructs for CDCP1: pLM-CMV-flCDCP1 was cloned by PCR using pDrive-flCDCP1 (OpenBiosystems, Huntsville, AL #IHS1382-8427202) as a template. Since pDrive-flCDCP1 contained 5 mismatches

when aligned to WT CDCP1 referenced in Cosmic database, all mismatches in pLM-CMV-flCDCP1 were reverted to WT sequence using the Lightning Site Directed Mutagenesis kit (Stratagene, Santa Clara, CA #210516).

pLM-CMV-flCDCP1-Flag and pLM-CMV-flCDCP1-His were cloned by PCR using pLM-CMV-flCDCP1 as a template.

pLM-CMV-cCDCP1-Flag and pLM-CMV-cCDCP1-His were cloned in two steps. First, cCDCP1 was amplified by PCR using pLM-CMV-flCDCP1 as a template. Second, the SP was cloned upstream of cCDCP1 by PCR using pLM-CMV-flCDCP1 as a template.

pLM-CMV-cCDCP1-Y734F-Flag and pLM-CMV-cCDCP1-Y734F-His were generated from pLM-CMV-cCDCP1-Flag and pLM-CMV-cCDCP1-His by site-directed mutagenesis (SDM) using the Lightning Site Directed Mutagenesis kit (Stratagene).

pLM-CMV-ECC-His was cloned by PCR using pLM-CMV-flCDCP1 as a template.

pLM-CMV-cCDCP1-N'luc, pLM-CMV-cCDCP1-C'luc, pLM-CMV-flCDCP1-N'luc, pLM-CMV-flCDCP1-C'luc were cloned in two steps. First, N'luciferase and C'luciferase were PCR amplified from the constructs described by Choi et al. [103]. Second, cCDCP1 and flCDCP1 were cloned upstream of N'luc and C'luc. cCDCP1 was amplified from pLM-CMV-cCDCP1-Flag, which had already a SP. flCDCP1 was amplified from pLM-CMV-flCDCP1.

To make shRNA-insensitive flCDCP1 (pLM-CMV-sh-ins-flCDCP1), the third nucleotides of each codon in the regions of flCDCP1 recognized by the shRNAs were mutated to interfere with shRNA binding but carefully maintain WT flCDCP1 protein sequence. The 985 bp sh-ins-CDCP1 fragment with NheI and BamHI restriction sites at

the 5’ and 3’ ends respectively was synthetized by GenScript (Piscataway, NJ) and cloned to pUC57 by EcoRV. The fragment (+1 to +650 bp downstream of the start codon) was cloned to pLM-CMV-flCDCP1 by NheI and BamHI restriction sites.

To make shRNA-insensitive ncCDCP1 (pLM-CMV-sh-ins-ncCDCP1), the cleavage site in pLM-CMV-sh-ins-flCDCP1 was mutated: RK368-9QN. A gBlock containing CDCP1 fragment flanking the cleavage site (+977 to +1257 bp downstream of the start codon) with BamHI and AgeI was synthesized. This gBlock was cloned into pLM-CMV-sh-ins-flCDCP1 by BamHI and AgeI restriction sites.

Each construct originally had a puromycin resistance cassette. Puromycin was replaced with hygromycin and neomycin in pLM-CMV-cCDCP1-His and pLM-CMV-sh-ins-ncCDCP1, respectively. Hygromycin and neomycin resistance cassettes were obtained from pLM-CMV-H4-hygro and pLM-CMV-H4-neo plasmids using the SpeI and SalI restriction enzymes and cloned into SpeI and SalI digested pLM-CMV-cCDCP1-His and pLM-CMV-sh-ins-ncCDCP1, respectively.

pLKO.1shCDCP1-1 was purchased from OpenBiosystems (#RHS3979-98822176). pLKO.1shScrambled was purchased from Addgene (Cambidge, MA, #1864). pLKO.1shCDCP1-7 was cloned using two annealed complimentary oligos and ligated to AgeI and EcoRI digested pLKO.1 empty vector (Addgene #8453).

All oligonucleotides and gBlocks in this section were synthesized by IDT (Coralville, IA) and are all listed in the Supplemental Table 2.

Cell transfections with overexpression constructs: HEK 293T cells were transfected using Lipofectamine and Plus reagents (Life Tech, Carlsbad, CA #18324-012 and

#11514-015) following the manufacturer's protocol and used for experiments 2-3 days post-transfection.

Virus production and infection of target cells: Detailed protocol is described in Razorenova et al. [117]. To produce virus, HEK 293T cells were transfected with each lentiviral plasmid along with packaging plasmids, pVSVG and ΔR8.2 using standard $CaCl_2$ transfection protocol. Virus-containing media with 6 µg/mL polybrene filtered through a 0.45 µm PES filter was transferred to MDA-MB-231 cells, which were selected in antibiotic-containing media for minimum one week.

ECC detection in cell media: HEK 293T were transfected with pLM-CMV-ECC-His using Lipofectamine and Plus reagents following the manufacturer's protocol (Life Tech) in a 6-well plate. 24 hours after transfection the media was changed to 1 mL fresh DMEM with 10% FBS. 48 hours later, 50 µL of media was collected and denatured in 12.5 µL 5x sample loading buffer (312 mM Tris-HCl, pH 6.8, 10% SDS, 0.05% bromophenol blue, 50% glycerol, 10% β-mercaptoethanol). Samples were analyzed by WB.

qRT-PCR: qRT-PCR was performed as previously described (10) using the ViiA 7 Real-Time PCR System (Life Tech). Human TATA-binding protein (hTBP) primers were chosen as an internal control. Primers listed in Supplemental Information (Supplemental Table 2).

Immunocytochemistry: Cells were fixed with 4% paraformaldehyde for 10 min, then treated with 0.3% Triton X-100 in 1xPBS for 5 minutes prior to blocking for 1 hour in 5% bovine serum albumin (BSA) in 1xPBS. Cells were then incubated overnight in primary antibody at 4 °C, followed by incubation for 2 hours in secondary antibody at RT in the dark. Antibodies used are listed in Supplemental Table 1. Both primary and secondary antibodies

were diluted in 1% BSA in 1xPBS. Cell nuclei were counterstained with Hoechst 33342 at 1:500 in 1xPBS for 1 minute. Coverslips were mounted with Vectashield (Vector #H-1000) and imaged using a Nikon Eclipse Ti microscope with a 40x or 63x objective and NIS element AR3.10 software. Images for sh-ins-ncCDCP1 transfected HEK 293T cells were taken using a Zeiss Spinning Disc Confocal Microscope with a 63x objective and AxioVision software.

Duolink PLA Assay: The assay was performed according to the manufacturer's protocol (Sigma Aldrich #DUO92008, #DUO92009, #DUO92010). Primary antibody probes were made using goat anti-CDCP1 antibody (Abcam #ab1377). Images were collected as for immunofluorescence staining analysis. 12 mm coverslips were used with 20 µL reaction volumes.

Co-immunoprecipitation: 400 µg of protein in 200 µL of cell lysis buffer (see recipe in "Primary specimen acquisition and lysis") was incubated with 4 µL of anti-Flag antibody (Sigma Aldrich #F1804) for 16 hours at 4°C with gentle agitation. Then 20 µL Protein G Dynabeads (Life Tech #10003D) were added, followed by incubation for 1 hour at 4°C. Immunoprecipitated proteins were collected using magnetic stand, washed 3 times for 5 minutes on ice with cell lysis buffer without protease or phosphatase inhibitors, boiled in 1x sample loading buffer for 6 minutes and analyzed by WB.

Transwell migration: Transwell inserts (Corning Life Sciences Plastic, Corning, NY #3464) were coated in 50 mg/mL fibronectin (Sigma Aldrich #F2006-2) in DMEM for 4 hours at 37 °C. HEK 293T cells were treated with 10 µM mitomycin C for 2.5 hours before being detached with 2% EDTA in 1xPBS. 50,000 cells in serum-free DMEM were added to the top chamber of the inserts immersed in 10% FBS-containing media in the bottom

chamber. Cells were allowed to migrate for 24 hours. Cells from the top of the transwell inserts were removed with a cotton swab and cells that migrated through the transwell inserts were fixed and stained using the Richard Allen 3 Step Staining Kit (Thermo Scientific #3300), photographed and counted.

Scratch Assay: 400,000 MDA-MB-231 cells were plated per well of a 6-well plate. 24 hours later, cell monolayers were treated with mitomycin C for 2 hours in serum free DMEM and then scratched with a 200 µL pipette tip. The bottom of the plate was marked at 3 points on the scratch for triplicate measurements. Cells were washed once with 1xPBS and incubated in DMEM with 2% FBS, 2 mM L-glutamine, 100 u/mL penicillin and 100 µg/mL streptomycin. Pictures of the scratch were taken at the time of the scratch (T_0) and at 6 hours after the scratch (T_6). % wound closure was calculated as $(1-(T_6/T_0))*100$.

Split-luficerase assay: HEK 293T cells were plated at 10,000 cells/well in a black-walled 96-well plate. 16 hours later they were transfected with CDCP1-N'luc, CDCP1-C'luc and either a VC or ECC using Lipofectamine and Plus reagents (Life Tech) following the manufacturer's protocol. 48 hours after transfection dimerization was analyzed with D-luciferin (Promega, Madison, WI, #E1605) on an IVIS Lumina Imager (PerkinElmer, Waltham, MA).

3D assays: MDA-MB-231, MDA-MB-468, and UCI-082014 cell lines were plated at 3,000 cells in 50 uL of 1:1 collagen (BD Biosciences #354249):matrigel (BD Biosciences #356234) gel. Collagen was initially prepared at 6.4 mg/mL according to the manufacturer's protocol before being mixed with matrigel for a final concentration in the gels of 3.2 mg/mL collagen, similar to that in transformed breast tissue [118, 119]. Gels were plated onto 12 mm coverslips. Media on the cells was changed every two days and cells

were allowed to proliferate/invade the gel for 6 days. Gels were fixed in 4% PFA for 20 minutes, washed 4x15 minutes with 1xPBS, permeabilized with 0.3% Triton X-100 in 1xPBS for 15 minutes, washed 4x15 minutes with 1xPBS, incubated in blocking solution (10% donkey serum, 5% BSA, 0.1% Triton X-100 in 1xPBS) overnight at 4 °C with gentle agitation. Antibodies used for fluorescent staining in 3D are provided in Supplemental Table 1. Phase contrast images were taken using an EVOS xl Microscope (AMG, Bothell, WA) with a 10x objective. Fluorescent images were taken using a Zeiss Spinning Disc Confocal Microscope with a 20x objective with numerical aperture 0.8 and AxioVision software. Quantitation was the average of 5 images/gel for three biological replicates.

CHAPTER 3: CDCP1 DRIVES TRIPLE-NEGATIVE BREAST CANCER METASTASIS THROUGH REDUCTION OF LIPID DROPLET ABUNDANCE AND STIMULATION OF FATTY ACID OXIDATION.

Introduction

The transmembrane glycoprotein, CUB-domain containing protein 1 (CDCP1), is a driver of migration and invasion in multiple forms of carcinoma including renal[17, 20], ovarian[42, 120], prostate[28], pancreatic[43, 44], colon[1, 39, 50, 121, 122], and triple-negative breast[5, 30] carcinomas among others. Furthermore, CDCP1's role in tumor metastasis was confirmed *in vivo* in lung[22, 49], ovarian[123], prostate[28], and colon[121] cancers. Although CDCP1's role in TNBC metastasis was not established to date, high CDCP1 expression has been validated as a prognostic marker of poor survival in TNBC when combined with positive node status[67].

Our understanding of CDCP1's upstream regulators, its mechanism of activation, and downstream signaling continues to expand (recently reviewed[124]). Studies by others[28] and our group[5] have demonstrated that CDCP1 cleavage is necessary for its activation, and recently we have further shown that cleavage stimulates CDCP1 homo-dimerization[5]. Homo-dimeric CDCP1 stimulates phosphorylation of protein kinase C delta (PKCδ) by Src kinase, leading to migration and invasion of TNBC cells *in vitro*[5]. Adding to our knowledge of CDCP1's downstream signaling, we report that CDCP1 regulates lipid metabolism in TNBC by reducing cytoplasmic lipid droplet (LD) abundance and promoting fatty acid oxidation (FAO) in TNBC cells.

Breast tissue is known to be a dynamic site of lipid metabolism[125] and LD abundance changes dramatically during development[126, 127], menstruation, pregnancy, and lactation[128]. LDs are formed by budding off of the endoplasmic reticulum (ER) and store fatty acids (FAs) in the form of diacyl- and triacylglycerol (DAG and TAG, respectively) and cholesterol in the form of cholesteryl esters. LDs interact with a multitude of organelles (i.e. peroxisomes, autophagosomes, and mitochondria) to shuttle FAs for incorporation into cell membranes, post-translational modifications, and FAO[129]. In order for long chain FAs to enter any of these pathways they must first be activated to become acyl-CoAs. Long-chain (12-20 carbons) FAs are activated by typical acyl-CoA synthetase ligase (ACSL) enzyme family, including members 1, 3, 4, and 5[130]. Acyl-CoAs may enter FAO, which yields acetyl-CoAs utilized in the tricarboxylic acid cycle (TCA), generating nicotinamide adenine dinucleotide (NADH) utilized for oxidative phosphorylation (OxPhos) to ultimately produce adenosine triphosphate (ATP). Acyl-CoAs can also enter anabolic pathways and the shuttling of acyl-CoAs into either anabolic or catabolic pathways depends significantly on their localization within the cells[130, 131]. While there is conflicting data of the respective role and cell-type specificity of each ACSL in catabolic and anabolic pathways, ACSL3 has mainly been implicated in lipid anabolism (lipid storage) in mouse adipocytes and primate kidney cells[132, 133].

Dysregulated lipid metabolism and FAO have recently been linked to breast cancer progression. Photoacoustic imaging of the MMTV-PyMT-driven breast cancer model demonstrated that transformation of normal breast tissue to invasive carcinoma resulted in a progressive decrease of cytoplasmic LD abundance[69]. In line with this, pharmacological activation of peroxisome proliferator-activated receptor γ (PPARγ)

caused accumulation of LDs in breast cancer cells and decreased their proliferation[70]. Furthermore, Src[71] and Myc[72] oncogenes were recently reported to contribute to lipid metabolism dysregulation in TNBC. Src kinase has been reported to stimulate FAO in a positive feedback loop, and pharmacological and genetic inhibition of FAO blocked TNBC metastasis *in vivo*[71]. Myc has also been reported to stimulate FAO and pharmacological inhibition of FAO blocked tumor growth of Myc-driven TNBC tumors[72]. These data indicate that lipid metabolism represents a potential therapeutic target in TNBC.

Lipid metabolism dysregulation has also been reported in other types of cancer. Pharmacological inhibition of Myc in neuroblastoma increases LD abundance, accompanied by growth arrest and apoptosis *in vitro* and increased animal survival *in vivo*[73]. High-passage prostate cancer cells (comparable to metastatic cells) have lower LD abundance than their low-passage (comparable to primary tumor) counterparts[74]. In a spontaneous mouse model of pancreatic cancer the synthesis of acyl-CoA-modified lipids was found to be the most downregulated metabolic pathway compared to normal pancreatic tissue[75]. These data indicate that dysregulated lipid metabolism is characteristic of progression of multiple forms of cancer.

Here, we used coherent anti-Stokes Raman scattering (CARS) and two-photon excited fluorescence (TPEF) microscopy methods to assess TNBC metabolism. CARS microscopy detects the C-H bond in FAs, allowing quantification of the LD abundance[134]. TPEF microscopy detects fluorescence from reduced NADH and oxidized flavin adenine dinucleotide (FAD^+). The relative ratio of the two fluorophores is defined as optical redox ratio (ORR)[135], which we have previously correlated with OxPhos rate[68]. Previously, we found that CDCP1 is overactivated in TNBC compared to normal breast epithelial cells[5].

Here, we demonstrate that CDCP1 dysregulates lipid metabolism in TNBC: CDCP1 by inactivating ACSLs reduces LD abundance and stimulates FAO, which increases OxPhos. This results in a "low lipid" phenotype, a high migratory ability *in vitro*, and metastasis *in vivo*. These findings provide a novel insight into CDCP1 as a regulator of LD abundance and FAO. Since CDCP1 is a druggable target[5, 28], these findings have important implications for TNBC therapeutic targeting and development of prognostic markers.

Results

CDCP1 lowers intracellular LD abundance in breast cancer cells. We have previously identified CDCP1 protein as a master-regulator of migration and invasion in TNBC[5]. To get insight into the signaling pathways it regulates, we conducted a mass spectrometric (MS) analysis of proteins interacting with CDCP1. We overexpressed CDCP1 with a C-terminal Flag-tag in HEK 293T cells and conducted co-immunoprecipitation (co-IP). Unexpectedly, we found that CDCP1 interacts with multiple proteins involved in metabolism based on PANTHER analysis (http://www.pantherdb.org/) (Supplemental Figure 3.1). Among these proteins was ACSL3, involved in lipid metabolism.

To assess CDCP1's role in lipid metabolism, we first analyzed the effect of CDCP1 knockdown on LD abundance in three TNBC cell lines, MDA-MB-231, MDA-MB-468, and UCI-082014[5], using two different shRNAs. We found that knocking down CDCP1 expression in all three cell lines increased LD content as analyzed by CARS microscopy (Figure 3.1A). Second, we overexpressed CDCP1 in MDA-MB-231, MDA-MB-468, UCI-082014, and MCF7 cells and found that overexpression of CDCP1 decreased LD content

of these cells (Figure 3.1B). These results demonstrate that CDCP1 decreases LD abundance in breast cancer cells.

We further analyzed which lipid types were affected by CDCP1 expression in MDA-MB-231 and MDA-MB-468 cells using gas chromatography and found that multiple long-chain (16 and 18 carbons) FAs had lower abundance in shScramble-transduced control cells compared to shCDCP1-transduced cells (Supplemental Figure 3.2).

CDCP1 expression correlates with breast cancer cell invasiveness and causes appearance of low-lipid broken spheroids in 3D culture. Since primary mammary epithelium cells (PME) were reported to have abundant LDs[70], we sought to compare their LD content to breast cancer cells. We found that PME and a non-malignant breast cell line MCF10A had at least a two-fold higher LD content than a panel of six breast cancer cell lines as analyzed by CARS microscopy (Figure 3.2A i-ii).

We found that CDCP1 was expressed in five out of six breast cancer cell lines in the panel, as well as in PME and MCF10A (Figure 3.2A iii). Studies by others[28] and our group[5] have shown that CDCP1 cleavage leads to its activation to stimulate migration, invasion, and metastasis. Importantly, CDCP1 appears to be mostly full-length in PME and MCF10A and cleaved in five out of five breast cancer cell lines that express CDCP1. Although CDCP1 is mostly full-length in SUM159 cells, the abundance of cleaved CDCP1 is still higher than in PME and MCF10A. Accordingly, all of the breast cancer cell lines formed irregular acini structures, spheroids, in 3-dimensional (3D) culture and invaded the surrounding matrix compared to the normal hollow acini formed by PME and MCF10A

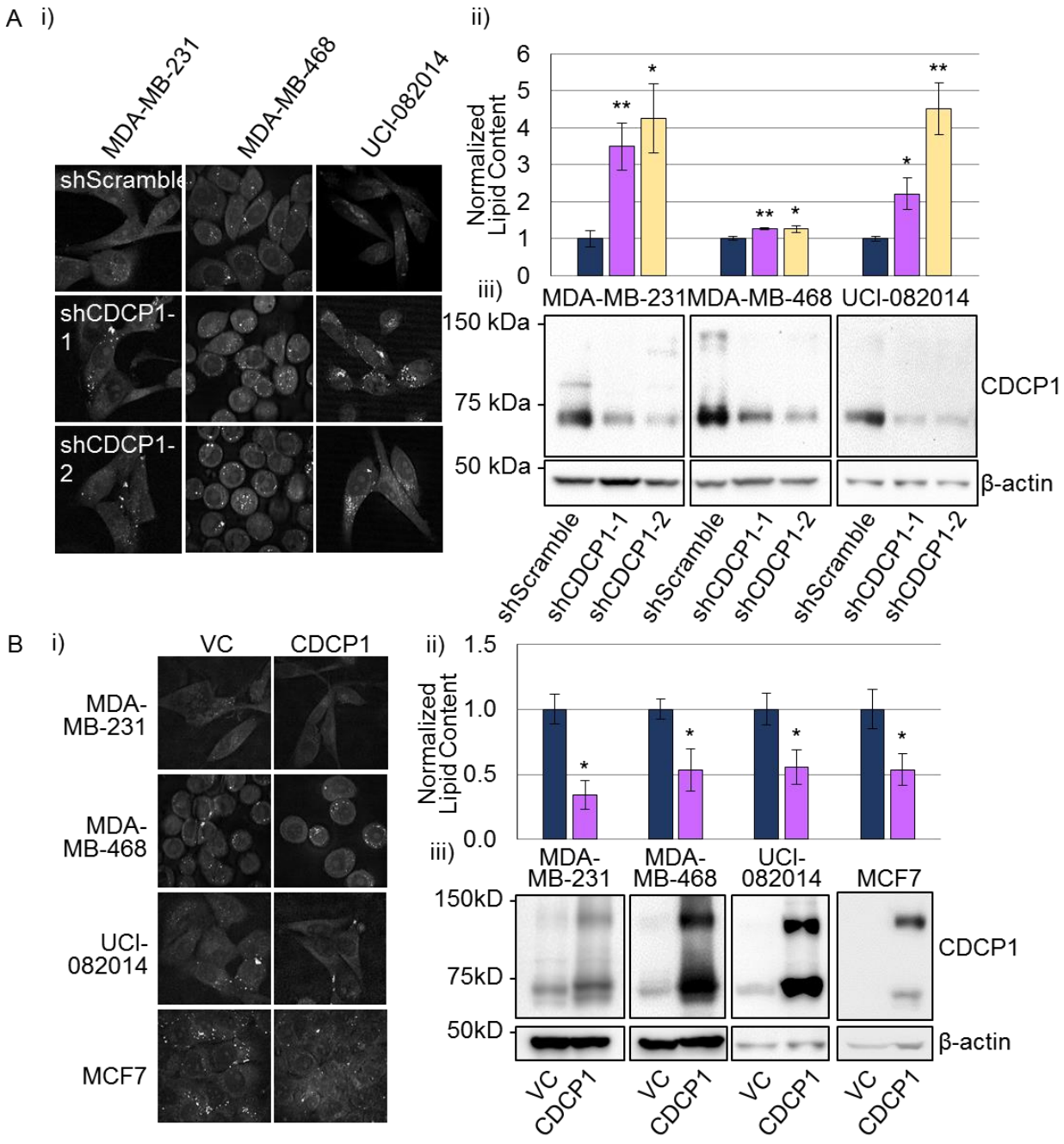

Figure 3.1 | CDCP1 lowers intracellular Lipid Droplet (LD) abundance of breast cancer cells. **A**) CDCP1 knockdown increases LD abundance in three TNBC cell lines. i) representative 40x CARS images; ii) quantitation of CARS; iii) Western blot confirming CDCP1 knockdown. **B**) CDCP1 overexpression decreases LD abundance in three TNBC cell lines and ER$^+$ MCF7 breast cancer cell line not expressing endogenous CDCP1. i) representative 40x CARS images; ii) quantitation of CARS; iii) Western blot confirming CDCP1 overexpression. N=3 for **A**) and **B**). P values analyzed by one way analysis of variance (ANOVA) with multiple comparison post hoc T-test and error bars represent SEMs. *P<0.05, **P<0.01.

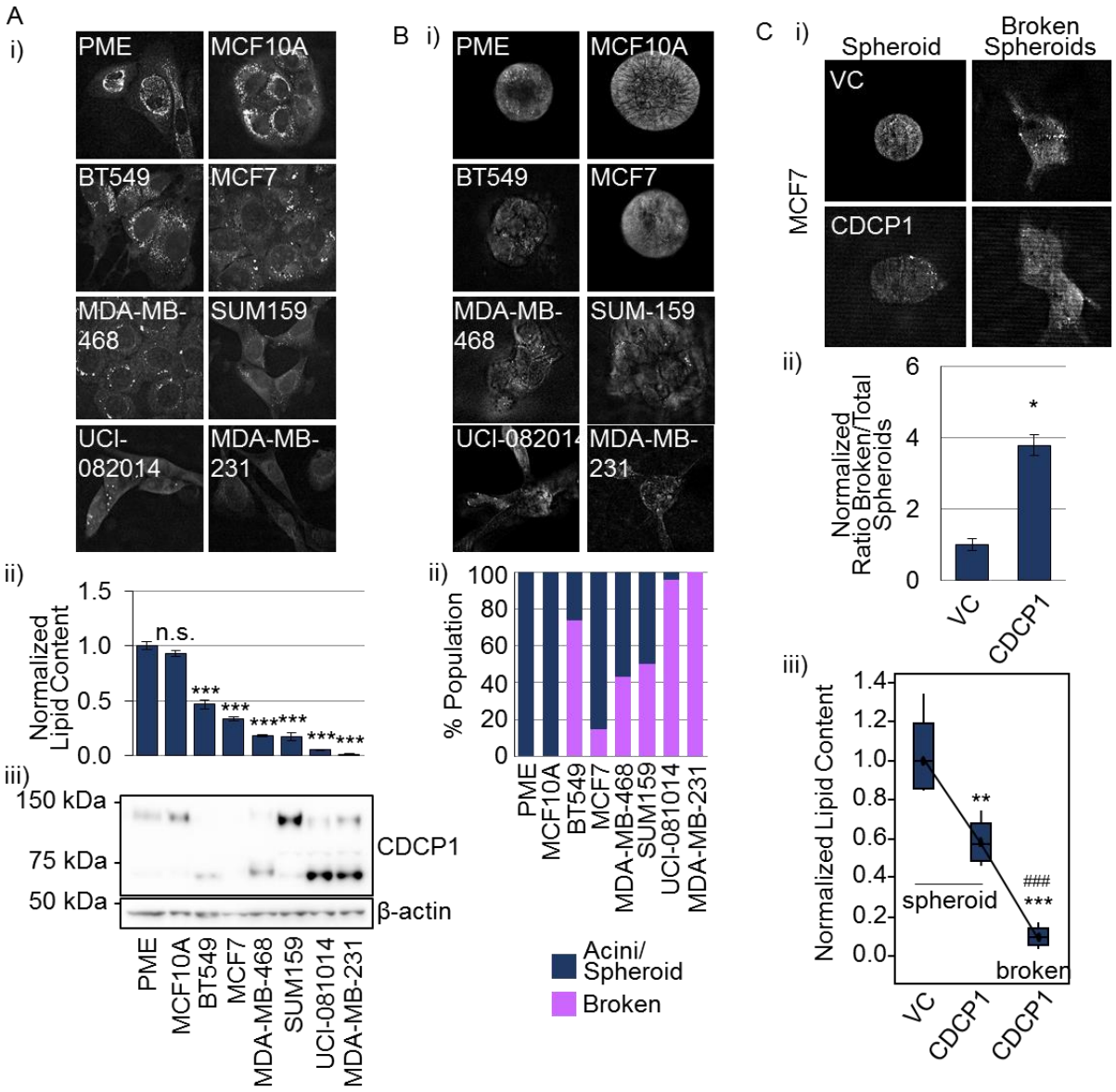

Figure 3.2 | Expression of cleaved CDCP1 isoform correlates with breast cancer cell invasiveness and causes appearance of low-lipid broken acini in 3D culture. A) The LD abundance is lower in breast cancer cells compared to primary mammary epithelial (PME) and non-tumorigenic breast epithelial (MCF10A) cells in 2D culture. i) representative 40x CARS images; ii) quantitation of CARS, statistics based on comparison to PME; iii) Western blot of CDCP1 expression. **B**) Lower LD abundance correlates with invasiveness in 3D culture. i) representative 40x CARS images of breast cancer cell lines in 3D culture; ii) quantitation of intact acini (PME and MCF10A), intact spheroids and broken spheroids (breast cancer cell lines). **C**) CDCP1 overexpression in MCF7 cells promotes invasion observed as broken spheroids in 3D culture, which have lower LD content than intact spheroids. i) representative 40x CARS images; ii) quantitation of the ratio of broken spheroids to total spheroids in VC- and CDCP1-transduced MCF7 cells; iii) quantitation of LD abundance in spheroids formed by VC- and CDCP1-transduced MCF7 and broken spheroids formed by CDCP1-transduced MCF7 cells. *compared to VC, #compared to CDCP1 spheroids. N=3 in **A** ii) and **C** iii). P values analyzed by one way ANOVA with multiple comparison post hoc T-test and error bars represent SEMs. *P<0.05, **P<0.01, ***,###P<0.001.

cells (Figure 3.2B). Moreover, when we overexpressed CDCP1 in MCF7 cells (lacking endogenous CDCP1), they became more invasive and formed more broken spheroids (Figure 3.2C i-ii). Importantly, we observed heterogeneity in lipid content in 3D culture: intact spheroids had higher lipid content than broken spheroids (Figure 3.2C iii). These data suggest a link between lipid droplet abundance and invasiveness, both of which are regulated by CDCP1.

CDCP1 interacts with ACSL family of proteins involved in lipid metabolism. To investigate the molecular mechanism of the LD regulation by CDCP1, we decided to validate the interaction of CDCP1 with ACSL3 found by MS. CDCP1 and ACSL3 interact in HEK 293T cells overexpressing cCDCP1-Flag and ACSL3 as shown by co-IP (Figure 3.3A). We further found that CDCP1 interacts with ACSL3 endogenously in MDA-MB-231 cells by proximity ligation assay (PLA) using shCDCP1-1 and shACSL3 as negative controls (Figure 3.3B i).

ACSL3 belongs to an ACSL protein family, including typical members 1, 3, 4, and 5[131, 136]. Thus, we conducted additional PLA assays and found that CDCP1 interacts with ACSL1, 3, 4, and 5 (Figure 3.3B ii-iii; RhoC antibody was used as a negative control). All ACSL antibodies and RhoC antibody used for PLA were verified to work for immunofluorescence (Supplemental Figure 3.3).

CDCP1 regulates ACSL activity. The CDCP1/ACSL interaction suggested that CDCP1 is an ACSL regulator. We analyzed the CDCP1's effect on ACSL activity using a previously established assay[137-140] based on mid-chain BODIPY labeled palmitate

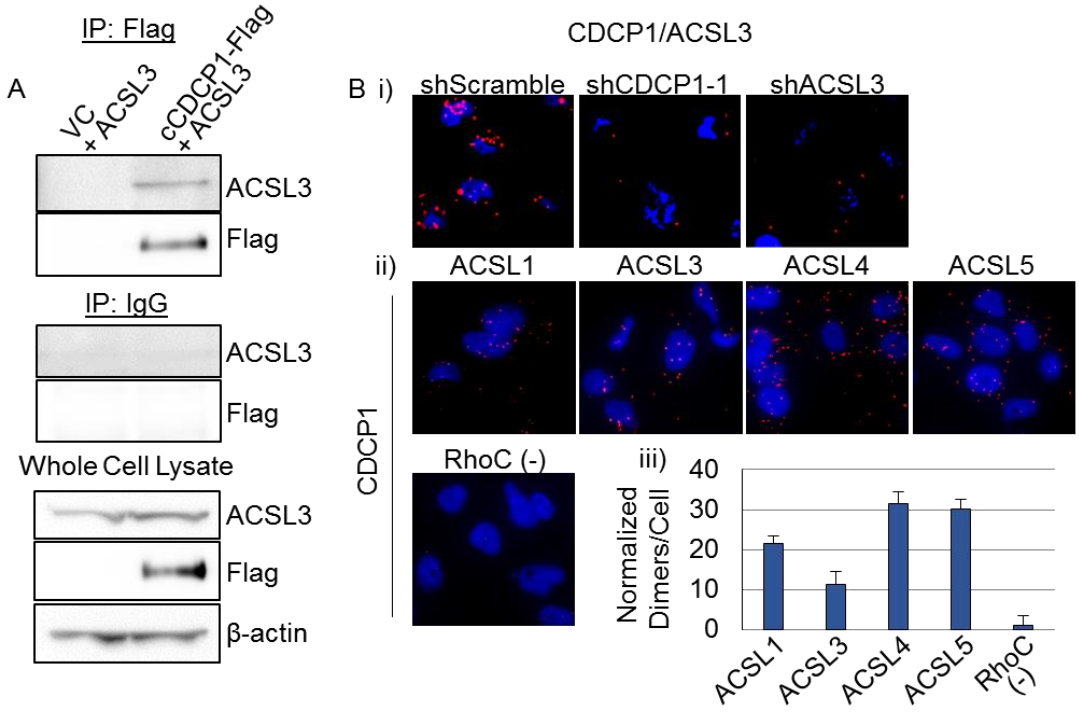

Figure 3.3 | CDCP1 interacts with ACSL family of proteins involved in lipid metabolism. A) CDCP1 co-immunoprecipitates with ACSL3 in HEK 293T cells overexpressing ACSL3 and Flag-tagged cleaved CDCP1. **B**) 40x images of proximity ligation assay (PLA) conducted in MDA-MB-231 cells demonstrating that i) CDCP1 interacts with ACSL3 endogenously; negative controls: shCDCP1-1- and shACSL3-transduced cells; ii) CDCP1 interacts with ACSL family members endogenously; negative control: anti-CDCP1 + anti-RhoC antibody pair, based on no reports of CDCP1 and RhoC interaction; iii) quantitation of PLA in (ii).

(structure in Figure 3.4A). First, we validated the assay in TNBC cell lines treated with a pan-ACSL inhibitor, Triacsin C (Figure 3.4B), and shACSL3-transduced TNBC cell lines (Figure 3.4C). In both cases we observed a decrease in ACSL activity as compared to vehicle-treated cells and shScramble-transduced cells. Second, we analyzed ACSL activity in the same TNBC cell lines with manipulated CDCP1 expression. We found that ACSL activity was increased on average by 40% in shCDCP1-transduced cells compared to shScramble-transduced cells (Figure 3.4D). Accordingly, ACSL activity was decreased on average by 15% in CDCP1 overexpressing cells compared to vector-control (VC) cells (Figure 3.4E). CDCP1 expression was assessed by western blot in Figure 1A iii and 1B iii. These data suggest that CDCP1-mediated reduction of ACSL activity leads to decreased acyl-CoA production and storage in LDs.

Low lipid content favors pro-migratory phenotype of breast cancer cells. We have shown that CDCP1 decreases cytoplasmic LD abundance and stimulates invasiveness in TNBC cells; and previously we have shown that CDCP1 stimulates TNBC cell migration[5]. Our findings that CDCP1 interacts with ACSLs and negatively regulates their activity led us to investigate the effect of ACSL expression on migration. Consistent with the above data we found that knocking down ACSL3 expression reduced LD abundance (Figure 3.5A), increased TNBC cell migration (Figure 3.5B) and invasion (Supplemental Figure 3.4A), and lung metastasis of MDA-MB-231 cells injected into the mammary fat pad of $RAG2^{-/-}$ mice (Supplemental Figure 3.4B). We further found that treatment of shCDCP1-transduced TNBC cells with pan-ACSL inhibitor, Triacsin C, reduced the LD abundance to the level of shScramble-transduced cells or greater (Figure

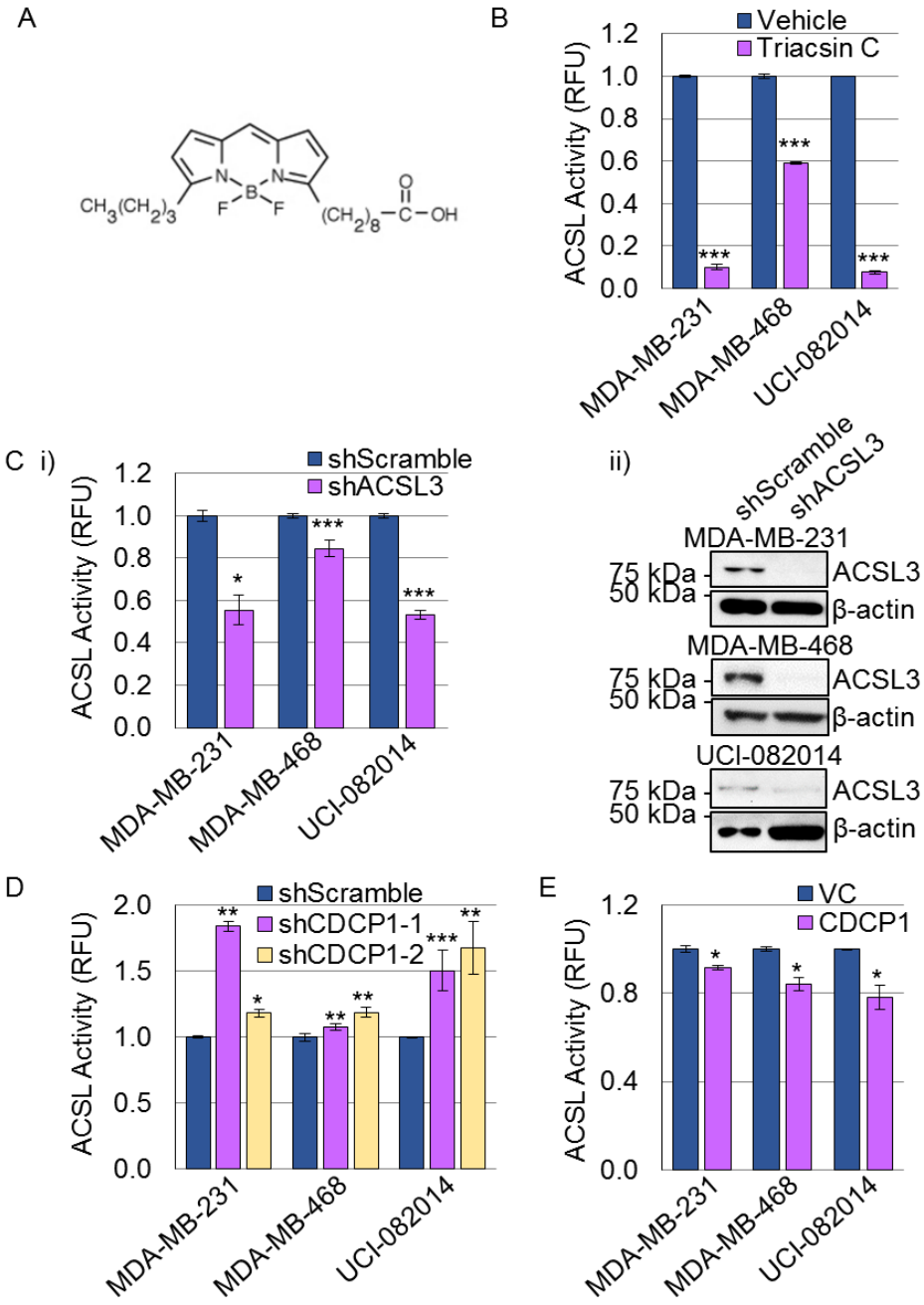

Figure 3.4 | CDCP1 regulates ACSL activity. A) Structure of BODIPY used for ACSL activity assays. **B**-**C**) Validation of ACSL activity assay in TNBC cells. **B**) 5 μM Triacsin C reduces ACSL activity compared to DMSO vehicle. **C**) i) ACSL3 knockdown reduces ACSL activity; ii) Western blot confirming ACSL3 knockdown. **D**) CDCP1 knockdown increases ACSL activity in TNBC cells. **E**) CDCP1 overexpression decreases ACSL activity in TNBC cells. P values analyzed by one way ANOVA with multiple comparison post hoc T-test and error bars represent SEMs. *P<0.05, **P<0.01, ***P<0.001. Quantitation is the average of an N≥3 for each panel. RFU; relative fluorescence units.

3.5C) and partially rescued the migration defects caused by CDCP1 knockdown (Figure 3.5D and Supplemental Figure 3.5). The data acquired with genetic (shACSL3) and pharmacologic (Triacsin C) inhibition of ACSL activity generated consistent results.

Interestingly, we observed distinct effects of ACSL3 and CDCP1 knockdowns on cell proliferation: ACSL3 knockdown decreased proliferation of MDA-MB-231, MDA-MB-468, and UCI-082014 cells (Supplemental Figure 3.6A), while CDCP1 knockdown did not change proliferation (Supplemental Figure 3.6B), consistent with previous reports for cell types other than TNBC[14, 141]. Since CDCP1 is known to regulate multiple pathways in addition to ACSL[5, 13, 15, 17, 28, 30], it is likely that these override the effect of CDCP1/ACSL axis on cell proliferation.

To further investigate the contribution of the ACSL pathway to CDCP1's effect on LD abundance and invasion, we simultaneously knocked down ACSL3 and CDCP1 in MDA-MB-231 and UCI-082014 cells (see Supplemental Figure 3.6A for knockdown validation) and conducted 3D assays (similar to Figure 3.2). We found that the increase in LD abundance seen by knocking down CDCP1 was rescued by co-knockdown of ACSL3 in MDA-MB-231 and UCI-082014 cells (Figure 3.5E and Supplemental Figure 3.7B). Furthermore, we found that the decrease in ORR seen by knocking down CDCP1 was partially rescued by co-knockdown of ACSL3 (Supplemental Figure 3.7C). Upon culturing the cells in 3D, we found that knocking down CDCP1 reduced invasiveness and growth of the cells (consistent with our previous findings[5]), and that co-knocking down ACSL3 rescued invasiveness of the cells and did not rescue the reduced growth (Figure 3.5Fiii). These data link inhibition of ACSL activity occurring downstream of CDCP1 to decreased LD abundance, and increased migration and invasion.

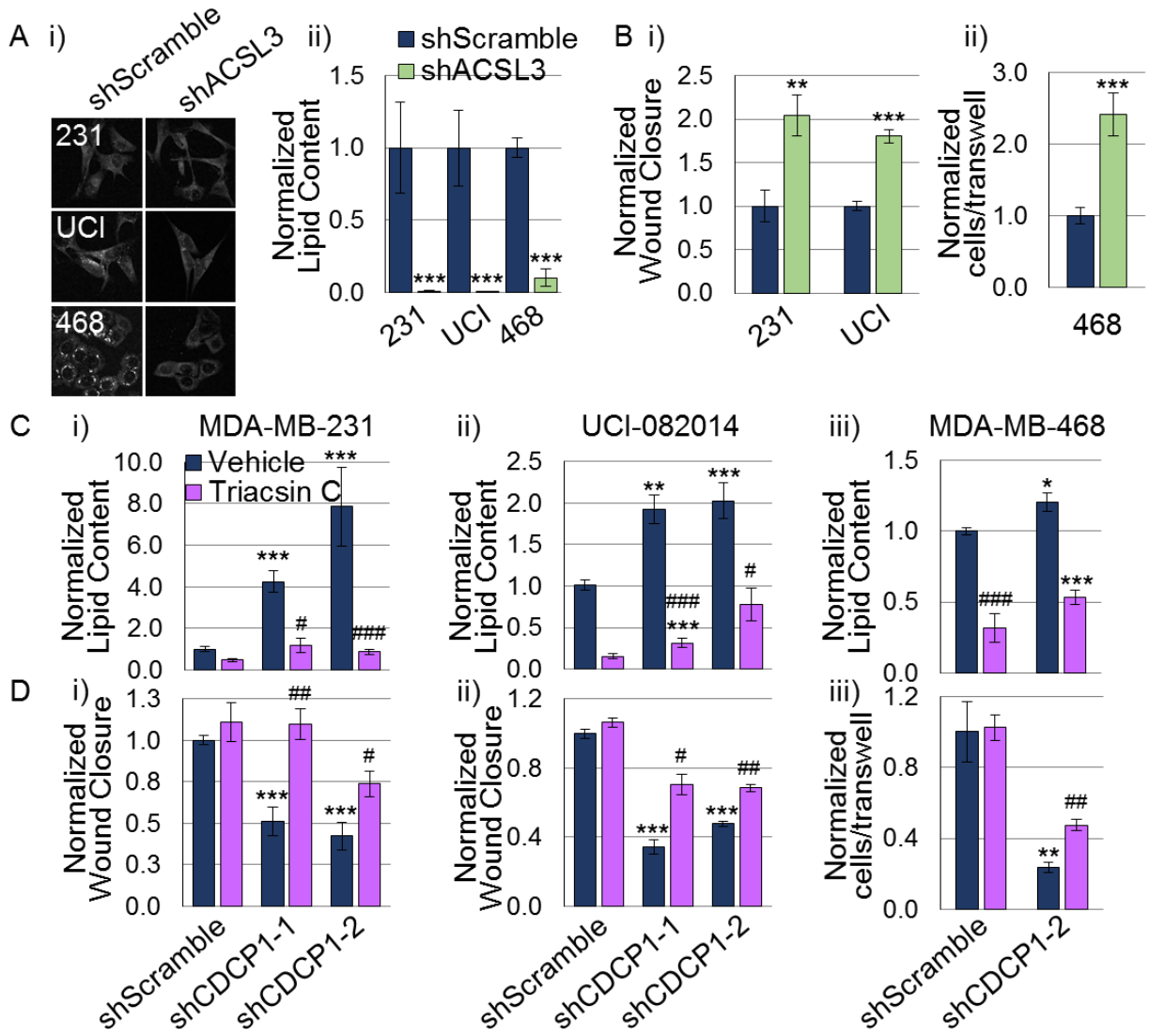
A i)
shScramble
shACSL3
231
UCI
468
ii)
shScramble
shACSL3
Normalized Lipid Content
231
UCI
468
B i)
Normalized Wound Closure
231
UCI
ii)
Normalized cells/transwell
468
C
i) MDA-MB-231
ii) UCI-082014
iii) MDA-MB-468
Vehicle
Triacsin C
Normalized Lipid Content
D
i)
ii)
iii)
Normalized Wound Closure
Normalized cells/transwell
shScramble
shCDCP1-1
shCDCP1-2

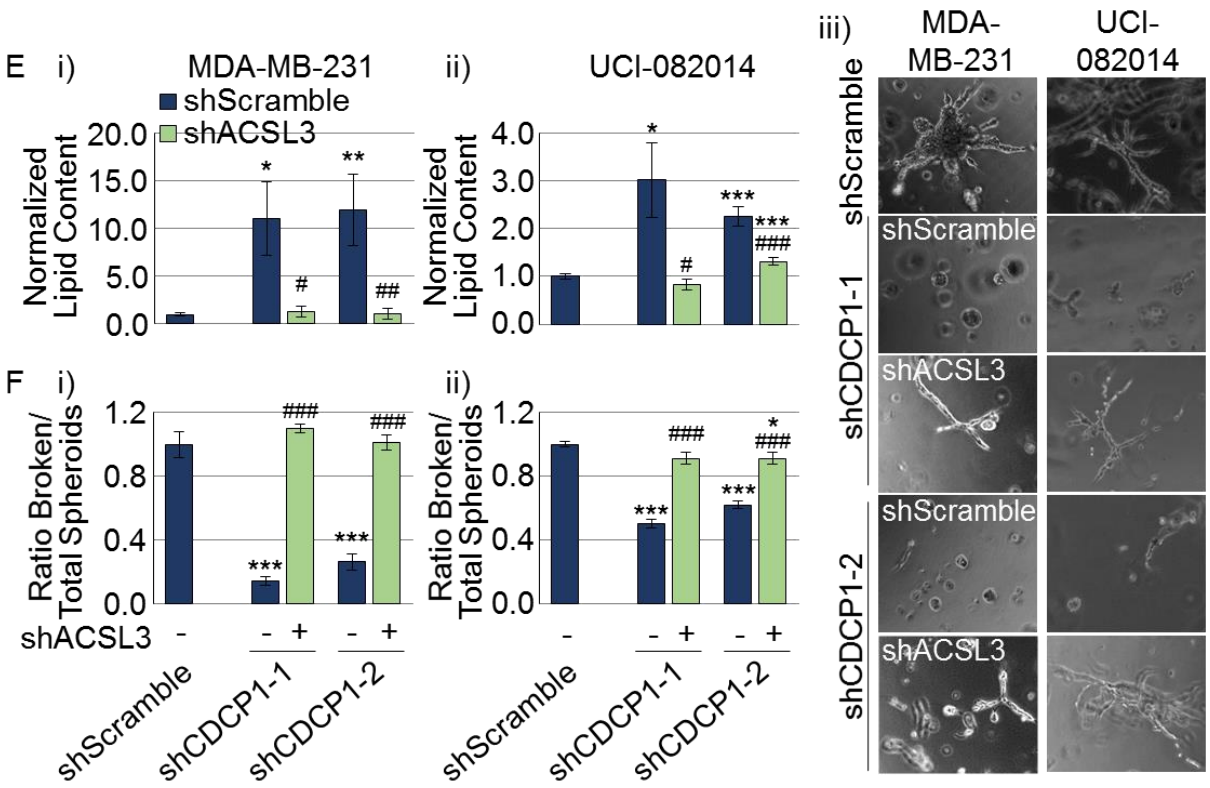

Figure 3.5 | Low lipid content favors pro-migratory phenotype of TNBC. A) ACSL3 knockdown reduces LD abundance in TNBC cell lines. i) Representative 40x CARS images. ii) Quantitation of CARS. **B**) ACSL3 knockdown increases migration of MDA-MB-231 and UCI-082014 (i) and MDA-MB-468 (ii) cells. **C**-**D**) CDCP1 knockdown increases LD abundance (**C**) and reduces migration (**D**) in MDA-MB-231 (i), UCI-082014 (ii), and MDA-MB-468 cells (iii), and 5 μM Triacsin C treatment for 16 hours (lowering lipids) partially rescues migration of shCDCP1-transduced cells. **E**-**F**) Increase in LD abundance (**E**) and reduction in invasion (**F**) by CDCP1 knockdown can be rescued by co-knockdown of ACSL3. **E**) Quantitation of LD abundance measured by Oil Red O (ORO) staining. **F**) Quantitation of the ratio of broken/total spheroids in MDA-MB-231 (i) and UCI-082014 (ii) 3D cultures. iii) Representative 20x phase contrast images of 3D MDA-MB-231 and UCI-082014 cultures. N=3 for **A**-**F**. P values analyzed by one way ANOVA with multiple comparison post hoc T-test and error bars represent SEMs. *,#P<0.05, **,##P<0.01 and ***,###P<0.001; *compared to respective vehicle-treated shScramble cells; #compared to respective vehicle-treated shCDCP1 cells.

CDCP1 increases FAO in breast cancer cells. Interestingly, recent studies conducted in TNBC report two opposing disturbances in lipid metabolism: downregulation of activators of lipid synthesis, along with upregulation of activators of FAO[72, 73]. We next sought to determine if the “low lipid” phenotype caused by CDCP1 is due to increased lipid utilization by FAO, in addition to decreased lipid activation for storage in LDs. First, we found that shCDCP1-transduced MDA-MB-231, MDA-MB-468, and UCI-082014 cells had lower levels of OxPhos than shScramble-transduced cells measured by ORR (Supplemental Figure 3.8A). Second, to assess the contribution of FAO in OxPhos, we measured ORR after cell treatment with DMSO vehicle or FAO inhibitor Etomoxir[142, 143]. We found that the ΔORR between DMSO- and Etomoxir-treated cells was lower in shCDCP1-transduced than in shScramble-transduced cells (Figure 3.6A iii), indicating that FAO rates decrease upon CDCP1 knockdown, lowering OxPhos dependent on the products of FAO. Third, to assess if CDCP1/ACSL axis contributes to OxPhos, we treated TNBC cells with Triacsin C and found that OxPhos increased as measured by ORR (Supplemental Figure 3.8B). We verified that Triacsin C treatment increased FAO in TNBC cells (Supplemental Figure 3.8C) using the same analysis as in Figure 6A iii. Furthermore, we found that the decrease in FAO in MDA-MB-231 cells by CDCP1 knockdown was rescued by Triacsin C treatment (Supplemental Figure 3.8D). Finally, treatment of TNBC cells with Etomoxir to inhibit FAO increased LD abundance (Supplemental Figure 3.9A) and reduced migration (Supplemental Figure 3.9B) of TNBC cell lines, consistent with previous studies[71-73]. These data indicate that CDCP1 contributes to “low lipid” TNBC phenotype by increasing FAO and OxPhos, and ACSL

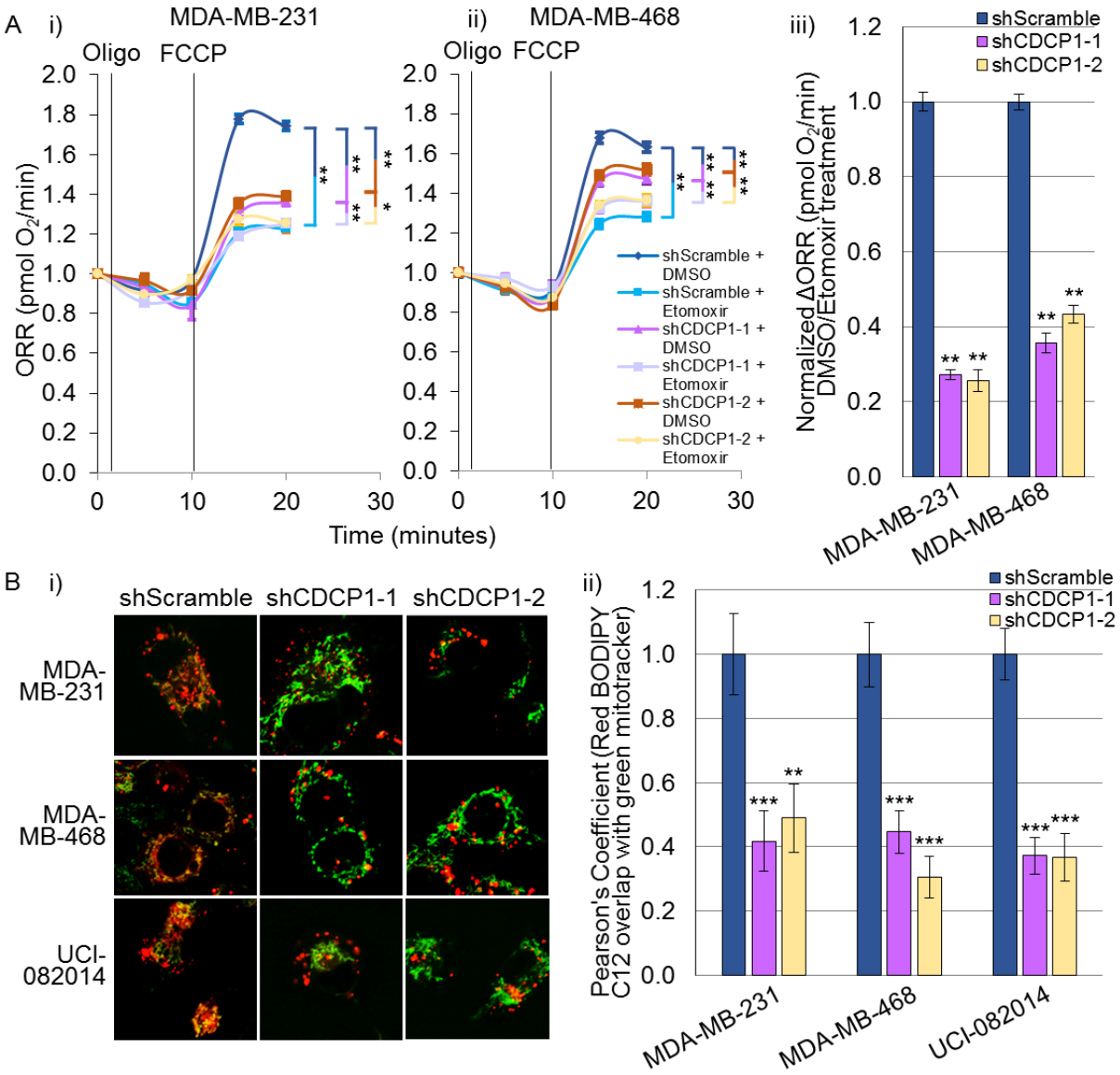

Figure 3.6 | CDCP1 knockdown reduces FAO in TNBC cells. A) CDCP1 knockdown reduces FAO as measured by optical redox ratio (ORR) in MDA-MB-231 (i) and MDA-MB-468 (ii) cells. Oligomycin (Oligo, ATP synthase inhibitor) followed by carbonyl cyanide-4-phenylhydrazone (FCCP, ATP synthesis uncoupler) treatment allowed measurement of maximum respiration potential. Etomoxir (FAO inhibitor, blocking transport of fatty acids (FAs) into the mitochondria) treatment allowed measurement of FAO fueled by FAs already present in mitochondria. iii) shCDCP1-transduced cells have lower ΔORR (calculated as 1-[DMSO-treated ORR/Etomoxir-treated ORR] and then all data were normalized to shScramble control, which was set to 1) than shScramble-transduced cells, indicating that CDCP1 knockdown reduces lipid stores in the mitochondria available for FAO. **B**) Representative 63x images (i) and quantitation (ii) of co-localization of red BODIPY C12 (lipids) with green MitoTracker (mitochondria), indicating that less lipids co-localize with the mitochondria 16 hours after BODIPY C12 addition. N=3 for **A**) and **B**). P values analyzed by one way ANOVA with multiple comparison post hoc T-test and error bars represent SEMs. *P<0.05, **P<0.01, ***P<0.001.

inhibition by CDCP1 increases FAO and OxPhos. These data are in line with reports on CDCP1[1, 5, 17, 20, 28, 30, 39, 42-44, 50, 120-122], FAO[71], and OxPhos[144-146] promoting cell migration.

We also assessed the differences in lipid transport to mitochondria between shScramble- and shCDCP1-transduced cells, as described in[147]. We pulsed TNBC cell lines with red C12 BODIPY (structure in Supplemental Figure 3.10A) for 16 hours and then co-stained with green MitoTracker to visualize mitochondria. Co-localization quantitated by Pearson's coefficient of red (lipid) and green (mitochondria) staining indicated that CDCP1 knockdown reduced transport of lipids into the mitochondria (Figure 3.6B). We verified that mitochondrial mass did not differ in shScramble- and shCDCP1-transduced cells (Supplemental Figure 3.10B).

Extracellular portion of cleaved CDCP1 (ECC) blocks CDCP1 dimerization *in vivo*, which is accompanied by high LD abundance and reduced metastasis. We previously demonstrated that CDCP1 cleavage and dimerization are important for driving TNBC migration and invasion[5]. Moreover, we were able to block CDCP1 dimerization and activity by the expression of the secreted extracellular portion of cleaved CDCP1 (ECC)[5]. Thus, we hypothesized that *in vivo* ECC would block TNBC metastasis and increase the LD abundance in primary tumors. First, we found that LD abundance was higher in ECC-transduced UCI-082014 and MDA-MB-231 cells than in VC-transduced cells *in vitro* (Supplemental Figure 3.11A). Second, we implanted VC- or ECC-firefly luciferase-labeled UCI-082014 and MDA-MB-231 cells to fat pads of RAG2$^{-/-}$ mice. Five (UCI-081014) to eight (MDA-MB-231) weeks after cell implantations, mice were imaged and then sacrificed (Figure 3.7A). We found that ECC inhibited the primary tumor growth

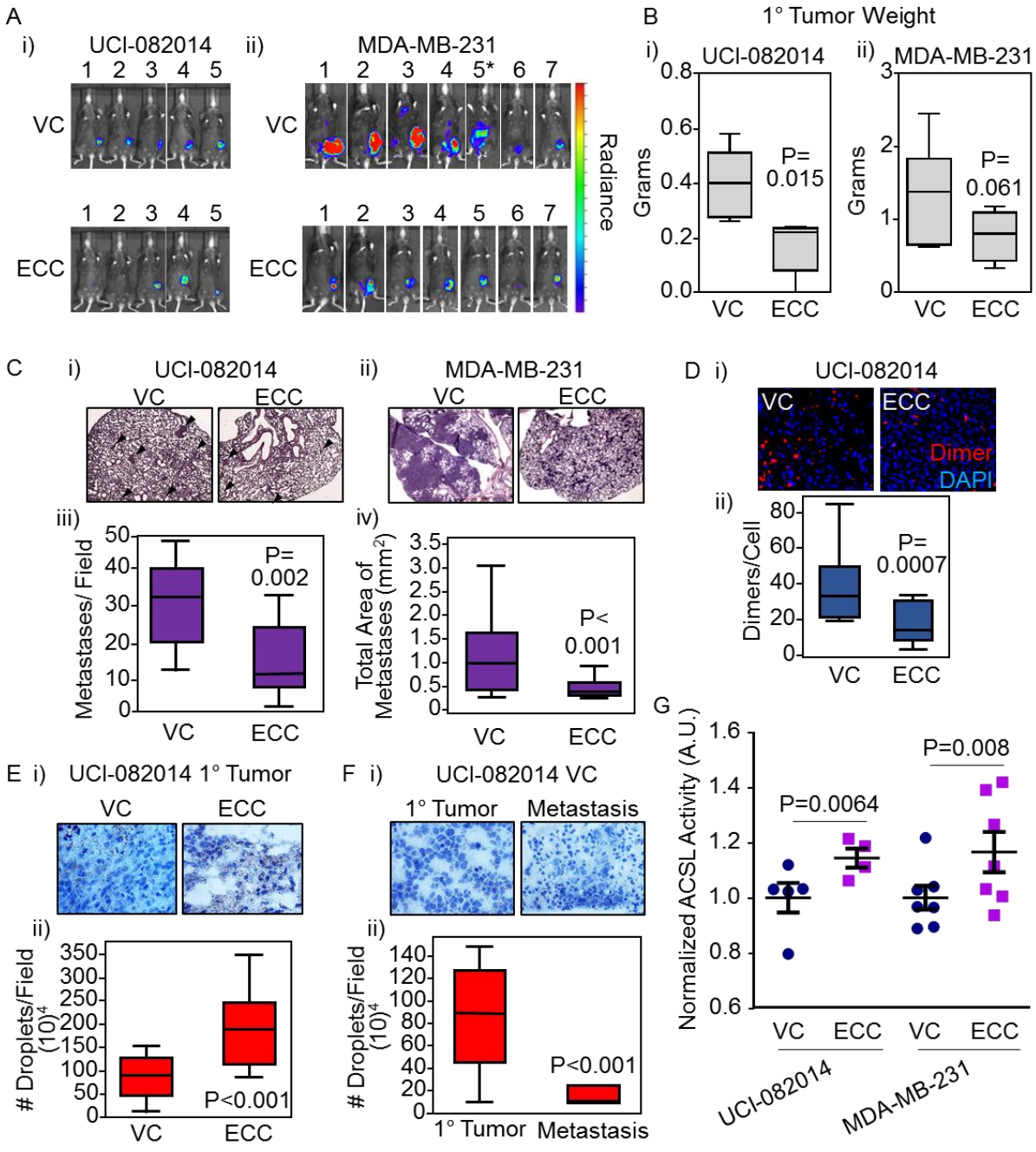
A
i) UCI-082014
ii) MDA-MB-231
1 2 3 4 5
1 2 3 4 5* 6 7
VC
ECC
Radiance
B
1° Tumor Weight
i) UCI-082014
ii) MDA-MB-231
Grams
P= 0.015
P= 0.061
VC
ECC
C
i) UCI-082014
ii) MDA-MB-231
iii) Metastases/ Field
P= 0.002
iv) Total Area of Metastases (mm2)
P< 0.001
D i) UCI-082014
Dimer
DAPI
ii) Dimers/Cell
P= 0.0007
E i) UCI-082014 1° Tumor
ii) # Droplets/Field (10)4
P<0.001
F i) UCI-082014 VC
1° Tumor
Metastasis
ii) # Droplets/Field (10)4
P<0.001
G
Normalized ACSL Activity (A.U.)
P=0.0064
P=0.008
UCI-082014
MDA-MB-231

Figure 3.7 | Expression of a CDCP1-blocking fragment, ECC, increases LD abundance and reduces metastasis. A) Representative images of mice with luciferase-labeled UCI-082014 (i) or MDA-MB-231 (ii) tumors at week 5 and 8 post tumor implantation, respectively. * VC-5 euthanized 2 weeks early due to extensive disease progression and visibly reduced quality of life. **B**) ECC reduces primary (1°) tumor growth of UCI-082014 (i) and trends towards reducing 1° tumor growth of MDA-MB-231 (ii) cells implanted into the fat pad of RAG2$^{-/-}$ mice. **C**) ECC expression reduces lung metastasis of UCI-082014 and MDA-MB-231 tumors. (i-ii) representative 4x images of H&E-stained lungs from mice implanted with UCI-082014 (i), metastases are shown by arrowheads, and MDA-MB-231 (ii) cells. (iii-iv) quantitation of UCI-082014 (iii) and MDA-MB-231 (iv) metastasis. **D**) ECC reduces CDCP1 dimer formation in 1° tumors as assessed by PLA. Representative 20x images (i) and quantitation (ii) of PLA. **E**) ECC increases LD abundance in 1° tumors. Representative 20x images (i) and quantitation (ii) of Oil Red O (ORO) staining. **F**) VC-transduced 1° tumors have higher LD abundance than the corresponding metastatic nodules. Representative 20x images (i) and quantitation (ii) of ORO staining. **G**) ECC stimulates ACSL activity in 1° tumors. Quantitation of ACSL activity in VC- and ECC-transduced UCI-082014 and MDA-MB-231 primary tumor tissue. Each point represents an individual tumor. P values (as indicated) analyzed by one way ANOVA with multiple comparison post hoc T-test and error bars represent SEMs.

in the UCI-082014-based model (Figure 3.7B i). Although the same tendency was observed in the MDA-MB-231-based model (Figure 3.7B ii)), the data did not reach statistical significance (P=0.0613). Furthermore, ECC inhibited metastasis to the lungs in both mouse models (Figure 3.7C). We verified that ECC was expressed by western blot (Supplemental Figure 3.11B) and inhibited CDCP1 dimerization as assessed by PLA in the primary tumors (Figure 3.7D and Supplemental Figure 3.11C). As expected, we found that ECC increased the intracellular LD abundance in the primary tumors (Figure 3.7E and Supplemental Figure 3.11D). Importantly, we also found that the lung metastases of the VC-transduced cells had lower LD abundance than their corresponding primary tumors (Figure 3.7F), providing further support to the “low lipid” phenotype supporting metastasis. Finally, we found that ACSL activity was higher in ECC-expressing UCI-082014 and MDA-MB-231 tumors compared to VC control tumors (Figure 3.7G).

In summary, our data indicate that CDCP1 promotes TNBC metastasis by reducing LD abundance, promoting lipid accumulation in the mitochondria for FAO to fuel OxPhos and promote cell migration. CDCP1 regulates those processes, in part, by suppressing ACSL activity. As a result, TNBC tumors have “low lipid” phenotype.

CDCP1 interacts with CPT2 involved in FAO. We have validated CDCP1’s interaction with ACSL family proteins but understand that CDCP1 likely regulates lipid metabolism via additional pathways. Therefore, it will be important to validate the interactions of CDCP1 with the other proteins identified as binding partners by MS (Supplemental Table 3.1). Among these, preliminary studies have validated the interaction of CDCP1 with carnitine palmitoyltransferase 2 (CPT2), a CPT family member

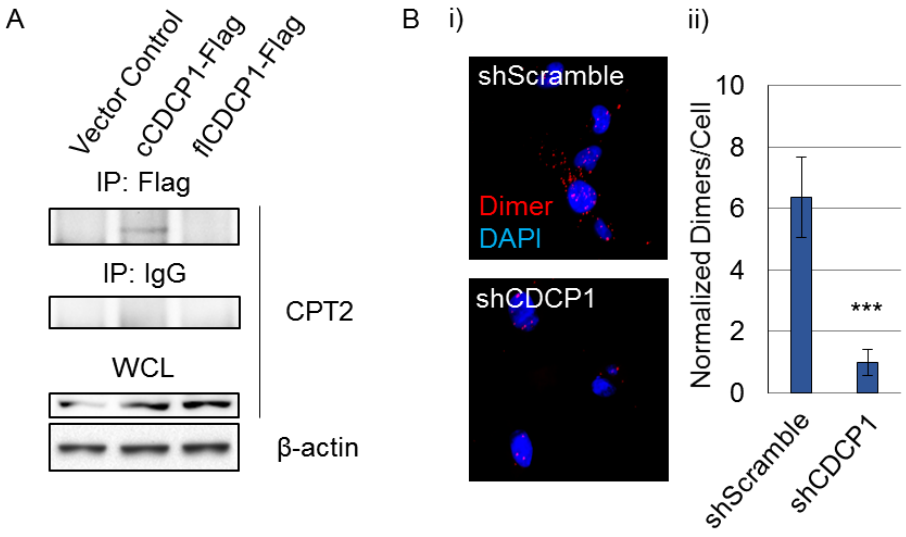

Figure 3.8 | CDCP1 interacts with CPT2 involved in FAO. A) cleaved CDCP1 co-immunoprecipitates with CPT2 while full-length CDCP1 does not in HEK 293T cells overexpressing Flag-tagged CDCP1 isoforms. The anti-Flag and normal mouse IgG control antibodies were used and all six co-IP samples were processed at the same time. **B)** i) CDCP1 interacts with CPT2 at the endogenous level in MDA-MB-231 cells as shown by the proximity ligation assay (PLA); shCDCP1-1 was used as a negative control; ii) quantitation of PLA in (i) is the average of 3 biological replicates. ***P<0.001, error bars represent SEMs.

that is expressed on the inner mitochondrial membrane (IMM) to revert acyl-carnitines shuttled in by CPT1 back into acyl-CoAs for further catabolism. CPT2 works with CPT1 [expressed on the outer mitochondrial membrane (OMM)] [148-150] and is a gatekeeper to FAO. We found that CPT2 interacts with only the cleaved isoform of CDCP1 in HEK 293T cells overexpressing cleaved CDCP1-Flag (Figure 3.8A). We further found that CDCP1 interacts with CPT2 at the endogenous level in MDA-MB-231 cells by PLA. We used MDA-MB-231 cells expressing shRNA targeting CDCP1 as a negative control (Figure 3.8B). We have yet to determine the consequence of this interaction.

Discussion

CDCP1 function-blocking antibodies have demonstrated effectiveness at inhibiting tumor growth[54] and metastasis[28] *in vivo.* We have previously shown that the CDCP1 function-blocking fragment, ECC, inhibits CDCP1 dimerization and activation *in vitro*[5] and here show its efficacy *in vivo* in two animal models of TNBC. Our data support targeting CDCP1 in TNBC to block metastasis and provide novel insight into the mechanism of CDCP1-induced metastasis. We demonstrate that CDCP1 regulates lipid metabolism, reducing LD abundance and stimulating FAO. Products of FAO, in turn, stimulate OxPhos, which contributes to TNBC migration and metastasis. Our data also show that the CDCP1/ACSL axis contributes to dysregulated lipid metabolism.

Importantly, the contributions of FAO[71, 72] and OxPhos[144] to TNBC migration and metastasis and OxPhos to metastasis of other cancers[151, 152] have been recently documented, supporting our proposed mechanism. Accordingly, pharmacological and genetic inhibitors of carnitine palmitoyltransferases (CPTs) blocked lipid transport to

mitochondria, FAO, OxPhos, and metastasis of TNBC cells[71, 72]. Recently, Myc overexpression has been shown to drive FAO in TNBC[72, 73]. All of the cancer cell lines used in this study overexpress Myc compared to MCF10A cells (Supplemental Figure 3.12). Importantly, MCF7 cells, which do not express endogenous CDCP1, overexpress Myc, which might explain their CDCP1-independent “low lipid” phenotype (Figure 3.2A). Since both Myc and CDCP1 are overexpressed in TNBC cell lines used in this manuscript, it is worth investigating if Myc and CDCP1 pathways contribute to TNBC lipid metabolism independently or there is a cross-talk. Interestingly, several studies have shown that proteins involved in the CDCP1 pathway, Src[15] and PKCδ[17], are involved in lipid metabolism as well. FAO and OxPhos activate Src, which, in turn, induces OxPhos in TNBC[71]; and OxPhos activates PKCδ[153]. The contribution of CDCP1 in Src/PKCδ pathway crosstalk with OxPhos is under investigation. Together, these data suggest that targeting lipid metabolism in general, and CDCP1 in particular, are viable therapeutic strategies to inhibit FAO, OxPhos, and metastasis of TNBC.

In this study we suggest that, through FAO and subsequent OxPhos, lipids provide energy contributing to migration and metastasis. However, though the NADH and $FADH_2$ of FAO are generally shuttled into OxPhos, the acetyl-CoA produced from FAO can enter many different pathways, including the TCA cycle, which feeds into OxPhos, post-translational modifications, and biosynthetic pathways. In addition, we envision other mechanisms linking lipid metabolism to migration and metastasis. For instance, LDs appear to be not merely inert structures for lipid storage, but dynamic signaling organelles[154, 155]. The literature supports the cross-talk between cellular LDs and membrane lipid rafts[156-158], where multiple proteins involved in migration, including the

integrin family[159, 160] and CDCP1[29, 54] reside. On the other hand, the biophysical properties of “high lipid” vs “low lipid” cells remain unknown and await investigation. Thus, our study opens a novel research direction for dissecting the mechanism of LD contribution to cancer cell migration and metastasis, which will be instrumental in revealing new pathways for therapeutic targeting of TNBC.

Here we show that CDCP1 promotes FAO in normoxia. Our observations put CDCP1 at the crossroads of metabolic pathways as we[5, 17] and others[20] have previously shown that CDCP1 activity increases under hypoxia recognized to favor the metabolic shift from OxPhos to glycolysis[161]. CDCP1 activity increases through its cleavage and phosphorylation, likely through activation of Src kinase[20]. Since most TNBC tumors have multiple hypoxic areas[162], it raises the question of regional CDCP1 activation status and coordination of FAO/OxPhos and glycolysis. Further investigations are needed to establish the role of CDCP1 in FAO under a range of oxygen tensions, and the role of lipids supplied by the microenvironment vs endogenously synthetized.

In this study we concentrated on CDCP1-driven TNBC metastasis and it is worth investigation if our data translate to other types of breast cancer. The only cell line we used, which is not TNBC, but an ER^+ breast cancer, is MCF7, and although CDCP1 overexpression leads to increased invasiveness in 3D and decreased LD abundance, these cells do not endogenously express CDCP1. It is important to keep in mind that the role of CDCP1 in $HER2^+$ breast cancer was addressed just on the level of primary tumor growth, not metastasis, generating controversial results. Homozygous germline CDCP1 knockout in MMTV-PyMT spontaneous mouse model lead to increased tumor growth rate[38]. However, in a BT474-based mouse model, CDCP1 overexpression led to

increased tumor growth[14]. Furthermore, high co-expression of CDCP1 and HER2 was correlated with decreased patient survival[14]. It will be important to investigate the regulation of lipid metabolism by CDCP1 across breast cancer subtypes.

In this study we used two animal models of TNBC. While ECC reduced primary tumor growth in UCI-082014-based animal model, it only trended towards reducing primary tumor growth in MDA-MB-231-based model. However, in both models ECC reduced metastasis. Although both MDA-MB-231 and UCI-082014 are triple-negative, they have different genetic backgrounds, which likely contribute to the degree of their dependency on CDCP1 pathway for tumor growth. In this respect, we recently established UCI-082014 from a primary tumor specimen and they are still to be characterized for driver mutations; MDA-MB-231 harbor mutations in BRAF and KRAS, which are potent inducers of tumor growth[163, 164]. In addition, UCI-082014 cell implantations generate large primary tumors, which micro-metastasize to the lungs; MDA-MB-231 cell implantations generate rather small primary tumors, which at the same time effectively macro-metastasize. This difference in the two tumor models' dynamics also likely contributes to the observed primary tumor growth phenotype. Since CDCP1 represents a potential therapeutic target, it will be important to determine the genetic and epigenetic factors informing on the effect of CDCP1 blockage on the primary tumor growth. Accordingly, ECC-based therapeutic could be potentially used in neo-adjuvant or adjuvant setting.

To date, the ACSL activity was predominantly studied in the liver, where it does not affect FAO. This is highlighted by a study that found that the pan-ACSL inhibitor, Triacsin C, preferentially inhibited TAG synthesis and did not affect FAO[165]. Furthermore, though both ACSL1 and ACSL5 have been reported to localize at the mitochondrial and

the LD membranes[166] and ACSL1 has been reported to upregulate genes involved in FAO[167], they do not affect the FAO rate[168, 169]. Based on our data, ACSLs promote lipid storage in LDs (Supplemental Figure 3.6), inhibit OxPhos (Supplemental Figure 3.7B), and inhibit FAO (Supplemental Figure 3.7C), in TNBC. Considering that ACSL products, acyl-CoAs, are competed for by enzymes involved in LD storage, incorporation into lipid membranes, post-translational modifications, and FAO[130, 170] our data that ACSL activity inhibits FAO are consistent with a choice to direct acyl-CoAs toward storage in LDs. Accordingly, when ACSL activity is blocked, acyl-CoAs become limited and may preferentially enter FAO, and when ACSL activity is induced, acyl-CoAs become abundant and may preferentially enter LDs for storage. Further studies are needed to investigate the regulatory mechanism, as well as the cell-type-specific roles of ACSLs in lipid metabolism. Since CDCP1 has a large effect on LD abundance and a modest effect on ACSL activity, we expect that CDCP1 interacts with and regulates additional metabolic proteins that are yet to be uncovered.

Interestingly, ACSL3 was recently reported to promote lung cancer growth in a $KRAS^{G12D}$-driven mouse model, although its contribution to metastasis was not investigated[171]. Our *in vitro* data show that ACSL3 increases TNBC cell proliferation and at the same time decreases TNBC migration (Figure 3.5, Supplemental Figure 3.6). Our *in vivo* data show that ACSL3 reduces metastasis (Supplemental Figure 3.4)

The observation that VC-transduced UCI-082014 generated metastases with lower LD abundance than the corresponding primary tumors suggests that cells in primary tumors with low LD abundance effectively migrate and metastasize and keep the low LD abundance phenotype at metastatic sites. Importantly, it raises the question of TNBC

tumor heterogeneity in terms of CDCP1 expression and activity, as well as CDCP1-dependent and -independent regulation of LD abundance. Thus, the frequency of cells with high CDCP1 activity and low LD abundance in primary tumors might represent a prognostic marker for metastatic potential. This observation also implies that the average CDCP1 expression and activity should be higher at metastatic sites than in corresponding primary tumors. Accordingly, *Alajati et al.* reported that CDCP1 expression is higher in $HER2^+$ patient breast cancer metastases than the primary tumors [14]. It is important to note that although our data support the mechanism where low LD abundance stems from CDCP1 overexpression and lipid FAO, thus depleting LDs, the dynamics of lipid metabolism in TNBC tumor tissue is largely unknown. The low LD abundance phenotype can arise from low lipid synthesis and high lipid consumption. In both cases the amount of lipids detected in the tumor tissue will decrease. Adding to complexity are the additional cell types present in the tumor microenvironment, including adipocytes, potentially capable of supplying lipids to breast cancer cells for FAO. Supporting the importance of lipid FAO for metastasis, are the results from Park et al., which show that Etomoxir, blocking mitochondrial lipid consumption, does block metastasis[71]. Further studies are needed to clarify those important considerations.

In conclusion, our data establish CDCP1 as a master-regulator of lipid metabolism in TNBC, lowering LD abundance and increasing FAO, leading to “low lipid” phenotype of TNBC. This signaling pathway is partially regulated by CDCP1/ACSL axis. Due to interconnection of metabolic pathways, increased FAO leads to increased OxPhos, contributing to migration and metastasis. As a result, CDCP1 represents a potential therapeutic target for TNBC management, along with other components of lipid

metabolism pathway. Thus, our findings have important implications for therapeutic targeting and development of prognostic markers of TNBC.

Materials and Methods

CARS Microscopy: A 76-MHz mode-locked Nd:Vanadate laser provides a beam at 1064nm functioning as the Stokes beam and a second harmonic generated beam at 532nm to pump an optical parametric oscillator. The pump beam generated by the optical parametric oscillator is spatially and temporally overlapped with the Stokes beam and sent to the microscope. The two beams are focused on the cells through a 60x, 1.2 numerical aperture water objective lens. The generated CARS signals are collected through the condenser and focused onto a Hamamatsu photomultiplier tube with a 650±50nm bandpass filter in front.

TPEF Microscopy: A scanning laser TPEF microscope was used to measure the metabolic states of the cell lines. The laser was set to 740 nm to excite NADH (480 nm±50nm bandpass filter) and tuned to 900nm to excite FAD^+ (530 nm±50nm bandpass filter). We used 20mW for 740nm and 40mW for 900nm with 6µs pixel dwell time. The laser power was kept constant and the response of the photo multiplier tubes was calibrated with a reference sample (0.02µM fluorescein solution at pH 7.0). The images of NADH and FAD^+ of the same cells were taken sequentially and were used to calculate ORR, defined as $FAD^+/(NADH+FAD^+)$.

FAO analysis: Two dishes for each experimental group were prepared. On each imaging dish, 80,000 cancer cells were plated and cultured in full-growth medium (DMEM, 10% fetal bovine serum (FBS), 25 mM glucose, 2 mM GlutaMAX , 1% penicillin/streptomycin)

for 24 hours to allow cell attachment. The growth medium was exchanged to substrate-limited medium (DMEM, 0.5 mM glucose, 1 mM GlutaMAX, 0.5 mM carnitine, and 1% FBS) a day before the experiment. The cancer cells were switched to basal FAO medium (DMEM, 2.5mM glucose, 0.5mM carnitine and 5mM HEPES) 45 minutes before the experiment. Etomoxir was added to the medium 15 minutes before the experiment at a final concentration of 40 µM. In each imaging dish, three locations were randomly chosen. The baseline ORRs were measured at time 0 before Oligo addition. The optical redox changes were monitored every 5 minutes for a total of two measurements. Then, 5 µL of FCCP was added and the ORRs were measured at 15 minutes and 20 minutes. Images were taken using TPEF Microscopy (see above). All ORR measurements were done in the absence of exogenous lipid sources.

Virus production and infection of target cells: Detailed protocol is described in Razorenova et al.[117]. HEK 293T cells were transfected with each lentiviral plasmid along with packaging plasmids, pVSVG and ΔR8.2. Virus-containing media was transferred to target TNBC cells, which were selected in antibiotic-containing media for minimum one week.

Western blotting: Protocol was adapted from Razorenova et al.[116]. 40 µg of protein was used per lane. Antibodies used are listed in Supplemental Table 3.1.

Scratch Assays: Detailed protocol is described in Wright et al.[5]. 400,000 MDA-MB-231 or UCI-082014 cells were plated per well of a 6-well plate. 24 hours later, cells were treated with DMSO control or 5 µM Triacsin C for 16 hours prior to assay. Cells were allowed to migrate for 6 hours.

Transwell migration: Detailed protocol of assay and quantitation is described in

Thompson et al.[172]. MDA-MB-468 cells were treated with DMSO control or 5 μM Triacsin C for 16 hours prior to assay. Cells were allowed to migrate for 16 hours.

***In vivo* experiments:** UCI-082014 and MDA-MB-231 cells were transduced with VC or pLM-CMV-ECC-His[5]. RAG2$^{-/-}$ mice were orthotopically injected in the 4th mammary fat pad with 10^6 cells mixed with matrigel. Before sacrifice at 5 weeks for UCI-082014-based model and at 8 weeks for MDA-MB-231-based model mice were intraperitoneally injected with 150 mg/kg D-luciferin and imaged for 2 minutes on large-binning using the IVIS lumina imager. Mice were then sacrificed, and tumors and lungs were collected for analysis. UCI-082014 metastases were quantitated as the average number of metastases per field in 3-5 images taken from three non-serial sections per lung per mouse. MDA-MB-231 metastases were quantitated as the total area of metastases per field due to the metastatic burden being too large to quantitate individual metastases. Quantitation of Oil Red O staining was done using Image J to quantitate the number of lipid droplets per cell. Quantitation of PLA assay was done by manually counting the number of dimers per cell.

CARS microscopy equipment: 76-MHz mode-locked Nd:Vanadate laser (Picotrain, High-Q, Hohenems, Austria), optical parametric oscillator (OPO; Levante, Emerald OPO, Berlin, Germany), CARS microscope (IX71, Olympus), NA water objective lens (UPlanS Apo, Olympus), Hamamatsu photomultiplier tube (R2658, Hamamatsu).

TPEF microscopy equipment: TPEF microscope (Zeiss #LSM 510), TPEF laser (Chameleon, Coherent Inc.).

Cell lines and media: HEK 293T, MDA-MB-231, MDA-MB-468, UCI-082014, and MCF7 cells lines were grown in Dulbecco's Modified Eagle Medium (DMEM) (Genesee, San Diego, CA #25-500) with 10% Fetal Bovine Serum (FBS) (Omega Scientific, Tarzana, CA

#FB-12), 100 u/mL penicillin and 100 µg/mL streptomycin (1% P/S). Cells were grown in mixed gas CO_2 water-jacketed incubators (21% O_2, 5% CO_2). PME cells were grown in Mammary Epithelial Cell Basal Medium (ATCC, Manassas, VA #PCS-600-030) supplemented with growth kit (ATCC #PCS-600-040). MCF10A cells were grown in DMEM F12 (Genesee #10-090-CV) with 5% horse serum (Thermo Fisher #16050-130) supplemented with 20 ng/mL EGF (PeproTech, Rock Hill, NJ #AF-100-15) and 10 µg/mL insulin (Roche, San Francisco, CA #11376497001). SUM159 cells were grown in DMEM F12 with 5% FBS, 1% P/S, 5 µg/mL insulin, 1 µg/mL hydrocortisone, and 10 mM HEPES. BT549 cells were grown in Roswell Park Memorial Institute Medium with 10% FBS and 1% P/S. MDA-MB-231 and MDA-MB-468 cell lines, extensively used in this study, were validated using short tandem repeat (STR) profiling by the American Type Culture Collection (Manassas, VA). All cells were regularly tested for mycoplasma contamination and confirmed to be negative.

3D culturing: MDA-MB-231, MDA-MB-468, and UCI-082014 cell lines were plated at 3,000 cells in 50 µL of 1:1 collagen (BD Biosciences #354249) and matrigel (BD Biosciences #356234) gel. Collagen was initially prepared at 6.4 mg/mL according to the manufacturer's protocol before being mixed with matrigel for a final concentration in the gels of 3.2 mg/mL collagen, similar to that in transformed breast tissue[118, 119]. Gels were plated onto 12 mm coverslips. Media on the cells was changed every two days and cells were allowed to grow for up to 12 days. Gels were fixed in 4% PFA for 20 minutes and then analyzed by CARS microscopy.

Fatty acid oxidation (FAO) analysis reagents: Substrate-limited medium was made from SILAC Advanced DMEM/F-12 Flex media (Gibco #A2494301) supplemented with 0.5 mM glucose (Sigma-Aldrich #G7021), 1.0mM GlutaMAX (Life Technologies #35050-061), 0.5mM carnitine (Sigma-Aldrich #C0283) and 1% charcoal stripped fetal bovine serum (Thermo Fisher #12676011). The basal FAO medium composition: 111mM NaCl, 4.7mM KCl, 1.25mM $CaCl_2$, 2mM $MgSO_4$ and 1.2mM NaH_2PO_4. Etomoxir (Cayman Chemical, Ann Arbor, MI #11969-5mg). 8-well chamber slides (Lab-Tek #155411).

Co-localization of red C12 BODIPY and green MitoTracker: Cells were plated in 8-well chamber slides (Lab-Tek #155411), let attach overnight, and treated with 1 μM BODIPY 558/568 C12 (Life Tech #D3835) for 16 hours before staining with 200 nM MitoTracker Green FM (Cell Signaling #9074) for 30 minutes at 37 °C. The media was changed to phenol-free media and the cells were immediately imaged at 63x on a Zeiss spinning disk confocal microscope. Five to seven Z-stack images were captured per condition. Co-localization of red and green channels was quantitated for Z-stacks using Co-localization Threshold analysis with ImageJ software.

Quantitation of mitochondrial mass: Mitochondrial mass was analyzed by averaging the intensity of MitoTracker immunofluorescence using ImageJ in 3-5 of the images for each condition. Data were normalized to shSramble of each cell line. Three biological replicates were used for quantitation.

Oil Red O (ORO) Staining: Cells were plated on coverslips and allowed to grow to 60-

70% confluency. Coverslips were fixed with 10% PFA for 10 minutes at RT. They were then equilibrated with 60% IPA diluted in de-ionized (di) H_2O for 5 minutes. A 3:2 mixture of 3 mg/mL ORO: diH_2O was prepared, mixed thoroughly, and filtered using VWR 415 15 cm filter paper (VWR #28320-121). Cells were stained with ORO for 15 minutes at RT then rinsed twice before being counter stained in a 1:20 dilution of hematoxylin (VWR #101411-198): diH_2O for 30 seconds. Coverslips were rinsed 3 times and dried for at least 6 hours before being mounted in Permount (Fisher #SP15-500) for imaging.

Western blotting reagents: protease inhibitors (Thermo Fisher, Pittsburgh, PA #P1-88266), phosphatase inhibitors (Roche #04906845001), BCA Protein Assay kit (Pierce).

Scratch and transwell migration assay reagents and materials: Triacsin C (Enzo Life Sciences, Farmingdale, NY #BML-EI218-0100); mitomycin C (Thermo Fisher #BP2531-2); transwell inserts (Corning Life Sciences Plastic, Corning, NY #3464); fibronectin to coat transwell inserts for migration (Sigma Aldrich #F2006-2); Richard Allen 3 Step Staining Kit to stain transwell inserts for quantitation (Thermo Fisher #3300).

MS: 4 µg of mouse anti-Flag antibody (Sigma Aldrich #F1804) was crosslinked to 15 µL Protein G Dynabeads (Life Tech #10003D) with 5 mM bis(sulfosuccinimidyl)suberate (BS3) in 250 µL of conjugation buffer (20 mM sodium phosphate, 150 mM sodium chloride, pH 8.61) for 30 minutes at room temperature (RT) with rotation. The reaction was stopped with the addition of quenching buffer (1 M Tris-HCl, pH 7.5) for 15 minutes

at RT with rotation. Antibody crosslinked to beads was then incubated with lysates for 16 hours at 4 °C. Immunoprecipitates were eluted with 35 µL of 0.1 M glycine-HCl, pH 3.5 into 5 µL 0.5 M Tris-HCl, pH 7.4 and sent to UCSD Biomolecular and Proteomics Mass Spectrometry Core for analysis.

Gas chromatographic analysis of cellular lipids: Lipids were extracted using the method of Folch-Lees[173]. The extracts were filtered, and lipids recovered in the chloroform phase. Individual lipid classes were separated by thin layer chromatography using Silica Gel 60 A plates developed in petroleum ether, ethyl ether, acetic acid (80:20:1) and visualized by rhodamine 6G. Phospholipids, diglycerides, triglycerides and cholesteryl esters were scraped from the plates and methylated using BF3 /methanol as described by Morrison and Smith[174]. The methylated fatty acids were extracted and analyzed by gas chromatography. Gas chromatographic analyses were carried out on an Agilent 7890A gas chromatograph equipped with flame ionization detectors, a capillary column (SP2380, 0.25 mm x 30 m, 0.25 µm film, Supelco, Bellefonte, PA). Helium was used as a carrier gas. The oven temperature was programmed from 160 °C to 230 °C at 4 °C/min. Fatty acid methyl esters were identified by comparing the retention times to those of known standards. Inclusion of lipid standards with odd chain fatty acids permitted quantitation of the amount of lipid in the sample. Dipentadecanoyl phosphatidylcholine (C15:0), diheptadecanoin (C17:0), trieicosenoin (C20:1), and cholesteryl eicosenoate (C20:1) were used as standards.

Immunofluorescent staining: Cells were fixed with 4% paraformaldehyde for 10 min, then treated with 0.3% Triton X-100 in 1xPBS for 5 minutes, and blocked for 1 hour in 5% bovine serum albumin (BSA) in 1xPBS. Slides were then incubated overnight in primary antibody at 4 °C, followed by incubation for 2 hours in secondary antibody at RT in the dark. Antibodies used are listed in Supplemental Table 1. Both primary and secondary antibodies were diluted in 1% BSA in 1xPBS. Coverslips were mounted with Vectashield containing DAPI to stain nuclei (VWR #89139-054). Cells were imaged using a Nikon Eclipse Ti microscope with a 20x objective and NIS element AR3.10 software.

Duolink Proximity Ligation Assay (PLA): The assay was performed according to the manufacturer's protocol (Sigma Aldrich #DUO92105). Primary antibodies used are in Supplemental Table 1. 12 mm coverslips were used with 20 µL reaction volumes. Images were collected as for immunofluorescent staining analysis. Formalin-fixed paraffin-embedded MDA-MB-231 and UCI-082014 tumor tissue was used to analyze CDCP1-dimerization *in vivo*. Briefly, 10 µm non-serial sections were blocked with 10% FBS in 1xPBS for 30 minutes at RT, and then incubated in primary antibodies (Supplemental Table 1) overnight at 4 °C. PLA was carried out using the manufacturer's protocol.

Co-immunoprecipitation: 400 µg of protein in 200 µL of cell lysis buffer (20 mM Tris-HCl [pH 7.5], 150 mM NaCl, 1 mM EDTA, 1 mM EGTA, 1% Triton X100, 2.5 mM $Na_4P_2O_7$, 1 mM β-glycerophosphate, 1 mM Na_3VO_4) with protease inhibitors (Fisher Scientific, Pittsburgh, PA #P1-88266) and phosphatase inhibitors (Roche #04906845001) was incubated with 4 µL of primary antibody for 16 hours at 4°C with gentle agitation. Then 20

µL Protein G Dynabeads were added, followed by incubation for 1 hour at 4°C. Immunoprecipitated proteins were collected using magnetic stand, washed 3 times for 5 minutes on ice with cell lysis buffer without protease or phosphatase inhibitors, boiled in 1x sample loading buffer for 6 minutes and analyzed by western blot.

ACSL activity assays: Cells were collected in ACSL activity buffer (250 mM sucrose, 10 mM Tris-HCl [pH 7.5], 1 mM EDTA) with protease inhibitors (Thermo Fisher, Pittsburgh, PA #P1-88266) and phosphatase inhibitors (Roche #04906845001), lysed by freeze-thaw and stored at -80 °C. Protein was measured using BCA Protein Assay kit (Pierce). 130 µL of reaction mixture (125 mM Tris-HCl [pH 7.5], 10 mM ATP, 10 mM $MgCl_2$, 0.25 mM CoA, 5 mM DTT, 0.5 mM Triton X100, 0.05 mM BODIPY 500/510 C4, C9 (Thermo Fisher #B-3824)) was mixed with 10-20 µg of cell lysate for 30 minutes at 37 °C. The reaction was stopped by the addition of 2 mL Dole's reagent (40:10:1 Isopropanol:Heptane:H_2SO_4) and the BODIPY-CoA was extracted in the aqueous phase after 4 x 3 mL heptane washes for analysis of fluorescence intensity on a Biotek Synergy HT spectrophotometer.

Proliferation assays: MDA-MB-231, MDA-MB-468, and UCI-082014 cells were serum starved for 6 hours prior to plating. On Day 0, 10,000 cells per well were plated in duplicate in a 24-well plate in complete DMEM. Cells were counted every two days for 4 days (Day 0, Day 2, and Day 4) using a hemocytometer.

Plasmid constructs and cloning: pLKO.1shCDCP1-1 was purchased from OpenBiosystems (#RHS3979-98822176). pLKO.1shScramble was purchased from Addgene (Cambidge, MA, #1864). pLKO.1shCDCP1-2 is the same sequence as pLKO.1shCDCP1-7 in Chapter 2.

shACSL3 was cloned into pLKO.1-puromycin vector as described in Obata et al.[175]:

ACSL3 cDNA was cloned into the pLM-CMV-H4-blasticidin vector from the ACSL3 expression plasmid (Origene #SC126917).

Cleaved CDCP1-Flag and full-length CDCP1-Flag were previously described[5].

All primers used for cloning are listed in Supplemental Table 2.

Cell transient transfections: HEK 293T cells were transfected using Lipofectamine and Plus reagents (Life Tech, Carlsbad, CA #18324-012 and #11514-015) following the manufacturer's protocol and used for experiments 2-3 days post-transfection.

Mice and *in vivo* experiments: RAG2$^{-/-}$ mice were generously provided (see Acknowledgements) by Dr. Boiko from his UCI in-house colony. Mice were imaged using IVIS Lumina Imager (PerkinElmer, Waltham, MA) with D-luciferin (Promega, Madison, WI, #E1605).

Quantitative reverse transcription-polymerase chain reaction (qRT-PCR) analysis of lung metastasis: RAG2-/- mice were orthotopically injected with 1 million MDA-MB-231 cells. Mice were sacrificed after 4 weeks and lungs were harvested for RNA isolation

using the TRI Reagent (Sigma Aldrich #T9424) following the manufacturer's protocol. cDNA was synthesized using Superscript II reverse transcriptase (Invitrogen #18064014) following the manufacturer's protocol. qRT-PCR was performed using Power SYBR Green (Thermo Fisher #4367660) on an ABI ViiA7 qPCR machine. Primers used are listed in Supplemental Table 2. All SYBR Green primer pairs were validated for specificity using a Tm gradient protocol prior to the experiments performed. A serial dilution of MDA-MB-231 cells was used to create a standard curve for hCDCP1 expression. A serial dilution of naïve mouse lung tissue was used to create a standard curve for mβ-actin. The following PCR conditions were used: denaturation at 95 °C for 13 min followed by 40 cycles of denaturing at 95 °C for 15 sec, and annealing at 60 °C for 1 min. Reactions were run in triplicate. Using the C_T value of the y-intercept of the standard curve as a representation of 1 cancer cell, we were able to correlate the number of cancer cells the hCDCP1 qRT-PCR yielded to the number of cells present in the mouse lung. Results were analyzed as $\Delta\Delta C_T$= [(hCDCP1 RNA/mβ-actin RNA for each condition)/(shScramble control hCDCP1 RNA/mβ-actin RNA)].

CHAPTER 4: STRUCTURAL INSIGHTS INTO THE CDCP1 HOMO-DIMERIZATION INTERFACE

Introduction

We have demonstrated the relevance of CDCP1 as a therapeutic target to treat cancer. The development of therapeutics that target CDCP1 have been ongoing. A few antibodies have been isolated that inhibit CDCP1 activity by either inhibiting cleavage[2, 13, 28, 32, 52, 97, 176] of CDCP1, inducing degradation of CDCP1[54, 177], or by currently unknown mechanisms[178] to reduce cell growth, migration, and metastasis of multiple forms of cancer. We have developed a small peptide biologic that inhibits CDCP1 activity by inhibiting homo-dimerization[5] to inhibit TNBC metastasis. Furthermore, a small molecule has recently been demonstrated to inhibit the interaction of PKCδ with phosphorylated CDCP1 to reduce peritoneal dissemination of gastric adenocarcinoma cells[46]. Where and in what orientation these antibodies, peptide, and small molecules bind to CDCP1 to promote their effects are not fully understood. Our ability to develop and utilize optimized therapeutics to target CDCP1 will be dependent on uncovering the crystal structure of the protein. Furthermore, we need to resolve a crystal structure to more fully understand the biophysical properties of CDCP1 to elucidate targetable pockets and inform therapeutic development.

Here, we analyzed each CUB domain in CDCP1 for its importance in dimerization. We determined that CUB2 was indispensable for homo-dimerization and collaborated with Dr. Tom Poulos' lab to deduce a 3D model of CUB2. We validated our theoretical model using molecular dynamics and then estimated a dimer interface between two

CUB2 monomers. From this, we determined and validated which residues were important in our theoretical dimer interface.

Results

CDCP1 CUB domains have varying effects on cCDCP1 homo-dimerization and TNBC invasion. The amino acid sequence of CDCP1 (Figure 4.1) demonstrates where the CUB domains are in relation to the extracellular cleavage site and the transmembrane span. Each CUB domain was cloned and expressed in HEK 293T cells with cCDCP1-N'luc and cCDCP1-C'luc for analysis of their effects on cCDCP1 dimerization by luminescent readout (see Chapter 2). ECC was used as a positive control for dimer inhibition (contains CUB2 and CUB3). We found that CUB2 and CUB3 reduced luminescent signal (inhibited dimerization) to an equal level as ECC while CUB1 had no significant effect (Figure 4.2A). These data indicate that CUB2 and CUB3 are equally important for cCDCP1 homo-dimerization. We validated that CUB1, CUB2, and CUB3 were expressed and secreted by transfecting HEK 293T cells with N-terminally HA-tagged CUB1, CUB2, or CUB3 constructs (Figure 4.2B). We next expressed untagged constructs of each CUB domain in MDA-MB-231 cells and plated the cells in 3D culture to analyze their effect on invasiveness and cell death as compared to ECC. We found, again, that CUB2 and CUB3 had equivalent effects to ECC at reducing invasiveness, as visualized by bright field imaging of the 3D culture. CUB2 and CUB3 also increased apoptosis to a similar extent as ECC as measured by positive cleaved-caspase 3 staining (Figure 4.2C). Again, these data indicate that CUB2 and CUB3 are equally important for cCDCP1 homo-dimerization activity.

MAGLNCGVSIALLGVLLLGAARLPRGAEAFEIALPRESNITVLIKLGTPTLLAKPCYIVISKRHITMLSI
KSGERIVFTFSCQSPENHFVIEIQKNIDCMSGPCPFGEVQLQPSTSLLPTLNRTFIWDVKAHKSIGL
ELQFSIPRLRQIGPGESCPDGVTHSISGRIDATVVRIGTFCSNGTVSRIKMQEGVKMALHLPWFHP
RNVSGFSIANRSSIKRLCIIESVFEGEGSATLMSANYPEGFPEDELMTWQFVVPAHLRASVSFLNF
NLSNCERKEERVEYYIPGSTTNPEVFKLEDKQPGNMAGNFNLSLQGCDQDAQSPGILRLQFQVLV
QHPQNESNKIYVVDLSNERAMSLTIEPRPVKQSRKFVPGCFVCLESRTCSSNLTLTSGSKHKISFLC
DDLTRLWMNVEKTISCTDHRYCQRKSYSLQVPSDILHLPVELHDFSWKLLVPKDRLSLVLVPAQKL
QQHTHEKPCNTSFSYLVASAIPSQDLYFGSFCPGGSIKQIQVKQNISVTLRTFAPSFQQEASRQGLT
VSFIPYFKEEG*VFTVTPDTKSKVYLRTPNWDRGLPSLTSVSWNISVPRDQVACLTFFKERSGVVCQ*
*TGRAFMIIQEQRTRAEEIFSLDEDVLPKPSFHHHSFWVNISNCSPTSGKQLDLLFSVTL*TPRTVDLT
VILIAAVGGGVLLLSALGLIICCVKKKKKKTNKGPAVGIYNDNINTEMPRQPKKFQKGRKDNDSHVY
AVIEDTMVYGHLLQDSSGSFLQPEVDTYRPFQGTMGVCPPSPPTICSRAPTAKLATEEPPPRSPPE
SESEPYTFSHPNNGDVSSKDTDIPLLNTQEPMEPAE*

CUB1
CUB2
CUB3
Cleavage site
Transmembrane sequence
* Termination

Figure 4.1 | CDCP1 amino acid sequence and notable features for modeling dimerization. CUB1 is blue and double underlined; CUB2 is red and single underlined; CUB3 is green and italicized; cleavage site between CUB1 and CUB2 is orange and single underlined; transmembrane sequence is light purple and bold; * C'terminus of CDCP1.

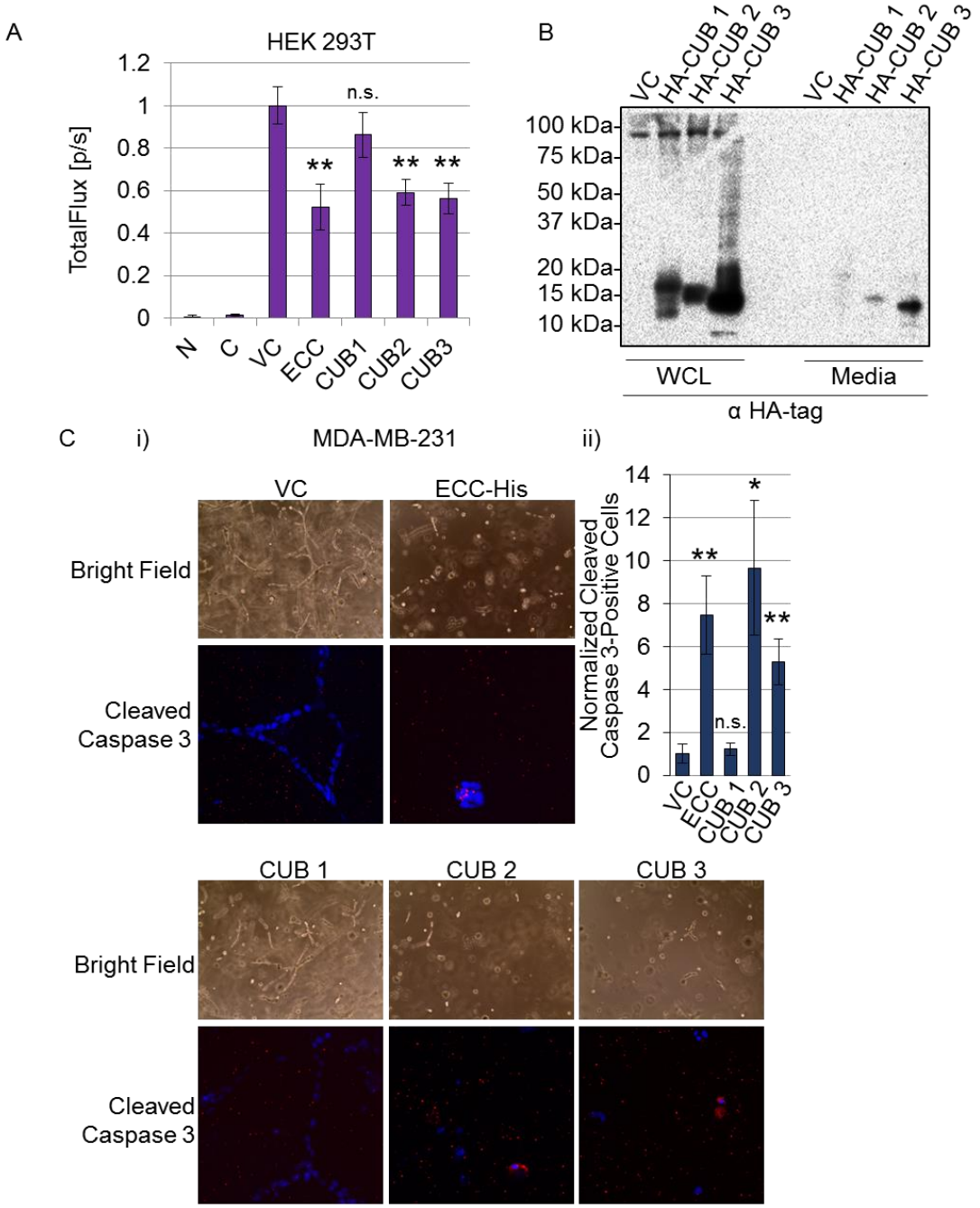

Figure 4.2 | Effect of CUB domains on cCDCP1 dimerization and MDA-MB-231 invasiveness. **A)** Quantitation of split luciferase assay demonstrating that CUB2 and CUB3 inhibit dimerization comparable to ECC while CUB1 has little effect on dimerization. **B)** Western blot analysis of N-terminally tagged HA-CUB expression in whole cell lysate (WCL) and media (to check if they are secreted) of HEK 293T cells using an anti-HA-tag antibody. **C)** i) 10x bright field images showing gross morphology of 3D cultures MDA-MB-231 cells and 20x fluorescent images demonstrating cleaved caspase-3 staining in MDA-MB-231 cells. ii) Quantitation of cleaved caspase 3 staining from (i). Quantitation in A and B is the average of three biological replicates. *P<0.05, **P<0.01 analyzed by one way ANOVA with multiple comparison post hoc T-test and error bars represent SEMs.

3D Modeling and molecular dynamics (MD) analysis of CUB2 structure stability. There is no crystal structure of CDCP1 and because our data *in vitro* demonstrated that CUB2 and CUB3 may be equally important in cCDCP1 dimerization, we focused on modeling CUB2. In collaboration with Dr. Tom Poulos' lab we used the Robetta online server (http://robetta.bakerlab.org/) to model CUB2 (sequence in Figure 4.1). We obtained five 3D models based off of previously deposited structures of CUB domain containing proteins: spermadhesin (PDB# 1SPP)[179], amyloid p component bound to phosphoethanolamine (PDB# 3KQR)[180], and MASP2 CUB1-EGF-CUB2 (PDB# 1NT0)[6] (Figure 4.3A). We then used MD simulation in a periodic cell of water to analyze the stability of the top candidate Robetta CUB2 model. Measurements were taken every nanosecond over the course of the 170 nanosecond simulation and overlayed to demonstrate the total CUB2 model flux in the presence of water (Figure 4.3B). Root mean squared displacement (RMSD) (Figure 4.3C) and fluctuation (RMSF) (Figure 4.3D) were calculated from measurements taken every 10 ps during the 170 ns simulation. RMSD measures the difference between the positions of the Cα atoms of each residue for every time point in the simulation and RMSF measures the flexibility of each residue within the protein (terminal and loop region residues having the highest flexibility due to a lack of secondary structure). The RMSD for our CUB2 model equilibrated a bit high, reaching an equilibrium of 4.25 angtroms (Å) (optimal ~1-2 Å) in approximately 50 ns. However, this is understandable considering that it is a model and not an actual structure. The RMSF helped us in the consideration of residues with potential involvement in the dimer interface as we assumed the residues with very high flexibility were not involved in the dimer interface.

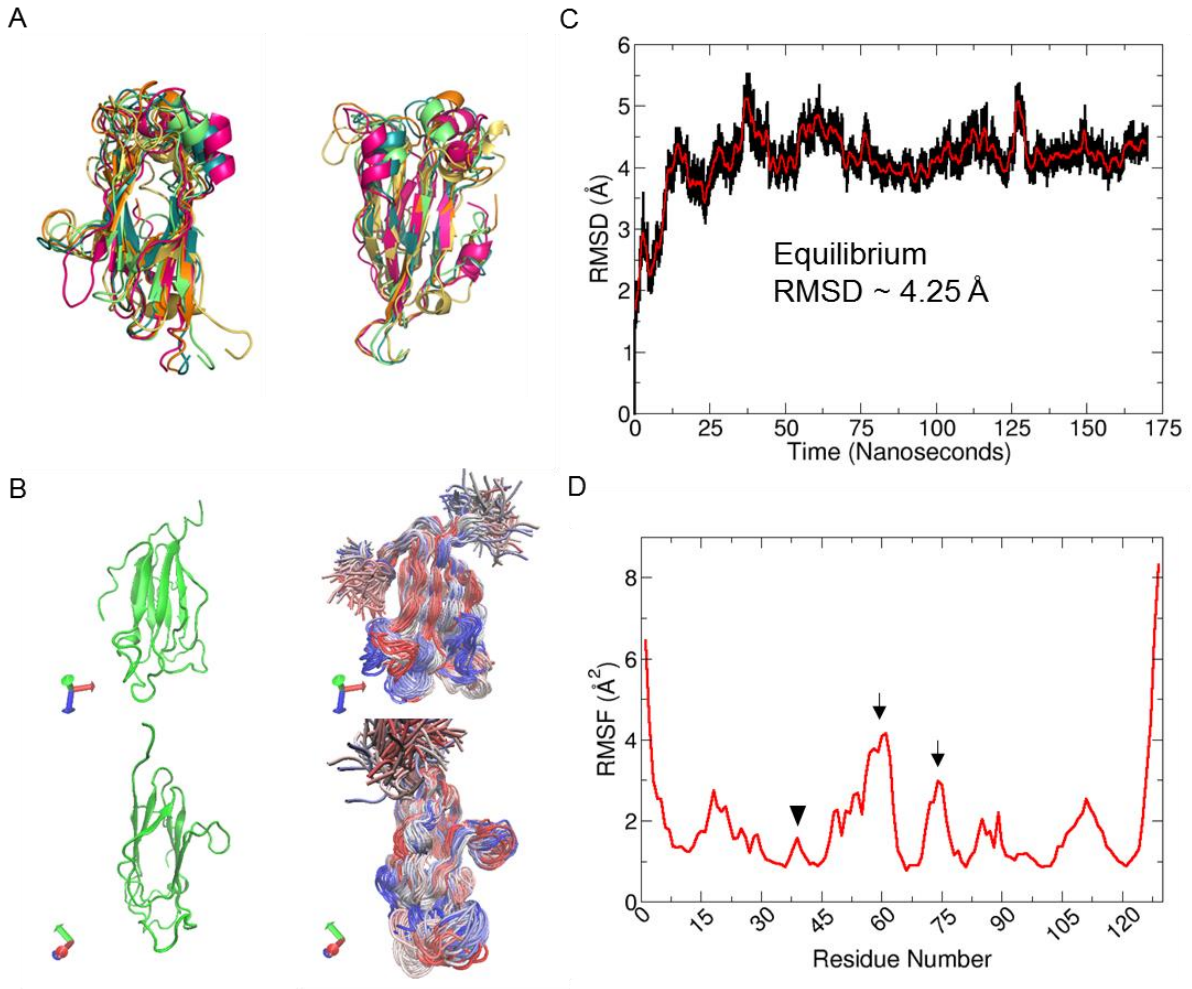

Figure 4.3 | Robetta modeling and molecular dynamic simulation of CUB2 3D model. A) Overlay of all five Robetta generated 3D reconstructions of CUB2 in two different planes. **B)** (left) view of CUB2 that MD overlay (right) images are viewed in, (right) overlay of all images taken from every time point in MD simulation demonstrating total flexibility of Robetta generated CUB2 model. **C)** RMSD plot for Robetta generated CUB2 model derived from MD simulation demonstrating stability of CUB2 structure equilibrates at 4.25 Å. **D)** RMSF plot of Robetta generated CUB2 model derived from MD simulation demonstrating specific amino acid flexibility along the entire sequence of CUB2. Arrowhead, antiparallel beta sheet; arrow, loop region.

Analysis of CUB2-CUB2 dimer interface using ROSIE docking. After we confirmed the integrity of our CUB2 model using MD we used it in Rosetta Online Server that Includes Everyone (ROSIE) (http://rosie.rosettacommons.org/) docking simulations to determine putative homo-dimer interfaces between CUB2 monomers. We obtained 10 docking models and analyzed all of the residues who's Cα resided within five angstroms of the dimer interface (arbitrary distance to be involved in dimerization) (Figure 4.4A). Figure 4.4B illustrates visualization in VMD software of the Model 1 dimer interface with key residues highlighted.

Site-directed Mutagenesis validation of dimer interface residues determined by ROSIE docking. To validate if the residues we identified by 3D modeling were important for homo-dimerization, we sought to mutate each of them in the split-luciferase assay. We utilized site-directed mutagenesis of cCDCP1-N'luc and combined either WT or mutant cCDCP1-N'luc with WT cCDCP1-C'luc to test for effects on dimerization. We found that the R5A, Q75A, and combination R5Q75AA (double mutant, DM) mutation had no effect on expression of cCDCP1-N'luc (Figure 4.5A). We found that R5A reduced dimerization by approximately 30% in a split-luciferase assay while Q75A had no effect (Figure 4.5B). The DM replicated the single Q5A mutation, further demonstrating the lack of necessity of the Q75 residue in dimerization (Figure 4.5B). These data also validate our assumptions of residue flexibility negatively correlating with importance at the dimer interface as R5 is located in an antiparallel beta-sheet and seems to be important for dimerization and Q75 is located very near to a dynamic loop region and does not contribute to dimerization.

A

Model 1
1 3 4 5 25 26 28 29 31 33 35 62-65 67 70-72 73 74 75 97 98 100 102 104- 107

Model 2
4 25 28 29 59-67 73 74 75 78 80-83 102 104- 108 110

Model 3
1 4 5 6 8 10 33 35-38 70 71 72 73 75 76 77 96 97 98

Model 4
3 4 5 25 26 28 29 31 32 33 60-65 67 70-72 73 74 75 98 100 102 104 107 108

Model 5
1 3 4 5 25 26 28 29 31 33 35 63 65 67 70-72 73 74 96 97 98 100 102 104- 108

Model 6
1 2 3 4 5 6 22 25 26 28 29 31 33 67 72 73 74 75 102 104 107 110

Model 7
1 2 3 4 5 6 25 26 28 29 31 33 72 73 74 75 102 104 107 108 110

Model 8
1 3 4 5 25 26 28 29 31 33 72 73 74 75 100 102 104 105 107 108

Model 9
1 2 3 4 22 23 25 26 28 29 31 33 67 72 73 74 75 102 104 107 108 110

Model 10
1 2 3 4 5 6 8 25 26 28 29 31 32 33 35 71 72 73 74 75 102

Amino Acid Sequence of CUB2
CTDHRYCQRKSYSLQVPSDILHLPVELHDFSWKLLVPKDRLSLVLVPAQKLQQHTHEKPCNTSFSYLVASAI
PSQDLYFGSFCPGGSIKQIQVKQNISVTLRTFAPSFQQEASRQGLTVSFIPYFKEEG

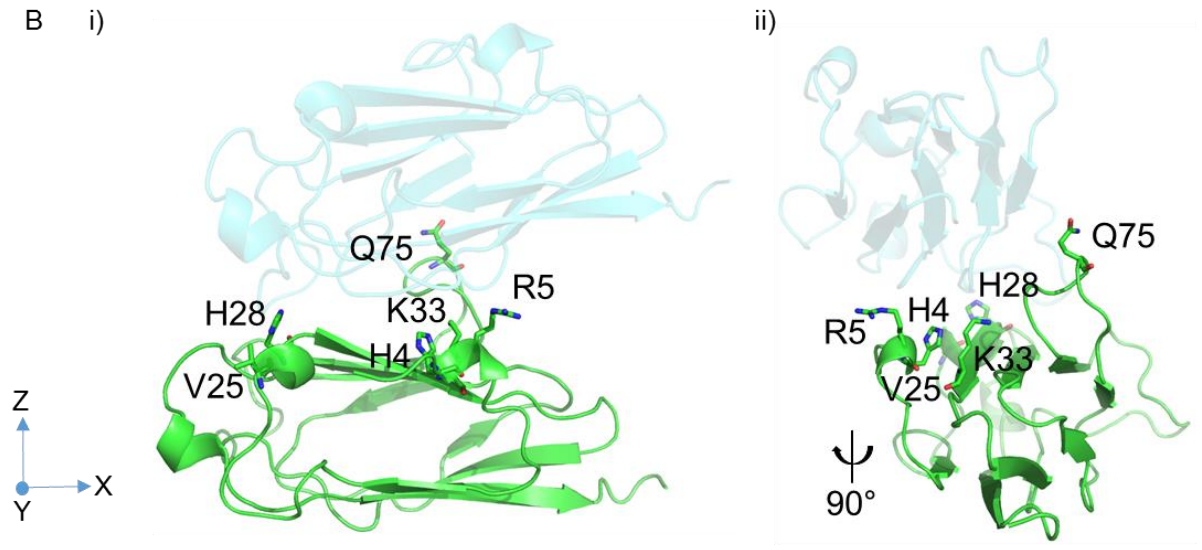

Figure 4.4 | ROSIE docking of CUB2-CUB2 homo-dimers. A) Amino acids that lie within 5 angstroms of the dimer interface of each of the 10 ROSIE models generated . Blue, residues present in all models; red, residues present in all but one model; yellow, present within five angstroms lacking proper hydrogen bonding; green, present in loop region of all models. **B)** Images of CUB2-CUB2 dimer interface in an arbitrary plane (i) and 90° clockwise around the z-axis of the same plane (ii) highlighting six putative residues important for cCDCP1 homodimerization.

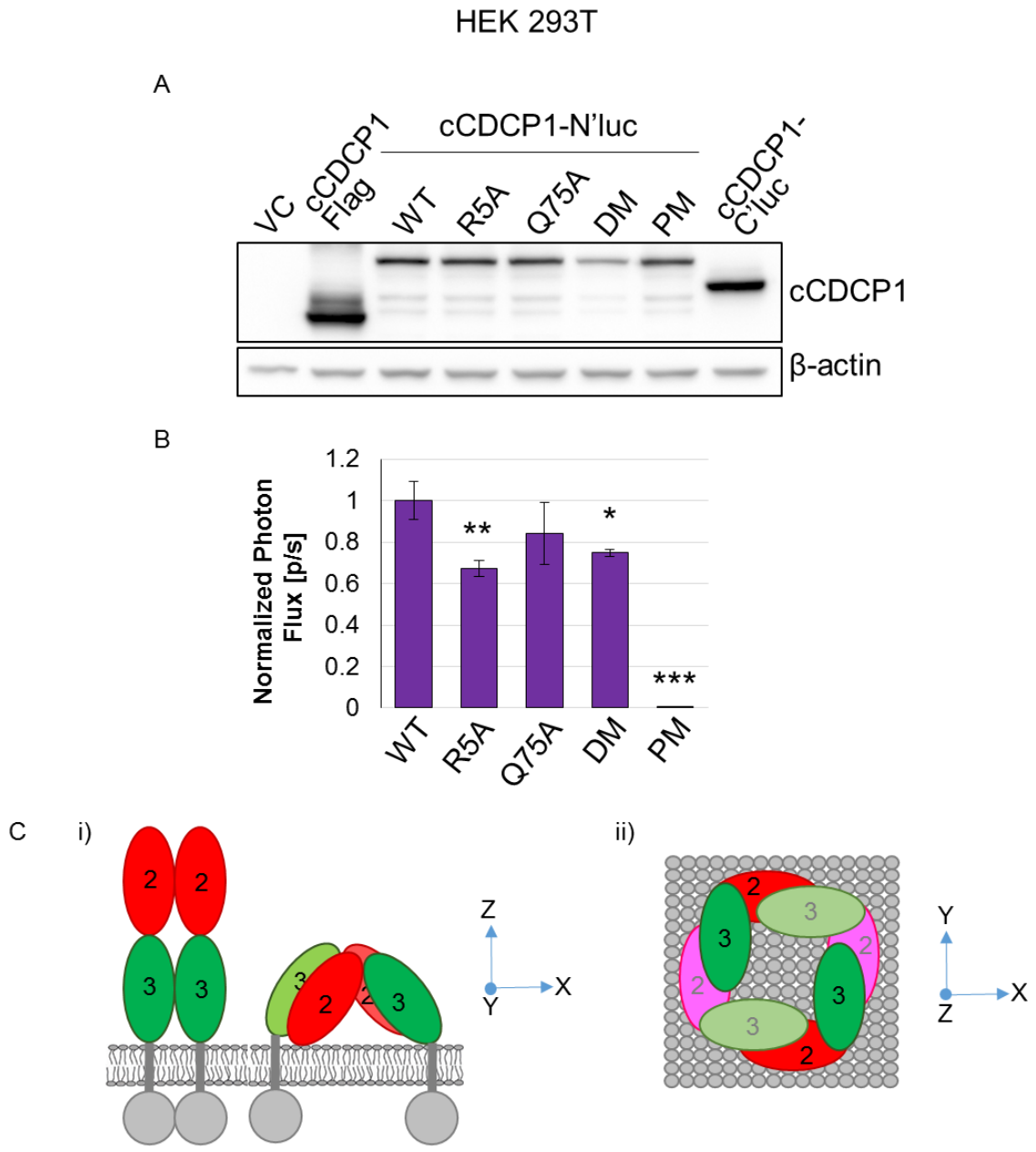

Figure 4.5 | Validation of putative residues involved in dimerization by split luciferase assay. A) Western blot analysis of WT and all mutant cCDCP1-N'luc and WT cCDCP1-C'luc used in the study. VC and cCDCP1-Flag were used as negative and positive controls for CDCP1 expression using an anti-CDCP1 antibody the Western blot. **B)** Quantitation of split luciferase assay comparing binding of cCDCP1-N'luc WT, R5A, Q75A, R5Q75-AA double mutant (DM), or H4R5V25H28K33-AAGAA pentamutant (PM) to WT cCDCP1-C'luc. These data need to be further validated for the PM. **C)** Putative orientations of cCDCP1 homo-dimerization (i) and one variant of a putative oligomer (tetramer) (ii). *P<0.05, **P<0.01, ***P<0.001. Error bars represent SEMs.

Discussion

Structural information is very useful in developing therapeutic targets, and towards that end we took a first step in identifying residues responsible for the dimer interface. However, further analysis of dimerization is needed to validate the 3D models. Our ROSIE docking simulations between CUB2 domains identified R5 as a potential binding residue which was confirmed using our split luciferase assay. However, CUB2 might bind CUB3 (see Figure 4.5C), which may depend on different residues and will require further modeling and mutagenesis. This hypothesis may also be tested using a split luciferase assay by co-expressing either CUB2-N'luc or CUB3-N'luc with CUB2-C'luc or CUB3-C'luc in HEK 293T cells. Furthermore, our initial Robetta 3D model was based on a poorly documented domain, which could misguide the docking algorithm and overestimate the relevant residues for dimerization. More direct methods of defining the binding interface are needed.

Towards that end, we have since moved away from 3D modeling and, in collaboration with Dr. Tom Poulos' lab, are now pursuing the purification and crystallization of ECC using the pET-28a+-His tag-thrombin cleavage site-ECC bacterial expression system. It would be optimal to resolve a crystal structure of flCDCP1 and cCDCP1 to determine any conformational changes that occur upon cleavage of CDCP1 in order to specifically design therapeutics that only inhibit cCDCP1 dimerization without interfering with flCDCP1 activity or other potential functions of cCDCP1. However, membrane proteins are inherently difficult to purify and crystal. Thus, we will currently focus on the soluble ECC.

The ability of CDCP1 to form higher order oligomers also needs to be considered. Figure 4.5C illustrates putative dimerization orientations and one putative oligomeric state (tetramer). In order to answer this question we plan to collaborate with Dr. Michelle Digman using Number and molecular Brightness analysis (N&B) to trace CDCP1 states (monomer/dimer/tetramer/etc.). To do this we will C-terminally fuse flCDCP1, cCDCP1, and ncCDCP1 to mApple fluorescent protein and express flCDCP1-mApple, cCDCP1-mApple, and ncCDCP1-mApple in TNBC cells to assess oligomeric states and localization.

Materials and Methods

Robetta Modeling: CUB1, CUB2, and CUB3 amino acid sequences (Figure 5.1) were submitted to the Robetta 3D Modeling server (http://robetta.bakerlab.org/submit.jsp). Structures for each were built off of sequence conservation from previously published structures 1SPP (spermadhesin)[179], 3KQR (amyloid p component bound to phosphoethanolamine)[180], and 1NT0 (MASP2 CUB1-EGF-CUB2)[6]. Five .pdb files for each domain were visualized with Visual Molecular Dynamics 1.9.3 (VMD) software. Only the five CUB2 models were used for further simulations as it is likely that CUB2 plays a key role in homo-dimerization of cCDCP1 monomers.

Molecular Dynamic simulations: To verify the structural integrity of the 3D Model generated in Robetta, we first calculated the overall charge of the system and added counter ions to bring the system to a neutral net charge. Then a water box was added to solvate the system. The simulation was then carried out using a periodic cell. Simulations were carried out for 170 ns taking pictures every 1 ns.

RMSD Analysis of MD Simulation: To measure the stability of the structure during the MD simulation, the root mean squared displacement (RMSD) of the structure was measured as the difference between the positions of the Cα atoms of each residue for every time point in the simulation (calculated every 10 picoseconds over the full 170 nanosecond trajectory).

RMSF Analysis of MD Simulation: The root mean squared fluctuation (RMSF) was used to analyze the dynamics of each residue. The RMSF value corresponds to how dynamic the residue it; higher values means that the residue is more dynamic and less stable while low values means that residue is more stable and less dynamic. The terminal regions were excluded from final analysis as they naturally have a much higher RMSF due to lack of secondary structure. Data calculated from measurements taken every 10 picoseconds over the full 170 nanosecond trajectory.

Rosetta Docking Simulation: All five .pdb files generated in Robetta 3D Modeling software were used with and against eachother to construct a putative dimer interface. All docking models were visualized in VMD 1.9.3 software and all residues in the dimer interface were mapped.

SDM: See Chapter 2 methods. Primers in Supplemental Table 2. All mutations made in CUB2 of pLM-CMV-cCDCP1-N'luc template.

Transfection: See chapter 2 methods.

Western blot: See Chapter 2 methods.

Split luciferase assay: See Chapter 2 methods. pLM-CMV-cCDCP1-N'luc WT. R5A, Q75A, R5Q75-AA, and H4R5V25H28K33-AAAAA combination mutations were used with pLM-CMV-cCDCP1-C'luc WT in assays.

CHAPTER 5: SURROGATE BIOMARKERS FOR CDCP1 ACTIVITY IN BREAST CANCER.

Introduction

The significance of CDCP1 as a marker of poor prognosis has been demonstrated in multiple types of cancer including pancreatic[44], colorectal[51], lung [40], renal [17], endometrioid[45], gastrointestinal[46], esophageal[181] and triple-negative breast cancer (TNBC)[67]. In TNBC, positive staining of this protein by immunohistochemistry (IHC) or mRNA transcript by fluorescent *in situ* hybridization indicated an >80% chance of local and distant recurrence when combined with positive node status[67].

CDCP1 was first described as a biomarker for TNBC by Turdo et al.[67] However, they were not able to differentiate between the cleaved and full-length form of CDCP1. Our previous studies described in Chapter 2 demonstrate that CDCP1 is only active in TNBC after it has been cleaved and formed a homo-dimer[5]. The cleaved CUB1 domain would be the logical choice to monitor cCDCP1 activation, but this method is not feasible as it would be impossible to distinguish from flCDCP1 by IHC. Thus, there is a need for a new biomarker of CDCP1 activity in TNBC.

One method to quantitate CDCP1 cleavage is through extraction of protein from formalin-fixed paraffin embedded (FFPE) tissue. The protein can then be run on a Western blot to separate cCDCP1 and flCDCP1 by size. However, there are limitations to this method. The main limitation is sample availability as a larger tissue sample is needed to get enough protein to run for a Western blot compared to that needed for IHC staining.

It has been previously established that the cCDCP1 homo-dimer stimulates phosphorylation of PKCδ at Y311[5]. Therefore, phospho-PKCδ Y311 may have potential as a surrogate biomarker of cCDCP1 activity. The preliminary studies described below are an initial step at evaluating this hypothesis. First, we demonstrate that cCDCP1 can be detected in FFPE archival tissue. Next, we show phospho-PKCδ Y311 can also be detected in these same tissue samples.

Results

cCDCP1 can be detected by Western blot from FFPE tissue. The aim of this study is to positively correlate CDCP1 cleavage to PKCδ phosphorylation because this would indicate that phospho-PKCδ Y311 staining could be used in place of cCDCP1 detection by protein extraction from FFPE tissue. In order to investigate the possibility of phospho-PKCδ Y311 as a surrogate marker of CDCP1 activity, we first needed to demonstrate our ability to detect CDCP1 cleavage in archived formalin fixed paraffin embedded (FFPE) tissue. In collaboration with Dr. Scott Heinemann at Hoag Hospital in Newport Beach, CA, and utilizing the standardized protocol developed by Armed Forces Institute of Pathology [182, 183, 184] for extraction of protein from FFPE tissue for analysis by Western blot, we analyzed CDCP1 cleavage in a few normal breast and TNBC FFPE tissue samples (Figure 5.1). We observed higher CDCP1 expression and cleavage in all TNBC tissue samples tested compared to the four normal breast tissue samples tested, where CDCP1 was barely expressed and insignificantly cleaved. Interestingly, we were able to evaluate the difference in CDCP1 cleavage between one primary tumor sample and its corresponding metastasis, which demonstrated much higher CDCP1 expression and

cleavage in the metastasis compared to the primary tumor (Figure 5.1A). This is consistent with previous reports[14] of CDCP1 expression between primary and metastatic tissue. This data demonstrates our ability to measure CDCP1 cleavage for use in correlation studies with phospho-PKCδ Y311 staining.

Phospho-PKCδ Y311 can be detected by IHC. After we confirmed that we could measure cCDCP1 levels by Western blot our next goal was to reliably analyze phospho-PKCδ Y311 by IHC. First, we genetically altered PKCδ expression in MDA-MB-231 and HEK 293T cells for validation of the phospho-PKCδ Y311 for IHC. We knocked down PKCδ in MDA-MB-231 cells and overexpressed PKCδ with cCDCP1 and Src in HEK 293T cells to induce phosphorylation[5] and analyzed PKCδ phosphorylation by Western blot (Figure 5.2A i and ii). Next, we inhibited CDCP1 cleavage using 100 ng/mL dexamethasone in MDA-MB-231 cells, which was previously demonstrated to inhibit PKCδ phosphorylation (Chapter 2) (Figure 5.2A iii). After validating the effects of these conditions on phospho-PKCδ Y311 by Western blot, we used the same cells from Figure 5.2A to analyze phospho-PKCδ Y311 IHC staining (Figure 5.2B). We found that differences in PKCδ phosphorylation were consistent between Western blot and IHC staining. We then analyzed phospho-PKCδ Y311 in the normal breast and breast cancer tissues from Figure 5.1 (Figure 5.2C) and found that we could detect the target at varying levels in all of the FFPE samples.

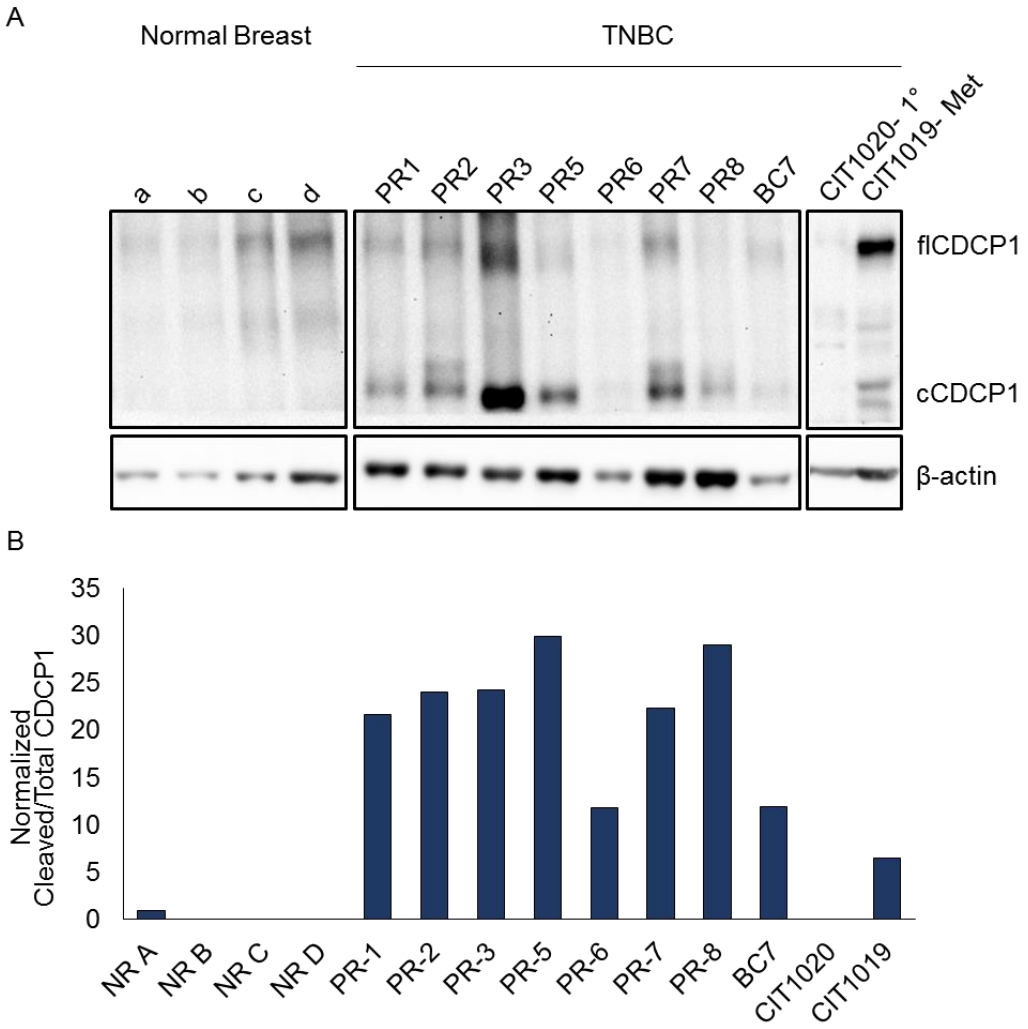

Figure 5.1 | CDCP1 cleavage in primary tissue can be analyzed by Western blot. A) Western blot analysis of CDCP1 expression and cleavage in primary human normal breast and TNBC tissue. **B)** Quantitation of CDCP1 cleavage measured as (intensity of the cCDCP1 band)/(∑ total CDCP1= cCDCP1+flCDCP1 bands) in each sample. All samples were normalized to Normal Breast sample a.

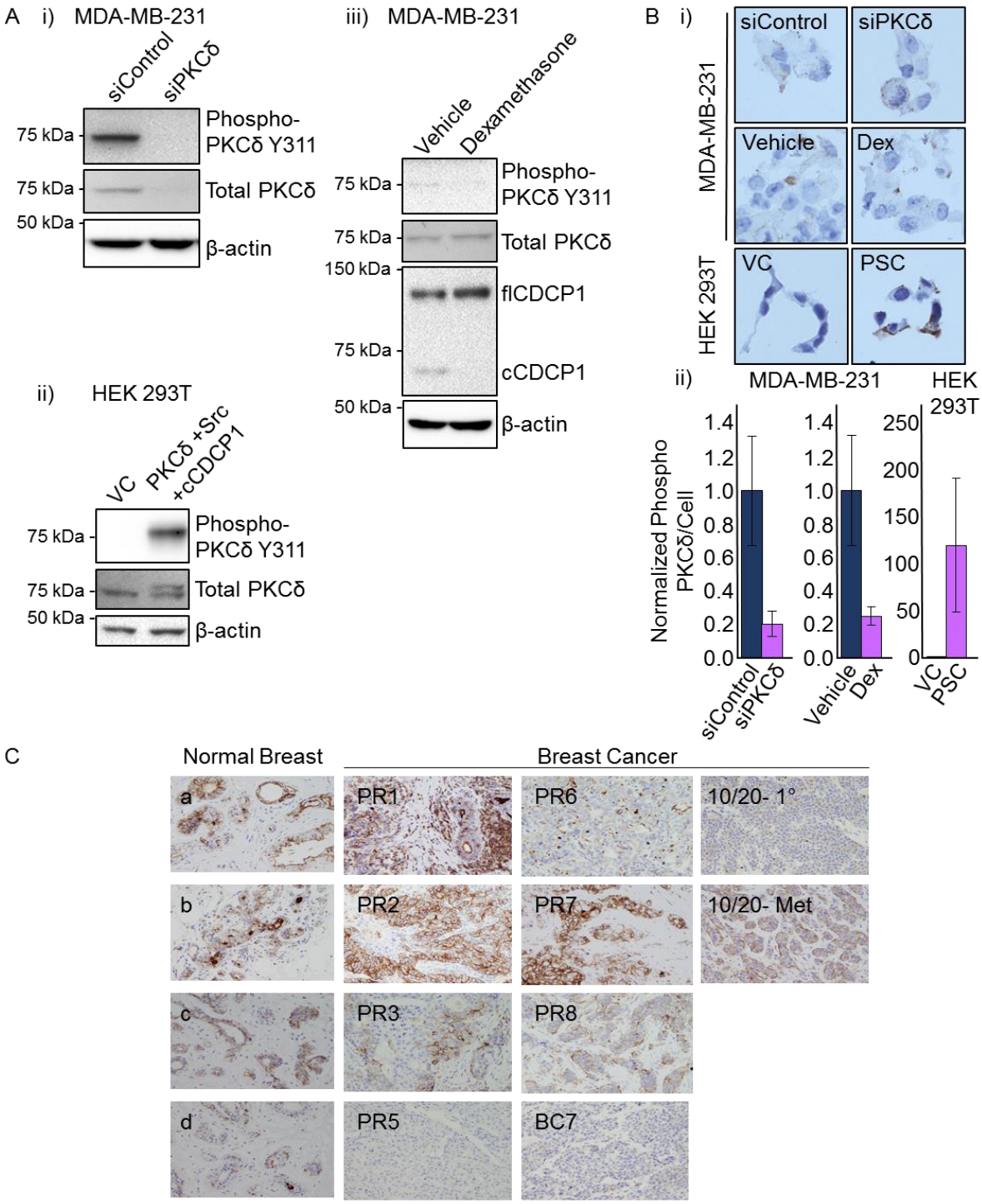

Figure 5.2 | Phospho-PKCδ Y311 can be detected by IHC. A) Western blot validation of PKCδ expression and phosphorylation after siRNA knockdown in MDA-MB-231 cells (i), overexpression with cCDCP1 and Src in HEK 293T cells (ii), and treatment with 100 ng/mL dexamethasone (iii) in MDA-MB-231 cells. **B)** i) 20x IHC images of phospho-PKCδ Y311 staining of cells from (A); ii) quantitation of phospho-PKCδ Y311 staining in samples in (i). Dex, Dexamethasone; PSC, PKCδ+Src+cCDCP1. **C)** IHC analysis of phospho-PKCδ Y311 in primary human normal breast and breast cancer tissue.

Correlation between CDCP1 cleavage and phospho-PKCδ Y311. We have demonstrated our ability to both detect CDCP1 cleavage and PKCδ phosphorylation in FFPE samples. To determine if there was a correlation between the two, we first quantified and normalized the cCDCP1 WB signal from each sample along the ordinate axis, and plotted against PKCδ phosphorylation quantified by IHC on the Y-axis. The calculated trendline resulted in an R^2 value of R^2=0.0031. According to this data, there was no correlation between CDCP1 cleavage and PKCδ phosphorylation (Figure 5.3). As of now, these data indicate that phospho-PKCδ Y311 would not be a good surrogate biomarker for CDCP1 activity in TNBC. However, this result needs to be followed up with a larger sample size and consistent sample preparation.

Discussion

We started with the hypothesis that phospho-PKCδ Y311 could be a surrogate biomarker for cCDCP1. Our initial experiments suggest that the two are not sufficiently correlated to be a useful biomarker for TNBC. Among the technical hurdles for the analysis, we found the duration of time the samples are incubated in formalin introduces a large amount of variability in staining for both CDCP1 cleavage and phospho-PKCδ Y311. Phospho-PKCδ Y311 staining appears to be the more unstable of the two. Theoretically, once the samples are fixed, PKCδ phosphorylation signal should not change. We have not yet been able to directly test how the signal holds up after months or years of sample storage at room temperature.

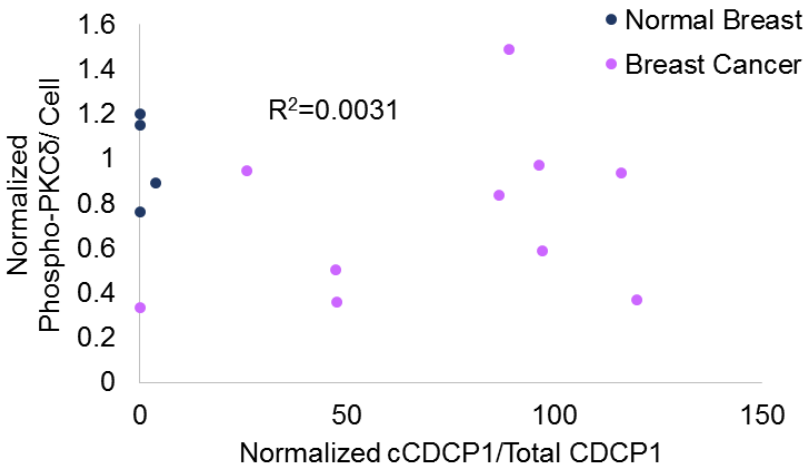

Figure 5.3 | Correlation of CDCP1 cleavage and PKCδ phosphorylation. Correlation plot of normalized CDCP1 cleavage quantitated from Western blot (x-axis) and normalized phospho-PKCδ Y311 IHC staining (y-axis). Both CDCP1 cleavage and PKCδ phosphorylation values were normalized to normal breast tissue. R2=0.0031, indicating there is no correlation between CDCP1 cleavage and PKCδ phosphorylation.

Thus far, we have been able to optimize our IHC protocol and protein extraction for WB protocol. To develop a reliable assay, we will need to be able to compensate for protein degradation in samples and normalize phospho-PKCδ IHC staining independent of sample age. This could be done in a few ways. First, sample tissue could be stained for both total PKCδ protein and also phospho-PKCδ Y311. The quantified data can then be expressed as (intensity of phospho-PKCδ Y311/ intensity of total PKCδ). Second, staining of phospho-PKCδ Y311 could be normalized to the intensity of staining of a housekeeping gene, like β-actin. Quantification of phospho-PKCδ would be expressed as (intensity of phospho-PKCδ Y311/ intensity of β-actin). A third approach could use a fresh tissue specimen as a control. In this scenario, the fresh tissue sample would be run with the sample lysates in order to compare the β-actin signal by Western blot. A coefficient of degradation [C_D=1/(sample β-actin/ control β-actin)] could be determined and quantitation of phospho-PKCδ would be (intensity of phospho-PKCδ Y311 x C_D). These methods of normalizing phospho-PKCδ Y311 IHC staining will not need to be used for analyzing CDCP1 cleavage by Western blot as the cleavage status would probably remain the same independent of the ratio of protein degraded over time. Also, these methods of normalizing IHC signal should not be needed in the clinic, as samples would be stained immediately after collection and FFPE processing from the patient. Therefore, it may be important to continue this study using only freshly FFPE processed tissue samples to avoid and protein degradation artifacts and more reliably determine the correlation between CDCP1 cleavage and PKCδ phosphorylation.

We have demonstrated the feasibility of testing phospho-PKCδ Y311 as a surrogate biomarker for CDCP1 activity and described the many road blocks that were

faced during this study. As mentioned previously, it will be necessary to normalize all of the data to incorporate correction for protein degradation. The most quantitative option for this would be via IHC staining of the tissue for total PKCδ protein and normalize phospho-PKCδ Y311 to total PKCδ protein signal. Many factors dictate protein stability in FFPE tissue, and this may not be as simple or reliable as using a typical housekeeping gene. The other proposed option would be to quantitate protein degradation by Western blot, as previously mentioned.

Sample variability was the limiting factor in this study, and must be addressed if this biomarker were to be used in the clinic. Fortunately, clinical samples would experience less degradation than the samples tested in our pilot experiments, which were obtained through a tissue bank. The samples would be processed directly in parallel with controls, and staining would occur immediately after tissue processing instead of weeks to years as was the case in our pilot. With this in mind, it may be more informative to move forward with samples that are less than 2 weeks old. The goal remains to successfully normalize phopsho-PKCδ Y311 to CDCP1 cleavage for use as a diagnostic marker.

However, it should be highlighted that CDCP1 is not the only regulator of PKCδ phosphorylation. For example, PKCδ has been shown to associate with the insulin receptor to become phosphorylated and activated by Src kinase in response to insulin signaling in skeletal muscle cells[185, 186]. PKCδ upregulation has also been demonstrated by cytochrome c in the mitochondria of mouse embryonic fibroblasts[187]. Furthermore, PKCδ can be activated through interaction with the type I interferon receptor to induce its phosphorylation and activation of Stat1[188]. Finally, in breast cancer, PKCδ interacts with

the HER2 receptor, resulting in its activation by Src kinase to drive HER2 expressing breast cancer tumorigenesis[189]. These are just a few examples of the differential regulation of PKCδ across cell types. This demonstrates that the lack of correlation between phospho-PKCδ Y311 and CDCP1 cleavage that we observe may not be the result of technical error but could very well be due to other regulatory pathways activating PKCδ in TNBC independently of CDCP1 cleavage.

It may be interesting to analyze the potential of the cCDCP1 dimer as a surrogate biomarker of CDCP1 activity instead of phospho-PKCδ as it can be detected by PLA in FFPE sections (Chapter 3, Figure 3.7). CDCP1 cleavage could be validated by Western blot and compared to total CDCP1 levels. We hypothesize that there will be a positive correlation between PLA signal (CDCP1 dimerization) and CDCP1 cleavage as well as between PLA signal and total CDCP1 measured by IHC.

Finally, as phospho-PKCδ Y311 IHC staining is a more cost effective biomarker option than PLA analysis, we hypothesize that phospho-PKCδ Y311 would have a positive correlation with PLA signal. In this case, we could use CDCP1 dimerization in place of CDCP1 cleavage measured by Western blot as a control for future tumor samples. This would completely eliminate a need to extract protein from FFPE tissue and would likely result in more consistent data as the group size gets larger.

Materials and Methods

Preparation of low cell density tissue culture cell blocks for immunohistochemistry: Tissue culture cells were fixed in 10% zinc buffered formalin (Scigen Scientific Inc #1480Z, Gardena CA) for ten minutes, centrifuged and suspended in phosphate buffered saline. To prepare low cell density agarose cell blocks for

immunohistochemistry, cells were collected by centrifugation and suspended in 50 µL of 3% type IX-A agarose (Sigma #A2576). The agarose was drawn into a 1 ml syringe and gelled at 4 °C. The agarose discs were removed from the syringe and processed for paraffin embedding using standard techniques.

Preparation of high cell density tissue culture cell blocks: High cell density tissue culture cell blocks of tissue culture cells were prepared as follows: 200 µL Type I-A agarose (Sigma #A0169) cushions were prepared at the bottom of 1 ml syringes. Formalin fixed cells were suspended in 3% type IX-A agarose and pipetted into the syringe barrel on top of the agarose cushion. The syringes were centrifuged for 10 minutes at 800 g in a desk top centrifuge with a swinging bucket rotor. Following centrifugation, the syringes were placed in a 4 °C refrigerator to harden the type IX-A agarose. The agarose cylinders containing concentrated cells were removed from the syringes, fixed in formalin and processed for paraffin embedding using standard techniques. This procedure generates cylindrical cell pellets whose high uniform cell density closely resembles clinical samples of tumor tissue.

Deparaffinization and solubilization of FFPE tissue for WB analysis: Paraffin blocks were sectioned at 40 microns and the paraffin rolls were collected into screw cap polypropylene tubes. The FFPE tissue was deparaffinized in xylene in a heating block at 65 °C and residual xylene was extracted with reagent alcohol at room temperature. The reagent alcohol was extracted with methanol at room temperature and the tissue was then rehydrated with water at 65 °C. The volume of the FFPE tissue sample was estimated as the product of the cross-sectional area of the tissue in the paraffin block and the total thickness of the sections cut. The rehydrated tissue was solubilized in 50

volumes of extraction buffer. Unless otherwise stated, ffpe solubilization buffer contained 4%SDS, 125 mM Tris HCl pH 8.0, 100 mM DTT and 10% glycerol. After an appropriate volume of buffer was added to the rehydrated FFPE tissue, the tubes were capped tightly and place in a heating block at 95-97 °C. After 60 minutes, the tubes were removed from the heating block and allowed to cool at room temperature.

Immunohistochemistry: Immunohistochemical staining was performed on an automated instrument (Leica Biosystems Bond III). Four micron tissue sections were baked at 60 °C for 60 minutes, deparaffinized in xylene and rehydrated by sequential immersion in 100% ethanol, 95% ethanol, 80% ethanol and deionized water. Antigen retrieval was performed offline; slides were immersed in epitope retrieval solution 2 (Leica product code AR9640) and heated in a pressure cooker for 20 minutes. The slides were cooled and assembled with cover tiles on the Leica Bond III instrument slide racks. Primary antibody incubations were for 30 minutes. Bound antibody was detected with the Bond™ Polymer Refine Detection system and nuclei were counterstained with hematoxylin following the manufacturer's protocol. All antibodies used are listed in Supplemental Table 1.

Correlation analysis: CDCP1 cleavage was quantitated in Image J by measuring the intensity of the cCDCP1 band and dividing it by total CDCP1 quantitated as the sum of the cCDCP1 and flCDCP1 bands. Phospho-PKCδ Y311 staining was quantitated in Image J using Image> Color> Color Deconvolution> H DAB. Measurement was taken from the appropriate channel. Measurements were normalized to the number of cells/field quantitated by manually quantitating nucleus staining. Values for CDCP1 cleavage and PKCδ phosphorylation was quantitated to the average measurement for each in normal

breast tissue. Correlation plot was constructed using CDCP1 cleavage on the x-axis and PKCδ phosphorylation on the y-axis. R^2 value was calculated in Excel.

CHAPTER 6: CDCP1 IN LIVER DISORDERS AND WOUND HEALING

Introduction

Outside of cancer, lipid metabolism (and CDCP1 activity) is central to the overall health of an individual. To expand our understanding of the role of CDCP1, we identified and specifically focused on two areas with deficiencies in LD metabolism; liver disorders and wound healing. The goal of these studies was two-fold: 1) Begin characterization of our CDCP1 knockout (KO) mice and 2) Investigate the physiological roles of CDCP1. To do this we analyzed the most highly metabolic organ in the body, the liver, and any differences in wound healing as a validation of previous work done on CDCP1 in the skin[32].

The liver is an important site for metabolic processes such as macronutrient metabolism, xenobiotics metabolism, bile synthesis for fat absorption, plasma protein synthesis, and immunity[190]. The regulation of glucose levels in the blood is one of the liver's most well-known functions and can be a diagnostic marker for metabolic syndrome (MetS). MetS is a set of risk factors that increase one's chance of developing health problems like artherosclerosis, stroke, chronic kidney disease, non-alcoholic fatty liver disease (NAFLD), and type 2 diabetes mellitus (T2DM). The broad effect of MetS does not stop there, it is also associated with polycystic ovarian disease, obstructive sleep apnea, sexual dysfunction, and cancer[191].

NAFLD encompasses a spectrum of liver damage ranging from steatosis (increased LD abundance of hepatocytes) to fibrosis to cirrhosis[192]. T2DM is characterized by abnormally high blood glucose levels and reduced glucose-stimulated

insulin production[193]. Patients with MetS (35% Western population[194]) often have NAFLD (~25% Western population[192]) and/or T2DM (~8.4% Western population[195]). Additionally, patients with T2DM frequently also have NAFLD, further exemplifying that these diseases are tightly intertwined in their prevalence and pathophysiology. There are reliable clinical criteria for the diagnosis of MetS (abdominal obesity, elevated triglycerides, reduced HDL-C, hypertension, and elevated fasting glucose levels[192]), NAFLD (dyslipidemia, fatty infiltration of the liver by ultrasound, MetS symptoms[196]), and T2DM (elevated glycated hemoglobin, elevated fasting and regular glucose levels, reduced glucose tolerance[197]).

Patients with T2DM have a wealth of health complications including impaired wound healing, often resulting in amputations and increased morbidity and mortality post-amputation[198]. This is due to a combination of decreased immune function, neuropathy, arterial occlusion, and other poorly understood factors[199]. Keratinocyte proliferation, migration, and differentiation are reduced in diabetic patient wounds partially caused by abnormal EGFR signaling[200] and activation of the glucocorticoid pathway to suppress c-myc signaling[201].

Wound healing has four main stages: Coagulation, inflammation, proliferation/migration, and remodeling. Coagulation and inflammation occur immediately after an injury. Coagulation results in hemostasis and provides a temporary fibronectin extracellular matrix (ECM)[202] that eventually gets remodeled[203] to allow cell migration into the wound area. Coagulation also acts to sequester cytokines and growth factors that promote wound healing[204]. Coagulation is dominated by the platelet cell population. However, platelets secrete cytokines to attract neutrophils, monocytes, and fibroblasts to the wound site resulting in inflammation. Hypoxia also plays a role in the release of

chemoattractants in the wound environment by activating hypoxia inducible proteases in the ECM. Inflammation is dominated by monocytes, which enter the wound site to phagocytose and kill bacteria and remove other debris. Proliferation/migration and remodeling of wound sites relies, at first, on reepithelialization via movement of keratinocytes into the wound to seal it. This process is complex and relies on the interdependence of keratinocytes, surrounding fibroblasts and endothelial cells, and ECM formation and remodeling. The hypoxic environment of the wound enhances keratinocyte migration[205] and stimulates secretion of VEGF and other growth factors by endothelial cells to promote angiogenesis[206], which then stimulates fibroblast proliferation and secretion of collagen ECM[207]. MetS[208] and diabetes[209] have been demonstrated to impede wound healing by negative affecting keratinocyte proliferation, differentiation, and migration.

Given our previous data showing CDCP1's role in lipid metabolism, we investigated its expression as it relates to liver disorders and wound healing. CDCP1 has been previously shown in stratum basale and spinosum keratinocytes. Further, CDCP1 was demonstrated to drive *in vitro* keratinocyte migration[32], main players in reepithelialization of wounds (occurs within 96 hours of wounding[210]). Utilizing our established germline CDCP1 KO mice, we probed the effects on lipid metabolism by first looking at the liver and then extended our studies into the wound healing capacity of the mice. We observed KO mice on a mixed background have fattier livers and reduced ability to heal wounds than CDCP1 heterozygous (Het), both indicators of MetS, NAFLD, and T2DM. These findings are a good first step towards fully characterizing CDCP1 KO

mice and understanding CDCP1's physiological roles. However, further work is needed to link the two phenotypes together in these mice.

Results

CDCP1 knockout mice have increased lipid accumulation in the liver. Using CARS microscopy, we found that the livers of CDCP1 KO mice had almost two times the amount of lipid compared to CDCP1 Het mice at 21 days of age (Figure 6.1A). We noticed that the liver LD difference between CDCP1 Het and KO mice is slightly reduced but still significant as the mice age. We were interested to see if changes in diet would induce any pathology. So, we challenged the mice with either a normal or high fat (HF) diet for 12 weeks and found that CDCP1 Het mice on a HF diet had increased liver lipid content, which was comparable to that of CDCP1 KO mice on a normal diet (Figure 6.1B). Furthermore, the liver lipid content of CDCP1 KO mice on a HF diet increased even more than CDCP1 Het mice on a HF diet (Figure 6.1B). These changes in liver lipid content did not manifest in total body weight gain, as there was no significant difference in weight gain between each group (Figure 6.1C i) and their final body weights were not significantly different (Figure 6.1C ii) after correcting for gender. Furthermore, we did not notice any difference in the fibrotic phenotype (characterized by excessive extracellular matrix deposition and stiffening of the tissue) of the livers between groups (data not shown). These data indicate that CDCP1 regulates LD metabolism in the mouse liver.

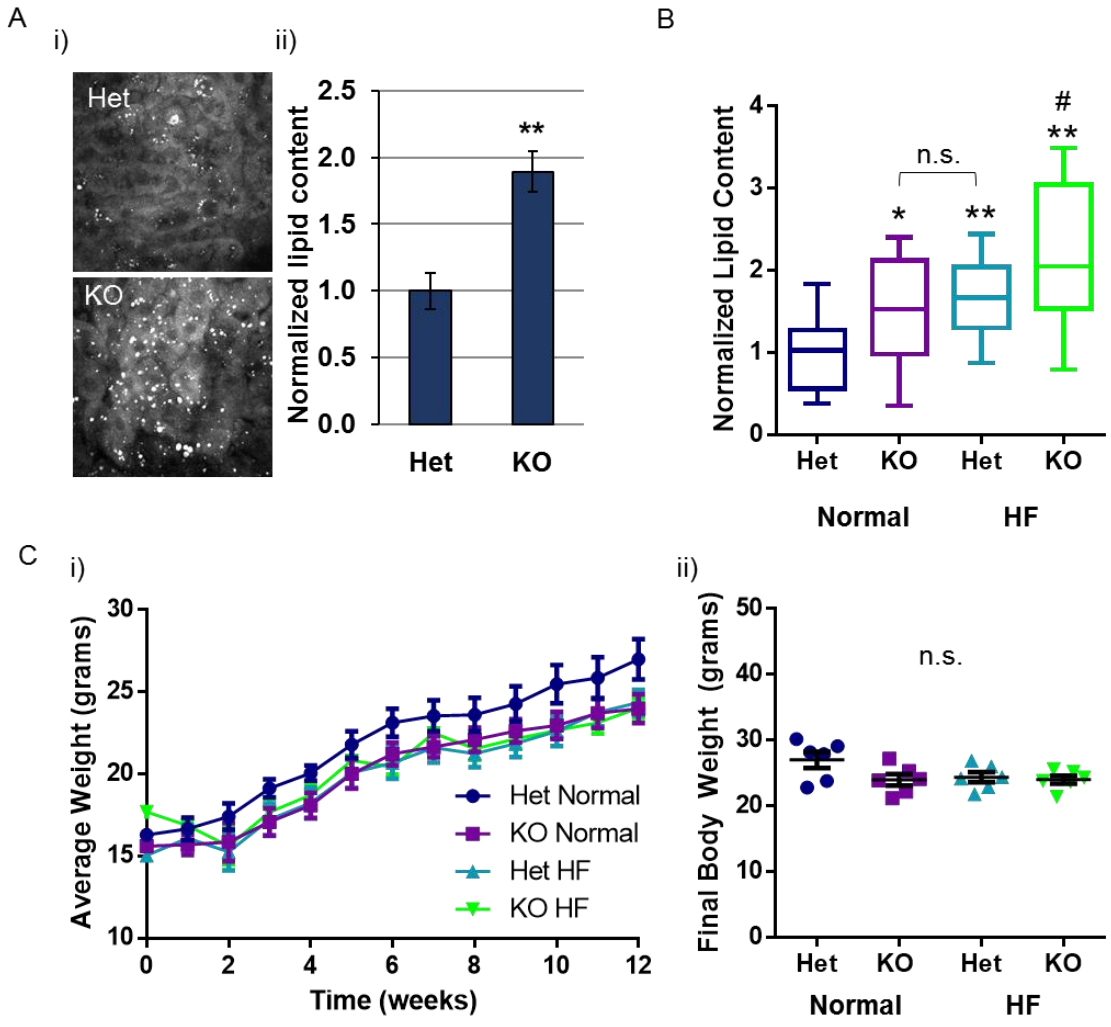

Figure 6.1 | CDCP1 knockout mice have more lipid accumulation in the liver than CDCP1 heterozygous mice. (**A**) i) Representative CARS images of lipid droplet accumulation in the livers of 21-day old CDCP1 heterozygous (Het) and CDCP1 knockout (KO) mice on a mixed background. ii) Quantitation of lipid content. Quantitation is the average of 3-5 images taken from different locations of fresh liver specimens from 4 heterozygous and 3 knockout mice normalized to heterozygous mice. (**B**) Quantitation of lipid content in Het and KO mice fed normal chow or high fat (HF) chow for 12 weeks. Quantitation of lipid content. Quantitation is the average of 3-5 images taken from different locations of fresh liver specimens from 6 mice per group normalized to Het-normal. *compared to Het-Normal, #compared to KO-Normal. *P<0.01, **P<0.001 analyzed by one way ANOVA. Error bars represent SEMs.

CDCP1 expression in keratinocytes increases with time during wound healing. Because increased LD content in the liver is a symptom of NAFLD and may also be related to T2DM, we wanted to investigate any differences in wound healing between CDCP1 Het and KO mice. However, because CDCP1 is also known to be expressed in the skin, we initially looked at the dynamics of CDCP1 expression during wound healing in WT mice. We found that the transcript expression of CDCP1 increased with time during wound healing, measured up to 24 hours (Figure 6.2). This is indicative that CDCP1's contribution to keratinocyte migration and proper wound repair may increase during the initial phases of wound healing when keratinocytes are most actively proliferating, migrating, and differentiating to reepithelialize a wound.

CDCP1 knockout mice have reduced wound healing potential. Because reepithelialization of wounds is active within 24 hours of wounding and CDCP1 has been implicated in inducing keratinocyte migration (main players in reepithlialization) we decided to analyze the migratory potential of CDCP1 Het and KO mouse keratinocytes. We first started by isolating P0 keratinocytes for a transwell migration assay and found that CDCP1 KO keratinocytes migrated less through a transwell membrane than CDCP1 Het keratinocytes (Figure 6.3A). We then tested keratinocyte migration in an *ex vivo* assay in which skin punch biopsies from the ears of mice were cultured in vitro and keratinocytes were allowed to migrate radially for 10 days. We found that, again, CDCP1 KO keratinocytes had reduced migratory potential in the *ex vivo* system compared to CDCP1 Het keratinocytes (Figure 6.3B). Finally, we compared the wound healing abilities of CDCP1 Het and KO mice in response to dermal punch biopsies. We found that the first

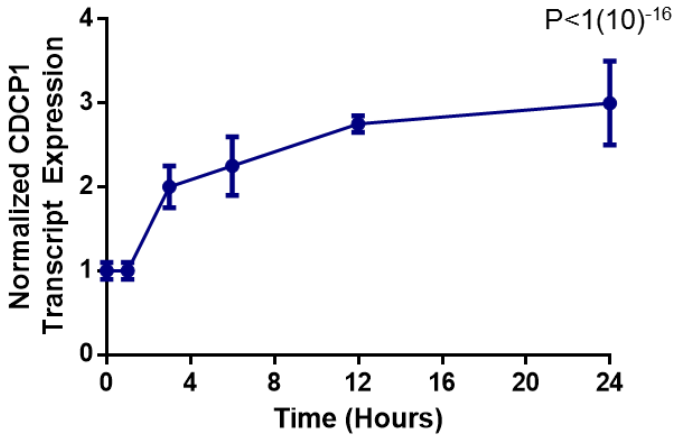

Figure 6.2 | CDCP1 mRNA expression in mouse skin during wound healing. CDCP1 expression increases with time. At 24 hours, wounds are actively being re-epithelialized via proliferation, migration, and differentiation of keratinocytes.

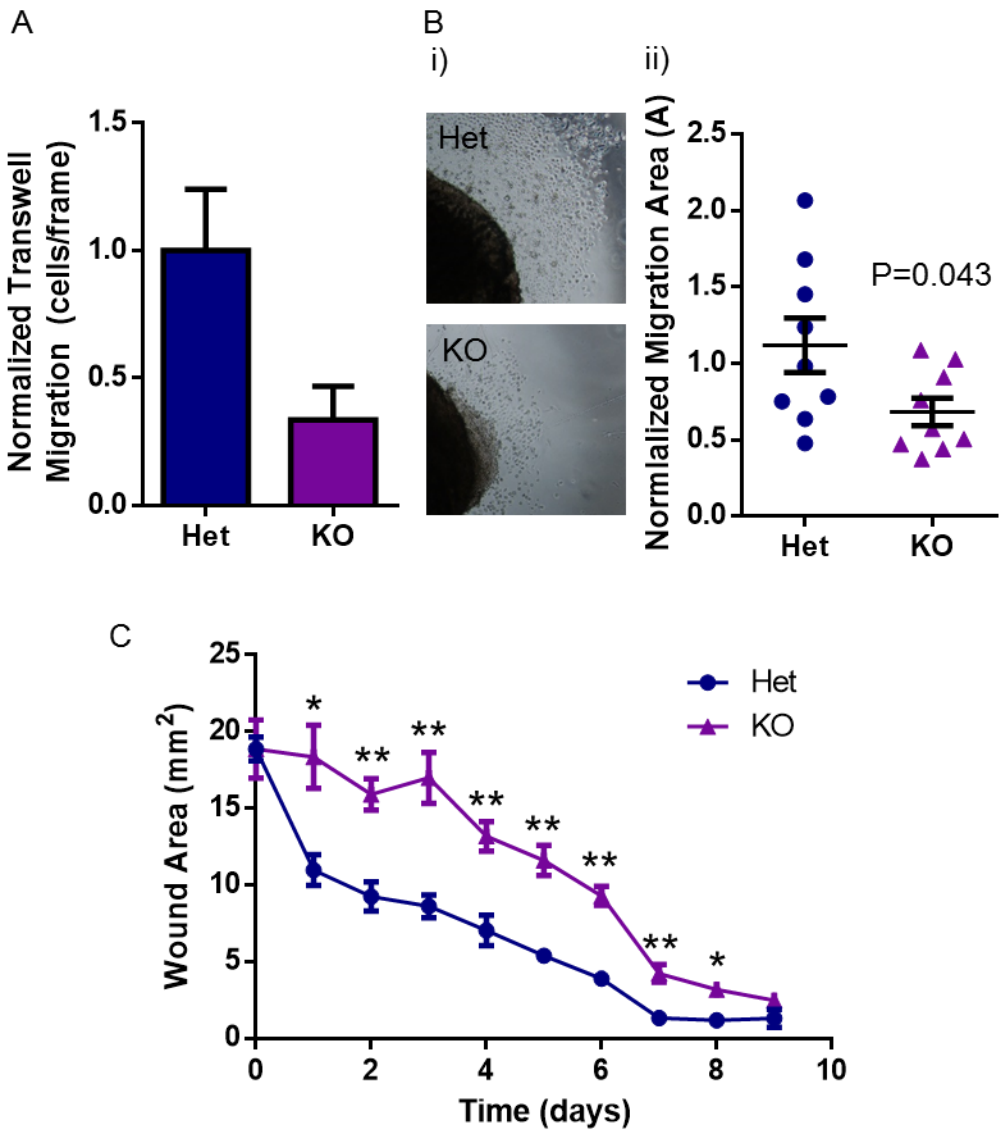

Figure 6.3 | CDCP1 KO mouse keratinocytes have deficient migratory potential. A) P0 isolates CDCP1 KO keratinocytes migrate less than CDCP1 Het keratinocytes in a transwell migration assay. Keratinocytes from each mouse were run in individual transwells, N=2 for both genotypes, error bars represent standard deviation. B) Keratinocytes from CDCP1 KO mouse skin punch biopsies migrate slower than CDCP1 Het keratinocytes. i) Representative 4x images of *ex vivo* punch biopsies; ii) quantitation of radial migration of punch biopsies from N=9 mice per genotype, error bars represent SEM. C) *In vivo* wound closure of epidermal punch biopsies on the backs of CDCP1 Het and CDCP1 KO mice, N=10/genotype, error bars represent SEM. *P≤0.005, **P<0.001.

week of wound healing was severely impaired in CDCP1 KO mice compared to Het mice, but wounds from both groups were essentially healed by the same time (Figure 6.3C). These data are consistent with the observed increase in CDCP1 mRNA expression within the first 24 hours of wound healing. CDCP1 may drive reepithelialization in the early stages of wound healing, and the effects of CDCP1 may be compensated for by other factors/ cells during the migratory, inflammatory, or remodeling stages of wound healing.

Discussion

The body of work presented here surrounding the activity of CDCP1 continually points towards the theme of lipid metabolism, whether it be in cancer or other diseases. The data presented in this chapter demonstrate that CDCP1 is important for maintaining lipid homeostasis in the liver. Our KO mouse model shows CDCP1 is necessary to prevent the development of a pathology that is reminiscent of MetS, NAFLD, and T2DM. It also demonstrates the importance of CDCP1 in keratinocyte migration and proper wound repair. The link between these two observed phenotypes in the CDCP1 KO mice remains to be investigated. We do not know if the fatty liver phenotype in CDCP1 KO mice has a causal relationship with wound healing or if the wound healing phenotype we see in these mice is independent of their fatty livers. One way to separate these two possibilities experimentally would be to virally transduce CDCP1 KO mouse livers and skin (in separate experiments) with cCDCP1 and then compare skin wound healing of CDCP1 Het mice, CDCP1 KO mice, and cCDCP1-transduced (liver or skin) CDCP1 KO mice. Furthermore, it would also be important to isolate liver cells and test function, via alanine transaminase (ALT) or aspartate aminotransferase (AST) activity, between

CDCP1 Het and KO mice. This would inform if the mice were in a pre-diabetic or diabetic state, in which abnormal liver function would indicates a reduction in multi-organ health and would suggest a causal role for the fatty livers of CDCP1 KO mouse on impaired skin wound healing.

However, it is possible that even a heterozygous deletion of the CDCP1 allele is sufficient to induce fatty liver and impair wound healing. This possibility is accentuated by our findings that most of the mice (Het and KO) in the normal vs. HF diet experiment, regardless of which diet they were on, had extremely high random blood glucose levels (measured at the same time each day, not necessarily after fasting), indicating that they were all diabetic. This speculation can be tested by repeating the experiments performed in this chapter using CDCP1 homozygous, heterozygous, and KO mice.

Addressing the wound healing phenotype directly using our KO mouse model, we observed an increase of CDCP1 mRNA expression over time during the acute phase of wound healing (Figure 6.2). We are interested in tracking CDCP1 expression for the entire length of the wound healing assay (Figure 6.3), which could identify which steps in wound healing require CDCP1. The measurements in Figure 6.2 were made during the inflammation period (0-96 hours). This raises the question of inflammatory control of CDCP1 expression and activity. CDCP1 cleavage is induced by serine proteases, which are secreted by immune cells like neutrophils and macrophages, highly abundant in the early wound environment[211, 212]. CDCP1 expression and activation may diminish as wounds progress in the healing process due to the diminished presence of immune cells. Alternatively, other signaling pathways may dominate wound healing in later stages, masking either highly active or dampened CDCP1 signaling. This would explain why

CDCP1 KO wounds catch up in healing to CDCP1 Het wounds as time progresses, compensatory pathways either mask or take over for CDCP1 signaling, which could rescue the initially slow wound healing.

Our data support previous work demonstrating CDCP1's role in wound healing[32]. CDCP1 has been demonstrated as a hypoxia-inducible gene in ccRCC[17]. Another mechanism that may lead to an equilibration of or reduction in CDCP1 expression and activity during would healing would be the reinstatement of proper oxygenation to the tissue after revascularization (within days of wounding[213]). It would also be interesting to test CDCP1 expression in the wounds of hypoxia-inducible factor (HIF) deficient mice to see how much of the increase of CDCP1 mRNA expression is due to the sudden hypoxia of the wound environment before revascularization.

To decipher the mechanistic detail of CDCP1 activity during wound healing, it is worthwhile to determine the role of CDCP1's downstream target, PKCδ, in this process. To accomplish this, Ca^{2+} independent PKC (δ, ε, and η) activators (L–α–Phosphatidylinositol-3,4,5-trisphosphate•7Na[PtdIns-3,4,5-P3]; L-α-Phosphatidylinositol-3,4-bisphosphate, Dipalmitoyl-, Pentaammonium Salt; L-α-Phosphatidylinositol-3,4,5-trisphosphate, Dipalmitoyl-, Heptaammonium Salt), which mimic phosphatidylinositol, could be used locally on the wound in CDCP1 KO mice to potentially rescue migration of keratinocytes or promote wound healing to rates similar to those observed in the CDCP1 Het animal. Furthermore, studies have demonstrated the importance of PKCs in promoting wound healing of corneal injuries[214-216]. However, aberrant PKCδ signaling has been linked to faulty wound repair of diabetic human fibroblasts[217], this study did not investigate PKCδ signaling in keratinocytes. Previous

studies on the role of the CDCP1-PKCδ signaling pathways in migration[5, 17, 218] support the hypothesis that restoring PKCδ activity in CDCP1 KO mouse skin would normalize wound healing.

Multiple mouse models are available that recapitulate MetS, NAFLD, T2DM, and obesity, and could be useful in determining CDCP1's role in these diseases. One useful model would be SREPB-1c transgenic mice[219] which replicate MetS, NAFLD, and T2DM. Two additional mouse models which replicate obesity, MetS, NAFLD, T2DM, and wound healing are B6.Cg-Lep^{ob}/J (ob/ob) and BKS.Cg-Dock7$^{m+/+}$Lepr^{db}J (db/db) mice[220]. We would expect that CDCP1 expression is reduced in the livers of the obese mice compared to WT mice. If this were the case, it would be interesting the test the causal relationship, i.e. did a reduction in CDCP1 expression influence the increased lipid content or did the increased lipid content reduce CDCP1 expression. Evidence that obesity is linked to dysregulated DNA and histone methylation[221] combined with data from Chapter 3 that CDCP1 regulates lipid metabolism, make the epigenetic and transcriptional regulation of CDCP1 and/or the role of CDCP1 in epigenetic and transcriptional regulation, in obesity a very interesting topic to study.

Materials and Methods

Liver LD quantitation: Liver LD abundance was quantitated using CARS microscopy (See Chapter 3 methods). Livers were harvested and cut into thin slices. They were either fixed in 4% paraformaldehyde prior to imaging or imaged fresh.

Normal chow vs. high-fat diet feeding: Mice were fed normal chow (Envigo #2920X.10) or HF chow (Envigo #2919.10) for 12 weeks started at the day they are weaned. Mice were weighed once a week for the duration of the experiment. At the end of the

experiment mice were euthanized by CO_2 and cervical dislocation, weight, and their livers were harvested for CARS microscopy.

Analysis of CDCP1 expression in wounds: Whole wounds were collected and flash frozen. Samples were homogenized for TRIzol RNA extraction and reverse transcription into cDNA. CDCP1 expression was analyzed by qPCR.

Keratinocyte culture conditions: P0 keratinocytes were cultured in EpiLife CF/PRF medium (Thermo Fisher #M EPICFPRF 500) with EpiLife defined growth supplement (EDGS) (Thermo Fisher #S-012-5).

Keratinocyte harvesting: 10 mL of 1:2 solution of 5 mg/mL Dispase (StemCell #07446):EpiLife CF/PRF was prepared prior to isolation. P0 pups were euthanized by CO_2 and decapitation. Skin was removed and placed in Dispase:EpiLife solution. Skin incubated overnight at 4 ˚C with gentle rocking to loosen epidermal and dermal layers from eachother. The epidermal layer (mainly keratinocytes, solid white color) was removed from the dermal layer and used for experiments. The dermal layer was discarded.

Transwell migration: See Chapter 2 methods. Keratinocytes were harvested from P0 CDCP1$^{+/-}$ (Het) or CDCP1$^{-/-}$ (KO) mice, counted with a hemacytometer and 50,000 cells were immediately plated in EpiLife with EDGS in the top chamber of transwell inserts in duplicate for migration. Cells were allowed to migrate for 16 hours.

***Ex vivo* migration:** 1 mm punch biopsies were taken from the ears of CDCP1 Het and CDCP1 KO mice. Punch biopsies were placed in the center of individual wells in a 24 well plate in 500 µL of EpiLife with EDGS. Keratinocytes were allowed to migrate for 10 days. Media was changed every 2 days. Area of migration was quantitated as (total area of

migrated cells) – (area of the initial punch biopsy). Final quantitation was normalized to CDCP1 Het mice.

***In vivo* punch biopsy wound healing:** CDCP1 Het and KO mice were anesthetized with 90 mg/kg ketamine mixed with 4.5 mg/kg xylazine. Hair was removed from the backs of the mice and then two 4 mm punch biopsies (Thermo Fisher #NC9840633) were made on the upper backs of the mice. Each wound was treated as a biological replicate. The area of each wound was measured with calipers daily for 9 days. Mice were euthanized by CO_2 and cervical dislocation at the end of the experiment.

CHAPTER 7: DISCUSSION AND FUTURE DIRECTIONS

Opening statement: TNBC accounts for 10-20% of all breast cancer cases in the US and have fewer treatment options that non-TNBC subtypes, making new diagnostics and treatment justifiably a hot topic for research. The focus of this work has been to offer insight into novel nodes of regulation of and by CDCP1 to drive TNBC metastasis. We also offer preliminary investigations into the 3D structure of CDCP1 to optimize therapeutic targeting, the use of CDCP1 downstream targets as surrogate biomarkers, and findings to support CDCP1's role in a physiological setting. These studies set the stage and offer future directions to understand and exploit CDCP1's complex role in not only TNBC, but the whole spectrum of cancers and other metabolic diseases.

In Chapter 2, we explored the difference in signaling between cCDCP1 and flCDCP1, CDCP1's ability to form a homo-dimer, and the role of homo-dimerization in TNBC migration and invasion. Briefly, we demonstrated that cleavage of flCDCP1 to cCDCP1 leads to homo-dimerization, which we were able to inhibit using ECC. The activated cCDCP1 homo-dimer is necessary to stimulate PKCδ phosphorylation. Lastly, we found this activation and phosphorylation step to be necessary for migration of TNBC.

Looking at this Chapter in the context of the rest of the work, it is important for us to find out if CDCP1 is capable of forming higher order oligomers other than the observed homo-dimers. The evidence supporting localization of CDCP1 to lipid rafts[29] corroborates the idea that flCDCP1 or cCDCP1 could cluster into pseudo-oligomers in membrane lipid rafts. However, it is also possible that cCDCP1 is capable of specifically forming

oligomers (Figure 5C ii). To determine this, we will rely on our pending collaboration with Dr. Digman's lab (see Chapter 5: Discussion).

Another big question regarding CDCP1 dimerization lies in the cell/organ type specificity of the interaction. We demonstrated that only cleaved CDCP1 forms a dimer in TNBC cells. However, it would be interesting to determine the oligomeric status of CDCP1 in different types of tissue, like the liver, and different types of cancer that have varying cytoplasmic LD abundances (i. e. TNBC low LD abundance vs. renal cancer high abundance). To do this in tissue, we should use PLA to analyze CDCP1 homo-dimerization in CDCP1 Het tissue. We could extend this to comparing dimerization between CDCP1 Het mice fed normal and HF diets. To do this in cancer, we should analyze PKCδ phosphorylation after 1) knockdown CDCP1 expression in TNBC cells (high CDCP1 cleavage and low lipid content) and 786-0 and RCC4 ccRCC cell lines (low CDCP1 cleavage and high lipid content) and 2) treat 786-0 and RCC4 ccRCC cell lines with either dexamethasone[30] or monoclonal antibodies[13, 28, 52] to inhibit CDCP1 cleavage.

Finally, we were not able to demonstrate direct evidence of CDCP1-dependent trans-phosphorylation of PKCδ by Src. To validate the necessity of the cCDCP1 dimer for PKCδ trans-phosphorylation by Src, we will use cCDCP1 mutants to inhibit either Src and/or PKCδ binding. We will then transfect HEK-293T cells with either the Src only-binding cCDCP1 mutant (cCDCP1s, PKCδ cannot bind), the PKCδ only-binding cCDCP1 mutant (cCDCP1p, Src cannot bind), or the combination of cCDCP1s and cCDCP1p (Src and PKCδ can both bind a monomer of the cCDCP1 dimer). If the dimer is required for trans-phosphorylation then cCDCP1s or cCDCP1p alone will not induce PKCδ phosphorylation because either the kinase (Src) or the substrate (PKCδ) will not be bound

to either monomer of the cCDCP1 dimer and thus will not be able to interact. However, the combination of cCDCP1s and cCDCP1p will allow the phosphorylation of PKCδ because in cCDCP1 dimers that form between cCDCP1s and cCDCP1p, Src will be able to bind the cCDCP1s monomer and PKCδ will be able to bind the cCDCP1p monomer, allowing the interaction of Src and PKCδ and transphosphorylation of PKCδ.

Extending our findings from Chapter 2 that CDCP1 homo-dimerizes, we investigated CDCP1's interactions with other proteins in Chapter 3. Chapter 3 explored the interaction between CDCP1 and ACSL family proteins in TNBC, and the impact that CDCP1 had on lipid metabolism. Briefly, we demonstrated that CDCP1 reduces LD abundance and stimulates FAO to drive metastasis, partially by reducing ACSL activity. Further, we found that regulation of lipid metabolism by CDCP1 is dependent on homo-dimerization, as ECC treatment increased LD abundance and reduced metastasis of TNBC tumors *in vivo*.

In the absence of CDCP1, the inhibition of acyl-CoA use in FAO may indirectly force the lipid into storage. In order for acyl-CoAs to undergo FAO they must go through 2 chemical conversions: 1) CPT1, present on the outer-mitochondrial membrane, converts acyl-CoA into acyl-carnitine, which can be transported into the mitochondria, where 2) CPT2 reverts acyl-carnitine back into acyl-CoA, which can then enter FAO[148-150]. The increase in ACSL activity with the knockdown of CDCP1 may not merely be explained by the absence of CDCP1 protein physically inhibiting ACSL activity but may also be the result of a positive feedback loop in which the co-reduction in FAO caused by the absence of CDCP1 and increase in ACSL activity further activates ACSLs to increase the concentration of acyl-CoAs in the cytoplasm that so that CPT1 could have a higher

chance of converting them to acylcarnitines for transport into the mitrochondria for FAO. This makes sense when we notice that the effect on ACSL activity is not proportionally different with CDCP1 overexpression. The slight reduction in ACSL activity due to CDCP1 overexpression can be explained by the already high levels of CDCP1 expressed in the cells used. However, it could also be the result of a negative feedback loop, in which sufficient/saturating ATP concentration from CDCP1-driven FAO and subsequent OxPhos starts inhibiting acyl-CoA production by either ACSLs or CPT2 to slow FAO, allowing the cell to equilibrate its ATP stores.

The FAO inhibitor, Etomoxir, acts specifically through CPT1 inhibition and indirectly on CPT2, as CPT2 functions downstream of CPT1[222]. In addition, many other binding partners of CDCP1 determined by MS are active in the mitochondria and represent additional candidates (Supplemental Table 3.1). Importantly, we have validated the interaction of CDCP1 with another protein identified by MS (Supplemental Table 3.1), CPT2, as well as ACSL family enzymes. Though we have demonstrated that CDCP1 reduces ACSL activity, we have yet to determine the consequence of the CDCP1-CPT2 interaction. We initially analyzed both tyrosine and serine/threonine phosphorylation of CPT2 and found no difference in phosphorylation in the presence of CDCP1, PKCδ, and Src. There is a well-established assay to measure CPT1 activity[223, 224] in live cells using acyl-CoA, radiolabeled carnitine, and ATP. Theoretically, we should be able to use radiolabeled acyl-carnitine, CoA, and ATP to analyze CPT2 activity in live cells by scintillation counting. This will need to be further investigated.

Our findings that CDCP1 interacts with both ACSL family members and CPT2 supports the hypothesis that ACSL and CPT act antagonistically in the same pathway.

Accordingly, CDCP1 knockdown inhibits the CPT1/CPT2 pathway, stalling transport of acyl-CoAs (generated by ACSLs) to mitochondria for FAO. In order to compensate for decreased FAO, CDCP1 knockdown stimulates ACSL activity to produce more acyl-CoAs to fuel FAO. Since CPT1 cannot convert acyl-CoAs to acyl-carnitines, diacylglycerol acyltransferase (DGAT) and other enzymes involved in lipid anabolism direct the acyl-CoAs into LDs for storage. As a result, inhibition of CPT1/CPT2 pathway favors lipid storage. It will be important to more fully understand the interplay between these proteins and the result of dysregulating this axis on not just cancer, but normal tissue function.

Though not on the MS list of CDCP1 binding partners, PLIN proteins[225], and PLIN5 in particular, have been demonstrated to be important for the LD:mitochondria[226] interaction, and their interplay with CDCP1 deserves investigation. While it is possible that CDCP1 directly regulates lipid transport into the mitochondria by inducing transport of lipid from the LD into the mitochondria[227], it may also regulate LD-mitochondrial interactions indirectly by inhibiting interactions of the LDs with other organelles to indirectly promote LD-mitochondria interactions[228]. Further studies will be important to uncover the other molecular targets of CDCP1 to complete the picture of CDCP1's regulation of lipid metabolism.

Finally, it will be necessary to determine the location of the interaction between CDCP1 and these lipid metabolic proteins as the fate of the products of ACSLs and FAO are heavily dependent on the localized regulation. For example, acetyl-CoA has been demonstrated to stimulate TCA cycle[229] and drive NADPH production[230] to ameliorate ROS production[231]; drive biosynthetic pathways of fatty acids, sterols, ketone bodies, amino acids, and nucleotides[232]; and promote histone, enzyme, and protein

acetylation[233]. Hypothetically, if CDCP1 interacts with ACSLs or CPTs at the mitochondrial membrane then knockdown of CDCP1 may not only reduce accumulation of lipids within the mitochrondia (as demonstrated in Figure 3.6) but may also reduce localized pressure to shuttle FAO produced acetyl-CoA into TCA and instead allow it to be used for lipid anabolism. In order to determine the fate of acetyl-CoA in the context of CDCP1 regulation, we could treat shScramble control and shCDCP1 cells with [^{14} C]-Acetate. We could then analyze incorporation of radioactive acetate into lipids (anabolic) and histones following Comerford et al. 2014[233] and incorporation into TCA intermediates (catabolic) following Mashimo et al. 2014[229].

The knowledge that CDPC1 interacts with itself and other proteins is important for therapeutic development, but these findings also underscore the need to more fully understand the structure of CDCP1 and which domains are relevant to CDCP1 homo- and hetero-interactions. The main questions of Chapter 4 were: 1) What is the effect of individual CUB domains on cCDCP1-dimerization and MDA-MB-231 invasiveness? 2) Can we computationally model CUB2 based on homology sequences? 3) Can we determine residues important for cCDCP1 dimerization using our 3D model in docking simulations? We successfully created a model of the CUB2 domain and simulated a docking interface between two CUB2 domains. Using this information, we identified and validated residue R5 as potentially important for CDCP1 dimerization.

Simulations and computational models are only as good as the datasets they draw from, and in this case, our structural model fell short of what would be considered an optimal structure. Nonetheless we moved forward and were able to show making the R5A and HRVHK-AAGAA mutations had the desired effect. A more direct approach will

be necessary to fully understand CDCP1's biophysical properties, and therefore we are working towards solving the crystal structure of CDCP1. Currently, we are in collaboration with Dr. Tom Poulos' lab to express, purify, and solve the crystal Structure of ECC. This will give us insight into the domain structure, orientation of interactions with itself, and the residues present in the protein-interaction interfaces.

In addition to structural studies, the purified ECC, as well as CUB2 and CUB3 could be used to treat TNBC tumors *in vivo*. It will be very exciting to learn about the bioavailability, tolerance, efficacy, and pharmacokinetics of the purified proteins on the tumors when introduced via intraperitoneal injection. Preliminary studies using a His-tag to purify ECC demonstrated that Nickel resin could pull down the protein. However, the purification was subpar and the concentration remained very low. This study will offer potentially new treatments for TNBC, however it is still in the early stages.

We demonstrated in Chapter 2 that CDCP1 is instrumental in driving migration and in Chapter 3 we further demonstrate that cCDCP1 dimerization is important for metastasis of TNBC. In Chapter 5, we sought to develop a surrogate biomarker of cCDPC1 activity (dimerization) in TNBC. This study is relevant to diagnosis and prognosis of TNBC. Therefore, developing a diagnostic biomarker is of extreme interest. We first demonstrated that we could analyze CDCP1 cleavage in FFPE tissue by Western blot. We were able to expand the protocol to FFPE tissue section for IHC and found that the antibody against phospho-PKCδ Y311 is reliable. We were not able to show a correlation between CDCP1 cleavage and PKCδ phosphorylation, however, we are actively pursuing methods to more directly address our hypothesis in the future.

As mentioned in the discussion of Chapter 5, we will need to control for tissue sample preparation and age. However, these preliminary studies open up interest in the use of this biomarker not just in TNBC but in other forms of cancer too and potentially in other pathological diseases. We hypothesize that if flCDCP1 or cCDCP1 homo-dimerize in normal tissue, this supports healthy tissue function. Once, a driver mutation occurs in these cells, however, the CDCP1 signaling pathway works to promote cancer progression and migration. It will be important to assess the status of CDCP1 dimerization across cancer lines as well as in normal tissue to either prove or disprove this hypothesis.

We discovered in Chapter 3 that CDCP1 regulates lipid metabolism in cancer cell lines. The next logical question becomes: Does CDCP1 regulate lipid metabolism in a physiological setting? In Chapter 6 we analyzed the role of CDCP1 in the liver and in the context of wound healing. Using the CDCP1 KO mice we developed, we found that KO mice, as expected, had higher lipid content when compared to their Het counterparts. Interestingly, we observed the KO mice also had an impaired ability to heal dermal wounds during the first week of the healing process.

This mouse strain will also potentially be useful as a model for liver disorders. Further characterization of the CDCP1 KO mice is necessary to determine their pre-diabetic state. The evidence that CDCP1 KO mice have higher liver lipid content begs the question of whether these mice would be at higher risk of developing liver cancer, as non-alcoholic fatty liver disease is the leading cause of hepatocellular carcinoma[234]. Many methods could be used to test this hypothesis (discussed by Caviglia and Schwabe[235]). One of these methods involves chemically wounding the liver to induce carcinogenesis

with carbon tetrachloride in the presence of the mutagen, diethylnitrosamine. This method may be the best route for our mice as they are on a mixed background with a fully intact immune system.

We hypothesize that CDCP1 KO mice will be more prone to developing liver tumors, which may grow faster than those that develop in CDCP1 Het mice. However, because CDCP1 is absent in CDCP1 KO mice, we do not hypothesize that these tumors will effectively metastasize but will rather kill the animal by disrupting liver function faster than CDCP1 Het liver tumors.

Closing Statement. We have demonstrated the wide range of roles that CDCP1 plays under a variety of physiological stressors; cancer, liver disease, and wound healing. Our studies add to the growing body of work on the importance of CDCP1 in driving tumor pathogenesis and wound healing, and offers a new paradigm for CDCP1's role as a regulator of metabolism in cancer and the liver. We have also paved the way for further investigation into the structure of CDCP1 and the use of its activated downstream target, phospho-PKCδ, as a surrogate biomarker of disease- and distant disease-free survival in breast cancer patients. Combined, these studies offer a comprehensive look into the previously unknown multi-functional capacities of the highly intriguing membrane protein, CDCP1. We are excited to see further development of the field of CDCP1 research.

REFERENCES

1. Scherl-Mostageer M, Sommergruber W, Abseher R, Hauptmann R, Ambros P, Schweifer N. Identification of a novel gene, CDCP1, overexpressed in human colorectal cancer. Oncogene 2001; 20:4402-8.
2. Hooper JD, Zijlstra A, Aimes RT, Liang H, Claassen GF, Tarin D, Testa JE, Quigley JP. Subtractive immunization using highly metastatic human tumor cells identifies SIMA135/CDCP1, a 135 kDa cell surface phosphorylated glycoprotein antigen. Oncogene 2003; 22:1783-94.
3. Wortmann A, He Y, Deryugina EI, Quigley JP, Hooper JD. The cell surface glycoprotein CDCP1 in cancer--insights, opportunities, and challenges. IUBMB Life 2009; 61:723-30.
4. Ng D, Pitcher GM, Szilard RK, Sertié A, Kanisek M, Clapcote SJ, Lipina T, Kalia LV, Joo D, McKerlie C, et al. Neto1 is a novel CUB-domain NMDA receptor-interacting protein required for synaptic plasticity and learning. PLoS Biol 2009; 7:e41.
5. Wright HJ, Arulmoli J, Motazedi M, Nelson LJ, Heinemann FS, Flanagan LA, Razorenova OV. CDCP1 cleavage is necessary for homodimerization-induced migration of triple-negative breast cancer. Oncogene 2016; 35:4762-72.
6. Feinberg H, Uitdehaag JC, Davies JM, Wallis R, Drickamer K, Weis WI. Crystal structure of the CUB1-EGF-CUB2 region of mannose-binding protein associated serine protease-2. EMBO J 2003; 22:2348-59.
7. Bork P, Beckmann G. The CUB domain. A widespread module in developmentally regulated proteins. J Mol Biol 1993; 231:539-45.
8. Brown TA, Yang TM, Zaitsevskaia T, Xia Y, Dunn CA, Sigle RO, Knudsen B, Carter WG. Adhesion or plasmin regulates tyrosine phosphorylation of a novel membrane glycoprotein p80/gp140/CUB domain-containing protein 1 in epithelia. J Biol Chem 2004; 279:14772-83.
9. He Y, Wortmann A, Burke LJ, Reid JC, Adams MN, Abdul-Jabbar I, Quigley JP, Leduc R, Kirchhofer D, Hooper JD. Proteolysis-induced N-terminal ectodomain shedding of the integral membrane glycoprotein CUB domain-containing protein 1 (CDCP1) is accompanied by tyrosine phosphorylation of its C-terminal domain and recruitment of Src and PKCdelta. J Biol Chem 2010; 285:26162-73.
10. Zarif JC, Lamb LE, Schulz VV, Nollet EA, Miranti CK. Androgen receptor non-nuclear regulation of prostate cancer cell invasion mediated by Src and matriptase. Oncotarget 2015; 6:6862-76.
11. Bhatt AS, Erdjument-Bromage H, Tempst P, Craik CS, Moasser MM. Adhesion signaling by a novel mitotic substrate of src kinases. Oncogene 2005; 24:5333-43.
12. Lin CY, Chen HJ, Huang CC, Lai LC, Lu TP, Tseng GC, Kuo TT, Kuok QY, Hsu JL, Sung SY, et al. ADAM9 promotes lung cancer metastases to brain by a plasminogen activator-based pathway. Cancer Res 2014; 74:5229-43.
13. Casar B, Rimann I, Kato H, Shattil SJ, Quigley JP, Deryugina EI. In vivo cleaved CDCP1 promotes early tumor dissemination via complexing with activated β1 integrin and induction of FAK/PI3K/Akt motility signaling. Oncogene 2014; 33:255-68.
14. Alajati A, Guccini I, Pinton S, Garcia-Escudero R, Bernasocchi T, Sarti M, Montani E, Rinaldi A, Montemurro F, Catapano C, et al. Interaction of CDCP1 with HER2

Enhances HER2-Driven Tumorigenesis and Promotes Trastuzumab Resistance in Breast Cancer. Cell Rep 2015; 11:564-76.
15. Benes CH, Poulogiannis G, Cantley LC, Soltoff SP. The SRC-associated protein CUB Domain-Containing Protein-1 regulates adhesion and motility. 2011.
16. Kollmorgen G, Bossenmaier B, Niederfellner G, Häring HU, Lammers R. Structural requirements for cub domain containing protein 1 (CDCP1) and Src dependent cell transformation. PLoS One 2012; 7:e53050.
17. Razorenova OV, Finger EC, Colavitti R, Chernikova SB, Boiko AD, Chan CK, Krieg A, Bedogni B, LaGory E, Weissman IL, et al. VHL loss in renal cell carcinoma leads to up-regulation of CUB domain-containing protein 1 to stimulate PKC{delta}-driven migration. Proc Natl Acad Sci U S A 2011; 108:1931-6.
18. Spassov DS, Ahuja D, Wong CH, Moasser MM. The structural features of Trask that mediate its anti-adhesive functions. PLoS One 2011; 6:e19154.
19. Benes CH, Wu N, Elia AE, Dharia T, Cantley LC, Soltoff SP. The C2 domain of PKCdelta is a phosphotyrosine binding domain. Cell 2005; 121:271-80.
20. Emerling BM, Benes CH, Poulogiannis G, Bell EL, Courtney K, Liu H, Choo-Wing R, Bellinger G, Tsukazawa KS, Brown V, et al. Identification of CDCP1 as a hypoxia-inducible factor 2α (HIF-2α) target gene that is associated with survival in clear cell renal cell carcinoma patients. Proc Natl Acad Sci U S A 2013; 110:3483-8.
21. Uekita T, Fujii S, Miyazawa Y, Iwakawa R, Narisawa-Saito M, Nakashima K, Tsuta K, Tsuda H, Kiyono T, Yokota J, et al. Oncogenic Ras/ERK Signaling Activates CDCP1 to Promote Tumor Invasion and Metastasis. Mol Cancer Res 2014.
22. Chiu KL, Kuo TT, Kuok QY, Lin YS, Hua CH, Lin CY, Su PY, Lai LC, Sher YP. ADAM9 enhances CDCP1 protein expression by suppressing miR-218 for lung tumor metastasis. Sci Rep 2015; 5:16426.
23. Bonuccelli G, Casimiro MC, Sotgia F, Wang C, Liu M, Katiyar S, Zhou J, Dew E, Capozza F, Daumer KM, et al. Caveolin-1 (P132L), a common breast cancer mutation, confers mammary cell invasiveness and defines a novel stem cell/metastasis-associated gene signature. Am J Pathol 2009; 174:1650-62.
24. Adams MN, Harrington BS, He Y, Davies CM, Wallace SJ, Chetty NP, Crandon AJ, Oliveira NB, Shannon CM, Coward JI, et al. EGF inhibits constitutive internalization and palmitoylation-dependent degradation of membrane-spanning procancer CDCP1 promoting its availability on the cell surface. Oncogene 2015; 34:1375-83.
25. Park JJ, Jin YB, Lee YJ, Lee JS, Lee YS, Ko YG, Lee M. KAI1 suppresses HIF-1α and VEGF expression by blocking CDCP1-enhanced Src activation in prostate cancer. BMC Cancer 2012; 12:81.
26. Hu Y, Tang Z, Jiang B, Chen J, Fu Z. miR-198 functions as a tumor suppressor in breast cancer by targeting CUB domain-containing protein 1. Oncol Lett 2017; 13:1753-60.
27. Iwata M, Torok-Storb B, Wayner EA, Carter WG. CDCP1 Identifies a CD146 Negative Subset of Marrow Fibroblasts Involved with Cytokine Production. PLoS One 2014; 9:e109304.
28. Casar B, He Y, Iconomou M, Hooper JD, Quigley JP, Deryugina EI. Blocking of CDCP1 cleavage in vivo prevents Akt-dependent survival and inhibits metastatic colonization through PARP1-mediated apoptosis of cancer cells. Oncogene 2012; 31:3924-38.

29. Miyazawa Y, Uekita T, Ito Y, Seiki M, Yamaguchi H, Sakai R. CDCP1 regulates the function of MT1-MMP and invadopodia-mediated invasion of cancer cells. Mol Cancer Res 2013; 11:628-37.
30. Law ME, Corsino PE, Jahn SC, Davis BJ, Chen S, Patel B, Pham K, Lu J, Sheppard B, Nørgaard P, et al. Glucocorticoids and histone deacetylase inhibitors cooperate to block the invasiveness of basal-like breast cancer cells through novel mechanisms. Oncogene 2013; 32:1316-29.
31. Uekita T, Fujii S, Miyazawa Y, Hashiguchi A, Abe H, Sakamoto M, Sakai R. Suppression of autophagy by CUB domain-containing protein 1 signaling is essential for anchorage-independent survival of lung cancer cells. Cancer Sci 2013; 104:865-70.
32. McGovern JA, Heinemann JR, Burke LJ, Dawson R, Parker TJ, Upton Z, Hooper JD, Manton KJ. Stratum basale keratinocyte expression of the cell-surface glycoprotein CDCP1 during epidermogenesis and its role in keratinocyte migration. Br J Dermatol 2013; 168:496-503.
33. Larsson A, Carlsson L, Gordh T, Lind AL, Thulin M, Kamali-Moghaddam M. The effects of age and gender on plasma levels of 63 cytokines. J Immunol Methods 2015; 425:58-61.
34. Bühring HJ, Kuçi S, Conze T, Rathke G, Bartolović K, Grünebach F, Scherl-Mostageer M, Brümmendorf TH, Schweifer N, Lammers R. CDCP1 identifies a broad spectrum of normal and malignant stem/progenitor cell subsets of hematopoietic and nonhematopoietic origin. Stem Cells 2004; 22:334-43.
35. Kimura H, Morii E, Ikeda JI, Ezoe S, Xu JX, Nakamichi N, Tomita Y, Shibayama H, Kanakura Y, Aozasa K. Role of DNA methylation for expression of novel stem cell marker CDCP1 in hematopoietic cells. Leukemia 2006; 20:1551-6.
36. Shia WC, Ku TH, Tsao YM, Hsia CH, Chang YM, Huang CH, Chung YC, Hsu SL, Liang KW, Hsu FR. Genetic copy number variants in myocardial infarction patients with hyperlipidemia. BMC Genomics 2011; 12 Suppl 3:S23.
37. Spassov DS, Wong CH, Harris G, McDonough S, Phojanakong P, Wang D, Hann B, Bazarov AV, Yaswen P, Khanafshar E, et al. A tumor-suppressing function in the epithelial adhesion protein Trask. Oncogene 2012; 31:419-31.
38. Spassov DS, Wong CH, Wong SY, Reiter JF, Moasser MM. Trask loss enhances tumorigenic growth by liberating integrin signaling and growth factor receptor cross-talk in unanchored cells. Cancer Res 2013; 73:1168-79.
39. Perry SE, Robinson P, Melcher A, Quirke P, Bühring HJ, Cook GP, Blair GE. Expression of the CUB domain containing protein 1 (CDCP1) gene in colorectal tumour cells. FEBS Lett 2007; 581:1137-42.
40. Ikeda J, Oda T, Inoue M, Uekita T, Sakai R, Okumura M, Aozasa K, Morii E. Expression of CUB domain containing protein (CDCP1) is correlated with prognosis and survival of patients with adenocarcinoma of lung. Cancer Sci 2009; 100:429-33.
41. Siva AC, Wild MA, Kirkland RE, Nolan MJ, Lin B, Maruyama T, Yantiri-Wernimont F, Frederickson S, Bowdish KS, Xin H. Targeting CUB domain-containing protein 1 with a monoclonal antibody inhibits metastasis in a prostate cancer model. Cancer Res 2008; 68:3759-66.
42. He Y, Wu AC, Harrington BS, Davies CM, Wallace SJ, Adams MN, Palmer JS, Roche DK, Hollier BG, Westbrook TF, et al. Elevated CDCP1 predicts poor patient

outcome and mediates ovarian clear cell carcinoma by promoting tumor spheroid formation, cell migration and chemoresistance. Oncogene 2015.
43. Miura S, Hamada S, Masamune A, Satoh K, Shimosegawa T. CUB-domain containing protein 1 represses the epithelial phenotype of pancreatic cancer cells. Exp Cell Res 2014; 321:209-18.
44. Miyazawa Y, Uekita T, Hiraoka N, Fujii S, Kosuge T, Kanai Y, Nojima Y, Sakai R. CUB domain-containing protein 1, a prognostic factor for human pancreatic cancers, promotes cell migration and extracellular matrix degradation. Cancer Res 2010; 70:5136-46.
45. Mamat S, Ikeda J, Enomoto T, Ueda Y, Rahadiani N, Tian T, Wang Y, Qiu Y, Kimura T, Aozasa K, et al. Prognostic significance of CUB domain containing protein expression in endometrioid adenocarcinoma. Oncol Rep 2010; 23:1221-7.
46. Uekita T, Tanaka M, Takigahira M, Miyazawa Y, Nakanishi Y, Kanai Y, Yanagihara K, Sakai R. CUB-domain-containing protein 1 regulates peritoneal dissemination of gastric scirrhous carcinoma. Am J Pathol 2008; 172:1729-39.
47. Liu H, Ong SE, Badu-Nkansah K, Schindler J, White FM, Hynes RO. CUB-domain-containing protein 1 (CDCP1) activates Src to promote melanoma metastasis. Proc Natl Acad Sci U S A 2011; 108:1379-84.
48. Leroy C, Shen Q, Strande V, Meyer R, McLaughlin ME, Lezan E, Bentires-Alj M, Voshol H, Bonenfant D, Alex Gaither L. CUB-domain-containing protein 1 overexpression in solid cancers promotes cancer cell growth by activating Src family kinases. Oncogene 2015.
49. Uekita T, Jia L, Narisawa-Saito M, Yokota J, Kiyono T, Sakai R. CUB domain-containing protein 1 is a novel regulator of anoikis resistance in lung adenocarcinoma. Mol Cell Biol 2007; 27:7649-60.
50. Orchard-Webb DJ, Lee TC, Cook GP, Blair GE. CUB Domain Containing Protein 1 (CDCP1) modulates adhesion and motility in colon cancer cells. BMC Cancer 2014; 14:754.
51. Chou CT, Li YJ, Chang CC, Yang CN, Li PS, Jeng YM, Chen ST, Kuo ML, Lin IC, Lin BR. Prognostic Significance of CDCP1 Expression in Colorectal Cancer and Effect of Its Inhibition on Invasion and Migration. Ann Surg Oncol 2015; 22:4335-43.
52. Deryugina EI, Conn EM, Wortmann A, Partridge JJ, Kupriyanova TA, Ardi VC, Hooper JD, Quigley JP. Functional role of cell surface CUB domain-containing protein 1 in tumor cell dissemination. Mol Cancer Res 2009; 7:1197-211.
53. Gao W, Chen L, Ma Z, Du Z, Zhao Z, Hu Z, Li Q. Isolation and phenotypic characterization of colorectal cancer stem cells with organ-specific metastatic potential. Gastroenterology 2013; 145:636-46.e5.
54. Kollmorgen G, Niederfellner G, Lifke A, Spohn GJ, Rieder N, Harring SV, Bauss F, Burtscher H, Lammers R, Bossenmaier B. Antibody mediated CDCP1 degradation as mode of action for cancer targeted therapy. Mol Oncol 2013; 7:1142-51.
55. Rampurwala M, Wisinski KB, O'Regan R. Role of the androgen receptor in triple-negative breast cancer. Clin Adv Hematol Oncol 2016; 14:186-93.
56. Singh J, Novik Y, Stein S, Volm M, Meyers M, Smith J, Omene C, Speyer J, Schneider R, Jhaveri K, et al. Phase 2 trial of everolimus and carboplatin combination in patients with triple negative metastatic breast cancer. Breast Cancer Res 2014; 16:R32.

57. Gonzalez-Angulo AM, Akcakanat A, Liu S, Green MC, Murray JL, Chen H, Palla SL, Koenig KB, Brewster AM, Valero V, et al. Open-label randomized clinical trial of standard neoadjuvant chemotherapy with paclitaxel followed by FEC versus the combination of paclitaxel and everolimus followed by FEC in women with triple receptor-negative breast cancer†. Ann Oncol 2014; 25:1122-7.
58. Gucalp A, Tolaney S, Isakoff SJ, Ingle JN, Liu MC, Carey LA, Blackwell K, Rugo H, Nabell L, Forero A, et al. Phase II trial of bicalutamide in patients with androgen receptor-positive, estrogen receptor-negative metastatic Breast Cancer. Clin Cancer Res 2013; 19:5505-12.
59. Traina T, Miller K, Yardley D, O'Shaughnessy J, Cortes J, Awada A, Kelly CM, Trudeau ME, Schmid P, Gianni L, et al. Results from a phase 2 study of enzalutamide (enza), an androgen receptor (AR) inhibitor, in advanced AR+ triple-negative breast cancer. [ASCO abstract 1003]. J Clin Oncol, 2015.
60. Cameron D, Brown J, Dent R, Jackisch C, Mackey J, Pivot X, Steger GG, Suter TM, Toi M, Parmar M, et al. Adjuvant bevacizumab-containing therapy in triple-negative breast cancer (BEATRICE): primary results of a randomised, phase 3 trial. Lancet Oncol 2013; 14:933-42.
61. Nakai K, Hung MC, Yamaguchi H. A perspective on anti-EGFR therapies targeting triple-negative breast cancer. Am J Cancer Res 2016; 6:1609-23.
62. Shu S, Lin CY, He HH, Witwicki RM, Tabassum DP, Roberts JM, Janiszewska M, Huh SJ, Liang Y, Ryan J, et al. Response and resistance to BET bromodomain inhibitors in triple-negative breast cancer. Nature 2016; 529:413-7.
63. Le Du F, Eckhardt BL, Lim B, Litton JK, Moulder S, Meric-Bernstam F, Gonzalez-Angulo AM, Ueno NT. Is the future of personalized therapy in triple-negative breast cancer based on molecular subtype? Oncotarget 2015; 6:12890-908.
64. Uekita T, Sakai R. Roles of CUB domain-containing protein 1 signaling in cancer invasion and metastasis. Cancer Sci 2011; 102:1943-8.
65. Lounnas V, Ritschel T, Kelder J, McGuire R, Bywater RP, Foloppe N. Current progress in Structure-Based Rational Drug Design marks a new mindset in drug discovery. Comput Struct Biotechnol J 2013; 5:e201302011.
66. Anderson AC. The process of structure-based drug design. Chem Biol 2003; 10:787-97.
67. Turdo F, Bianchi F, Gasparini P, Sandri M, Sasso M, De Cecco L, Forte L, Casalini P, Aiello P, Sfondrini L, et al. CDCP1 is a novel marker of the most aggressive human triple-negative breast cancers. Oncotarget 2016.
68. Hou J, Wright HJ, Chan N, Tran R, Razorenova OV, Potma EO, Tromberg BJ. Correlating two-photon excited fluorescence imaging of breast cancer cellular redox state with seahorse flux analysis of normalized cellular oxygen consumption. J Biomed Opt 2016; 21:60503.
69. Wilson KE, Bachawal SV, Tian L, Willmann JK. Multiparametric spectroscopic photoacoustic imaging of breast cancer development in a transgenic mouse model. Theranostics 2014; 4:1062-71.
70. Uray IP, Rodenberg JM, Bissonnette RP, Brown PH, Mancini MA. Cancer-preventive rexinoid modulates neutral lipid contents of mammary epithelial cells through a peroxisome proliferator-activated receptor γ-dependent mechanism. Mol Pharmacol 2012; 81:228-38.

71. Park JH, Vithayathil S, Kumar S, Sung PL, Dobrolecki LE, Putluri V, Bhat VB, Bhowmik SK, Gupta V, Arora K, et al. Fatty Acid Oxidation-Driven Src Links Mitochondrial Energy Reprogramming and Oncogenic Properties in Triple-Negative Breast Cancer. Cell Rep 2016; 14:2154-65.
72. Camarda R, Zhou AY, Kohnz RA, Balakrishnan S, Mahieu C, Anderton B, Eyob H, Kajimura S, Tward A, Krings G, et al. Inhibition of fatty acid oxidation as a therapy for MYC-overexpressing triple-negative breast cancer. Nat Med 2016; 22:427-32.
73. Zirath H, Frenzel A, Oliynyk G, Segerström L, Westermark UK, Larsson K, Munksgaard Persson M, Hultenby K, Lehtiö J, Einvik C, et al. MYC inhibition induces metabolic changes leading to accumulation of lipid droplets in tumor cells. Proc Natl Acad Sci U S A 2013; 110:10258-63.
74. Yue S, Li J, Lee SY, Lee HJ, Shao T, Song B, Cheng L, Masterson TA, Liu X, Ratliff TL, et al. Cholesteryl ester accumulation induced by PTEN loss and PI3K/AKT activation underlies human prostate cancer aggressiveness. Cell Metab 2014; 19:393-406.
75. Guillaumond F, Bidaut G, Ouaissi M, Servais S, Gouirand V, Olivares O, Lac S, Borge L, Roques J, Gayet O, et al. Cholesterol uptake disruption, in association with chemotherapy, is a promising combined metabolic therapy for pancreatic adenocarcinoma. Proc Natl Acad Sci U S A 2015; 112:2473-8.
76. Paget S. The distribution of secondary growths in cancer of the breast. 1889. Cancer Metastasis Rev 1989; 8:98-101.
77. Langley RR, Fidler IJ. The seed and soil hypothesis revisited--the role of tumor-stroma interactions in metastasis to different organs. Int J Cancer 2011; 128:2527-35.
78. Valastyan S, Weinberg RA. Tumor metastasis: molecular insights and evolving paradigms. Cell 2011; 147:275-92.
79. Chaudary N, Hill RP. Hypoxia and metastasis in breast cancer. Breast Dis 2006; 26:55-64.
80. Gupta GP, Massagué J. Cancer metastasis: building a framework. Cell 2006; 127:679-95.
81. Joyce JA, Pollard JW. Microenvironmental regulation of metastasis. Nat Rev Cancer 2009; 9:239-52.
82. Chaffer CL, Weinberg RA. A perspective on cancer cell metastasis. Science 2011; 331:1559-64.
83. Hanahan D, Weinberg RA. Hallmarks of cancer: the next generation. Cell 2011; 144:646-74.
84. Vanharanta S, Massagué J. Origins of metastatic traits. Cancer Cell 2013; 24:410-21.
85. Alderton GK. Metastasis: Metabolic reprogramming in disseminated cells. Nat Rev Cancer 2014; 14:703.
86. Sulzmaier FJ, Jean C, Schlaepfer DD. FAK in cancer: mechanistic findings and clinical applications. Nat Rev Cancer 2014; 14:598-610.
87. Reddy KB, Nabha SM, Atanaskova N. Role of MAP kinase in tumor progression and invasion. Cancer Metastasis Rev 2003; 22:395-403.
88. Desgrosellier JS, Cheresh DA. Integrins in cancer: biological implications and therapeutic opportunities. Nat Rev Cancer 2010; 10:9-22.

89. Nguyen A, Yoshida M, Goodarzi H, Tavazoie SF. Highly variable cancer subpopulations that exhibit enhanced transcriptome variability and metastatic fitness. Nat Commun 2016; 7:11246.
90. Gilkes DM, Semenza GL, Wirtz D. Hypoxia and the extracellular matrix: drivers of tumour metastasis. Nat Rev Cancer 2014; 14:430-9.
91. Quail DF, Joyce JA. Microenvironmental regulation of tumor progression and metastasis. Nat Med 2013; 19:1423-37.
92. Kalluri R. The biology and function of fibroblasts in cancer. Nat Rev Cancer 2016; 16:582-98.
93. Ying H, Kimmelman AC, Lyssiotis CA, Hua S, Chu GC, Fletcher-Sananikone E, Locasale JW, Son J, Zhang H, Coloff JL, et al. Oncogenic Kras maintains pancreatic tumors through regulation of anabolic glucose metabolism. Cell 2012; 149:656-70.
94. Nimptsch K, Pischon T. Body fatness, related biomarkers and cancer risk: an epidemiological perspective. Horm Mol Biol Clin Investig 2015; 22:39-51.
95. Usui ML, Mansbridge JN, Carter WG, Fujita M, Olerud JE. Keratinocyte migration, proliferation, and differentiation in chronic ulcers from patients with diabetes and normal wounds. J Histochem Cytochem 2008; 56:687-96.
96. Metzger-Filho O, Tutt A, de Azambuja E, Saini KS, Viale G, Loi S, Bradbury I, Bliss JM, Azim HA, Ellis P, et al. Dissecting the heterogeneity of triple-negative breast cancer. J Clin Oncol 2012; 30:1879-87.
97. Wortmann A, He Y, Christensen ME, Linn M, Lumley JW, Pollock PM, Waterhouse NJ, Hooper JD. Cellular settings mediating Src Substrate switching between focal adhesion kinase tyrosine 861 and CUB-domain-containing protein 1 (CDCP1) tyrosine 734. J Biol Chem 2011; 286:42303-15.
98. Spassov DS, Wong CH, Sergina N, Ahuja D, Fried M, Sheppard D, Moasser MM. Phosphorylation of Trask by Src kinases inhibits integrin clustering and functions in exclusion with focal adhesion signaling. Mol Cell Biol 2011; 31:766-82.
99. Huang C, Jacobson K, Schaller MD. MAP kinases and cell migration. J Cell Sci 2004; 117:4619-28.
100. Romero A, Varela PF, Sanz L, Töpfer-Petersen E, Calvete JJ. Crystallization and preliminary X-ray diffraction analysis of boar seminal plasma spermadhesin PSP-I/PSP-II, a heterodimer of two CUB domains. FEBS Lett 1996; 382:15-7.
101. Lee HX, Mendes FA, Plouhinec JL, De Robertis EM. Enzymatic regulation of pattern: BMP4 binds CUB domains of Tolloids and inhibits proteinase activity. Genes Dev 2009; 23:2551-62.
102. Gandji LY, Proust R, Larue L, Gesbert F. The tyrosine phosphatase SHP2 associates with CUB domain-containing protein-1 (CDCP1), regulating its expression at the cell surface in a phosphorylation-dependent manner. PLoS One 2015; 10:e0123472.
103. Choi CY, Chan DA, Paulmurugan R, Sutphin PD, Le QT, Koong AC, Zundel W, Gambhir SS, Giaccia AJ. Molecular imaging of hypoxia-inducible factor 1 alpha and von Hippel-Lindau interaction in mice. Mol Imaging 2008; 7:139-46.
104. Cvetković D, Goertzen CG, Bhattacharya M. Quantification of breast cancer cell invasiveness using a three-dimensional (3D) model. J Vis Exp 2014.
105. Guiro K, Patel SA, Greco SJ, Rameshwar P, Arinzeh TL. Investigating breast cancer cell behavior using tissue engineering scaffolds. PLoS One 2015; 10:e0118724.

106. Tu YF, Kaipparettu BA, Ma Y, Wong LJ. Mitochondria of highly metastatic breast cancer cell line MDA-MB-231 exhibits increased autophagic properties. Biochim Biophys Acta 2011; 1807:1125-32.
107. Arora R, Yates C, Gary BD, McClellan S, Tan M, Xi Y, Reed E, Piazza GA, Owen LB, Dean-Colomb W. Panepoxydone targets NF-kB and FOXM1 to inhibit proliferation, induce apoptosis and reverse epithelial to mesenchymal transition in breast cancer. PLoS One 2014; 9:e98370.
108. Seidel J, Kunc K, Possinger K, Jehn C, Lüftner D. Effect of the tyrosine kinase inhibitor lapatinib on CUB-domain containing protein (CDCP1)-mediated breast cancer cell survival and migration. Biochem Biophys Res Commun 2011; 414:226-32.
109. Sandercock AM, Rust S, Guillard S, Sachsenmeier KF, Holoweckyj N, Hay C, Flynn M, Huang Q, Yan K, Herpers B, et al. Identification of anti-tumour biologics using primary tumour models, 3-D phenotypic screening and image-based multi-parametric profiling. Mol Cancer 2015; 14:147.
110. Qiu B, Ackerman D, Sanchez DJ, Li B, Ochocki JD, Grazioli A, Bobrovnikova-Marjon E, Diehl JA, Keith B, Simon MC. HIF2α-Dependent Lipid Storage Promotes Endoplasmic Reticulum Homeostasis in Clear-Cell Renal Cell Carcinoma. Cancer Discov 2015; 5:652-67.
111. Nieva C, Marro M, Santana-Codina N, Rao S, Petrov D, Sierra A. The lipid phenotype of breast cancer cells characterized by Raman microspectroscopy: towards a stratification of malignancy. PLoS One 2012; 7:e46456.
112. Kim S, Lee Y, Koo JS. Differential expression of lipid metabolism-related proteins in different breast cancer subtypes. PLoS One 2015; 10:e0119473.
113. Zhau HE, He H, Wang CY, Zayzafoon M, Morrissey C, Vessella RL, Marshall FF, Chung LW, Wang R. Human prostate cancer harbors the stem cell properties of bone marrow mesenchymal stem cells. Clin Cancer Res 2011; 17:2159-69.
114. Kim KH, Lee GY, Kim JI, Ham M, Won Lee J, Kim JB. Inhibitory effect of LXR activation on cell proliferation and cell cycle progression through lipogenic activity. J Lipid Res 2010; 51:3425-33.
115. Sowter HM, Raval RR, Moore JW, Ratcliffe PJ, Harris AL. Predominant role of hypoxia-inducible transcription factor (Hif)-1alpha versus Hif-2alpha in regulation of the transcriptional response to hypoxia. Cancer Res 2003; 63:6130-4.
116. Razorenova OV, Castellini L, Colavitti R, Edgington LE, Nicolau M, Huang X, Bedogni B, Mills EM, Bogyo M, Giaccia AJ. The apoptosis repressor with a CARD domain (ARC) gene is a direct hypoxia-inducible factor 1 target gene and promotes survival and proliferation of VHL-deficient renal cancer cells. Mol Cell Biol 2014; 34:739-51.
117. Razorenova OV, Ivanov AV, Budanov AV, Chumakov PM. Virus-based reporter systems for monitoring transcriptional activity of hypoxia-inducible factor 1. Gene 2005; 350:89-98.
118. Miroshnikova YA, Jorgens DM, Spirio L, Auer M, Sarang-Sieminski AL, Weaver VM. Engineering strategies to recapitulate epithelial morphogenesis within synthetic three-dimensional extracellular matrix with tunable mechanical properties. Phys Biol 2011; 8:026013.
119. Maller O, Hansen KC, Lyons TR, Acerbi I, Weaver VM, Prekeris R, Tan AC, Schedin P. Collagen architecture in pregnancy-induced protection from breast cancer. J Cell Sci 2013; 126:4108-10.

120. Vlad C, Kubelac P, Onisim A, Irimie A, Achimas-Cadariu P. The role of CDCP1 (CUB domain-containing protein 1) and ADAM12 (a disintegrin and metalloproteinase 12) in ovarian cancer. J BUON 2015; 20:673-9.
121. Gao W, Chen L, Ma Z, Du Z, Zhao Z, Hu Z, Li Q. Isolation and Phenotypic Characterization of Colorectal Cancer Stem Cells With Organ-Specific Metastatic Potential. Gastroenterology 2013; 145:636-+.
122. Yousef I, Bréard J, SidAhmed-Adrar N, Maâmer-Azzabi A, Marchal C, Dumas P, Le Naour F. Infrared spectral signatures of CDCP1-induced effects in colon carcinoma cells. Analyst 2011; 136:5162-8.
123. Harrington BS, He Y, Davies CM, Wallace SJ, Adams MN, Beaven EA, Roche DK, Kennedy C, Chetty NP, Crandon AJ, et al. Cell line and patient-derived xenograft models reveal elevated CDCP1 as a target in high-grade serous ovarian cancer. Br J Cancer 2016; 114:417-26.
124. Wright HJ, Police AM, Razorenova OV. Targeting CDCP1 dimerization in triple-negative breast cancer. Cell Cycle 2016; 15:2385-6.
125. Baenke F, Peck B, Miess H, Schulze A. Hooked on fat: the role of lipid synthesis in cancer metabolism and tumour development. Dis Model Mech 2013; 6:1353-63.
126. Russell TD, Palmer CA, Orlicky DJ, Fischer A, Rudolph MC, Neville MC, McManaman JL. Cytoplasmic lipid droplet accumulation in developing mammary epithelial cells: roles of adipophilin and lipid metabolism. J Lipid Res 2007; 48:1463-75.
127. Russell TD, Schaack J, Orlicky DJ, Palmer C, Chang BH, Chan L, McManaman JL. Adipophilin regulates maturation of cytoplasmic lipid droplets and alveolae in differentiating mammary glands. J Cell Sci 2011; 124:3247-53.
128. Rudolph MC, McManaman JL, Hunter L, Phang T, Neville MC. Functional development of the mammary gland: use of expression profiling and trajectory clustering to reveal changes in gene expression during pregnancy, lactation, and involution. J Mammary Gland Biol Neoplasia 2003; 8:287-307.
129. Zhang F, Du G. Dysregulated lipid metabolism in cancer. World J Biol Chem 2012; 3:167-74.
130. Grevengoed TJ, Klett EL, Coleman RA. Acyl-CoA metabolism and partitioning. Annu Rev Nutr 2014; 34:1-30.
131. Mashek DG, Li LO, Coleman RA. Long-chain acyl-CoA synthetases and fatty acid channeling. Future Lipidol 2007; 2:465-76.
132. Brasaemle DL, Dolios G, Shapiro L, Wang R. Proteomic analysis of proteins associated with lipid droplets of basal and lipolytically stimulated 3T3-L1 adipocytes. J Biol Chem 2004; 279:46835-42.
133. Poppelreuther M, Rudolph B, Du C, Großmann R, Becker M, Thiele C, Ehehalt R, Füllekrug J. The N-terminal region of acyl-CoA synthetase 3 is essential for both the localization on lipid droplets and the function in fatty acid uptake. J Lipid Res 2012; 53:888-900.
134. Suhalim JL, Parfitt GJ, Xie Y, De Paiva CS, De Pavia CS, Pflugfelder SC, Shah TN, Potma EO, Brown DJ, Jester JV. Effect of desiccating stress on mouse meibomian gland function. Ocul Surf 2014; 12:59-68.
135. Rice WL, Kaplan DL, Georgakoudi I. Two-photon microscopy for non-invasive, quantitative monitoring of stem cell differentiation. PLoS One 2010; 5:e10075.

136. Mandal S, Khan P, Li L, Davie JR. Metabolomics and Transcriptional Responses in Estrogen Receptor Positive Breast Cancer Cells. Breast Cancer - Carcinogenesis, Cell Growth and Signalling Pathways: In Tech, 2011 257-84.
137. Bu SY, Mashek MT, Mashek DG. Suppression of long chain acyl-CoA synthetase 3 decreases hepatic de novo fatty acid synthesis through decreased transcriptional activity. J Biol Chem 2009; 284:30474-83.
138. Zhou Y, Abidi P, Kim A, Chen W, Huang TT, Kraemer FB, Liu J. Transcriptional activation of hepatic ACSL3 and ACSL5 by oncostatin m reduces hypertriglyceridemia through enhanced beta-oxidation. Arterioscler Thromb Vasc Biol 2007; 27:2198-205.
139. Nchoutmboube JA, Viktorova EG, Scott AJ, Ford LA, Pei Z, Watkins PA, Ernst RK, Belov GA. Increased long chain acyl-Coa synthetase activity and fatty acid import is linked to membrane synthesis for development of picornavirus replication organelles. PLoS Pathog 2013; 9:e1003401.
140. Soupene E, Dinh NP, Siliakus M, Kuypers FA. Activity of the acyl-CoA synthetase ACSL6 isoforms: role of the fatty acid Gate-domains. BMC Biochem 2010; 11:18.
141. Ikeda JI, Morii E, Kimura H, Tomita Y, Takakuwa T, Hasegawa JI, Kim YK, Miyoshi Y, Noguchi S, Nishida T, et al. Epigenetic regulation of the expression of the novel stem cell marker CDCP1 in cancer cells. J Pathol 2006; 210:75-84.
142. Kang HM, Ahn SH, Choi P, Ko YA, Han SH, Chinga F, Park AS, Tao J, Sharma K, Pullman J, et al. Defective fatty acid oxidation in renal tubular epithelial cells has a key role in kidney fibrosis development. Nat Med 2015; 21:37-46.
143. Lin H, Patel S, Affleck VS, Wilson I, Turnbull DM, Joshi AR, Maxwell R, Stoll EA. Fatty acid oxidation is required for the respiration and proliferation of malignant glioma cells. Neuro Oncol 2016.
144. LeBleu VS, O'Connell JT, Gonzalez Herrera KN, Wikman H, Pantel K, Haigis MC, de Carvalho FM, Damascena A, Domingos Chinen LT, Rocha RM, et al. PGC-1α mediates mitochondrial biogenesis and oxidative phosphorylation in cancer cells to promote metastasis. Nat Cell Biol 2014; 16:992-1003.
145. Caino MC, Chae YC, Vaira V, Ferrero S, Nosotti M, Martin NM, Weeraratna A, O'Connell M, Jernigan D, Fatatis A, et al. Metabolic stress regulates cytoskeletal dynamics and metastasis of cancer cells. J Clin Invest 2013; 123:2907-20.
146. Rodrigues MF, Obre E, de Melo FH, Santos GC, Galina A, Jasiulionis MG, Rossignol R, Rumjanek FD, Amoêdo ND. Enhanced OXPHOS, glutaminolysis and β-oxidation constitute the metastatic phenotype of melanoma cells. Biochem J 2016; 473:703-15.
147. Rambold AS, Cohen S, Lippincott-Schwartz J. Fatty acid trafficking in starved cells: regulation by lipid droplet lipolysis, autophagy, and mitochondrial fusion dynamics. Dev Cell 2015; 32:678-92.
148. Liu PP, Liu J, Jiang WQ, Carew JS, Ogasawara MA, Pelicano H, Croce CM, Estrov Z, Xu RH, Keating MJ, et al. Elimination of chronic lymphocytic leukemia cells in stromal microenvironment by targeting CPT with an antiangina drug perhexiline. Oncogene 2016; 35:5663-73.
149. Longo N, Amat di San Filippo C, Pasquali M. Disorders of carnitine transport and the carnitine cycle. Am J Med Genet C Semin Med Genet 2006; 142C:77-85.
150. Nomura M, Liu J, Rovira II, Gonzalez-Hurtado E, Lee J, Wolfgang MJ, Finkel T. Fatty acid oxidation in macrophage polarization. Nat Immunol 2016; 17:216-7.

151. Lu CL, Qin L, Liu HC, Candas D, Fan M, Li JJ. Tumor cells switch to mitochondrial oxidative phosphorylation under radiation via mTOR-mediated hexokinase II inhibition--a Warburg-reversing effect. PLoS One 2015; 10:e0121046.
152. Porporato PE, Payen VL, Pérez-Escuredo J, De Saedeleer CJ, Danhier P, Copetti T, Dhup S, Tardy M, Vazeille T, Bouzin C, et al. A mitochondrial switch promotes tumor metastasis. Cell Rep 2014; 8:754-66.
153. Rybin VO, Guo J, Sabri A, Elouardighi H, Schaefer E, Steinberg SF. Stimulus-specific differences in protein kinase C delta localization and activation mechanisms in cardiomyocytes. J Biol Chem 2004; 279:19350-61.
154. Martin S, Parton RG. Lipid droplets: a unified view of a dynamic organelle. Nat Rev Mol Cell Biol 2006; 7:373-8.
155. Murphy S, Martin S, Parton RG. Lipid droplet-organelle interactions; sharing the fats. Biochim Biophys Acta 2009; 1791:441-7.
156. Galbiati F, Razani B, Lisanti MP. Emerging themes in lipid rafts and caveolae. Cell 2001; 106:403-11.
157. van Meer G. Caveolin, cholesterol, and lipid droplets? The Journal of cell biology 2001; 152:F29-34.
158. Brown DA. Lipid droplets: proteins floating on a pool of fat. Current biology : CB 2001; 11:R446-9.
159. Krauss K, Altevogt P. Integrin leukocyte function-associated antigen-1-mediated cell binding can be activated by clustering of membrane rafts. J Biol Chem 1999; 274:36921-7.
160. Gagnoux-Palacios L, Dans M, van't Hof W, Mariotti A, Pepe A, Meneguzzi G, Resh MD, Giancotti FG. Compartmentalization of integrin alpha6beta4 signaling in lipid rafts. J Cell Biol 2003; 162:1189-96.
161. Masson N, Ratcliffe PJ. Hypoxia signaling pathways in cancer metabolism: the importance of co-selecting interconnected physiological pathways. Cancer Metab 2014; 2:3.
162. Bernardi R, Gianni L. Hallmarks of triple negative breast cancer emerging at last? Cell Res 2014; 24:904-5.
163. Holderfield M, Deuker MM, McCormick F, McMahon M. Targeting RAF kinases for cancer therapy: BRAF-mutated melanoma and beyond. Nat Rev Cancer 2014; 14:455-67.
164. Pylayeva-Gupta Y, Grabocka E, Bar-Sagi D. RAS oncogenes: weaving a tumorigenic web. Nat Rev Cancer 2011; 11:761-74.
165. Muoio DM, Lewin TM, Wiedmer P, Coleman RA. Acyl-CoAs are functionally channeled in liver: potential role of acyl-CoA synthetase. Am J Physiol Endocrinol Metab 2000; 279:E1366-73.
166. Yan S, Yang XF, Liu HL, Fu N, Ouyang Y, Qing K. Long-chain acyl-CoA synthetase in fatty acid metabolism involved in liver and other diseases: an update. World J Gastroenterol 2015; 21:3492-8.
167. Schoonjans K, Staels B, Auwerx J. Role of the peroxisome proliferator-activated receptor (PPAR) in mediating the effects of fibrates and fatty acids on gene expression. J Lipid Res 1996; 37:907-25.
168. Parkes HA, Preston E, Wilks D, Ballesteros M, Carpenter L, Wood L, Kraegen EW, Furler SM, Cooney GJ. Overexpression of acyl-CoA synthetase-1 increases lipid

deposition in hepatic (HepG2) cells and rodent liver in vivo. Am J Physiol Endocrinol Metab 2006; 291:E737-44.
169. Lewin TM, Kim JH, Granger DA, Vance JE, Coleman RA. Acyl-CoA synthetase isoforms 1, 4, and 5 are present in different subcellular membranes in rat liver and can be inhibited independently. J Biol Chem 2001; 276:24674-9.
170. Ellis JM, Bowman CE, Wolfgang MJ. Metabolic and tissue-specific regulation of acyl-CoA metabolism. PLoS One 2015; 10:e0116587.
171. Padanad MS, Konstantinidou G, Venkateswaran N, Melegari M, Rindhe S, Mitsche M, Yang C, Batten K, Huffman KE, Liu J, et al. Fatty Acid Oxidation Mediated by Acyl-CoA Synthetase Long Chain 3 Is Required for Mutant KRAS Lung Tumorigenesis. Cell Rep 2016; 16:1614-28.
172. Thompson JM, Nguyen QH, Singh M, Pavesic MW, Nesterenko I, Nelson LJ, Liao AC, Razorenova OV. Rho-associated kinase 1 inhibition is synthetically lethal with von Hippel-Lindau deficiency in clear cell renal cell carcinoma. Oncogene 2017; 36:1080-9.
173. FOLCH J, LEES M, SLOANE STANLEY GH. A simple method for the isolation and purification of total lipides from animal tissues. J Biol Chem 1957; 226:497-509.
174. MORRISON WR, SMITH LM. PREPARATION OF FATTY ACID METHYL ESTERS AND DIMETHYLACETALS FROM LIPIDS WITH BORON FLUORIDE--METHANOL. J Lipid Res 1964; 5:600-8.
175. Obata Y, Fukumoto Y, Nakayama Y, Kuga T, Dohmae N, Yamaguchi N. The Lyn kinase C-lobe mediates Golgi export of Lyn through conformation-dependent ACSL3 association. J Cell Sci 2010; 123:2649-62.
176. Brooks PC, Lin JM, French DL, Quigley JP. Subtractive immunization yields monoclonal antibodies that specifically inhibit metastasis. J Cell Biol 1993; 122:1351-9.
177. Dong Y, He Y, de Boer L, Stack MS, Lumley JW, Clements JA, Hooper JD. The cell surface glycoprotein CUB domain-containing protein 1 (CDCP1) contributes to epidermal growth factor receptor-mediated cell migration. J Biol Chem 2012; 287:9792-803.
178. Fukuchi K, Steiniger SC, Deryugina E, Liu Y, Lowery CA, Gloeckner C, Zhou B, Kaufmann GF, Quigley JP, Janda KD. Inhibition of tumor metastasis: functional immune modulation of the CUB domain containing protein 1. Mol Pharm 2010; 7:245-53.
179. Romero A, Romão MJ, Varela PF, Kölln I, Dias JM, Carvalho AL, Sanz L, Töpfer-Petersen E, Calvete JJ. The crystal structures of two spermadhesins reveal the CUB domain fold. Nat Struct Biol 1997; 4:783-8.
180. Mikolajek H, Kolstoe SE, Pye VE, Mangione P, Pepys MB, Wood SP. Structural basis of ligand specificity in the human pentraxins, C-reactive protein and serum amyloid P component. J Mol Recognit 2011; 24:371-7.
181. Sawada G, Takahashi Y, Niida A, Shimamura T, Kurashige J, Matsumura T, Ueo H, Uchi R, Takano Y, Ueda M, et al. Loss of CDCP1 Expression Promotes Invasiveness and Poor Prognosis in Esophageal Squamous Cell Carcinoma. Ann Surg Oncol 2014.
182. Fowler CB, Waybright TJ, Veenstra TD, O'Leary TJ, Mason JT. Pressure-assisted protein extraction: a novel method for recovering proteins from archival tissue for proteomic analysis. J Proteome Res 2012; 11:2602-8.
183. Shi SR, Taylor CR, Fowler CB, Mason JT. Complete solubilization of formalin-fixed, paraffin-embedded tissue may improve proteomic studies. Proteomics Clin Appl 2013; 7:264-72.

184. Fowler CB, O'Leary TJ, Mason JT. Improving the Proteomic Analysis of Archival Tissue by Using Pressure-Assisted Protein Extraction: A Mechanistic Approach. J Proteomics Bioinform 2014; 7:151-7.
185. Jacob AI, Horovitz-Fried M, Aga-Mizrachi S, Brutman-Barazani T, Okhrimenko H, Zick Y, Brodie C, Sampson SR. The regulatory domain of protein kinase C delta positively regulates insulin receptor signaling. J Mol Endocrinol 2010; 44:155-69.
186. Rosenzweig T, Aga-Mizrachi S, Bak A, Sampson SR. Src tyrosine kinase regulates insulin-induced activation of protein kinase C (PKC) delta in skeletal muscle. Cell Signal 2004; 16:1299-308.
187. Acin-Perez R, Hoyos B, Gong J, Vinogradov V, Fischman DA, Leitges M, Borhan B, Starkov A, Manfredi G, Hammerling U. Regulation of intermediary metabolism by the PKCdelta signalosome in mitochondria. FASEB J 2010; 24:5033-42.
188. Uddin S, Sassano A, Deb DK, Verma A, Majchrzak B, Rahman A, Malik AB, Fish EN, Platanias LC. Protein kinase C-delta (PKC-delta) is activated by type I interferons and mediates phosphorylation of Stat1 on serine 727. J Biol Chem 2002; 277:14408-16.
189. Allen-Petersen BL, Carter CJ, Ohm AM, Reyland ME. Protein kinase Cδ is required for ErbB2-driven mammary gland tumorigenesis and negatively correlates with prognosis in human breast cancer. Oncogene 2014; 33:1306-15.
190. Campbell I. Liver: metabolic functions. Anaesthesia & Intensive Care Medicine, 2006:51-4.
191. Lam DW, LeRoith D. Metabolic Syndrome. Endotext [Internet]: MDText.com Inc, 2015.
192. Paschos P, Paletas K. Non alcoholic fatty liver disease and metabolic syndrome. Hippokratia 2009; 13:9-19.
193. Grenier-Larouche T, Carreau AM, Carpentier AC. Early Metabolic Improvement After Bariatric Surgery: The First Steps Toward Remission of Type 2 Diabetes. Can J Diabetes 2017.
194. Aguilar M, Bhuket T, Torres S, Liu B, Wong RJ. Prevalence of the metabolic syndrome in the United States, 2003-2012. JAMA 2015; 313:1973-4.
195. WHO. Global Report on Diabetes. available at http://www.who.int: WHO Press, 2016.
196. Chalasani N, Younossi Z, Lavine JE, Diehl AM, Brunt EM, Cusi K, Charlton M, Sanyal AJ, Association AG, Diseases AAftSoL, et al. The diagnosis and management of non-alcoholic fatty liver disease: practice guideline by the American Gastroenterological Association, American Association for the Study of Liver Diseases, and American College of Gastroenterology. Gastroenterology 2012; 142:1592-609.
197. Association AD. Diagnosis and classification of diabetes mellitus. Diabetes Care 2010; 33 Suppl 1:S62-9.
198. Moulik PK, Mtonga R, Gill GV. Amputation and mortality in new-onset diabetic foot ulcers stratified by etiology. Diabetes Care 2003; 26:491-4.
199. Al-Watban FA, Zhang XY, Andres BL. Low-level laser therapy enhances wound healing in diabetic rats: a comparison of different lasers. Photomed Laser Surg 2007; 25:72-7.
200. Brem H, Stojadinovic O, Diegelmann RF, Entero H, Lee B, Pastar I, Golinko M, Rosenberg H, Tomic-Canic M. Molecular markers in patients with chronic wounds to guide surgical debridement. Mol Med 2007; 13:30-9.

201. Stojadinovic O, Brem H, Vouthounis C, Lee B, Fallon J, Stallcup M, Merchant A, Galiano RD, Tomic-Canic M. Molecular pathogenesis of chronic wounds: the role of beta-catenin and c-myc in the inhibition of epithelialization and wound healing. Am J Pathol 2005; 167:59-69.
202. Clark RA, Lanigan JM, DellaPelle P, Manseau E, Dvorak HF, Colvin RB. Fibronectin and fibrin provide a provisional matrix for epidermal cell migration during wound reepithelialization. J Invest Dermatol 1982; 79:264-9.
203. Xue M, Le NT, Jackson CJ. Targeting matrix metalloproteases to improve cutaneous wound healing. Expert Opin Ther Targets 2006; 10:143-55.
204. Werner S, Grose R. Regulation of wound healing by growth factors and cytokines. Physiol Rev 2003; 83:835-70.
205. Guo X, Jiang X, Ren X, Sun H, Zhang D, Zhang Q, Zhang J, Huang Y. The Galvanotactic Migration of Keratinocytes is Enhanced by Hypoxic Preconditioning. Sci Rep 2015; 5:10289.
206. Pugh CW, Ratcliffe PJ. Regulation of angiogenesis by hypoxia: role of the HIF system. Nat Med 2003; 9:677-84.
207. Darby IA, Laverdet B, Bonté F, Desmoulière A. Fibroblasts and myofibroblasts in wound healing. Clin Cosmet Investig Dermatol 2014; 7:301-11.
208. Guo S, Dipietro LA. Factors affecting wound healing. J Dent Res 2010; 89:219-29.
209. Spravchikov N, Sizyakov G, Gartsbein M, Accili D, Tennenbaum T, Wertheimer E. Glucose effects on skin keratinocytes: implications for diabetes skin complications. Diabetes 2001; 50:1627-35.
210. Pastar I, Stojadinovic O, Yin NC, Ramirez H, Nusbaum AG, Sawaya A, Patel SB, Khalid L, Isseroff RR, Tomic-Canic M. Epithelialization in Wound Healing: A Comprehensive Review. Adv Wound Care (New Rochelle) 2014; 3:445-64.
211. Pham CT. Neutrophil serine proteases: specific regulators of inflammation. Nat Rev Immunol 2006; 6:541-50.
212. He L, Marneros AG. Macrophages are essential for the early wound healing response and the formation of a fibrovascular scar. Am J Pathol 2013; 182:2407-17.
213. Falanga V, Iwamoto S. Mechanisms of Wound Repair, Wound Healing, and Wound Dressing. Fitzpatrick's Dermatology in General Medicine: McGraw-Hill, 2012.
214. Mediero A, Crooke A, Guzmán-Aránguez A, Pintor J. Phospholipase C/Protein Kinase C pathway is essential for corneal re-epithelialization induced by Ap(4)A. Curr Eye Res 2011; 36:1108-15.
215. Joyce NC, Meklir B. Protein kinase C activation during corneal endothelial wound repair. Invest Ophthalmol Vis Sci 1992; 33:1958-73.
216. Lin N, Bazan HE. Protein kinase C substrates in corneal epithelium during wound healing: the phosphorylation of growth associated protein-43 (GAP-43). Exp Eye Res 1995; 61:451-9.
217. Khamaisi M, Katagiri S, Keenan H, Park K, Maeda Y, Li Q, Qi W, Thomou T, Eschuk D, Tellechea A, et al. PKCδ inhibition normalizes the wound-healing capacity of diabetic human fibroblasts. J Clin Invest 2016; 126:837-53.
218. Nakashima K, Uekita T, Yano S, Kikuchi JI, Nakanishi R, Sakamoto N, Fukumoto K, Nomoto A, Kawamoto K, Shibahara T, et al. Novel small molecule inhibiting CDCP1-PKCδ pathway reduces tumor metastasis and proliferation. Cancer Sci 2017; 108:1049-57.

219. Takahashi Y, Soejima Y, Fukusato T. Animal models of nonalcoholic fatty liver disease/nonalcoholic steatohepatitis. World J Gastroenterol 2012; 18:2300-8.
220. Wong SK, Chin KY, Suhaimi FH, Fairus A, Ima-Nirwana S. Animal models of metabolic syndrome: a review. Nutr Metab (Lond) 2016; 13:65.
221. Holmes D. Epigenetics: On-off switch for obesity. Nat Rev Endocrinol 2016; 12:125.
222. Houten SM, Wanders RJ. A general introduction to the biochemistry of mitochondrial fatty acid β-oxidation. J Inherit Metab Dis 2010; 33:469-77.
223. Jin YJ, Li SZ, Zhao ZS, An JJ, Kim RY, Kim YM, Baik JH, Lim SK. Carnitine palmitoyltransferase-1 (CPT-1) activity stimulation by cerulenin via sympathetic nervous system activation overrides cerulenin's peripheral effect. Endocrinology 2004; 145:3197-204.
224. Henique C, Mansouri A, Fumey G, Lenoir V, Girard J, Bouillaud F, Prip-Buus C, Cohen I. Increased mitochondrial fatty acid oxidation is sufficient to protect skeletal muscle cells from palmitate-induced apoptosis. J Biol Chem 2010; 285:36818-27.
225. Aon MA, Bhatt N, Cortassa SC. Mitochondrial and cellular mechanisms for managing lipid excess. Front Physiol 2014; 5:282.
226. Mason RR, Watt MJ. Unraveling the roles of PLIN5: linking cell biology to physiology. Trends Endocrinol Metab 2015; 26:144-52.
227. Scharwey M, Tatsuta T, Langer T. Mitochondrial lipid transport at a glance. J Cell Sci 2013; 126:5317-23.
228. Gao Q, Goodman JM. The lipid droplet-a well-connected organelle. Front Cell Dev Biol 2015; 3:49.
229. Mashimo T, Pichumani K, Vemireddy V, Hatanpaa KJ, Singh DK, Sirasanagandla S, Nannepaga S, Piccirillo SG, Kovacs Z, Foong C, et al. Acetate is a bioenergetic substrate for human glioblastoma and brain metastases. Cell 2014; 159:1603-14.
230. Carracedo A, Cantley LC, Pandolfi PP. Cancer metabolism: fatty acid oxidation in the limelight. Nat Rev Cancer 2013; 13:227-32.
231. Chio IIC, Tuveson DA. ROS in Cancer: The Burning Question. Trends Mol Med 2017.
232. Schug ZT, Vande Voorde J, Gottlieb E. The metabolic fate of acetate in cancer. Nat Rev Cancer 2016; 16:708-17.
233. Comerford SA, Huang Z, Du X, Wang Y, Cai L, Witkiewicz AK, Walters H, Tantawy MN, Fu A, Manning HC, et al. Acetate dependence of tumors. Cell 2014; 159:1591-602.
234. Starley BQ, Calcagno CJ, Harrison SA. Nonalcoholic fatty liver disease and hepatocellular carcinoma: a weighty connection. Hepatology 2010; 51:1820-32.
235. Caviglia JM, Schwabe RF. Mouse models of liver cancer. Methods Mol Biol 2015; 1267:165-83.

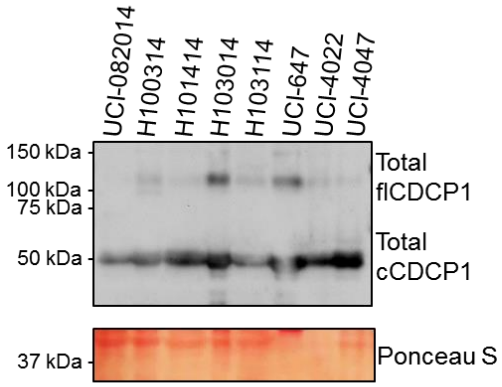

Supplemental Figure 2.1 | CDCP1 is expressed and cleaved in primary human TNBC samples. Since re-probing of the membrane from Figure 1c probed with the rabbit anti-Y734-CDCP1 antibody with rabbit anti-CDCP1 antibodies (Cell Signaling #4115) and development using horse radish peroxidase-based method resulted in almost identical pictures (compare this image to the image of phospho-CDCP1 in Figure 1c), we re-probed the same membrane with one more anti-CDCP1 antibody (goat from Abcam #ab1377) and developed the blot using an alkaline phosphatase-based method (shown in Figure 1c). flCDCP1 and cCDCP1 expression shown here correlates well with Figure 1c and the bands correspond to the molecular weights determined in Figure 1c. Equal protein amounts were loaded in each lane. A part of Ponceau-stained blot is also shown.

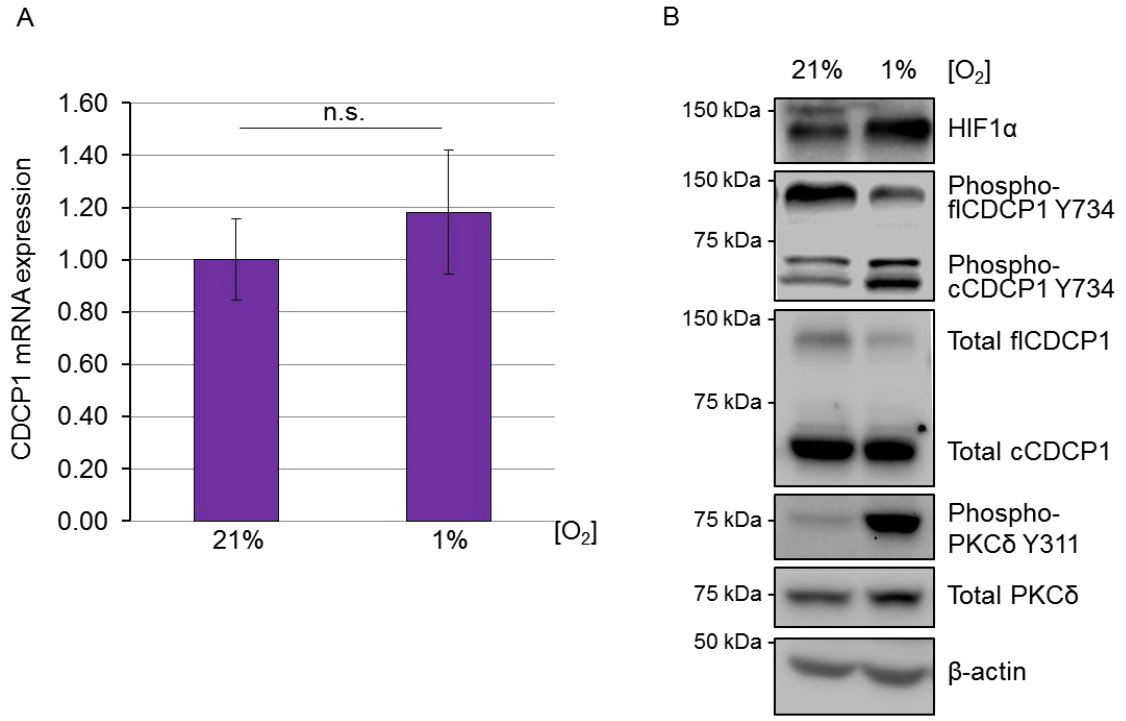

Supplemental Figure 2.2 | Phosphorylation of cCDCP1 is induced by hypoxia. (**a**) CDCP1 expression at mRNA level does not increase upon hypoxic exposure (1% O_2 for 24 hours) in MDA-MB-231 cells. The graphs represent CDCP1 transcript expression analyzed by qRT-PCR. This data represents the average of two independent experiments done in triplicate. P=0.795 analyzed by paired T-test. Error bars represent SEMs. (**b**) Phosphorylation of cCDCP1 at Y734, as well as phosphorylation of PKCδ at Y311 are induced in hypoxia. MDA-MB-231 were exposed to normoxia (21% O_2) or hypoxia (1% O_2) for 2 hours. CDCP1 and PKCδ expression and phosphorylation were analyzed by Western blot.

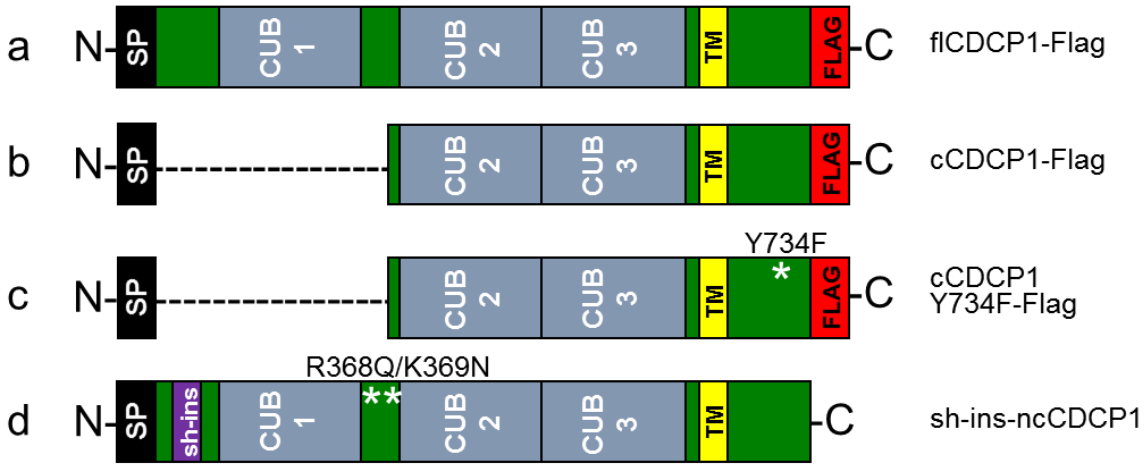

Supplemental Figure 2.3 | Schematics of CDCP1 constructs. (**a**) Full length CDCP1 (flCDCP1), (**b**) cleaved CDCP1 (cCDCP1), (**c**) Y734F mutant cleaved CDCP1 (cCDCP1 Y734F), as well as (**d**) sh-insensitive (sh-ins) non-cleavable (nc) R368Q/K369N mutant full length CDCP1 (sh-ins-ncCDCP1) constructs are shown. All shRNAs against CDCP1 used in this paper target the sequence upstream of CUB1, making cCDCP1 intrinsically sh-ins. The third positions of codons were changed in the regions where shRNAs were binding, preserving the WT amino acid sequence to create sh-ins-ncCDCP1. Purple, sh-ins region. flCDCP1 and both cCDCP1 constructs were Flag-tagged (shown) and His-tagged (not shown) at the C-terminus. The signal peptide was included at the N-terminus of cCDCP1 and cCDCP1 Y734F to ensure proper membrane localization. SP, signal peptide; CUB1-3, CUB domains; TM, trans-membrane domain; asterisk, mutation.

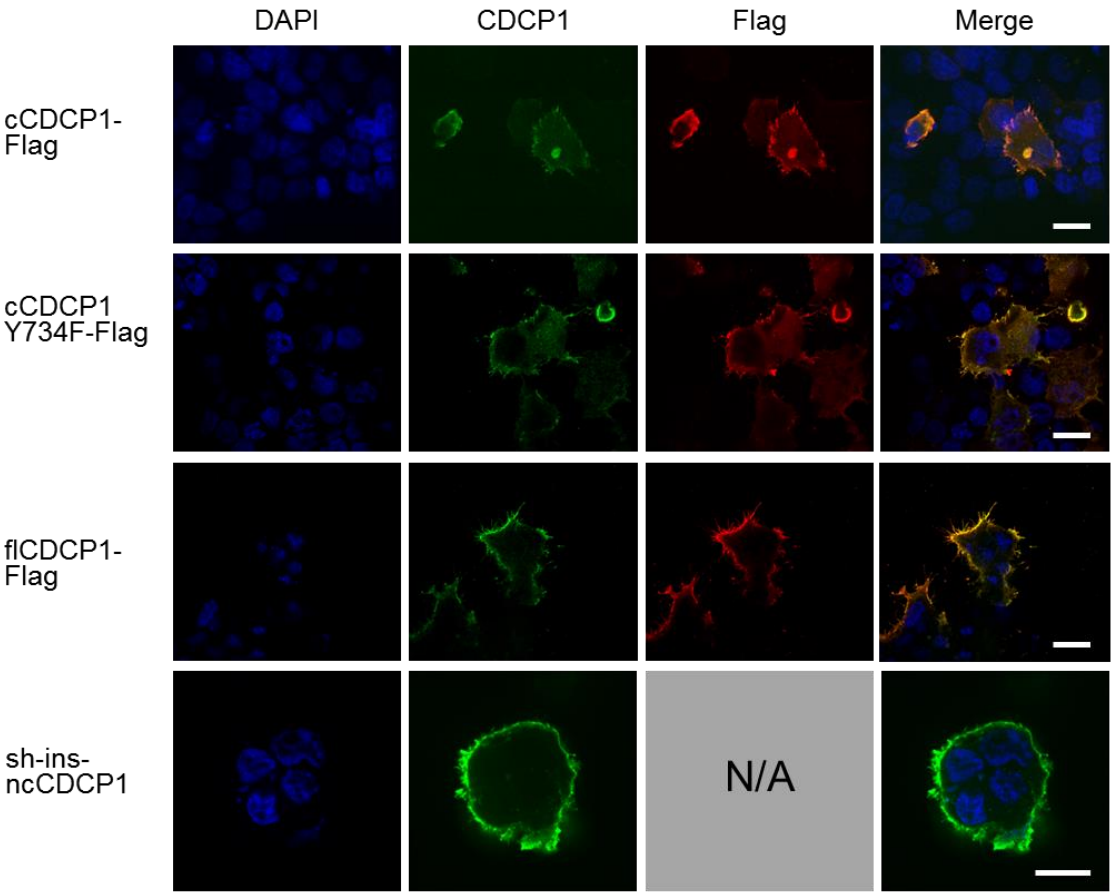

Supplemental Figure 2.4 | Membrane localization of CDCP1 overexpressed in HEK 293T cells. HEK 293T cells were transiently transfected with cCDCP1-Flag, cCDCP1 Y734F-Flag, flCDCP1-Flag, and sh-ins-ncCDCP1 constructs as indicated. Immunofluorescent staining was carried out using antibodies recognizing CDCP1 or Flag epitope. Nuclei were visualized with DAPI. Images were obtained with 40x and 63x objectives. Scale bars represent 10 μm. See Supplemental Figure 3 for construct details.

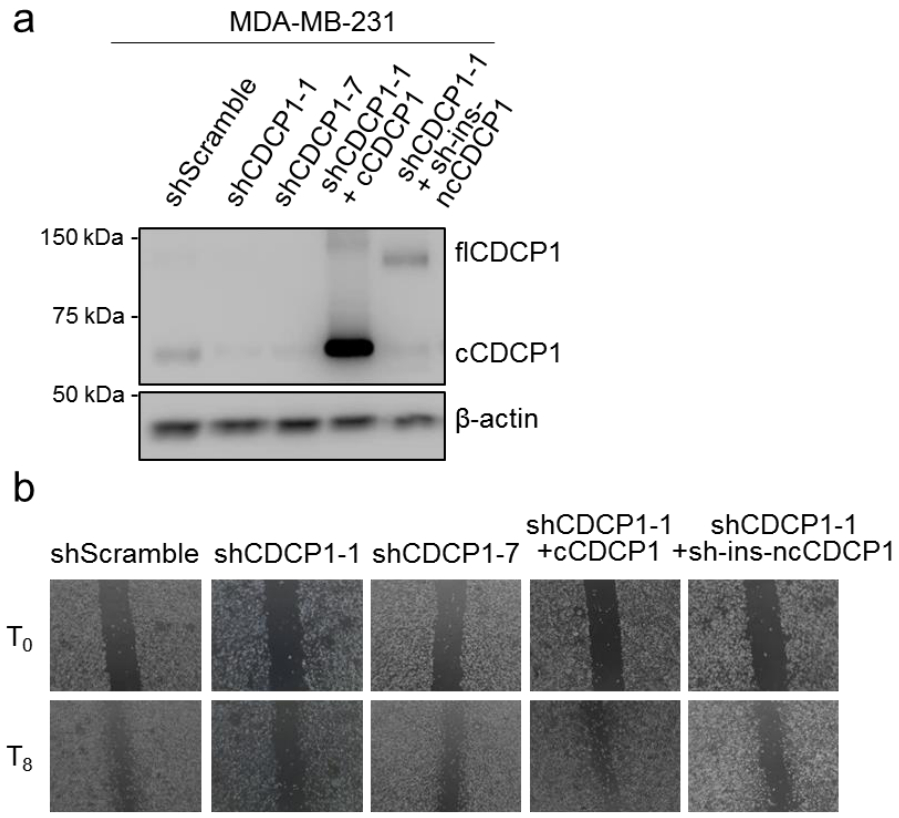

Supplemental Figure 2.5 | CDCP1 cleavage stimulates cell migration. (**a**) Western blot showing the level of CDCP1 expression in MDA-MB-231 breast cancer cells after infection with shRNA-expressing constructs targeting CDCP1: shCDCP1-1 and shCDCP1-7. cCDCP1 or sh-ins-ncCDCP1 were then overexpressed in shCDCP1-1-infected MDA-MB-231 cells. (**b**) Representative images of scratch assay quantitated in Figure 3. MDA-MB-231 cells transduced with the indicated plasmids were grown to confluency. The cells were treated with 10 µg/mL mitomycin C for 2 hours before being scratched at T_0 and allowed to migrate in serum free medium for 8 hours before stopping the assay at T_8.

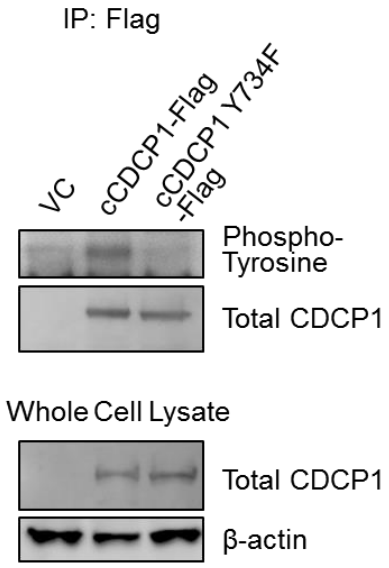

Supplemental Figure 2.6 | Y734F mutation in cCDCP1 disrupts its phosphorylation and downstream signaling to PKCδ. HEK 293T cells were transiently transfected with cCDCP1 WT and cCDCP1 Y734F Flag-tagged constructs, lysates were immunoprecipitated using an anti-Flag antibody and phosphorylation was analyzed by Western blot using an anti-Phospho-Tyrosine antibody. The cCDCP1 WT is phosphorylated while the cCDCP1 Y734F is not.

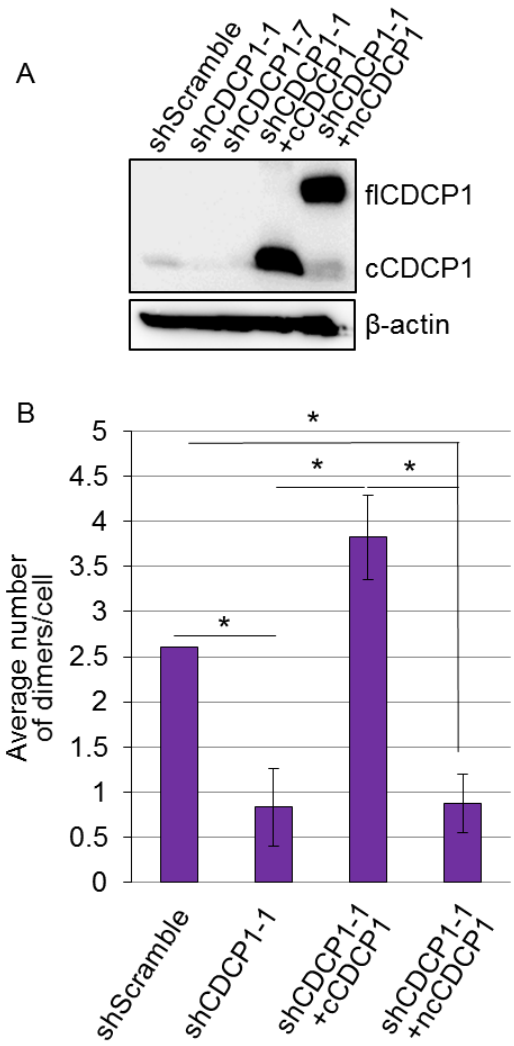

Supplemental Figure 2.7 | CDCP1 cleavage is necessary for dimer formation. (**a**) Western blot showing CDCP1 expression in MDA-MB-231-shScramble, MDA-MB-231-shCDCP1-1, MDA-MB-231-shCDCP1-7, MDA-MB-231-shCDCP1-1+cCDCP1, and MDA-MB-231-shCDCP1-1+sh-ins-ncCDCP1 cells. (**b**) Quantitation of PLA assay conducted with oligonucleotide-conjugated anti-CDCP1 antibody shown in Figure 4c. The graphs represent the average number of dimers per cell, which was obtained by counting the number of spots (each representing a dimer) per field and normalizing it to the number of nuclei per field. Bright (prevalent in cCDCP1 overexpressing cells) and dim (prevalent in MDA-MB-231-shScramble cells expressing endogenous cCDCP1) spots were considered to be dimers and counted. Four independent experiments were quantitated. *P≤0.0125 analyzed by one way ANOVA with multiple comparison post hoc T-test. Error bars represent SEMs.

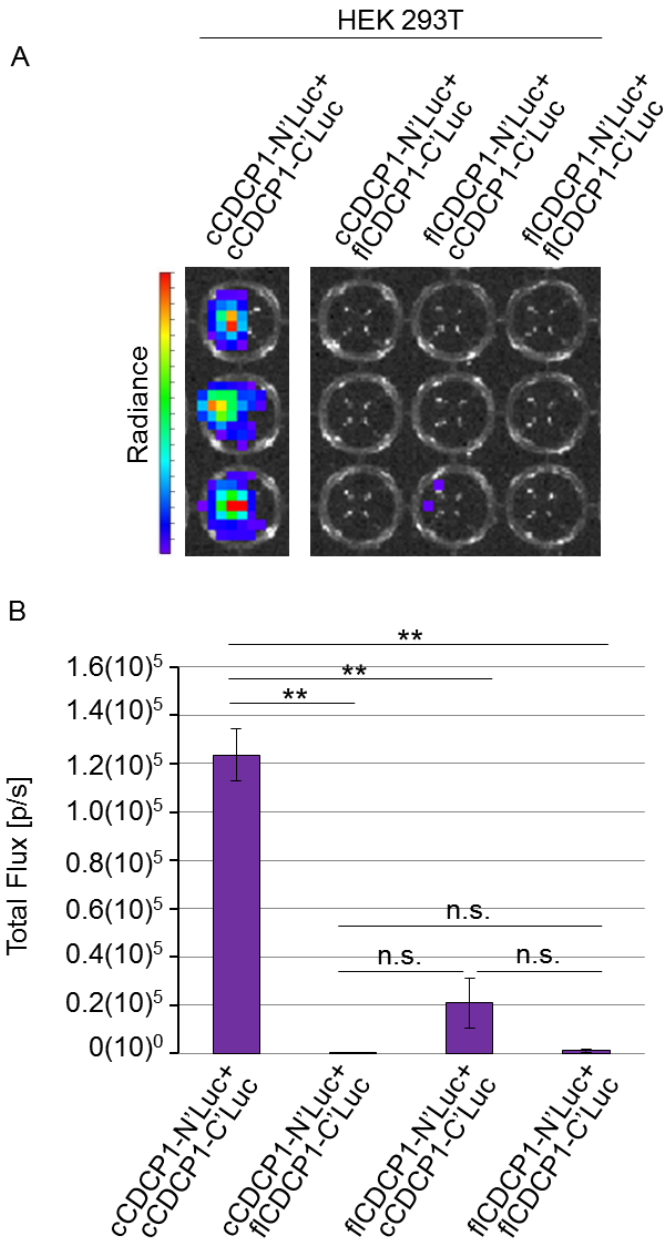

Supplemental Figure 2.8 | flCDCP1 does not form a homo-dimer with flCDCP1 or heterodimer with cCDCP1 as judged by split-luciferase assay. HEK 293T cells were transfected with split luciferase constructs as indicated. After the addition of D-luciferin, the luminescence was imaged with an IVIS Lumina system. (**a**) The representative image is shown. The luminescence was quantitated and normalized to protein content in each well. (**b**) The quantitation shown is the average of three independent experiments each done in triplicate. cCDCP1 is capable of forming a homo-dimer (positive control, high split-luciferase signal), and flCDCP1 is not capable of forming a homo-dimer or heterodimer with cCDCP1 (as indicated) as judged by extremely low split-luciferase signal. **P≤0.005 analyzed by one way ANOVA with multiple comparison post hoc T-test. Error bars represent SEMs.

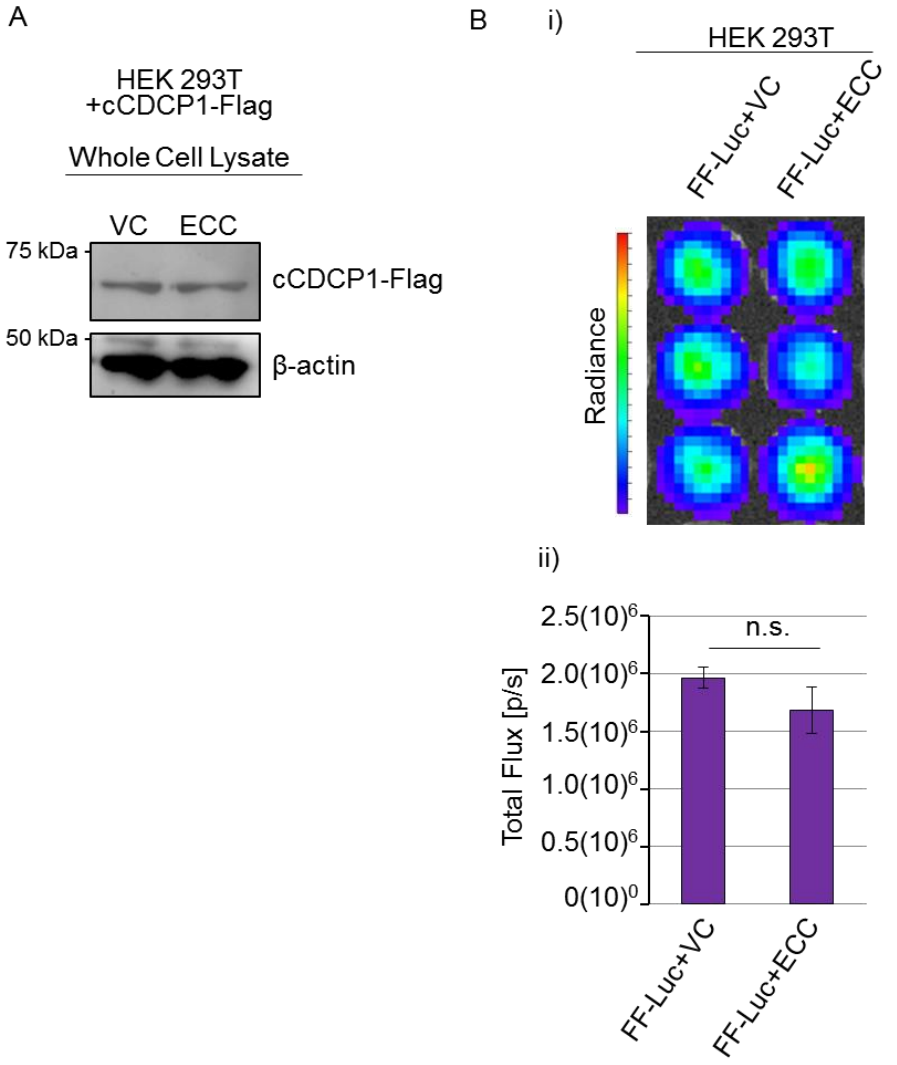

Supplemental Figure 2.9 | ECC does not interfere with CDCP1 expression or firefly luciferase function. (**a**) HEK 293T cells were transfected with cCDCP1-Flag and either vector control (VC) or ECC. Lysates were analyzed by Western blot. CDCP1 expression is not affected by ECC. (**b**) HEK 293T cells were transfected with firefly luciferase (FF-Luc) along with VC or ECC. After the addition of D-luciferin, the luminescence was imaged with an IVIS Lumina system. The representative image is shown in (i). The luminescence was quantitated and normalized to protein content in each well. The quantitation shown in (ii) is the average of three independent experiments each done in triplicate. ECC does not affect the activity of native FF-Luc. P=0.428, analyzed by paired T-test. Error bars represent SEMs.

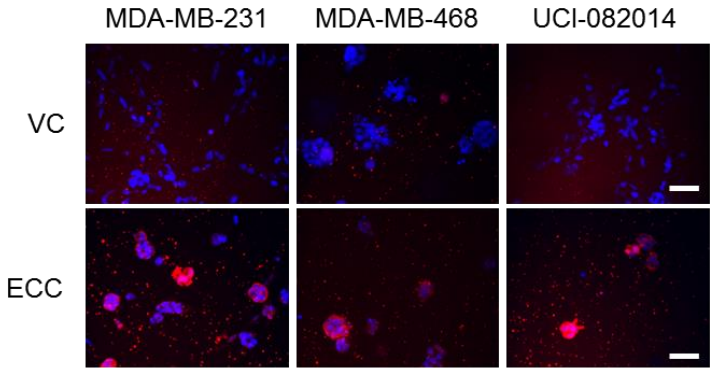

Supplemental Figure 2.10 | ECC staining in 3D. (**a**) ECC was detected with anti-His-tag antibody. Blue, DAPI; red, His-tag. Scale bar, 50 μm. One biological replicate was stained.

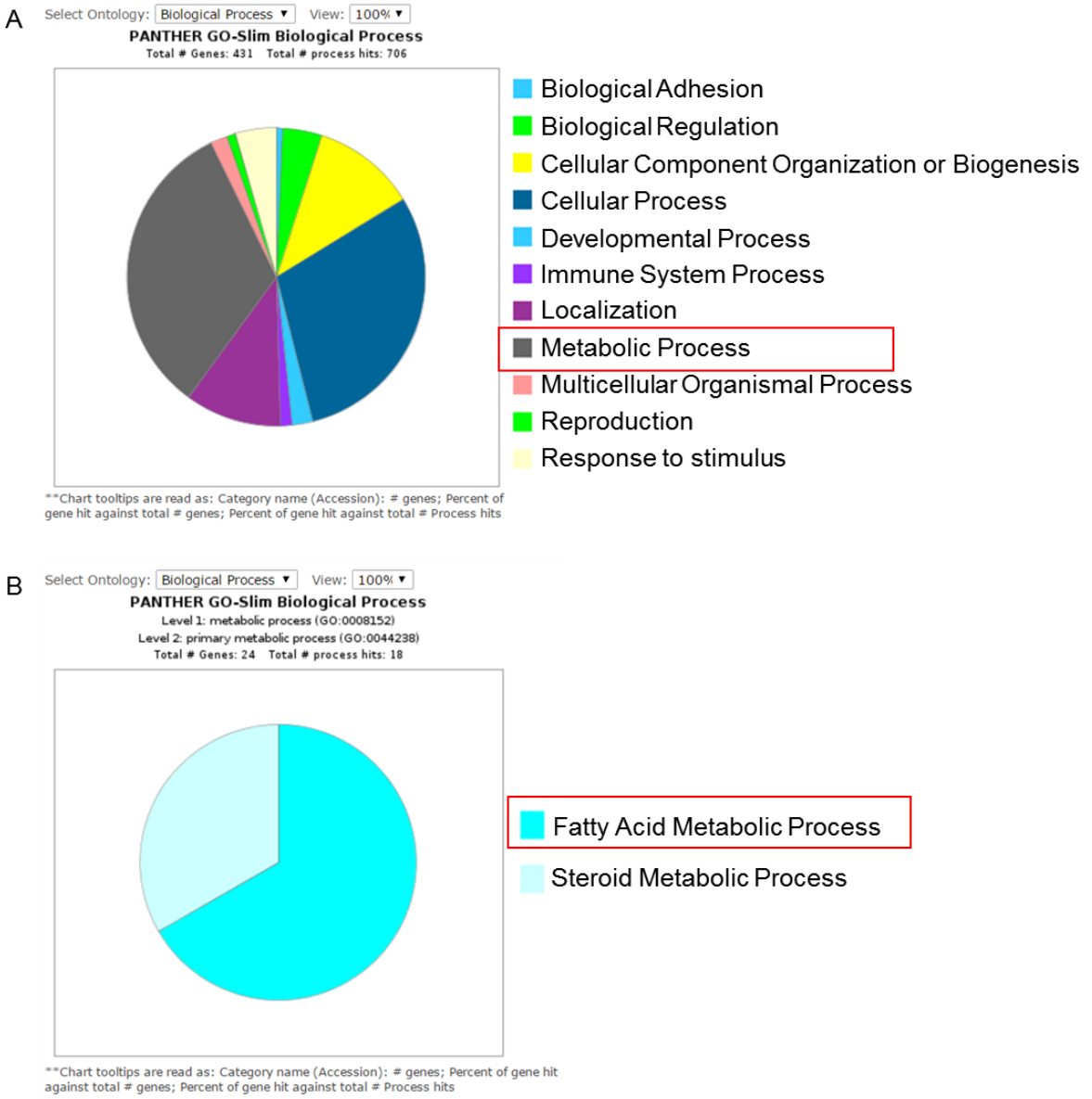

Supplemental Figure 3.1 | CDCP1 interacts with proteins involved in metabolism. CDCP1 with the Flag-tag was overexpressed in HEK 293T cells. The co-IP experiments were conducted using an anti-Flag antibody and co-immunoprecipitated proteins identified by mass spectrometry. CDCP1 predominantly co-immunoprecipitates with proteins involved in (**A**) metabolic pathways (grey) as analyzed by PANTHER (http://pantherdb.org/). Metabolic processes were narrowed down to primary metabolic processes, and then to lipid metabolic processes, where the majority belongs to fatty acid metabolic processes (**B**). ACSL3 was identified as a binding partner of CDCP1 based on peptides listed in Supplemental Table 1 with $7.26(10)^{-5}$ normalized spectral count.

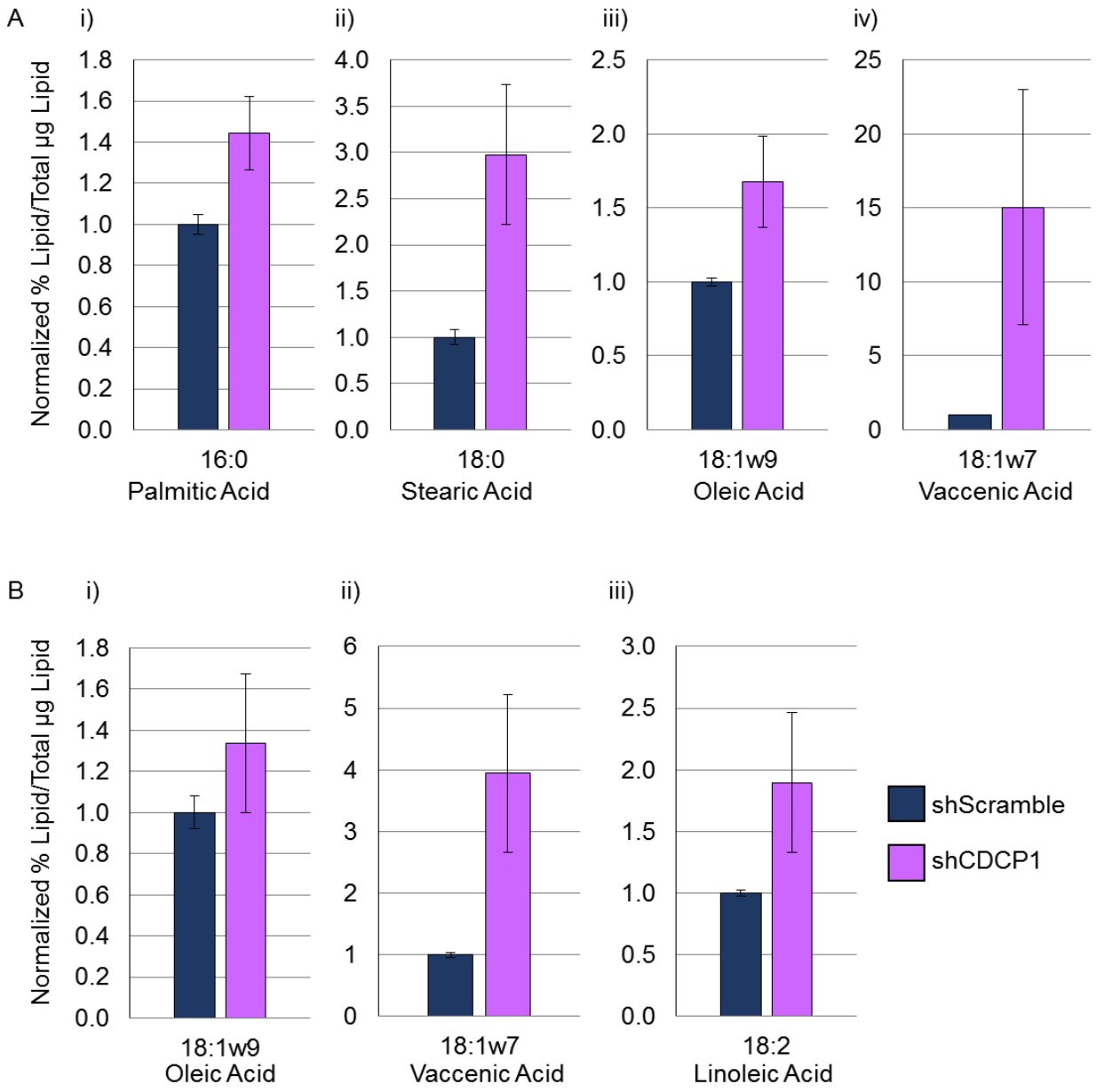

Supplemental Figure 3.2 | Lipid types affected by CDCP1 expression (related to Figure 3). Gas chromatographic analysis of the lipid content in TNBC cells demonstrated that CDCP1 decreases the abundance of multiple long-chain fatty acids in the forms of both triglycerides (**A**) and cholesteryl esters (**B**). Data was quantitated by pooling together two MDA-MB-231 and one MDA-MB-468 reapeats. shScramble values are the combination of MDA-MB-231 and MDA-MB-468 shScramble values (3 samples). shCDCP1 values are the combination of MDA-MB-231 and MDA-MB-468 shCDCP1-1 and shCDCP1-2 values (5 samples). All data normalized to pooled shScramble quantities.

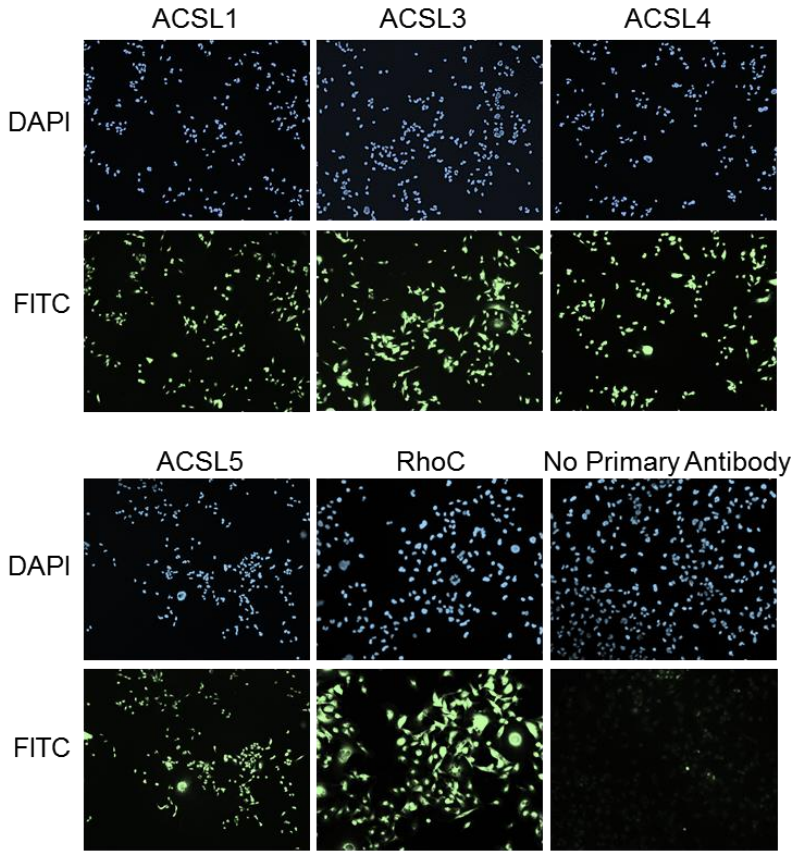

Supplemental Figure 3.3 | All antibodies used for PLA in Figure 3 work for immunofluorescence. 10x images are shown. AlexaFluor 488 conjugated goat anti-rabbit secondary antibodies were used at 1:200. Filters: DAPI, nucleus; FITC, protein of interest.

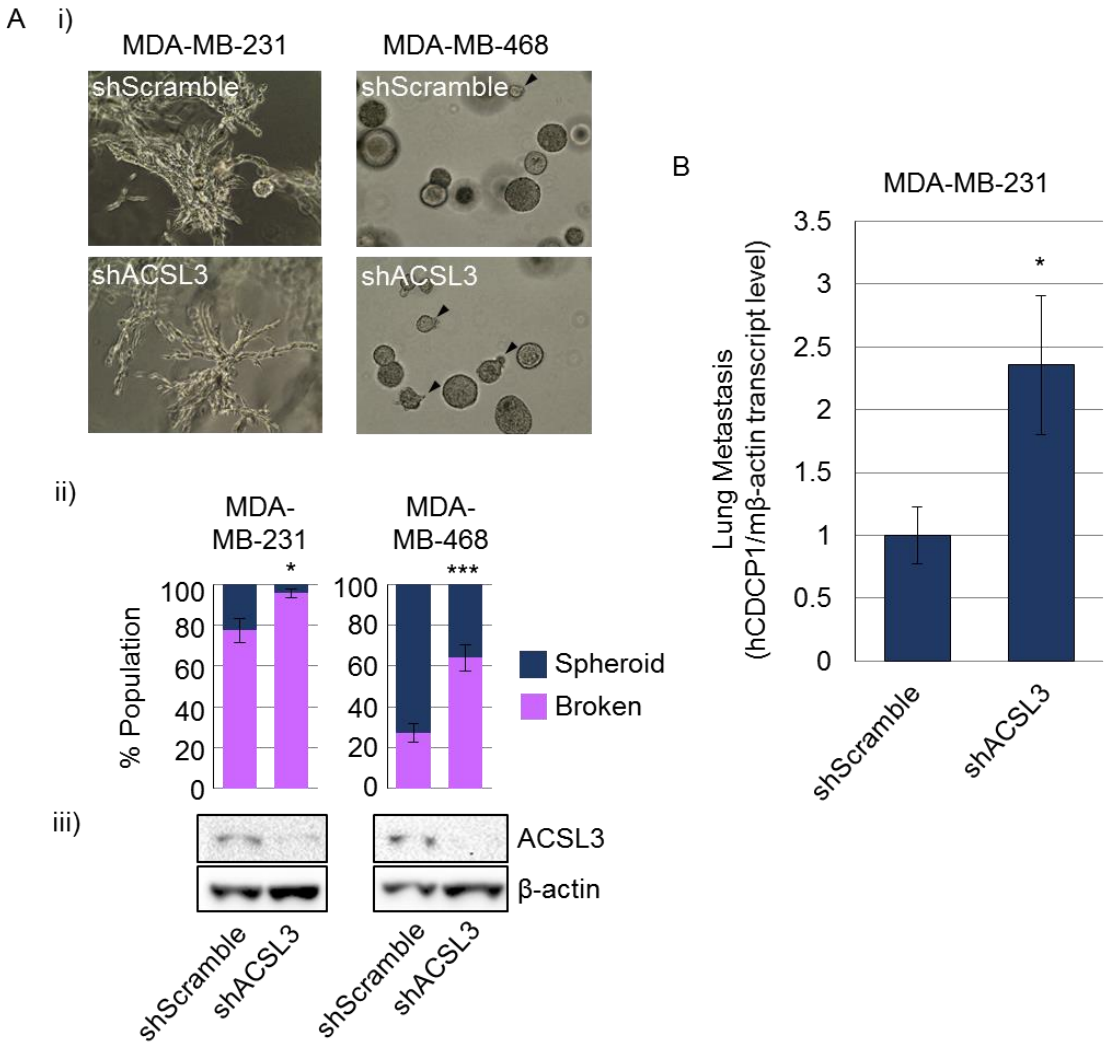

Supplemental Figure 3.4 | ACSL3 knockdown increases invasiveness and metastasis of TNBC cells. A) i) representative 20x phase contrast images of MDA-MB-231 and MDA-MB-468 cultured in 3D; ii) quantitation of broken/total spheroids for MDA-MB-231 and MDA-MB-468. Quantitation is the average of 3 images per N=3 biological replicates; iii) western blot confirming ACSL3 knockdown. ACSL3 knockdown induces invasion of both MDA-MB-231 and MDA-MB-468 cells in 3D culture. **B**) ACSL3 knockdown increases metastasis of MDA-MB-231 TNBC to the lungs. Metastatic burden was quantitated by qRT-PCR using primers specific to human cDNA (MDA-MB-231-derived) and mouse cDNA (lung-derived). The data is the average of 7-8 mice/condition. P values analyzed by one way ANOVA with multiple comparison post hoc T-test and error bars represent SEMs. *P<0.05, ***P<0.001.

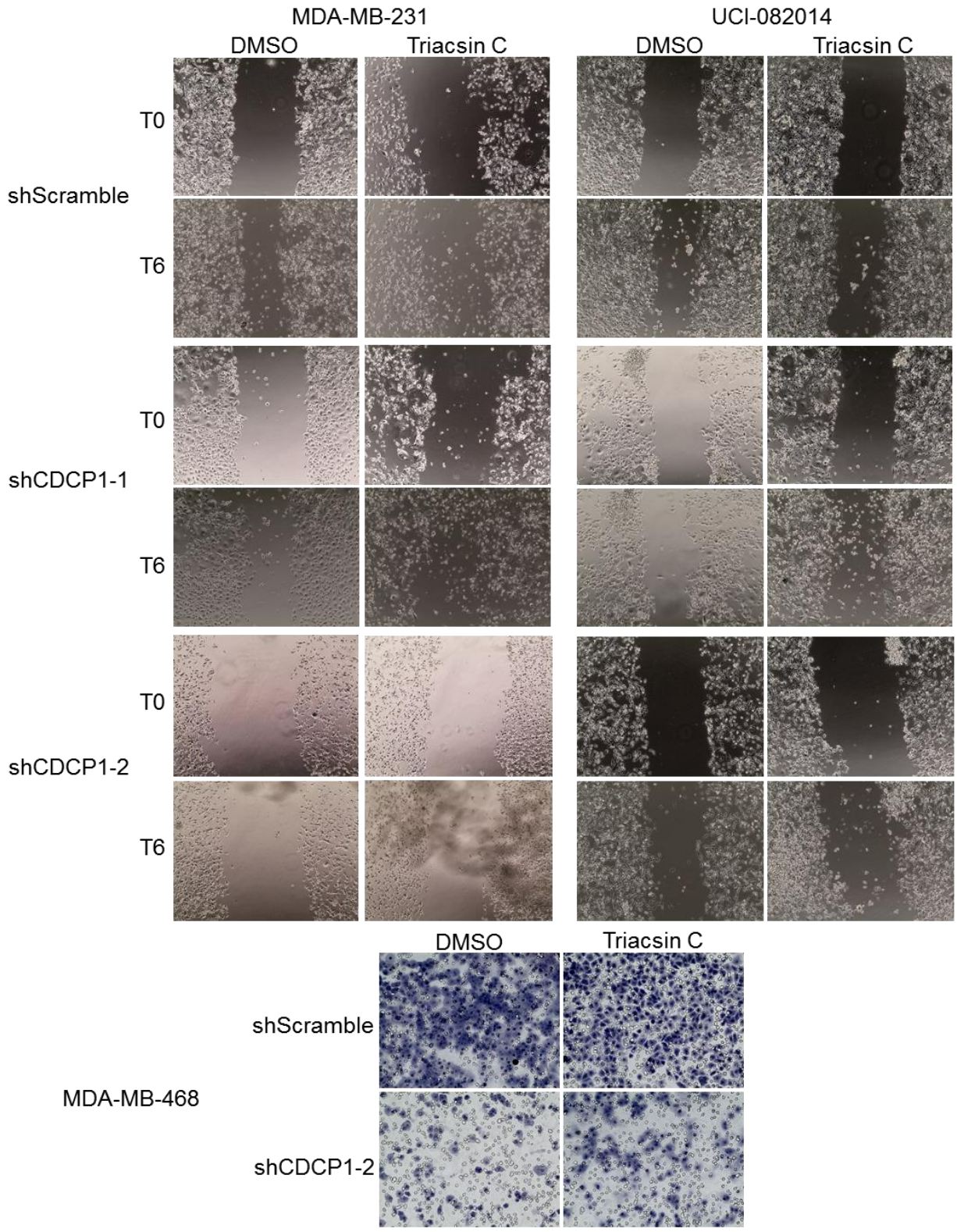

Supplemental Figure 3.5 | Representative images of migration assays at 0 hours (T0) and 6 hours (T6) after Triacsin C addition (5 μM) used for quantitation in Figure 5. Scratch (MDA-MB-231 and UCI-082014) and transwell (MDA-MB-468) migration assays were used. See Figure 5 for details.

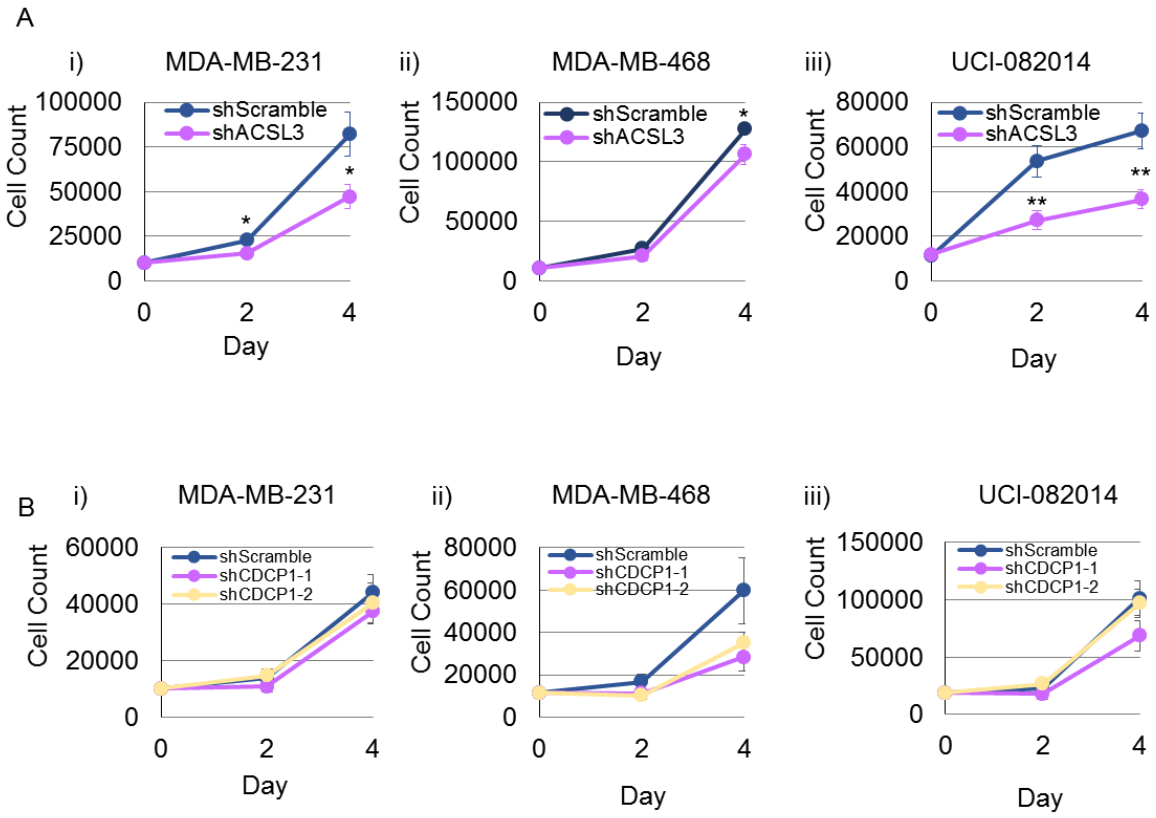

Supplemental Figure 3.6 | ACSL3 increases TNBC cell proliferation and CDCP1 does not. A) ACSL3 knockdown decreases proliferation of MDA-MB-231 (i), MDA-MB-468 (ii) and UCI-082014 (iii) cells to various degrees. **B**) CDCP1 knockdown with two different shRNAs does not significantly affect proliferation of MDA-MB-231 (i), MDA-MB-468 (ii) and UCI-082014 (iii) cells. Quantitation is the average of 3 biological replicates. P values were analyzed by one way ANOVA with multiple comparison post hoc T-test and error bars represent SEMs. *P<0.05, **P<0.01.

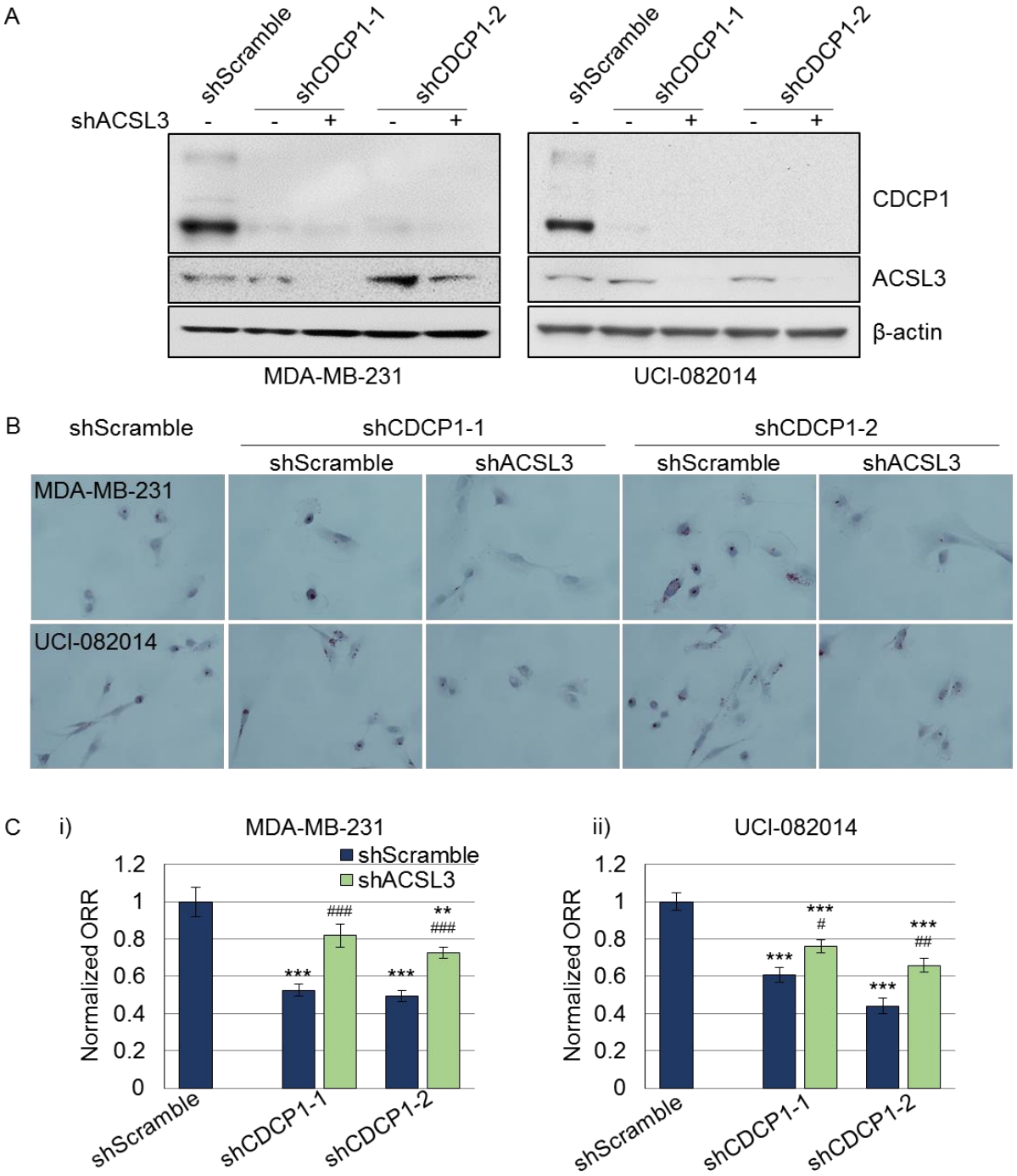

Supplemental Figure 3.7 | CDCP1 knockdown increases LD abundance and decreases ORR, which can be rescued by ACSL3 co-knockdown (Related to Figure 5). A) Western blot analysis confirming CDCP1 and ACSL3 knockdown in MDA-MB-231 and UCI-082014 cells used in Figure 5. **B**) Representative 60x images of ORO staining. **C**) Quantitation of ORR. The lower the ORR, the less oxidative the cells are. Quantitation is the average of 5 images per three biological replicates. N=3 for **B** and **C**. P values were analyzed by one way ANOVA with multiple comparison post hoc T-test. Error bars represent SEMs. $^{*,\#}P<0.05$, $^{**,\#\#}P<0.01$, $^{***,\#\#\#}P<0.001$; *compared to respective shScramble cells; $^{\#}$compared to respective shCDCP1 cells.

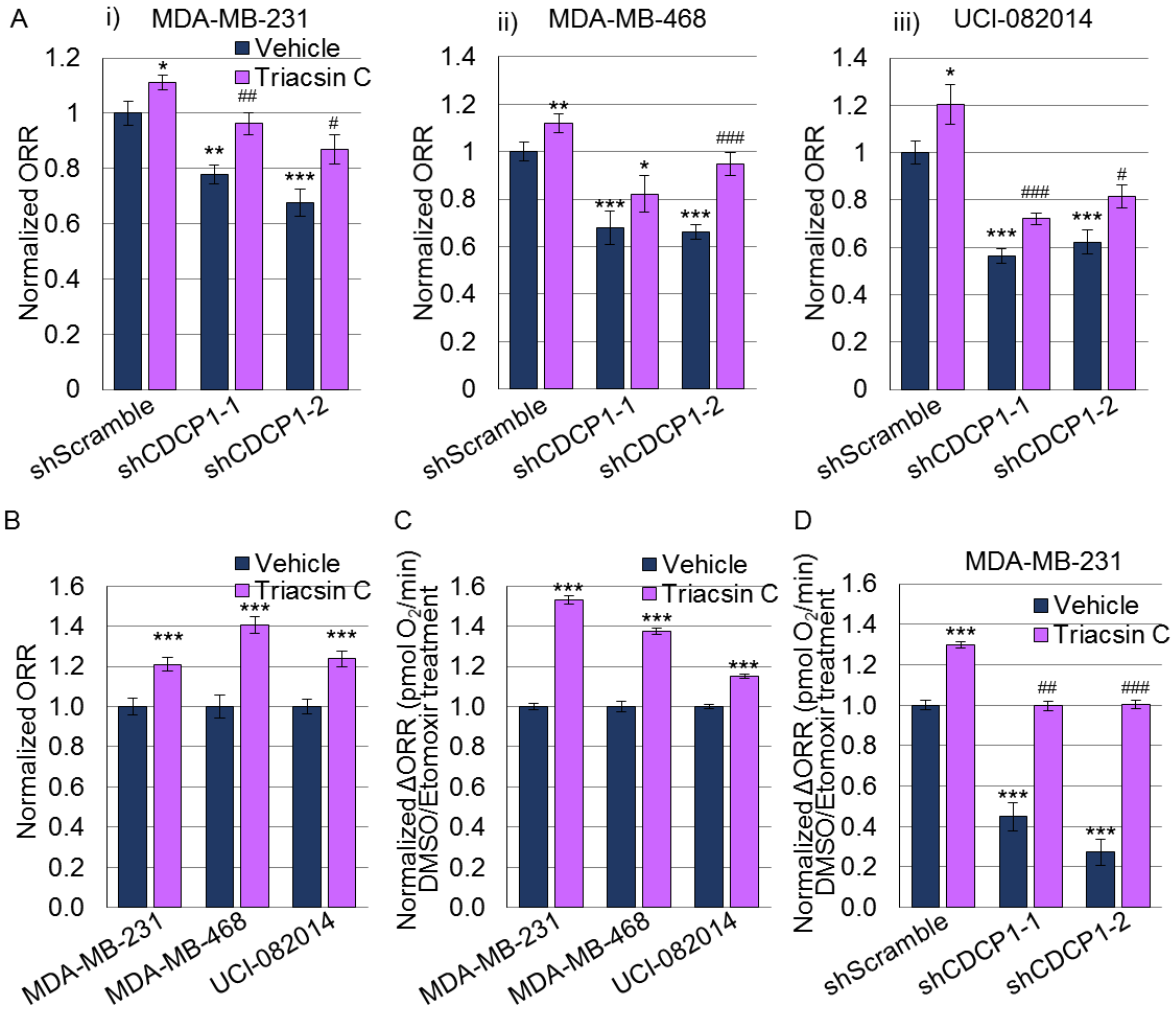

Supplemental Figure 3.8 | CDCP1 knockdown reduces ORR, indicating that they become less oxidative, and FAO in TNBC (related to Figure 6). A) Comparison of ORR between shScramble and two shRNAs targeting CDCP1 treated with either DMSO or Triacsin C. **B**) Comparison of ORR between DMSO control and Triacsin C treated cells. Results from A and B are in line with a more anabolic metabolism and production of lipids for storage in lipid droplets (LDs). **C**) Triacsin C-treated cells have higher ΔORR (calculated as 1-[DMSO-treated ORR/Etomoxir-treated ORR] and then all data were normalized to shScramble control, which was set to 1) than vehicle-treated cells, indicating that reducing ACSL activity increases lipid stores in the mitochondria available for FAO. ACSL activity reduces FAO in TNBC cells. **D**) Triacsin C treatment is sufficient to rescue reduction in ΔORR caused by CDCP1 knockdown in MDA-MB-231 cells. This indicates that ACSL is downstream of CDCP1 and that inhibiting ACSL activity is an important mechanism by which CDCP1 stimulates FAO in TNBC cells. Quantitation is the average of 5 images per N=2 biological replicates for **A**-**D**. P values were analyzed by one way ANOVA with multiple comparison post hoc T-test. Error bars represent SEMs. *,#P<0.05, **,##P<0.01, ***,###P<0.001; *compared to respective vehicle-treated shScramble cells; #compared to respective vehicle-treated shCDCP1 cells.

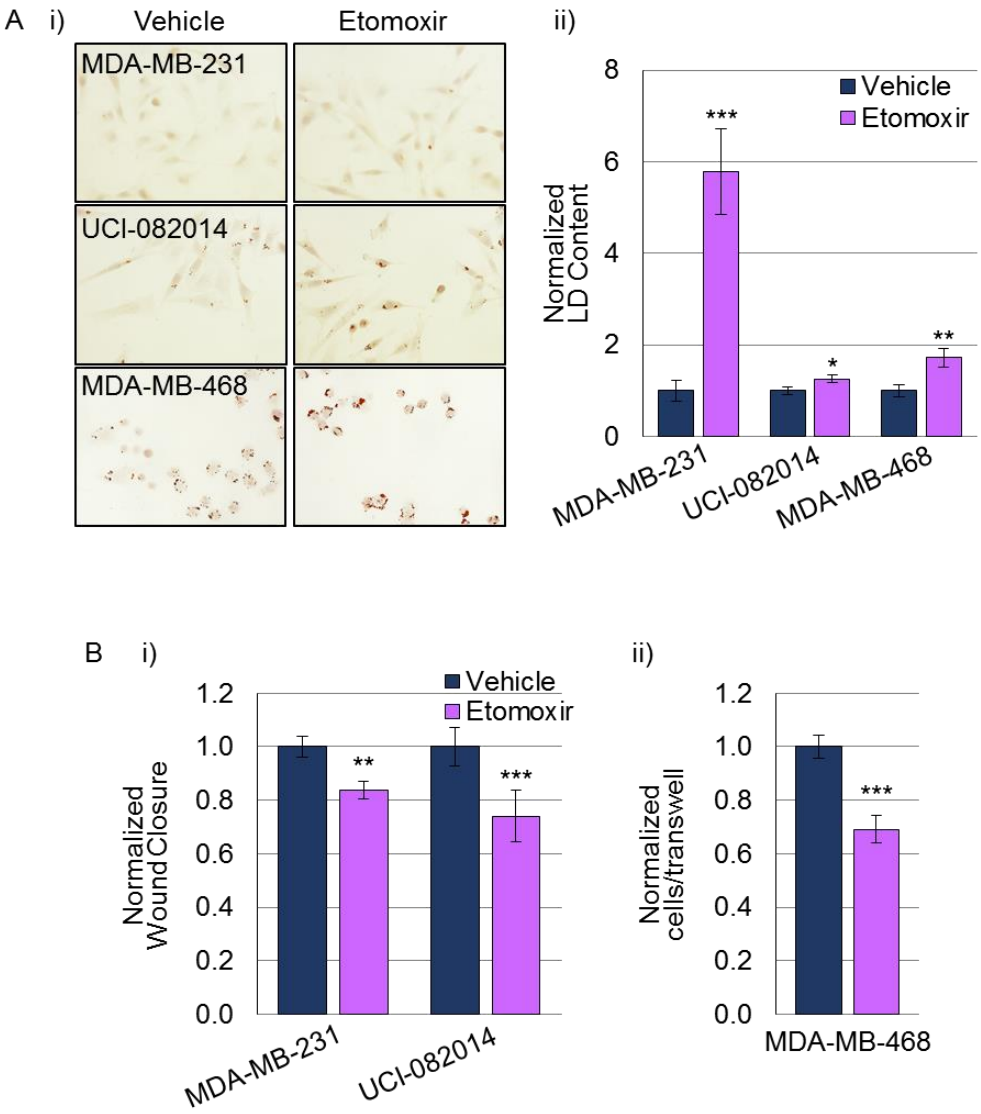

Supplemental Figure 3.9 | Etomoxir increases LD abundance and reduces migration of TNBC cells (related to Figure 6). A) i) Representative 60x images of ORO staining of TNBC cells treated with DMSO vehicle or 10 μM Etomoxir for 16 hours; ii) Quantitation of ORO, N=3. **B**) Scratch assays (i) with MDA-MB-231 and UCI-082014 and transwell migration assays (ii) with MDA-MB-468 cells reveal a decrease in migration after a 15 minute treatment with 40 μM Etomoxir compared to DMSO vehicle control. Quantitation is the average of N=3 biological replicates performed in duplicate. P values analyzed by one-way ANOVA with multiple comparison post hoc T-test and error bars represent SEMs. *P<0.05, **P<0.01, ***P<0.001.

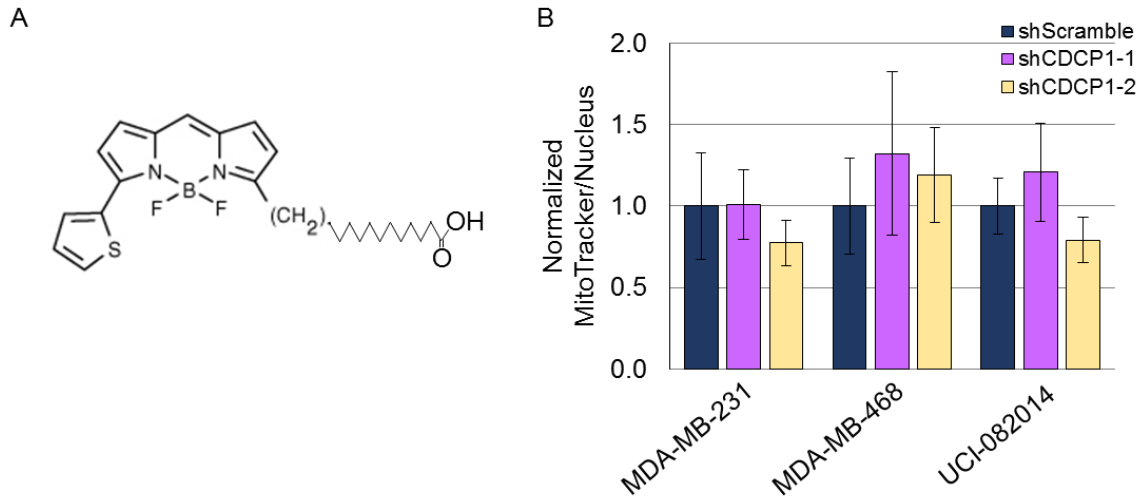

Supplemental Figure 3.10 | CDCP1 knockdown does not affect mitochondrial mass of cells (related to Figure 6). A) Structure of BODIPY used for experiments in Figure 6. **B**) Mitochondrial mass was quantitated as the intensity of MitoTracker stain per cell derived from the intensity of MitoTracker stain per field divided by the number of nuclei visualized by DAPI. shCDCP1 data were normalized to shScramble. Error bars represent SEMs.

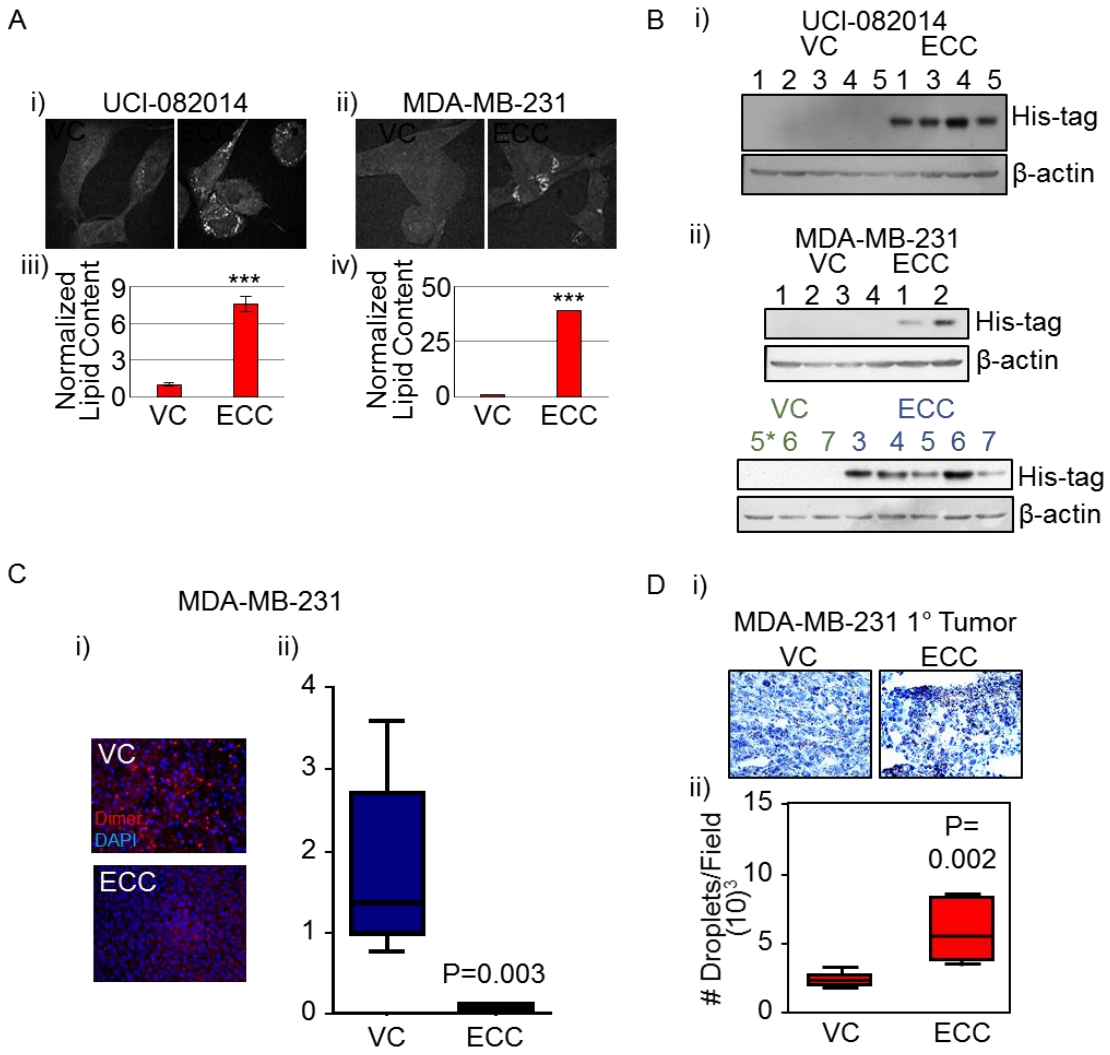

Supplemental Figure 3.11 | Expression of a CDCP1-blocking fragment, ECC, increases LD abundance and reduces metastasis of UCI-082014 and MDA-MB-231 tumors (related to Figure 7). A) ECC increases LD abundance in UCI-082014 and MDA-MB-231 cells cultured in 2D. (i-ii) Representative 40x CARS images of UCI-082014 (i) and MDA-MB-231 (ii) cells; (iii-iv) quantitation of CARS in UCI-082014 (iii) and MDA-MB-231 (iv) cells. **B**) Western blot analysis of ECC expression in UCI-082014 (i) and MDA-MB-231 (ii) primary tumors. **C**) ECC reduces CDCP1 dimer formation in MDA-MB-231 primary tumors as assessed by PLA. Representative 20x images (i) and quantitation (ii) of PLA. **D**) ECC increases LD abundance in MDA-MB-231 primary tumors. Representative 20x images (i) and quantitation (ii) of Oil Red O staining. P values (as indicated or ***P<0.001) analyzed by one way ANOVA with multiple comparison post hoc T-test and error bars represent SEMs.

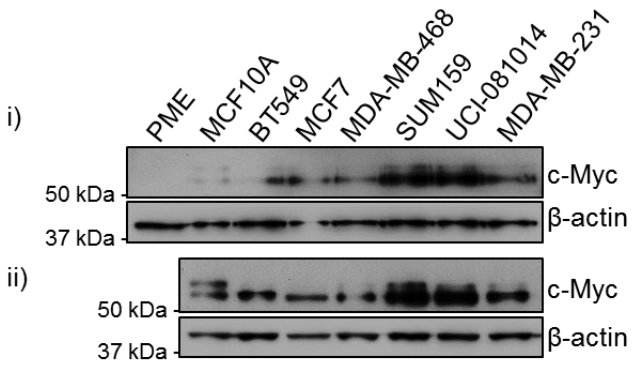

Supplemental Figure 3.12 | Myc expression analyzed by Western blot in the cell lines used in Figures 1 and 2. Western blot in (i) includes PME cells, and a replicate western blot (ii) does not due to the lack of the lysate. Some of the TNBC cell lines (SUM159 and UCI-082014) overexpress Myc, while others have equal (MCF7 and MDA-MB-468) to moderately overexpressed (BT549 and MDA-MB-231) Myc compared to MCF10A cells. β-actin was used as a loading control.

Supplementary Table 2.1 | Characterization of cell lines

	STAIN	UCI-082014			MDA-MB-468			MDA-MB-231		
		RESULT	% positive	intensity	RESULT	% positive	intensity	RESULT	% positive	intensity
EPITHELIAL MARKERS	pankeratin	POS			POS			POS		
	E-cadherin	NEG			NEG			NEG		
	MOC31	POS			POS			POS		
INTRINSIC SUBTYPE MARKERS	Estrogen Receptor	NEG			NEG			NEG		
	HER2	NEG			NEG			NEG		
TN SUBTYPE MARKERS	Androgen receptor	NEG			NEG			NEG		
	GATA3	NEG			POS			NEG		
	CK5/6	NEG			POS			NEG		
	EGFR	POS		1+	POS		3+	POS		2+
MESENCH MARKERS	Vimentin	POS			POS			POS		
	Smooth muscle actin	NEG			NEG			NEG		
MUTATION MARKERS	p16	NEG	<5		POS			NEG	<5	
	p53	POS			POS			POS		

* POS, positive; NEG, negative analyzed by immunocytochemistry.

Supplemental Table 3.1 | CDCP1 interacts with lipid metabolism proteins

Comprehensive table of lipid metabolism proteins pulled down with CDCP1-Flag in HEK 293T cells overexpressing CDCP1.

Accession #	Name	Peptides Identified	Normalized Spectral Count
gi|20127408	HADHA*	DLNSDMDSILASLK	0.001234
		DSIFSNLTGQLDYQGFEK	
		DTSASAVAVGLK	
gi|6552328	CYB5R3	APEAWDYGQGFVNEEMIR	0.000658
		STPAITLESPDIKYPLR	
		SVGMIAGGTGITPMLQVIR	
gi|4503607	ETFA*	AAVDAGFVPNDMQVGQTGK	0.00055
		GLLPEELTPLILATQK	
		LEVAPISDIIAIK	
gi|194097323	ECHS1*	AQFAQPEILIGTIPGAGGTQR	0.00027
		SLAMEMVLTGDR	
		KLFYSTFATDDRK	
gi|70995211	ECH1	VIGNQSLVNELAFTAR	0.000239
		VNLLYSR	
		ISWYLR	
gi|62530384	ECI1	DADVQNFVSFISK	8.66E-05
gi|530379431	MCCC2	AFYGDTLVTGFAR	0.000149
		TDFGIFR	
		FLYIWPNAR	
gi|4503023	CPT2	YILSDSSPAPEFPLAYLTSENR	0.000119
		AGLLEPEVFHLNPAK	
		LMSSGNEESLR	
gi|42794754	ACSL3*	LSPEPWTPETGLVTDAFK	7.26E-05
		GVMISHSNIIAGITGMAER	
		IGYSSPQTLADQSSK	
gi|4557817	OXCT1	AGGAGVPAFYTPTGYGTLVQEGGSPIK	5.03E-05
		GMGGAMDLVSSAK	
gi|76496475	ACADVL	GQLTTDQVFPYPSVLNEEQTQFLK	4.13E-05
gi|30089974	ACOX1	EFGIADPDEIMWFK	3.96E-05

*Only top three peptides listed.

Supplemental Table 1 | Antibodies

CHAPTER 2:

Western Blotting Primary Antibody	**Dilution**	**Company & catalog number**
rabbit anti-phospho CDCP1 Y734	1:1000	Cell Signaling #9050
rabbit anti-CDCP1	1:1000	Cell Signaling #4115
goat anti-CDCP1 antibody	1:1000	Abcam, Cambridge, MA #ab1377
mouse anti-Flag	1:1000	Sigma Aldrich #51804
rabbit anti-His-tag	1:1000	Cell Signaling #2365
rabbit anti-phospho PKCδ Y311	1:1000	Cell Signaling #2055
mouse anti-PKCδ	1:1000	Becton Dickinson Biosciences, San Diego, CA #610397
rabbit anti-Src	1:1000	Cell Signaling #2109
rabbit anti-Src	1:1000	SCBT, Santa Cruz, CA #sc-18
rabbit anti-phospho ERK 1/2 T202/T204	1:1000	Cell Signaling #4376
mouse anti-ERK	1:1000	Cell Signaling #9107
rabbit anti-phospho p38 MAPK T180/Y182	1:1000	Cell Signaling #9211
rabbit anti-p38 MAPK	1:1000	Cell Signaling #9212
mouse anti- phospho tyrosine	1:5000	Millipore #4G10
mouse anti-β-actin	1:1000	Sigma Aldrich #A5441
Western Blotting Secondary Antibody	**Dilution**	**Company & catalog number**
goat anti-mouse Horseradish Peroxidase (HRP) conjugate	1:5000	Pierce #31430
goat anti-rabbit HRP conjugate	1:5000	Pierce #31460
horse anti-mouse Alkaline Phosphatase (AP)	1:3000	Vector, Burlingame, CA #AP-2000
goat anti-rabbit AP	1:3000	Vector #AP-1000
rabbit anti-goat AP	1:3000	Thermo Scientific #31300

Immunocytochemistry Primary Antibody	**Dilution**	**Company & catalog number**
rabbit anti-CDCP1	1:200	Cell Signaling #4115
mouse anti-Flag	1:200	Sigma Aldrich #51804
Immunocytochemistry Secondary Antibody	**Dilution**	
donkey anti-mouse Alexa 488	1:200	Invitrogen #A-21202
donkey anti-rabbit Alexa 555	1:200	Invitrogen #A-31572
3D Assay Primary Antibody	**Dilution**	**Company & catalog number**
rabbit anti-Ki67	1:500	Leica Biosystems #KI67P-CE
mouse anti-phospho histone H3	1:200	Cell Signaling #9706
rabbit anti-cleaved caspase 3	1:200	Cell Signaling #9661
rabbit anti-His-tag	1:100	Cell Signaling #2365
3D Assay Secondary Antibody	**Dilution**	**Company & catalog number**
donkey anti-mouse Alexa 488	1:200	Invitrogen #A-21202
donkey anti-rabbit Alexa 555	1:200	Invitrogen #A-31572

CHAPTER 3:

Western Blotting Primary Antibody	**Dilution**	**Company & catalog number**
rabbit anti-CDCP1	1:1000	Cell Signaling #4115
Rabbit anti-ACSL3	1:1000	Thermo Fisher #PA5-42883
mouse anti- phospho tyrosine	1:1000	Millipore #4G10
mouse anti-β-actin	1:1000	Sigma Aldrich #A5441
Mouse anti-Flag	1:1000	Sigma Aldrich #51804
Western Blotting Secondary Antibody	**Dilution**	**Company & catalog number**
goat anti-mouse HRP conjugate	1:5000	Pierce #31430
goat anti-rabbit HRP conjugate	1:5000	Pierce #31460
horse anti-mouse Alkaline Phosphatase (AP)	1:3000	Vector, Burlingame, CA #AP-2000
Immunocytochemistry Primary Antibody	**Dilution**	**Company & catalog number**
rabbit anti-CDCP1	1:200	Cell Signaling #4115
goat anti-CDCP1	1:100	Abcam, Cambridge, MA #ab1377
Rabbit anti-ACSL1	1:100	Aviva #ARP32785_P050
Rabbit anti-ACSL3	1:200	Thermo Fisher #PA5-42883
Rabbit anti-ACSL4	1:100	Abgent #AP2536b
Rabbit anti-ACSL5	1:200	Novus Biologicals #NBP2-31995
Rabbit anti-RhoC	1:100	Cell Signaling #3430
Immunohistochemistry Primary Antibody		**Company & catalog number**
Goat anti-CDCP1	1:400	Abcam #ab1377
Rabbit anti-CDCP1	1:400	Cell Signaling #4115
Immunocytochemistry Secondary Antibody	**Dilution**	**Company & catalog number**
donkey anti-rabbit Alexa 555	1:200	Invitrogen #A-31572

CHAPTER 4:

Western Blotting Primary Antibody	**Dilution**	**Company & Catalog number**
rabbit anti-CDCP1	1:1000	Cell Signaling #4115
Western Blotting Secondary Antibody	**Dilution**	**Company & catalog number**
goat anti-rabbit HRP conjugate	1:5000	Pierce #31460
Immunocytochemistry Primary Antibody	**Dilution**	**Company & catalog number**
rabbit anti-cleaved caspase 3	1:200	Cell Signaling #9661
Immunocytochemistry Secondary Antibody	**Dilution**	**Company & catalog number**
donkey anti-rabbit Alexa 555	1:200	Invitrogen #A-31572

CHAPTER 5:

Western Blotting Primary Antibody	**Dilution**	**Company & Catalog number**
rabbit anti-CDCP1	1:1000	Cell Signaling #4115
Western Blotting Secondary Antibody	**Dilution**	**Company & catalog number**
goat anti-rabbit HRP conjugate	1:5000	Pierce #31460
Immunohistochemistry Primary Antibody	**Dilution**	**Company & catalog number**
rabbit anti-phospho PKCδ Y311	1:250	Abcam #ab76181
Immunohistochemistry Secondary Antibody	**Dilution**	**Company & catalog number**
Bond^{TM} Polymer Refine Detection system		Leica Biosystems #DS9800

Supplementary Table 2 | Oligonucleotides used for cloning.

CHAPTER 2:

Construct	Primers, gBlocks, and complimentary oligos (5'-3')	Restriction sites/ Notes
pLM-CMV-flCDCP1 from pDrive-flCDCP1	*F:ctctctgctagcgtcatggccggcctgaactg* *R:agagagctcgagttattctgctggctccatgg*	NheI XhoI
Reversion of mutated flCDCP1 to WT flCDCP1	*gcatcggtttagagctgcagTtttccatccctcgcctga g* *cagcctggtgctggtGccagcccAgaagctgcagc agcat* *tgtgggtatctacaatgAcaacatcaatactgagatgc cg* *gaaccgtacaccttctcccAtcccaacaatggggatg taa*	The WT nucleotides are capitalized
pLM-CMV-flCDCP1-Flag	*F:agagagggatcctcaacctctctctgcaaggc* *R:agagagctcgagtta**cttatcgtcgtcgtccttgt aatc**ttctgctggctccatgggct*	BamHI XhoI **Flag-tag**
pLM-CMV-flCDCP1-His	*F: agagagggatcctcaacctctctctgcaaggc* *R:agagagctcgagtta**atgatggtgatggtggtg**tt ctgctggctcatgggct*	BamHI XhoI **His-tag**
pLM-CMV-no-SP-cCDCP1-Flag	*F:ctctctgctagcaagtttgtccctggctgttt* *R:agagagctcgagtta**cttatcgtcgtcgtccttgt aatc**ttctgctggctccatgggct*	NheI XhoI **Flag-tag**
pLM-CMV-no-SP-cCDCP1-His	*F:ctctctgctagcaagtttgtccctggctgttt* *R:agagagctcgagtta**atgatggtgatggtggtg**tt ctgctggctcatgggct*	NheI XhoI **His-tag**
Addition of SP: pLM-CMV-cCDCP1-Flag and -His	*F:ctctcttctagaatggccggcctgaactgcgg* *R:agagaggctagcaaaagcttctgccccgcgcg*	XbaI NheI

pLM-CMV-cCDCP1-Y734F-Flag and -His	*aaggacaatgactcccatgtgtTCgcagtcatcgaggacaccatg*	Mutated nucleotides are capitalized
pLM-CMV-ECC-His	*F:ctctctgctagcaagtttgtccctggctgttt* *R:agagagctcgagttaatgatggtgatggtggtggtccacagtccttggggtaa*	NheI XhoI
pLM-CMV-N'luc	*F:agagagaccggt**ggtggaggcggttcaggcggaggtggcagcagatcc**atggaagacgccaaaaacat* *R:ctctctctcgagttacataatcataggtcctctga*	AgeI XhoI **linker**
pLM-CMV-C'luc	*F:agagagaccggt**ggtggaggcggttcaggcggaggtggcagcagatcc**atgtccggttatgtaaacaa* *R:ctctctctcgagttacacggcgatctttccgc*	AgeI XhoI **linker**
pLM-CMV-cCDCP1-N'luc and -C'luc	*F:agagagactagtatggccggcctgaactgcgg* *R:ctctctcgccggcggcttctgctggctccatgggct*	SpeI SgrAI
pLM-CMV-flCDCP1-N'luc and -C'luc	*F:ctctctgctagcatggccggcctgaactgcgg* *R:ctctctcgccggcggcttctgctggctccatgggct*	NheI SgrAI
pLM-CMV-sh-ins-flCDCP1	*gctagcgtcatggccggcctgaactgcggggtctctatcgcactgctagggttctgctgctgggtgcggcgcgcctgccgcgcggggcagaagcttttgagattgctctAccCcgCgaGagTaaTatCacTgtCctGatCaagctggggaccccgactctgctggcaaaGccGtgCtaTatAgtTatttctaaaagacatataaccatgttgtcTatTaaAtcGggCgaGagGatagtctttacctttagctgccagagtcctgaAaaCcaTttCgtTatCgagatccagaaaaatattgactgtatgtcaggcccatgtccttttggggaggttcagcttcagccctcgacatcgttgttgcctacctcaacagaactttcatctgggatgtcaaagcAcaCa*	NheI Mutated nucleotides are capitalized

	aAagTatAggGttGgagctgcagttttccatccctcg *cctgaggcagatcggtccgggtgagagctgcccaga* *cggagtcactcactccatcagcggccgaatcgatgcc* *accgtggtcaggatcggaaccttctgcagcaatggca* *ctgtgtcccggatcaagatgcaagaaggagtgaaaa* *tggccttacacctcccatggttccaccccagaaatgtct* *ccggcttcagcattgcCaaTcgTtcTtcAatTaaac* *gtctgtgcatcatcgagtctgtgtttgagggtgaaggct* *cagcaaccctgatgtctgccaactacccagaaggctt* *ccctgaggatgagctcatgacgtggcagtttgtcgttcc* *tgcacacctgcgggccagcgtctccttcctcaacttca* *acctctccaactgtgagaggaaggaggagcgggttg* *aatactacatcccgggctccaccaccaaccccgagg* *tgttcaagctggaggacaagcagcctgggaacatgg* *cggggaacttcaacctctctctgcaaggctgtgacca* *agatgcccaaagtccagggatcc*	BamHI
pLM-CMV-sh-ins-ncCDCP1	*gtacggcgcaatcgtagccagagatcgagtcgtggat* *tacgagcatcgagatatatggatcctccggctgcagtt* *ccaagttttggtccaacatccacaaaatgaaagcaat* *aaaatctacgtggttgacttgagtaatgagcgagccat* *gtcactcaccatcgagccacggcccgtcaaacagag* *ccAGaaCtttgtccctggctgtttcgtgtgtctagaatct* *cggacctgcagtagcaacctcaccctgacatctggct* *ccaaacacaaaatctccttcctttgtgatgatctgacac* *gtctgtggatgaatgtggaaaaaaccataagctgcac* *agaccaccggtgcgcgctgggtagacgtatgacgat* *agcatgcatgacgatcaaaccccgtgttgtgcatcag* *ctagcatcgttacatgactagtggtcagcggcaattac* *gatagggatacgacgtacatgcaga*	BamHI Mutated nucleotides are capitalized AgeI

pLKO.1shCDCP1-7	*F:ccggaaccctgttacatcgtcatctcgagatgacgatgtaacagggttttttg* *R:aattcaaaaaaaccctgttacatcgtcatctcgagatgacgatgtaacagggtt*	AgeI and EcoRI compatible sticky ends in complimentary oligos; shRNA binding sites
hTBP (qRT-PCR)	*F:cccgaaacgccgaat* *R:gactgttcttcactcttggctc*	
CDCP1 (qRT-PCR)	*F:gccacgagaaagcaacattaca* *R:aaaggacatgggcctgacata*	

CHAPTER 3:

Construct	Primers (5'-3')	Restriction Sites/ Notes
pLKO.1shCDCP1-2	See Chapter 2, pLKO.1shCDCP1-7	Wright et al. [5]
pLKO.1shACSL3	F:*ccggtgaccaacatcgccatcttcctcgaggaagatggcgatgttggtcttttg* R:*aattcaaaaagaccaacatcgccatcttcctcgaggaagatggcgatgttggtca*	AgeI and EcoRI; shRNA stem sequences See Obata et al. [175]
pLM-CMV-ACSL3-blasticidin	F:*atatatgctagcatgaataaccacgtgtcttc* R:*gcgcgcctcgagttattttcttccatacattc*	NheI and XhoI; sequences complementary to ACSL3

CHAPTER 5:

SDM Primer Name	**Sequence**
H4A Mutation	Single mutation: *cataagctgcacagaccacGCgtactgccaaaggaaatcctac* Double mutation with R5A: *cataagctgcacagacGCcGCgtactgccaaaggaaatcctac*
R5A Mutation	*cataagctgcacagacGCccggtactgccaaaggaaatcctac*
V25G Mutation	*catcctccacctgcctgGggagctgcatgacttctcctggaag*
H28A Mutation	*cctccacctgcctgtggagctgGCtgacttctcctggaagctgct*
K33A Mutation	*agctgcatgacttctcctggGCgctgctggtgcccaaggacag*
Q75A Mutation	*ggccagtgccatacccagcGCggacctgtacttcggctcc*
pET-28a+ Primers	**Sequence**
ECC	F: *ctctctcatatgatgaagtttgtccctggctgttt* R: *ctctctctcgagtcagtccacagtccttggggtaa*